Time-gated spectroscopy
for the classification and recycling
of fluorescently labeled waste plastics

Petr Fomin

Vollständiger Abdruck der von der Fakultät für Elektrotechnik und Informationstechnik der Universität der Bundeswehr München zur Erlangung des akademischen Grades eines

Doktor-Ingenieurs

genehmigten Dissertation.

Gutachter:

1. Univ.-Prof. Dr. Christian Kargel
2. Univ.-Prof. Dr.-Ing. habil Alexander Koch

Die Dissertation wurde am 31.10.2019 bei der Universität der Bundeswehr München eingereicht und durch die Fakultät für Elektrotechnik und Informationstechnik am 23.03.2020 angenommen. Die mündliche Prüfung fand am 23.10.2020 statt.

Acknowledgments

Throughout the writing of this dissertation as well as the preceding research, I received a great deal of support, both professionally and personally, from the following people:

First and foremost, I would like to express my deepest appreciation to my supervisor, Professor Christian Kargel, for the opportunity to work on this dissertation. His professional expertise was invaluable in formulating the research methodology and setting me on the scientific path. Without his constant guidance, encouragement, and patience, the completion of this dissertation would not have been possible.

Furthermore, I would like to thank Prof. Alexander W. Koch for being the second reviewer of my dissertation. I would also like to thank Prof. Walter Hansch for chairing the examination committee and organizing the defense.

I would like to extend my sincere thanks to Dr. Siegfied Brunner, insightful and long conversations with whom have helped me sharpen my thinking and were an immense source of knowledge. I am also grateful to Dr. Dmitry Zhelondz for assisting me with many electronic parts of the prototype system and later with the experiments. I very much appreciate the support of Dr. Heinrich Ruser. His valuable feedback has helped improve the quality of my research.

It is certainly thanks to Mr. Jürgen Lang and his natural hardware skills that the prototype system has come to life. Without his constant optimism and readiness to help it wouldn't have been possible to put all the parts together and get them going. Furthermore, I thank Mr. Heinz Ketzer and his apprentices for helping with the electronics of the system and many laboratory setups. I also thank Ms. Petra Heggenberger for providing her assistance with numerous administrative chores and paperwork.

Last but not least, and probably most importantly, I would like to thank my family for their continuous support. My wife Anna, who has been with me during all ups and downs of this long and certainly not straight path, and who joined me moving to Germany when it was not at all clear what the future might hold for us in a new and foreign country. She has always been and continues to be an inspiration. Warm thanks also go to my parents, who despite all difficulties and uncertainties of letting their only son (then in his early twenties) going to a foreign country with no relatives or friends, not only accepted my choice but in fact strongly encouraged and supported me throughout all the years. I thank you from the bottom of my heart!

Abstract

Plastics have long become indispensable materials in modern society. In light of the ever-growing production volumes of plastics, recycling of end-of-life plastic products becomes increasingly important every year. The recycling of plastics waste is attractive from both the environmental and economic points of view. It reduces the amounts of waste buried in landfills and the CO_2 emission associated with the production of new plastic resins and helps reduce the usage of strategic fossil resources such as crude oil. One of the main difficulties associated with the recycling of plastics is the need for mono-fractional sorting of plastics of different types and grades. If different types of plastics are mixed and used together for recycling, the resulting product has low quality and cannot compete with products made from brand new plastics. This is especially important in demanding applications where high-quality material properties are required. Thus sorting waste plastics is key to the success of recycling.

The goal of this dissertation is the development and practical evaluation of a spectroscopic measurement and classification system for the automated sorting of shredded flakes of different plastic types based on their fluorescence spectra. In contrast to the state-of-the-art spectroscopic approaches which rely on the intrinsic properties of the plastics, this work investigates the concept of "fluorescent labeling". The idea is to incorporate small amounts (at ppm concentration levels) of appropriate fluorescent tracers (or "markers") into the raw plastics during the manufacturing process thus generating unique fluorescence spectra emitted by the plastics. These fluorescence spectra can then be measured using a dedicated spectroscopic instrument and used for the plastics classification. Markers are incorporated into the plastics according to a certain (e.g. binary) coding scheme in order to increase the overall number of different plastics that can be labeled. Fluorescent markers can be especially helpful in the case of dark and black plastics with their normally flat, non-characteristic reflectance and/or fluorescence spectra by adding specific features to these spectra. Additionally, the use of fluorescence markers does not only allow the classification of plastics of different types (i.e. with different chemical structures), but also plastics of the same type that are produced by different manufacturers or sold to different customers. In fact, virtually any information can be encoded into plastics through fluorescence labeling. For example, fluorescent markers can help distinguish original plastic parts from counterfeit ones.

The idea of fluorescent labeling was first proposed about 20 years ago but has not yet been put into wide industrial practice. Some commercially available systems carry

out macro-sorting of plastics, i.e. the sorting of large objects such as for example plastic bottles. For complex assemblies consisting of many parts made of different plastic types, a prior disassembling is thus necessary. In contrast, micro-sorting deals with small (in the millimeter range) flakes of shredded plastics, does not require the labor-intensive prior disassembling, and is, therefore, more flexible and attractive for the recycling of plastic waste. This dissertation focuses on the micro-sorting approach.

Due to the chemical structure of the plastics and/or various additives such as brightening components or for UV-protection, many plastics exhibit the so-called autofluorescence. The autofluorescence spectrally overlaps with the fluorescence of the incorporated markers and may even completely mask it. A strong autofluorescence can make correct and reliable classification of fluorescently labeled plastics problematic or even impossible in practice. To combat the negative influence of the autofluorescence, a method called the time-gated fluorescence spectroscopy (TGFS) is proposed in this work. This method dwells on the fact that the fluorescence emission decays exponentially when the excitation light is turned off and that the fluorescence decay time constants of inorganic markers are usually orders of magnitude larger than those of the typical autofluorescence. Using a pulsed excitation light in combination with time-gated acquisition of the fluorescence emission makes it possible to (almost) completely avoid the presence of autofluorescence in the measured spectra. The obvious downside of this method is a decreased signal intensity and thus lower signal-to-noise ratio (S/N ratio) of the acquired fluorescence spectra in comparison to spectra acquired without pulsing and time-gating. Low fluorescence intensities and S/N ratios are disadvantageous for the classification performance and thus must be maximized. In the context of TGFS, the intensity of the acquired fluorescence spectra mainly depends on the fluorescence decay time constants of the markers and on the acquisition parameters of the time-gating. The former are governed by chemical/physical laws and are difficult to modify. The latter, however, can be easily varied in order to achieve the highest possible S/N ratio and in turn the best classification. For this purpose, a mathematical model for the fluorescence intensity of the TGFS spectra is proposed and investigated in this dissertation. This model is then used to find the best suitable acquisition parameters for TGFS.

In order to achieve the best possible classification performance, various approaches to the classification of the fluorescence spectra emitted from the labeled plastics are investigated including the relatively simple and thus numerically efficient naive Bayes' methods and spectral similarity measures, as well as more complex ones such as neural networks (NN), support vector machines (SVM) and random forests (RF). The classification algorithms are implemented in a simulation framework developed to allow the modeling of marker fluorescence spectra corrupted with different disturbances important in practice, such as the measurement noise, autofluorescence, etc. Classifiers are evaluated using computer simulations with respect to these disturbances.

In order to quantify the classification performance of a TGFS system for fluorescently labeled plastics in practice, a prototype system was built. The prototype was developed with a particular focus on an industrial environment in a typical recycling facility and designed to process shredded plastic flakes with sizes between approx. 3 mm and 10 mm

on a 500 mm wide conveyor belt in 50 parallel channels. Six fluorescent markers were used in binary combinations allowing to label up to $2^6 - 1 = 63$ different plastics. The prototype was thus capable to classify and sort flakes of up to 63 different fluorescently labeled plastics simultaneously with a mass throughput of up to about 250 kilogram per hour. Extensive experimental measurements with approximately 140 000 shredded flakes of different fluorescently labeled plastics and ∼10 000 unlabeled plastic flakes were carried out to evaluate the performance of the prototype. A very high classification performance was achieved: an average sensitivity (i.e. true positive rate, TPR) of 99.76% and an average precision (i.e. positive predictive value, PPV) of 99.88%. Additionally, measurements with fluorescently labeled black plastic flakes were carried out yielding virtually the same high performance: TPR of 99.76% and PPV of 99.60%. The results are not 100% perfect since some misclassifications occurred due to the low S/N ratio of the spectra measured from very small flakes (smaller than approx. 2 mm). The majority of the misclassifications are due to the unequal intensities of individual markers in the marker combinations which led to some "stronger" markers masking the presence of the "weaker" markers in the measured fluorescence spectra. Nevertheless, out of 150 000 experimentally investigated flakes only 338 were misclassified, which only is 0.23%.

The investigations in this dissertation show that a highly reliable classification of fluorescently labeled plastics is possible in practice. This work proves that the principle of fluorescent labeling is applicable not only for the macro-sorting of large plastic objects but also for the more versatile micro-sorting of small shredded plastic flakes. Moreover, this approach can be successfully implemented in an industrial environment. Clearly, certain adaptation and optimization steps must be taken especially with respect to achieving a higher mass throughput (several tons per hour) for an industry-scale operation. Using a larger number of markers is also possible and would allow labeling and classifying more plastics simultaneously. Overall, this dissertation demonstrates a promising way to make the recycling of waste plastics flexible, economically attractive, and successful.

Kurzfassung

In der modernen Gesellschaft sind Kunststoffe seit langem unverzichtbar. Angesichts der stetig steigenden Produktionsmengen von Kunststoffen wird das Recycling von Kunststoffabfällen von Jahr zu Jahr immer wichtiger. Recycling ist sowohl aus ökologischer als auch aus wirtschaftlicher Sicht attraktiv, da es nicht nur die Abfallmenge auf Mülldeponien und den CO_2-Ausstoß bei der Herstellung neuer Kunststoffe reduziert, sondern auch dazu beiträgt, den Verbrauch begrenzter fossiler Ressourcen wie Rohöl zu reduzieren. Eine der Hauptschwierigkeiten beim Recycling von Kunststoffen ist die Notwendigkeit einer sortenreinen Trennung von Kunststoffen verschiedener Typen. Wenn unterschiedliche Kunststofftypen beim Recycling miteinander vermischt werden, weist das resultierende Produkt eine geringere Qualität auf und kann deshalb nicht mit Produkten aus brandneuen Kunststoffen konkurrieren. Dies ist besonders wichtig bei anspruchsvollen Anwendungen, bei denen hochwertige, spezifische Materialeigenschaften erforderlich sind. Die Sortierung von Kunststoffabfällen ist daher der Schlüssel zum Erfolg des Recyclings.

Ziel dieser Dissertation ist die Entwicklung und praktische Umsetzung eines spektroskopischen Mess- und Klassifizierungssystems zur automatisierten Sortierung von typischem Kunststoffmahlgut ("Flakes") verschiedener Kunststofftypen anhand ihrer Fluoreszenzspektren. Im Gegensatz zu den bestehenden spektroskopischen Systemen, die intrinsische Eigenschaften der Kunststoffe nutzen, wird in dieser Arbeit das Konzept der "Fluoreszenzmarkierung" untersucht. Die Idee ist, kleine Mengen (in ppm-Konzentrationen) geeigneter Fluoreszenzleuchtstoffe (oder "Marker") in die Rohkunststoffe im Rahmen des Herstellungsprozesses einzubringen, um so den Kunststoffen einzigartige Fluoreszenzspektren zuzuweisen. Diese Fluoreszenzspektren können dann mit einem speziellen spektroskopischen Messsystem gemessen und für die Kunststoffklassifizierung verwendet werden. Um die Gesamtzahl der verschiedenen Kunststoffe, die markiert werden können, zu erhöhen, werden die Marker gemäß einem bestimmten (z.B. binären) Codierungsschema in die Kunststoffe eingebracht. Außerdem sind Fluoreszenzmarker besonders bei dunklen und schwarzen Kunststoffen mit ihren normalerweise flachen, nicht charakteristischen Reflexions- und/oder Fluoreszenzspektren hilfreich, indem diesen Spektren spezifische Merkmale hinzugefügt werden. Darüber hinaus ermöglicht die Verwendung von Fluoreszenzmarkern nicht nur die Klassifizierung von Kunststoffen unterschiedlicher Typen (d.h. mit unterschiedlichen chemischen Strukturen), sondern auch von Kunststoffen desselben Typs, die von unterschiedlichen Firmen hergestellt oder an unterschiedliche Kunden verkauft werden. Tatsächlich können praktisch beliebige Informationen durch Fluoreszenzmarkierung in Kunststoffe

kodiert werden. Beispielsweise können Fluoreszenzmarker dazu beitragen, originale Kunststoffteile von gefälschten zu unterscheiden.

Die grundsätzliche Idee der Fluoreszenzmarkierung wurde erstmals vor etwa 20 Jahren vorgeschlagen, aber noch nicht in die breite industrielle Praxis umgesetzt. Einige im Handel erhältliche Systeme setzten die Makrosortierung von Kunststoffen um, d.h. die Sortierung großer Objekte wie beispielsweise Plastikflaschen. Bei komplexen Baugruppen, die aus vielen unterschiedlichen Kunststofftypen bestehen, ist daher die vorherige Demontage erforderlich. Im Gegensatz dazu arbeitet die Mikrosortierung mit Kunststoffmahlgut (einige Millimeter große Kunststoff-Flakes), erfordert keine arbeitsintensive vorherige Demontage und ist daher flexibler und attraktiver für das Recycling von Kunststoffabfällen. Diese Dissertation konzentriert sich auf den Mikrosortierungsansatz.

Aufgrund der chemischen Struktur der Kunststoffe und/oder verschiedener Additive wie z.B. UV-Schutz weisen viele Kunststoffe die sogenannte Autofluoreszenz auf. Die Autofluoreszenz überlappt spektral mit der Fluoreszenz der eingebauten Marker und kann diese sogar vollständig maskieren. Eine starke Autofluoreszenz kann die korrekte und zuverlässige Klassifizierung der markierten Kunststoffe problematisch oder sogar unmöglich machen. Um dem negativen Einfluss der Autofluoreszenz entgegenzuwirken, wird in dieser Arbeit ein Verfahren vorgeschlagen, das als zeitaufgelöste Fluoreszenzspektroskopie (Time-Gated Fluorescence Spectroscopy, TGFS) bezeichnet wird. Dieses Verfahren beruht auf der Tatsache, dass die Fluoreszenzemission exponentiell abnimmt, nachdem das Anregungslicht ausgeschaltet wird, und dass die Fluoreszenzabklingzeitkonstanten anorganischer Fluoreszenzmarker üblicherweise um mehrere Zehnerpotenzen größer sind als die der typischen Autofluoreszenz. Die Verwendung eines geeigneten gepulsten Anregungslichts in Kombination mit einer zeitgesteuerten Erfassung der Fluoreszenzemission ermöglicht es, den Einfluss der störenden Autofluoreszenz im gemessenen Spektrum (fast) vollständig zu vermeiden. Der offensichtliche Nachteil dieses Verfahrens ist eine verringerte Signalintensität und damit ein geringeres Signal-zu-Rausch-Verhältnis (S/N-Verhältnis) der erfassten Fluoreszenzspektren im Vergleich zu Spektren, die mit nicht gepulstem Anregungslicht und ohne TGFS erfasst wurden. Eine geringe Fluoreszenzintensität bzw. ein niedriges S/N-Verhältnis sind für die Klassifizierungsleistung nachteilig und müssen daher maximiert werden. Bei der TGFS-Messung hängt die Intensität der erfassten Fluoreszenzspektren hauptsächlich von den Abklingzeitkonstanten der Marker-Fluoreszenz und von den Parametern der zeitgesteuerten Erfassung (time-gating) ab. Die Abklingzeitkonstanten unterliegen chemischen und physikalischen Gesetzen und sind schwer zu beeinflussen. Die zeitgesteuerte Erfassung kann jedoch leicht variiert werden, um das höchstmögliche S/N-Verhältnis und damit die beste Klassifizierungsleistung zu erreichen. Zu diesem Zweck wird in der vorliegenden Dissertation ein mathematisches Modell der Fluoreszenzintensität der TGFS-Spektren vorgeschlagen und dafür eingesetzt, die besten Parameter der Zeitsteuerung des TGFS zu finden.

Um die bestmögliche Klassifizierungsergebnisse zu erzielen, werden verschiedene Ansätze zur Klassifizierung der von den markierten Kunststoffen emittierten Fluoreszenzspektren untersucht, darunter die relativ einfachen und damit numerisch effizienten naiven Bayes-Methoden und spektralen Ähnlichkeitsmaße (similarity measures) sowie komplexere

wie künstliche Neuronale Netze (NN), Support Vector Machines (SVM) und Random Forests (RF). Die Klassifizierungsalgorithmen werden in einem dafür entwickelten Simulations-Framework implementiert und im Hinblick auf Störfaktoren wie insbesondere Sensor- bzw. Messrauschen und Autofluoreszenz miteinander verglichen.

Um die Klassifizierungsleistung des TGFS-Systems in der Praxis zu quantifizieren, wurde ein Prototypsystem gebaut. Der Prototyp wurde im Hinblick auf eine industrielle Umgebung einer typischen Recyclinganlage entwickelt, und für die Verarbeitung von Kunststoff-Flakes mit Abmessungen zwischen ca. 3 mm und 10 mm auf einem 500 mm breiten Förderband in 50 parallelen Vereinzelungskanälen ausgelegt. Sechs Fluoreszenzmarker wurden in binären Kombinationen verwendet, um bis zu $2^6 - 1 = 63$ verschiedene Kunststoffe zu markieren. Dieser Prototyp war somit in der Lage, Flakes von bis zu 63 verschieden markierten Kunststoffen gleichzeitig mit einem Massendurchsatz von bis zu etwa 250 Kilogramm pro Stunde zu klassifizieren bzw. zu sortieren. Um die Leistungsfähigkeit des Prototyps zu bewerten, wurden umfangreiche experimentelle Messungen mit ungefähr 140 000 Flakes von verschiedenen fluoreszenzmarkierten Kunststoffen und ca. 10 000 unmarkierten Kunststoff-Flakes durchgeführt. Dabei wurde eine sehr hohe Klassifizierungsleistung erreicht: eine durchschnittliche Sensitivität (d.h. Richtig-Positiv-Rate, True Positive Rate, TPR) von 99.76% und eine durchschnittliche Genauigkeit (d.h. Positiver Vorhersagewert, Positive Predictive Value, PPV) von 99.88%. Zusätzlich wurden Messungen mit fluoreszenzmarkierten schwarzen Kunststoff-Flakes durchgeführt, mit denen praktisch die gleiche hohe Klassifizierungsleistung erzielt wurde: TPR = 99.76% und PPV = 99.60%. Die Ergebnisse sind nicht zu 100% perfekt, weil aufgrund des niedrigen S/N-Verhältnisses der von sehr kleinen Flakes (kleiner als ca. 2 mm) gemessenen Spektren einige Fehlklassifizierungen auftraten. Die Mehrzahl der Fehlklassifizierungen ist auf die ungleichen Intensitäten einzelner Marker in den Markerkombinationen zurückzuführen, die dazu führten, dass einige "stärkere" Marker die Emission der "schwächeren" Marker in den gemessenen Fluoreszenzspektren maskierten. Von den 150 000 experimentell untersuchten Flakes wurden jedoch insgesamt nur 338 falsch klassifiziert, was einem Prozentsatz von nur 0.23% entspricht.

Die durchgeführten Untersuchungen zeigen, dass eine äußerst zuverlässige Klassifizierung von fluoreszenzmarkierten Kunststoffen in der Praxis möglich ist. Die vorliegende Dissertation zeigt, dass das Prinzip der Fluoreszenzmarkierung nicht nur für die Makrosortierung großer Kunststoffobjekte anwendbar ist, sondern auch für die wesentlich vielseitigere Mikrosortierung von kleinen Kunststoff-Flakes (Kunststoffmahlgut). Darüber hinaus kann dieses Verfahren in einem industriellen Umfeld erfolgreich umgesetzt werden. Dieses Verfahren stellt eine vielversprechende Möglichkeit dar, das Recycling von Kunststoffabfällen flexibel, wirtschaftlich attraktiv und erfolgreich zu gestalten.

Contents

List of figures

List of tables

List of acronyms

ABS acrylonitrile butadiene styrene. 6, 7

ADC analog-to-digital converter. 39

AF autofluorescence. 18, 19, 26, 27, 28, 64, 66, 76, 78, 80, 82, 83, 85, 93, 98, 102, 104, 105, 141, 159

AOTF acusto-optical tunable filters. 34, 100

CCD charge-coupled device. 37, 39, 40, 41, 43, 44, 66, 85, 86, 90, 100, 101, 102, 104, 118, 160

CMOS complementary metal-oxide-semiconductor. 37, 39, 40, 100, 160

DSCC differential spectral cross correlation. 48, 65, 73, 75, 76, 82

ED euclidean distance. 46, 47, 56, 65, 73, 75, 76, 82, 124

FCLS fully constrained least squares. 53, 71, 73, 75, 82

FN false negatives. 62, 63, 64, 132

FOV field of view. 113, 121

FP false positives. 62, 63, 64, 132, 146, 150

FPN fixed pattern noise. 119

FWHM full width at half maximum. 23, 82, 116, 119, 158

HDPE high-density polyethylene. 4, 5, 6, 8

ICCD intensified CCD. 100

IR infrared. 7, 8, 157, 158

LCTF liquid-crystal tunable filters. 34, 100

PPV positive predictive value. 62, 63, 64, 65, 67, 71, 128, 129, 131, 132, 133, 136, 137, 138, 140, 141, 142, 143, 144, 145, 146, 148, 149, 150, 152, 154, 159, 161

PRNU photo-response non-uniformity. 119

PS polystyrene. 4, 5, 6, 7, 8

PVC polyvinyl chloride. 3, 4, 5, 6, 7, 8

RF random forest. iv, 57, 65, 67, 70, 69, 71, 73, 74, 75, 74, 75, 76, 78, 79, 80, 82, 159

RFID radio-frequency identification. 8

RIC resin identification code. 8

ROI region of interest. 36, 37, 39, 100, 121

S/AF ratio signal-to-autofluorescence ratio. 27, 78, 79, 80, 79, 82, 85, 90, 91, 93, 167

S/N ratio signal-to-noise ratio. iv, 15, 17, 24, 26, 27, 35, 36, 39, 40, 41, 42, 43, 44, 50, 66, 67, 69, 70, 71, 73, 82, 83, 85, 86, 87, 90, 91, 98, 100, 101, 102, 103, 102, 105, 118, 120, 133, 138, 140, 141, 142, 145, 146, 147, 150, 151, 150, 151, 152, 159, 161, 162, 167, 173

SAD sum of absolute differences. 47

SAM spectral angle mapper. 48, 65, 71, 73, 75, 76, 80

SCC spectral cross correlation. 47, 48, 65, 71, 73, 75, 76, 80, 83, 85, 87, 88, 90, 91, 90, 124, 136, 137, 140, 145, 150, 152, 159, 161, 162

SCLS sum-to-one constrained least squares. 53, 65, 71, 73, 75, 82

SVM support vector machine. iv, 57, 58, 65, 71, 73, 75, 76, 79, 80, 82, 124, 159

TCSPC time-correlated single photon counting. 32, 94, 105, 106

TGFS time-gated fluorescence spectroscopy. iv, 19, 28, 39, 66, 93, 98, 100, 102, 103, 102, 104, 106, 107, 117, 118, 119, 120, 122, 133, 141, 142, 159, 160, 172

TN true negatives. 62

TP true positives. 62, 63, 132, 146, 150, 181

TPR true positive rate. 62, 63, 64, 65, 67, 71, 128, 129, 131, 132, 133, 136, 137, 138, 140, 141, 142, 143, 144, 145, 146, 148, 149, 150, 152, 154, 159, 161

List of symbols

a constant for conversion from light intensity to digital counts with units m^2/W. 29, 30, 105, 107

$\boldsymbol{\alpha}$ vector of marker abundance fractions. 51, 52, 53

α single marker abundance fraction in $\boldsymbol{\alpha}$. 51, 52, 53, 54

b width of the conveyor belt. 121

b' width of the conveyor belt projection on the image plane (sensor). 121

C number of classes ω. 47, 48, 50, 54, 55, 56, 58, 61, 63, 64, 136

c confidence interval. 131, 132, 133

$\boldsymbol{D}$ diagonal matrix composed of eigenvalues e of covariance matrix $\boldsymbol{\Sigma}$. 49

D duty cycle of the excitation light pulses in TGFS. 105, 106, 107, 106, 109, 110, 109, 110, 122, 133, 171, 172

d working distance of an optical instrument. 121, 122

$\boldsymbol{E}$ matrix composed of eigenvectors e of $\boldsymbol{\Sigma}$. 49

E excitation spectrum intensity at a certain wavelength λ. 12, 14, 15, 22, 23

$\boldsymbol{\Sigma}$ covariance matrix of the dataset $\boldsymbol{S}$. 49, 56

$\boldsymbol{e}$ eigenvector of covariance matrix $\boldsymbol{\Sigma}$. 49

e eigenvalue of covariance matrix $\boldsymbol{\Sigma}$. 49

ϵ neural network training error function. 60, 61

η LED overdrive factor. 109

$\boldsymbol{F}$ feature dataset. 57, 58, 61

F focal length of an objective lens. 121, 122

$\boldsymbol{f}$ feature vector. 48, 54, 55, 56, 57, 58, 59, 61, 69

f single feature in $\boldsymbol{f}$. 48, 54, 55, 56, 57, 58, 59

f_p frequency of the excitation light pulses. 105, 106

Γ emissive rate of a fluorophore. 14, 93, 94

$\boldsymbol{g}$ classification target vector. 58, 61, 65

$\hat{\boldsymbol{g}}$ classifier's output vector. 61

g class label or single element in the target vector $\boldsymbol{g}$. 57, 58, 61

$\hat{g}$ classifier's output, single element in $\hat{\boldsymbol{g}}$. 59, 61

$\boldsymbol{h}$ vector of weights of the SVM hyperplane. 57

h weights of the SVM hyperplane. 57

I fluorescence emission intensity at a particular wavelength band λ. 12, 14, 15, 29, 30, 31, 37, 42, 94, 97

I_d fluorescence intensity decay function. 104, 105

I_{d0} initial fluorescence intensity of the decay function at time instant $t = t_0$. 104

I_r fluorescence intensity rise function. 104

I_{r0} maximal steady-state fluorescence intensity. 104, 105, 107

J number of members in a dataset. 49, 50, 57, 58, 61

K number of features in $\boldsymbol{f}$. 55, 56, 57, 58, 59

k_{nr} non-radiative decay rate of a fluorophore. 14, 93, 94

L LDA objective function. 50

l' spectrograph slit width. 121, 122

l width of the spectrograph imaging line. 121, 122, 129

Λ number of discrete wavelength bands in the spectrum. 29, 31, 35, 37, 42, 43, 46, 47, 48, 49, 51, 64, 67, 133

λ discretized wavelength band. 12, 14, 15, 20, 22, 23, 29, 30, 31, 32, 35, 36, 37, 40, 41, 44, 46, 47, 48

$\Delta\lambda$ analog wavelength band. 14, 15, 29, 30, 31, 32, 34, 42, 94

$\boldsymbol{M}$ fluorescent markers signature matrix consisting of vectors $\boldsymbol{m}$. 51, 52, 53, 54

M overall number of fluorescent markers. 22, 51, 52, 53

$\boldsymbol{m}$ digitized marker fluorescence spectrum. 51, 52, 73, 74

m single element in $\boldsymbol{m}$. 51

$\boldsymbol{\mu}$ mean spectrum of a class. 50

N number of subframes acquired in "frame accumulation" mode. 43, 44, 100, 101, 105, 106, 107, 118, 122, 133, 142

$\boldsymbol{n}$ $\Lambda \times 1$ noise vector. 42, 52, 66, 86

n single noise component of the noise vector $\boldsymbol{n}$. 42, 43, 44, 66

ν number of excited fluorophores. 93, 94

P power of the signal. 27, 42, 43, 44, 66

ρ probability distribution of a random feature. 54, 55, 56

Φ SVM kernel transformation function. 58

φ neuron's activation function. 59

Ψ SVM kernel function. 58

Θ fluorescence quantum yield. 14, 15

R Bayes risk. 55

$\boldsymbol{r_i}$ mean (reference) spectral vector of class ω. 46, 47, 48

r_i single element in $\boldsymbol{r_i}$. 46, 47

$\boldsymbol{S}$ (spectral) dataset consisting of spectra $\boldsymbol{s}$. 49, 50

$\widetilde{\boldsymbol{S}}$ spectral dataset after transformation. 49

$\boldsymbol{S_B}$ between classes scatter matrix. 50, 51

$\boldsymbol{S_W}$ within classes scatter matrix. 50, 51

$\boldsymbol{s}$ digitized fluorescence emission spectrum. 29, 30, 35, 42, 44, 46, 47, 48, 49, 50, 51, 52, 53, 54, 56, 66, 67, 86

$\widetilde{\boldsymbol{s}}$ transformed vector in $\widetilde{\boldsymbol{S}}$. 49, 50

s digitized sensor signal equivalent to the fluorescence emission intensity at wavelength λ. 29, 30, 31, 35, 36, 37, 41, 42, 43, 44, 46, 47, 49, 64, 66, 104, 105, 107

s_N digitized sensor signal equivalent to the TGFS fluorescence intensity at wavelength λ accumulated over N subframes. 105, 106, 107, 106, 107, 109, 110, 109, 110, 109, 118, 171, 172

T period of the excitation light pulse in TGFS. 104, 105

T_m time available for one measurement. 101, 105, 106, 107, 122, 124, 171, 172

T_R read-out time: time needed to read-out of one frame. 101, 118, 122, 133

t_0 start time instant of the TGFS acquisition. 104, 105

t_e stop time instant of the TGFS acquisition. 104, 105

t_p excitation impulse duration. 103, 104, 105, 106, 107, 106, 109, 110, 109, 110, 122, 133, 171, 172

τ_d fluorescence decay time constant. 94, 95, 96, 97, 98, 104, 105, 106, 107, 106, 109, 110, 109

τ_r fluorescence rise time constant. 104, 105, 106, 107, 106, 109, 110, 109

$\boldsymbol{U}$ identity matrix. 53, 56

v_c conveyor belt velocity. 122

$\mathbf{W}$ matrix composed of $\mathbf{w}$ vectors. 50, 51

$\mathbf{w}$ LDA transformation operator. 51

w neural network's weight factor. 59, 60

ω label of class i. 46, 47, 50, 54, 55, 56, 57, 58, 61, 62, 63, 64, 138

X the x-size of the 3D hypercube. 29, 31, 35

x coordinate in the 3D hypercube corresponding to real world coordinate x. 29, 30, 35, 37, 44

x real world coordinate in the object plane along the conveyor belt movement. 29, 30, 35, 36, 37, 115, 119

ξ Bayes cost function. 55

Y the y-size of the 3D hypercube. 29, 31, 35, 37

y coordinate in the 3D hypercube corresponding to real world coordinate y. 29, 30, 35, 36, 37, 41, 44

y real world coordinate in the object plane across the conveyor belt movement. 29, 30, 35, 36, 37, 115, 119

Z number of actions in Bayes decision rule. 55

$\boldsymbol{z}$ set of actions z. 55

z action in Bayes decision rule. 55

Chapter 1

Introduction

The annual world production of plastics has been constantly growing in the recent few decades: between 2005 and 2016 it climbed from around 230 million tons to over 335 million tons [1]. The reason for that is the incredible versatility of plastic materials and the unique properties they possess. Nowadays, plastics are used virtually everywhere. For packaging and in buildings, electrical and electronic equipment, automotive and aeronautics industries are just a few examples of their application fields.

However, this incredible success of plastic materials has urged the need for recycling of plastics waste to become more and more noticeable. In 2016, alone in Europe approx. 27.1 million tons of post-consumer plastics waste landed in the official waste streams, of which only 31.1% were recycled and 41.6% went for energy recovery (incineration), while 27.3% ended up on landfills and scrap heaps [1]. Furthermore, the production of plastics involves the discharge of great amounts of CO_2 in the atmosphere and requires limited fossil resources such as crude oil.

Today plastics recycling receives both broad public and state support in industrial countries as current programs are being expanded and new ones initiated [1]. However, despite the significant progress achieved in plastics recycling technologies in recent years, the ultimate goal – recycling of 100% of all plastics waste – is yet to be achieved even in the most developed countries. The key to the long-term success of plastics recycling and the decrease of the plastics waste flow to the landfills is a large economic efficiency of recycling. Currently, the majority of recycled plastics have a quality inferior to raw plastics, which makes it impossible to use them in demanding applications like electronics or the automotive industry. In most cases the reason for the quality degradation is that incompatible waste plastics get mixed and are processed together. Separating such incompatible plastics before recycling can significantly increase the quality of recycled plastics and thus improve the overall economic efficiency.

The most advanced state of the art sorting systems use optical and spectral measurement instruments for the identification of different plastic types. These, however, have certain limitations to be discussed below. In order to overcome some of these limitations, the idea to label plastics with fluorescent dyes ("markers") during the manufacturing process and use the unique spectral signatures of these markers for the identification of plastics

was proposed by Bayer AG in 1992 [2]. However, this approach has not yet been implemented in an industrial environment. The industrial application sets high requirements not only on the robustness of the measurement equipment but also on the plastics mass throughput, identification quality, measurement rate, etc. Along with the development of suitable hardware and software, such implementation also involves the study, selection, and assignment of appropriate fluorescent markers to the plastics. The goal of this dissertation is the development of an industrially viable measurement and classification system for the identification of fluorescently labeled plastics. The thesis is organized as follows:

the rest of Chapter 1 gives an overview of the state-of-the-art plastics waste sorting systems and motivates further research in this area. Chapter 2 introduces the idea of fluorescent labeling of plastics and lays out the fundamentals of the fluorescence phenomena. Chapter 3 describes the basics of hyperspectral imaging with a focus on industrial applications. Chapter 4 elaborates on the classification of fluorescence spectra and compares the performance of different classification approaches in specific scenarios based on computer simulations. Chapter 5 introduces the time-gated fluorescence spectroscopy (TGFS) measurement technique used to overcome one of the most significant problems with the fluorescent labeling of plastics – the autofluorescence (AF) of the hosting plastics. Chapter 6 describes the setup of the developed measurement and classification system prototype. Finally, in Chapter 7 classification results achieved with the prototype are presented.

1.1   Recycling of plastics

As depicted in Fig. 1.1, plastics recycling techniques can be divided into 3 main groups based on the type of product obtained from plastics waste [3].

First, one of the most popular recycling techniques is waste-to-energy recycling. Typically, plastics waste is used in combustion chambers in power plants instead of natural gas or coal in order to reclaim the energy contained in them. The obvious downsides of this approach include a low energy recovery rate, danger to the environment, and thus a high demand on purification and filtering facilities [4]. In many cases, high costs associated with the filtering and maintenance make the economic advantages of plastics combustion negligible. Thus, waste-to-energy is only viable if strongly politically motivated.

The second group encompasses feedstock recycling, or chemical recycling with the goal of reclamation of valuable complex chemical structures and elements from the end-of-life plastic polymers. Pyrolysis is such a technique in widespread use. During pyrolysis, plastic polymers are usually heated in isolated chambers without oxygen in presence of catalytic agents. As a result, complex polymer molecules are chemically decomposed into simpler monomer structures. These structures can later be used as feedstock in the production of new complex polymers or as a fuel replacement. Since no combustion and no toxic emissions are involved, pyrolysis is also environmentally friendly. On the downside, pyrolysis becomes difficult and unstable in presence of additives in plastics leading to unpredictable results and operating problems. This is usually the case with plastics waste of unknown origin. Economically, pyrolysis is only feasible for specific polymers that yield high-value monomer
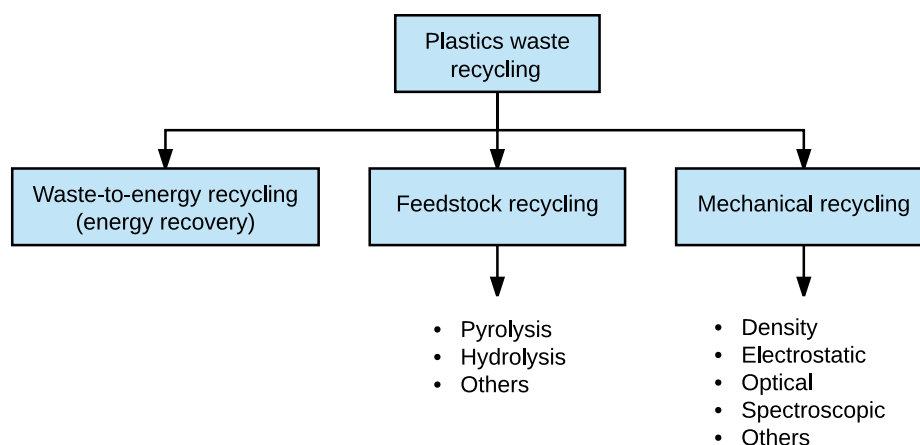
Figure 1.1: State of the art plastics waste recycling approaches.

products, e.g. polymethyl methacrylate (PMMA) and polyamide 6 (PA6) [5]. Similar to pyrolysis, recycling by hydrolysis uses the process of depolymerization of plastics into monomers when they react with water in an acid, alkaline or neutral environment [5, 6]. The disadvantages of hydrolysis include high temperatures, pressure, and a long time usually required for depolymerization. The main advantage of feedstock recycling is that it allows the treatment of unwashed and mixed plastics without prior sorting.

The third group of recycling techniques is mechanical recycling, i.e. the reuse of plastics in similar applications or reclamation of the plastic itself rather than of its composites. This group of techniques is the most challenging one, since it usually requires a prior sorting of the plastics waste, but is the most economically attractive [5]. If plastics waste is not sorted into fractions before reprocessing, the resulting product has poor quality and does not retain the properties of the original plastics due to the incompatibility of various components of mixed plastics. These low quality plastics can be used in certain undemanding products such as garden benches and tables, fences, playing facilities, etc. In the long run, however, this market cannot absorb the ever-growing amounts of plastics waste that is produced every year. Additionally, the quality of the plastics gets worse with every recycling run, which makes such plastics even less useful.

In contrast, products manufactured from recycled mono-fractional plastics waste have a quality far better than those made of mixed plastics waste. Moreover, such products retain the initial properties of the original plastics products, which allows for the reuse in similar (high demanding) applications and "closed circle" recycling. In order to obtain mono-fractional plastics waste, the sorting of different plastic types is mandatory. Sorting must be reliable and precise, as only 1% of incompatible polymers can significantly degrade the quality of the recycled material [4]. An extreme example: only a few parts per million of polyvinyl chloride (PVC) can ruin the entire whole of polyethylene terephthalate (PET) [7].

1.2 Sorting of plastics

Two plastics sorting approaches exist: macro-sorting and micro-sorting. Macro-sorting implies processing large plastic objects as is. Its advantages include large mass throughput and relative implementation simplicity, for example sorting based on the object shape or size. With macro-sorting, in addition to recycling, reverse distribution (deposit returns) can be employed for certain consumer plastic products such as plastic bottles. The main difficulty with macro-sorting in the industrial sectors is the variety of materials (plastic types) used to build single components. For example, a dashboard of a car may be composed of hundreds of pieces of different plastic types and/or colors. A large number of plastics and the high costs of dismounting different plastic pieces of a car pose a significant problem [3].

Micro-sorting is the approach that requires prior grinding of the plastics waste and deals with small plastic flakes. Grinding as such solves the problem of dismounting mechanically bound plastics of different types. In combination with washing and filtering extra small and extra large plastic flakes, it helps clean-up and decontaminate plastics waste before recycling. In addition, ground plastic flakes all have similar shape and size so that the same sorting machinery can be used for plastics of very different origins.

A variety of plastics sorting and identification methods exist, ranging from manual sorting to automated sensor-aided sorting. Manual sorting is still in widespread use in situations where humans can identify plastics by shape, color, or trademark. Manual sorting can be sometimes aided by using specific light conditions for different plastic types. For example UV light can help operators better distinguish between PVC and PET bottles [4]. Being relatively simple to implement, manual sorting is only economically viable if the sorted objects are large in size and high mass throughput can be achieved [8]. Additionally, it is ineffective and increasingly expensive as salaries increase in the majority of countries. Moreover, manual sorting is error-prone and due to its poor quality, the recycled material can only be used in cheap products rendering economical profit negligible. Therefore, the development of automated sorting systems is absolutely necessary. Most of the existing automated sorting technologies rely on certain distinctive chemical, optical, electrical, and/or physical properties of different plastic types. Sections 1.2.1–1.2.6 give a short overview of currently existing methods. Most of the sorting methods described below can be used in both macro- and micro-sorting set-ups.

1.2.1 Densimetric sorting

Sorting techniques based on the density of polymers are widely used due to their relative simplicity. For example, in sink-float separation methods, two polymers with different density are put in a reservoir with a liquid of density smaller than that of the first polymer and greater than that of the second polymer. While the first polymer sinks, the second polymer floats on the surface of this liquid, and separation is achieved. This method works very well for polymers that have very different densities but fails otherwise. For example, water can separate light polyolefins (high-density polyethylene (HDPE), low-

density polyethylene (LDPE), polypropylen (PP)) from heavier non-olefins (polystyrene (PS), PET, PVC) [7]. The small difference in densities of LDPE and HDPE of only approx. 0.001 g/cm$_3$ makes sink-float separation much more difficult and requires a different sink-float medium [4]. In addition, the separation of only 2 plastic types can be simultaneously achieved with this method. If more than 2 plastic types are present in the mixture, 2, 3, or more stages of sink-float separations are needed [9]. Moreover, since it is gravity that slowly separates the polymers, mass throughput is very low. The need to store and clean large amounts of water or other liquids/solutions adds up to the downsides of the sink-float method.

Froth-floatation [4] is an approach very similar to the sink-float method. The difference is that the materials are treated with specific chemicals before put into water. The chemicals are chosen such that only one of the plastic types reacts with it. Then air is pumped into the tank and air bubbles adhere only to this plastic type which then floats to the surface, while other plastic types sink. In contrast to the sink-float method, froth-floatation can separate PET from PVC very well. Other than that, it inherits the disadvantages of sink-float sorting such as moderate mass throughput and large amounts of liquids.

Air sorting is another example of density-based techniques. It uses a vertical stream of air to separate lighter plastic types from heavier ones [4].

In hydrocyclone sorting [4] a rotating conic tube with spiral blades and partially filled with water is used. Centrifugal force invoked by rotation is usually more than 1000 times stronger than gravity. As a result, water collects on the walls of the tube producing a barrier for lightweight plastic particles. Thus lightweight particles stay in the center of the tube before being directed to the exit of the tube by short spiral blades. Heavier particles penetrate the water barrier, reach the walls of the tube, and are routed to another exit by long spiral blades. Rotation speed can be adjusted to the specific densities of the plastics to be separated.

1.2.2 Dissolution and melting

In order to separate five most common waste plastics, namely PVC, PS, LDPE, HDPE and polyethylene (PE), xylene is used to individually dissolve each one of them [7]. The idea is based on the fact that each of the five plastics dissolves in xylene at different temperatures. At room temperature, for example, only PS dissolves leaving the remaining plastics untouched. PS dissolved in xylene is then moved to a separate tank, where it is heated above xylene's boiling point. Then the pressure is quickly lowered making xylene completely vaporize and leaving pure PS behind. The vaporized xylene is then recovered and used to dissolve the remaining plastics at their individual temperatures. Clearly, using the same xylene for all plastics is not optimal. Some portions of plastics may dissolve at temperatures lower than the nominal dissolving temperature and be mixed with other plastics thus reducing their purity. Furthermore, high temperatures involved in the process may result in the thermal degradation of polymers and lead to high equipment and maintenance costs.

Polymers can also be separated based on their different melting temperatures provided

that this difference is large enough [4, 10]. For example, PVC with its melting temperature of approx. 200 °C can be separated from PET (melting temperature approx. 260 °C). When transported by a heated conveyor belt, PVC melts and sticks to its surface, while PET remains in a solid state and falls off the conveyor belt at its end. Melted PVC flakes are then mechanically removed from the conveyor belt. This method can also be used in several stages with different heating temperatures in order to separate more than two plastic types.

1.2.3 Electrostatic sorting

In electrostatic sorting, the separation is achieved by charging different polymer types negatively and positively. Depending on the charge, shredded flakes of different plastic types are either attracted or pushed away by a high-voltage field. This is an established technology that allows an effective separation of mixes of PET/PVC, PS/acrylonitrile butadiene styrene (ABS), PS/PP, ABS/PMMA and others and achieves mass throughputs of several tons per hour [11, 12]. However, electrostatic sorting is highly dependent on the surface condition of the plastics. Moisture, dirt, paint, or paper labels can significantly change the electrostatic properties of the plastics and severely decrease the sorting quality [13]. For obvious reasons, electrostatic methods usually require micro-sorting set-ups.

1.2.4 Optical identification methods

The techniques described above have several disadvantages. First, they cannot distinguish different plastics colors. Yet, sorting plastics not only by type but also by color would allow the production of recycled plastics with the desired appearance. Especially in the consumer market, there is a high demand for certain optical properties of the plastics. Second, additives incorporated into the plastics may change the plastics' properties needed for separation, such as e.g. density, which requires adaptation of the corresponding sorting method. Finally, the need to implement multiple stages even with multiple sorting principles in order to distinguish between more than 2 plastic types increases the complexity of the entire system and makes it inflexible and expensive. Optical and spectroscopic (discussed in Section 1.2.5) identification methods are able to tackle these problems.

Optical sorting can be performed using a color camera that acquires images in the visible (VIS) wavelength range. The camera determines the color of light reflected from the plastics. The color of the investigated plastics is compared with the color of reference (known) plastics. In the case of a match, certain decision logic can be implemented and sorting can be carried out. The way the sorting is physically carried out is irrelevant for the system. For example, identified plastics can be blown away from the conveyor belt by a stream of pressurized air and land in a separate container, while unidentified plastics fall off at the end of the conveyor belt. A variety of optical sorting systems providing high sorting quality and mass throughput are currently available on the market [14]. Optical sorting can be combined with sorting techniques described in this section in order to achieve both plastic type and color sorting.

1.2.5 Spectroscopic identification methods

Spectroscopy allows the acquisition of light over a contiguous range of narrow spectral bands. The idea of using spectroscopy for the identification of plastics relies on the fact that different plastic types have different spectra due to the differences in their chemical structures. Spectroscopy identification methods in VIS, near infrared (NIR) and mid-range infrared (MIR) wavelength ranges are most commonly used. In the spectroscopic analysis, objects are irradiated with a beam of light with a certain wavelength and bandwidth, the reflected light is measured with a dedicated spectroscopic instrument and the resulting reflectance spectrum is compared with the spectra of known polymers for identification purposes [15]. With NIR spectroscopy it is possible to distinguish different types of polyolefin (PO), such as PP, PE, HDPE, LDPE, which are otherwise difficult to separate with e.g. density-based methods [16]. An additional advantage of spectroscopic methods is that they also can be used for online quality control of sorted plastics streams, independent from the sorting method.

Nevertheless, spectroscopic identification has several significant drawbacks. First, reflectance spectra are sensitive to the surface state of the analyzed object: a dirty or covered surface may result in reduced identification quality and sorting purity [17]. Second, due to the small penetration depth of the (infrared) light, reflectance spectra of painted objects represent the paint, rather than the polymer [4]. Finally and most importantly, "carbon black", the most popular colorant used to dye black plastics, absorbs most of the NIR radiation resulting in low-intensity and nearly featureless spectra rendering the identification of black plastics extremely difficult [18]. This problem is especially pronounced in industrial applications where high measurement rates are required (short exposure times). The use of other colorants that do not strongly absorb NIR radiation has been proposed as a solution and is currently under development [19]. Absorption of MIR light by carbon black is smaller, however, due to the lower energy of MIR the measurement time is significantly longer than with NIR, and the computational load is significantly higher due to the more complex MIR spectra. Additionally, MIR equipment is very expensive and currently not suitable for industrial environments due to the lack of robustness [19].

Despite these difficulties, several commercial solutions are available on the market (2018). For example, the STEINERT Group reports to be able to sort black PE, PP, PVC and PS with their newest product UniSort BlackEye using a hyperspectral NIR sensor and achieve an average throughput of 1 ton per hour with particle sizes between 10 mm and 30 mm [20]. Unfortunately, no further technical details are currently available. It should be pointed out that the majority of commercially available systems can sort only one (target) plastics type at a time. The given throughput values are valid for one pass of the plastics through the system, which results in only one target plastic type sorted out. In order to sort more than one target plastic type, more passes are necessary which decreases the overall throughput by the number of passes.

Raman spectroscopy is another technique used for plastics identification. Typically, a VIS or NIR laser is used to illuminate the objects to be analyzed and invoke characteristic infrared emissions due to the Raman scattering effect. Raman spectroscopy is less sensitive

than infrared (IR) spectroscopy to the object's surface quality, but also has difficulties with black plastics [17]. Even though carbon black does not absorb Raman emissions, it does absorb the excitation laser light, which reduces Raman emissions. Nevertheless, some products are available on the market. The POWERSORT 360 system provided by UNISENSOR uses laser-induced Raman spectroscopy to identify ABS, PS, polycarbonate acrylonitrile butadiene styrene (PC-ABS), PP and other polymers, including black ones, with a throughput of several tons per hour for objects between 15 mm and 75 mm in size and achieves a sorting purity of up to 98% according to the specifications [21].

X-ray spectroscopy is a well-established approach for detecting PVC objects. X-ray sensors are sensitive to the chlorine molecules present in PVC, making this technique very reliable when PVC needs to be recovered from a stream of other polymers [4]. Furthermore, in contrast to IR light, the penetration depth of X-ray is very high, which makes X-ray spectroscopy very useful for the identification of painted or dirty plastic objects. However, identification of PE, PP, PET and other common polymers is not possible with X-ray [19]. Additionally, due to the involved health risks, additional precautions are required with regard to the protection of human workers that operate the system.

1.2.6 Tracer-based identification systems

The resin identification code (RIC) system introduced by the Society of the Plastics Industry (SPI) in 1988 was the first attempt to use tracers (or labels) for the identification of plastics [18]. In this system, numbers from 1 to 6 are assigned to the 6 most commonly used plastics: (1) PET, (2) HDPE, (3) PVC, (4) LDPE, (5) PP, (6) PS, and number 7 signifies all other plastics such as polycarbonate, nylon, etc. Figure 1.2 shows labels of the 7 codes developed by SPI which are molded or imprinted on the products manufactured from the corresponding plastics. Labels are placed in inconspicuous locations on the manufactured products, such as the bottom of a bottle. Clearly, this method can only be used for macro-sorting of (large) objects consisting of only one plastic type. In addition, complex objects with parts made of different plastic types would first have to be manually disassembled, which is not economically viable.

Somewhat similar to RIC, radio-frequency identification (RFID) tags can be used for the tracking of relatively large plastic objects such as garbage containers or pallets [19]. These tags consist of integrated circuit chips that transmit a response at a certain radio frequency upon receiving a tracking radio signal. RFID tags do not need a battery since they can derive electrical power from the received signal radiation are approx. 1 mm in size and weigh approx. 0.25 g. The sorting process using RFID can be easily automated. However, the RFID approach cannot be used for micro-sorting and the recycling or re-use of the tags is problematic.

The idea to incorporate magnetic tracers into plastic polymers was proposed recently [22]. Such tracers would change the magnetic susceptibility of the target plastic thus enabling its separation from a waste stream. The main advantage of this approach is its independence of additives and colorants that may be present in polymers. In addition, the application of this approach in micro-sorting is straightforward. However, the incorporation of combi-
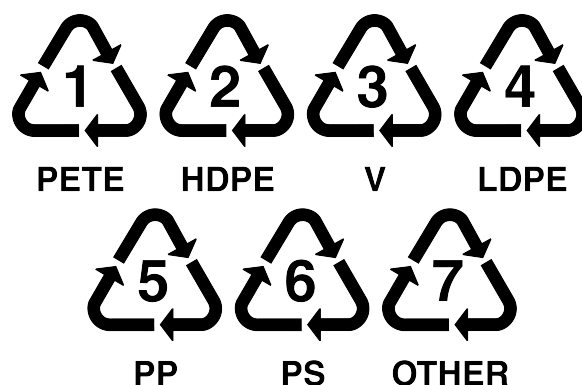
Figure 1.2: Labels of the RIC system which are molded or imprinted on plastic products.

nations of more than one magnetic tracer seems to be impossible, which limits the number of plastics that can be labeled to the number of available unique magnetic tracers. Additionally, the large concentration of magnetic tracers (in the percent range) required for efficient sorting may have a negative effect on the material properties of the plastics.

The idea to use fluorescent tracers (or markers) incorporated into virgin plastic resins during the production for the identification of plastics was first proposed by the Bayer AG in 1992 [18]. Such tracers would change the fluorescence spectra of the plastics in a predefined way by adding distinctive features (fluorescence emission peaks) to them. Thus, even plastics with similar or featureless reflectance spectra become distinguishable with spectroscopy equipment. These fluorescent tracers can be excited with a light beam of appropriate wavelength, their fluorescence emission can be measured with a dedicated spectroscopic instrument and used as a kind of "optical fingerprints" for identification purposes.

Several studies investigated the applicability of fluorescence tracers for the identification of plastics; however, no full-scale industrial system is currently available on the market. An attempt to put fluorescent tracers into industrial practice has been made recently [23, 24]. According to the report, plastic bottles labeled with fluorescent tracers were delivered on a conveyor belt moving at 3.5 m/s, such that each bottle was available for measurement during approx. 86 ms. With concentrations of tracers varying between 0.5 ppm and 5 ppm, a sorting purity of 95% was achieved. The authors have identified the problem of "fluorescence quenching" due to color pigments. Especially black plastics pose a problem.

The concentration of the tracer in the polymer plays a key role in the identification: while high concentrations may negatively influence the properties of the plastics, low concentrations may not provide a sufficiently high fluorescence emission for identification. The use of rare earth oxides for plastics labeling and their influence on mechanical properties of the plastics have been investigated [25]. It has been shown that concentrations less than 250 ppm do not affect the impact strength and flexural modulus of plastics and are sufficient for the identification [25].

Plastics labeling employing rare earth oxides in combination with X-ray spectroscopy has been reported [26, 27]. This approach enables the identification of black plastics,

however, requires measurement times in the order of minutes with tracers concentrations as high as 1450 ppm.

In this dissertation, the approach of plastics labeling with fluorescent tracers is pursued. The goal is to develop an industry-scale system capable to classify a variety of plastics (types) simultaneously, which would also be economically viable. The micro-sorting approach is chosen since it is more flexible and can be applied to very different plastics products independently of their shape. In Chapter 2 the basic principles of fluorescence are shortly described and the measurement problem is formulated.

Chapter 2

Fluorescent labeling

This chapter explains the idea of the fluorescent labeling of plastics for recycling in detail and is structured as follows. The basic principles of the fluorescence phenomenon are described in Section 2.1. In Section 2.3, the concept of fluorescent labeling of plastics for recycling is introduced. Section 2.4 reviews the properties of fluorescent markers relevant for the application. Finally, in Section 2.5 the incorporation of markers into plastics and problems associated with it are discussed.

2.1 Fluorescence basics

Fluorescence is a form of luminescence – the emission of light not resulting from heat. Light is electromagnetic radiation (within a certain wavelength range, typically visible, UV, and/or IR), which is electromagnetic waves (or their photons) propagating through space, carrying electromagnetic radiant energy. Hence, luminescence is accompanied by a loss of energy by the system that emits light and therefore continuous luminescence requires a continuous supply of energy. Forms of luminescence are usually specified based on the source of energy. For example, chemiluminescence derives the energy from a chemical reaction, whereas electroluminescence is a result of an electric current flowing through a luminescent substance.

Fluorescence belongs to a subgroup of luminescence called photoluminescence, which uses the energy of absorbed light (photons). Its mechanism can be best explained using the so-called Jablonski diagram, a simplified version of which is depicted in Fig. 2.1 [28]. When a fluorescent substance is illuminated, photons incident on its surface get absorbed by fluorophores, i.e. molecules responsible for fluorescence emission. The absorbed additional energy results in the transition of the fluorophore's electrons from the ground singlet state S_0 to the high-energy excited singlet states S_1 and S_2. The system thus becomes unstable and excited electrons tend to return to the stable ground singlet state S_0. This process of relaxation of the electrons back to the ground singlet state is accompanied by a loss of energy and causes the emission of photons in form of fluorescence emission $h\nu_F$. Additionally, in each of the singlet states the fluorophore can be in a number of vibrational energy
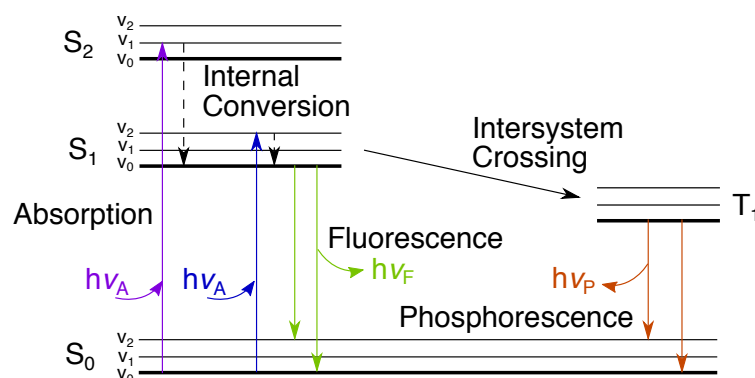
Figure 2.1: A simplified Jablonski diagram depicting movements of electrons in a fluorophore from the ground state S_0 to excited states S_1, S_2 and T_1 and back. Excitation of the electrons is caused by absorption of energy in form of light ($h\nu_A$). Relaxation of the electrons to S_0 is due to the instability of the excited states and is accompanied by emission of photons ($h\nu_F$, $h\nu_P$).

levels denoted by v_0, v_1 and v_2 in Fig. 2.1. Upon absorption of light, electrons usually move to one of the higher vibrational levels v_1, v_2 of S_1 or S_2, but quickly relax to v_0 of S_1. This process is called an internal conversion. It usually takes 10^{-12} s or less and occurs prior to fluorescence, which takes approx. 10^{-8} s. The loss of energy caused by the internal conversion results in lower energy of the emitted fluorescence light in comparison to the absorbed light. Furthermore, during fluorescence, the excited electrons usually move to the higher vibrational levels v_1 and v_2 of S_0 and return to v_0 via non-radiative transmission. As a result, the majority of fluorophores emit fluorescence light at longer wavelengths (lower energy) than those of the light they absorb. This effect is called the Stokes shift.

As can be seen in Fig. 2.1, some of the excited fluorophore molecules can undergo a spin conversion to the first triplet state T_1 (i.e. state with two unpaired electrons and a spin quantum number of 1). Relaxation from the triplet state to the ground singlet state S_0 is accompanied by photon emission $h\nu_P$ and called phosphorescence. Since the transition from the triplet state is a forbidden process, phosphorescence lasts orders of magnitude longer than fluorescence, up to several seconds. Especially molecules containing heavy atoms such as bromine or iodine are often phosphorescent [28].

Fluorescent properties of a fluorophore are best characterized by its excitation and emission spectra. Examples of such spectra belonging to organic fluorophore perylene are shown in Fig. 2.2. The emission spectrum $I(\lambda)$ depicts the spectral content of the emitted fluorescence light – here the relative emission intensity (see below) at different wavelengths λ. By measuring the fluorophore's emission spectrum one can conclude about its chemical components and identify the investigated fluorescent substance. In order to acquire the emission spectrum of a particular fluorophore, the wavelength of the excitation light is kept constant and the emitted fluorescence light is measured as a function of wavelength using a spectroscopic instrument.
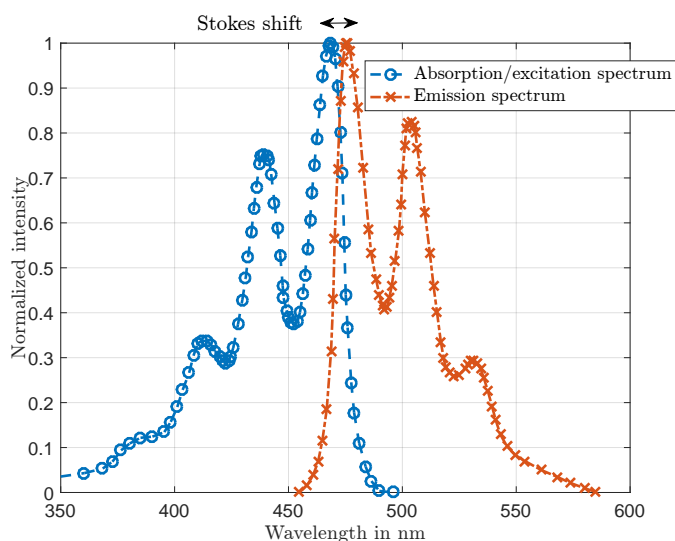
Figure 2.2: Fluorescence absorption/excitation and emission spectra of perylene.

The excitation spectrum $E(\lambda)$ reveals what emission intensity is achieved when the fluorophore is excited with light of the same intensity at different wavelengths λ. In order to acquire the excitation spectrum, the fluorescence emission intensity is measured only at a particular wavelength (usually one of the fluorophore's emission maxima, e.g. 475 nm or 504 nm for perylene), whereas the wavelength of excitation light is being changed. If the intensity of the excitation light is kept constant over all wavelengths, the resulting excitation spectrum is said to be corrected. The corrected excitation spectrum is equal to the absorption spectrum of the fluorophore [29], which essentially shows the probability for the absorption of incident photons at particular wavelengths. The higher the probability, the more fluorophore molecules are excited and emit afterward resulting in a higher fluorescence emission intensity. For example, as can be seen in Fig. 2.2, exciting perylene at the wavelength of its absorption maximum at approx. 470 nm will yield the strongest fluorescence emission. These spectra provide information about what wavelength of the excitation light should be used in order to stimulate strong fluorescence emission from a particular fluorophore.

The shapes of both excitation/absorption and emission spectra of different fluorophores do widely vary and are governed by the chemical structure of the fluorophores. In Fig. 2.2 one can notice that absorption and emission spectra are very similar mirrored copies of each other. This symmetric nature is the result of similar electrons transitions taking place during excitation and relaxation of fluorophore molecules. The shape of the absorption spectrum is mostly governed by the $S_0 \rightarrow S_1$ transition, whereas the shape of the emission spectrum is due to the backward transition $S_1 \rightarrow S_0$. The different peaks in the absorption spectrum correspond to the non-fluorescent internal conversion – fast relaxation from high vibrational energy levels v_1 and v_2 to the lowest v_0 of S_1. Peaks in the emission spectrum are due to a similar process in S_0. Since the energy spacing between the vibrational levels

of S_0 and S_1 is similar, peaks in the absorption and emission spectra are spaced similarly on the wavelength axis. The Stokes shift can be clearly seen in Fig. 2.2, which is approx. 10 nm here.

An exception to the "mirror rule" can occur in complex chemical structures where different molecules are responsible for absorption and emission. Within such structures, the transfer of energy acquired during excitation from one (donor) molecule to another (acceptor) can be due to internal processes such as ionization. In this case, the acceptor molecule is responsible for the emission and therefore the shape of the emission spectrum differs from that of the (mirrored) absorption spectrum. This behavior can be used for the design of fluorophores in order to adjust the shape of the absorption and emission spectra to specific needs.

2.2 Fluorescence emission intensity

For plastics sorting, the fluorescence emission intensity should be maximized. High intensities make it easier to measure and identify fluorescence markers. In this dissertation, the intensity I is defined as the radiant power received by a surface per unit area per wavelength and its unit is W/m^2/nm (or W/m^3). Furthermore, the continuous function $I(\lambda)$ represents the (analog) emission spectrum of a certain light source over a range $\Delta\lambda$ of wavelengths λ.

The emission intensity of a fluorophore depends on its so-called quantum yield Θ. Per definition, the quantum yield is the ratio of the number of emitted photons and the number of absorbed photons. It can also be expressed in terms of the emissive decay rate Γ and the non-radiative decay rate k_{nr} as follows [30]:

$$\Theta = \frac{\Gamma}{\Gamma + k_{nr}} < 1. \tag{2.1}$$

The sum $(\Gamma + k_{nr})$ of the emissive and non-radiative decay rates determines the relaxation rate of the fluorophore. The emissive decay rate Γ corresponds to the fluorophore's relaxation accompanied by photon emission, and the non-radiative rate k_{nr} is due to the non-emissive energy dissipation such as thermal processes. The non-radiative decay rate k_{nr} includes all possible relaxation processes and strongly depends on the chemical structure of the fluorophore. Since the fluorophore relaxation is an exponential process [28], the sum $(\Gamma + k_{nr})$ determines the exponential decay constant. The quantum yield Θ can also be thought of as the efficiency of the fluorophore. It can never reach 1 (100%), since at least some non-radiative energy losses are always present in fluorophores.

As explained in Section 2.1, the fluorescence emission intensity of a fluorophore also depends on the wavelength and intensity of the excitation light. Consequently, when a non-monochromatic light source such as a xenon lamp or an light-emitting diode (LED) is used, the resulting fluorescence emission intensity $I(\lambda)$ of a fluorophore is proportional to

the following integral [31]:

$$I(\lambda) \propto \int I_e(\lambda_e)E(\lambda_e)d\lambda_e, \tag{2.2}$$

where $I_e(\lambda_e)$ is the intensity spectrum of the excitation light, $E(\lambda_e)$ is the marker's absorption/excitation spectrum, and integration is carried out over the "excitation" wavelengths λ_e in the wavelength range $\Delta\lambda_e$ where both $I_e(\lambda_e)$ and $E(\lambda_e)$ are present.

Interestingly, the quantum yield Θ of the majority of fluorophores does not depend on the spectral content (wavelength) of the excitation light [29]. Hence, the resulting fluorescence emission intensity $I(\lambda)$ of a particular fluorophore increases when the value of the integral in Eqn. 2.2 is increased.

2.3 The concept of fluorescent labeling

In the context of recycling, fluorophores can be used as tracers (or markers) to uniquely label different plastics and thus facilitate their identification and sorting prior to recycling. The concept can be explained using Fig. 2.3.

Specifically designed fluorescent markers are incorporated into virgin plastic resins at low concentrations during the manufacturing process (phase 1). Markers can be incorporated alone and in combinations (groups) according to a certain coding scheme. The emission spectrum of a combination of different markers corresponds to the superposition of the individual marker spectra. Using the presence and absence of markers as "bits" in the coding scheme significantly increases the number of plastics that can be labeled. For example, with binary coding, whereas the presence and absence of a marker correspond to 1 and 0, respectively, having only 4 markers M1-M4 allows the labeling of up to $2^4 - 1 = 15$ different plastics (code "0000" is excluded). Each of the 15 binary 4-bit-combinations is assigned to a certain plastics, which enables their classification. Depending on the properties of the fluorescent markers, other coding schemes might be used [32]. These fluorescently labeled plastic resins are then used as feedstock for the production of various products.

During the life cycle of the labeled plastic products (phase 2), fluorescent markers must resist environmental influences such as for example UV radiation from sunlight, high/low temperatures, humidity, etc. In this dissertation, micro-sorting is favored, therefore, after the product life cycle, plastics are collected and shredded into small flakes (phase 3). Before plastic flakes can be fed into a classification system, they need to be washed and separated from other materials such as paper, glass, or metal. Plastic flakes are then distributed on a conveyor belt and fed to the classification system. The classification system measures the fluorescence spectra of the plastic flakes and performs classification based on the known emission spectra of the incorporated fluorescent markers and the coding scheme (phase 4). Once a plastics flake has been classified, it can be sorted according to its type (phase 5) and recycled.

It should be noted that in order for this approach to be economically successful, marker concentrations must be kept low. Less marker material means lower costs of the labeled
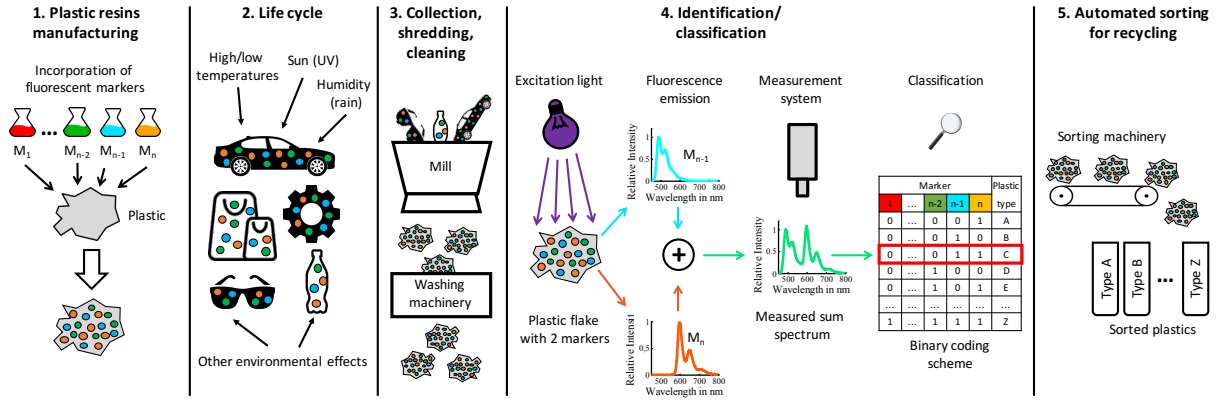
Figure 2.3: Concept of plastics labeling with fluorescent markers for end-of-life recycling (5 phases, see text).

plastics. Additionally, high marker concentrations might change mechanical, optical, or other relevant properties of the hosting plastics. The minimum marker concentrations depend on the minimum signal-to-noise ratio (S/N ratio) of the acquired fluorescence spectra and on the required classification performance (and therefore the quality of the resulting recycled plastics). The S/N ratio depends on several factors:

- quantum efficiency of the markers,

- light absorption of the hosting plastics,

- excitation light (intensity and wavelength),

- sensitivity of the measurement device (sensors),

- desired measurement rate and thus mass throughput.

These factors must be taken into consideration and shall be discussed in detail in this dissertation.

2.4 Fluorescent markers

Fluorescent markers are essential for the described concept. Several crucial requirements with regard to the design and properties of the markers can be postulated:

- Markers must be non-toxic.

- Neither the appearance nor the mechanical or chemical properties of the hosting plastics must be changed by the incorporation of fluorescent markers.

- Fluorescence emission intensity of the markers after the life cycle of plastics must be sufficiently large for identification purposes. This implies that environmental influences such as solar radiation, high temperatures, rain (humidity), etc. must not change the excitation and emission properties of the markers during the entire life cycle of the plastics products. Specifically, markers must sustain photobleaching, i.e. the destruction of fluorophore molecules via a photochemical reaction due to long-term exposure to (sun)light of high intensity resulting in the decrease of the fluorescence emission intensity.

In addition to the requirements above, the following recommendations with respect to the spectral properties of the markers facilitate the design of an industrially viable system and should thus be taken into consideration:

- Markers should absorb light in the wavelength range where high-power commercial illumination sources are available.

- Markers with excitation spectra in the UV wavelength region are preferable since then excitation by the sunlight is minimized and no fluorescence is visible to the human eye.

- Marker absorption/excitation spectra are preferred to be broad in order to absorb as much excitation light as possible (especially if a broadband excitation light source is used).

- Marker absorption/excitation spectra should not spectrally overlap with the emission spectra of other markers in order to avoid reabsorption effects.

- The excitation spectra of all markers should have a large spectral overlap, such that excitation with the same light source is possible. This considerably simplifies the design of the measurement system and reduces costs.

- Marker emission spectra should be in the visible wavelength range between approx. 450 nm and 900 nm where cost-effective and sensitive sensors and spectroscopic instruments are available.

- Marker emission spectra should be narrowband in order to maximize the number of markers that can fit in the target wavelength range of approx. 450 nm to 900 nm. More plastics that can then be uniquely labeled.

- Different marker emission spectra should have a minimal spectral overlap, i.e. emission spectra must be "orthogonal" in a coding sense to maximize classification performance.

- Since S/N ratio and thus fluorescence emission intensity is of the greatest importance for the classification of labeled plastics, the quantum yield of the fluorescent markers should be as high as possible.

The recommendations above should be kept in mind when developing or selecting appropriate fluorescent markers for the application at hand. However, both excitation and emission spectra of fluorophores strongly depend on their chemical structures. Thus chemical and physical limitations exist in terms of realizing optimal markers in practice.

2.4.1 Plastics labeling with organic markers

In this dissertation two groups of potentially applicable fluorescent markers were investigated: organic and inorganic.

First, 11 plastics labeled with binary combinations of 4 organic markers were investigated [33]. The spectroscopic measurement system was mounted on a conveyor belt that delivered the plastic flakes. An average classification performance (see Chapter 4) of more than 99% was achieved. The main advantage of organic markers is their broadband (approx. 150 nm wide) absorption/excitation spectra. This allows an efficient excitation of all 4 markers simultaneously using the same illumination source. Marker concentrations in the plastics as low as just a few ppm (parts per million) are sufficient for successful classification.

However, organic markers have also revealed some unconquerable disadvantages rendering their use for plastics labeling inappropriate. First, due to the mirror rule broadband absorption/excitation spectra of organic markers result in equally broadband fluorescence emission spectra. Only a small number of such spectra can be fit in the target wavelength range approx. 450 nm – 900 nm without large spectral overlap. Since the applicable number of markers is small, the number of possible marker combinations (codes) and thus the number of plastics that can be uniquely labeled is limited as well. In fact, 4 such markers are arguably the maximum number that can be used simultaneously in a plastic, and thus overall only $2^4 - 1 = 15$ plastics can be labeled using binary coding.

Second, broadband emission spectra are often difficult to distinguish from the intrinsic autofluorescence (AF) of the hosting plastics (see Section 2.5.4). Reliable classification of the marker emission spectra in the presence of strong AF can be problematic [34]. Sophisticated methods are needed to overcome the problem [35]. The employment of time-resolved spectroscopic methods as described in Chapter 5 that can suppress the influence of AF in the measured spectra is not possible with organic markers since their fluorescence decay time constants lie in the range of those of the plastics' AF.

Third, the incorporation of organic markers even at relatively low concentrations often results in a visible coloring of the hosting plastics. This effect is almost unnoticeable with dark-colored and black plastics but is pronounced with light-colored and white plastics.

Finally, the most critical disadvantage of organic markers is their very low photostability when incorporated in plastics. All organic markers investigated in this dissertation could resist high amounts of solar radiation when dissolved in chloroform or incorporated in transparent PE. Surprisingly, however, after incorporation in non-transparent plastics, the markers had a very low photostability. As an example, Fig. 2.4 shows the decrease of fluorescence emission intensity of one of the organic markers incorporated in a white polyoxymethylene (POM) plastic during exposure to the sunlight and a high-power UV
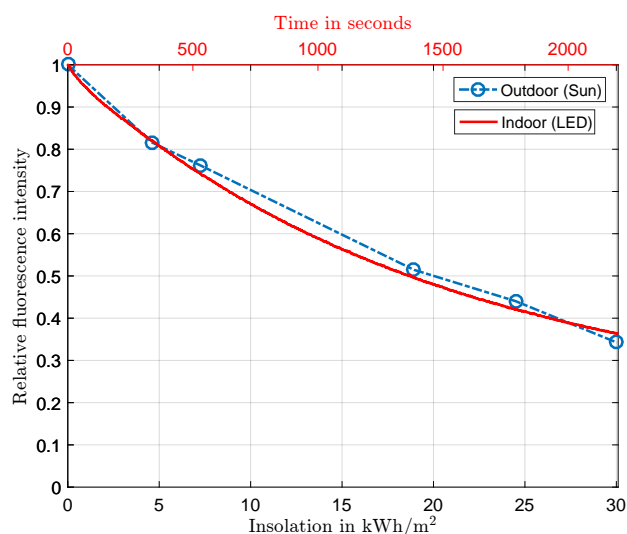
Figure 2.4: Photobleaching of an organic marker incorporated in white POM plastic. The broken line shows a significant decrease in the fluorescence intensity of the organic marker after one-week exposure to sunlight and approx. 30 kWh/m² of overall insolation. The solid line depicts photobleaching of the same marker in POM exposed to a high-power blue LED for approx. 2200 s.

LED. In the experiment, the fluorescence intensity of the fluorescently labeled plastics was first measured "freshly" from the extruder. Afterward, it was placed in the sun and the measurements were repeated every day over the course of one week. As can be seen in Fig. 2.4 (broken line), the fluorescence emission intensity decreased to approx. 65% of its initial value after just one week due to the photochemical destruction of the fluorescence molecules. The experiment was repeated using a high-power UV LED. The sample was illuminated for 2200 s with constant excitation intensity, during this time its fluorescence emission intensity was measured constantly. Illumination with the high-power LED accelerated the photobleaching. The result is shown in Fig. 2.4 (solid line) and confirms the finding from the previous experiment with sunlight. As can be seen, the marker's fluorescence intensity decays exponentially. After approx. 36 minutes only approx. 35% of the initial intensity is left. Similar findings were reported in [36].

2.4.2 Plastics labeling with inorganic markers

The disadvantages of organic fluorescent markers mentioned in Section 2.4.1 make them inappropriate for plastics labeling. For this reason, the focus of this dissertation was placed on inorganic markers. In contrast to organic markers, inorganic markers have narrowband emission spectra and have demonstrated significant photostability when incorporated into plastics, no coloring of plastics and a potential to solve the AF problem using the TGFS measurement approach (see Chapter 5).

The photobleaching experiment with inorganic markers incorporated into plastics was

carried out using an Atlas Suntest exposure chamber compatible with the ISO 4892-1 and -2 standards [37] for plastics exposure procedures. For the experiment, two inorganic markers (markers M4 and M6 in Table 2.1, see below) were each individually incorporated into white POM plastics samples. Fluorescence emission spectra of the samples were measured before exposure and after 100 hours of exposure in the Suntest chamber, which corresponds to the overall insolation of approx. 60 kWh/m². Figure 2.5 compares the (relative) fluorescence emission intensity before and after exposure for two inorganic and one organic marker. For each sample, fluorescence emission intensity was measured at 4 different areas on the sample and averaged. As can be seen, the organic marker has lost approx. 70% of its initial fluorescence intensity after a 100 h long exposure which confirms the findings shown in Fig. 2.4. In contrast, no noticeable decrease of fluorescence emission intensity of inorganic markers occurs.

However, despite this outstanding photostability, the incorporation of inorganic markers into plastics has proven not to be straightforward. Even when professional plastics extruders are used, very often fluorescent markers get destroyed during the incorporation process such that no marker fluorescence can be registered afterward. This turned out to be a serious problem, that did not occur with organic markers. Overall, 14 different inorganic markers were tested and numerous incorporation attempts were made. Experiments with the adaptation of the incorporation process by encapsulating marker molecules in silicon and/or paraffin oils and thus "protecting" them from destruction have not brought improvement. Clearly, more research in the chemical field is needed with this regard, which is beyond the scope of this dissertation. Out of 14 investigated markers, only 6 could be successfully incorporated into plastics. The 6 "working" markers are marked greed in Table 2.1. These 6 markers were used in the prototype system (see Chapters 6 and 7).

Excitation and emission spectra of the 6 markers are shown in Fig. 2.6. The excitation spectra a limited to the wavelength range ($\lambda_{e_{lower}} = 350$ nm; $\lambda_{e_{upper}} = 450$ nm) in Fig. 2.6a for demonstration purposes because exciting markers at wavelengths below 350 nm and above 450 nm is impractical in terms of the design of the measurement system. For wavelengths below 350 nm, it becomes increasingly difficult to find high-power excitation light sources on the market. Exciting markers at wavelengths above 450 nm would lead to spectral overlap of the excitation light with the marker emission (see Fig. 2.6b) and since the excitation light is orders of magnitude stronger than the fluorescence emission, this would lead to complete masking of the marker fluorescence.

As can be seen in Fig. 2.6b, all emission spectra are narrowband and characterized mostly by a single peak. All 6 peaks are situated between approx. 500 nm and 750 nm with a moderate spectral overlap.

As shown in Fig. 2.6a, all markers have their individual excitation maximum at different wavelengths and there is no wavelength band in which all markers can be simultaneously excited with the same excitation light source. Hence the integral in Eqn. 2.2 cannot be maximized for all 6 markers simultaneously which is why an optimal excitation of all 6 markers simultaneously is not possible. Using only one excitation light source facilitates the mechanical and electrical design of the measurement system a great deal (see Chapter 6).

In order to find the single wavelength at which all 6 markers can be best excited, the

Table 2.1: Inorganic markers investigated in this dissertation. Markers that could be successfully incorporated into plastics are marked green. CW and FWHM stand for central wavelength and full width at half maximum of the main peak of the marker's emission spectrum.

Nr.	Chemical formula	Alias	CW, nm	FWHM, nm	Excitation max, nm
1	$LiBa_2(La_{0.98}Dy_{0.02})_3(MoO_4)_8$				
2	$LiBa_2(La_{0.98}Er_{0.02})_3(MoO_4)_8$				
3	$Li(La_{0.95}Er_{0.05})Mo_2O_8$	LiEr (M2)	551	5	365, 378, 407
4	$Li(La_{0.95}Dy_{0.05})Mo_2O_8$	LiDy (M3)	571	7	353, 367, 388, 427
5	$Li(La_{0.95}Sm_{0.05})Mo_2O_8$	LiSm (M5)	643	7	363, 377, 405, 421
6	$GdAlO_3$				
7	$Gd(Al_{0.995}Cr_{0.005})O_3$				
8	$Gd(Al_{0.99}Cr_{0.01})O_3$				
9	$Al_2O_3:Cr_3+$	AlOCr (M6)	694	7	405
10	$ZnAl_2O_4:Cr_3+$				
11	$LiEuMo_2O_8$	LiEu (M4)	617	10	362, 382, 395, 416
12	$(La_{0.97}Pr_{0.03})_2W_3O_{12}$				
13	$(Ba_{0.98}Eu_{0.02})(Mg_{0.8}Mn_{0.2})Al_{10}O_{17}$	BaM (M1)	516	25	350
14	$Sr_2SiO_4:Eu_2+$				
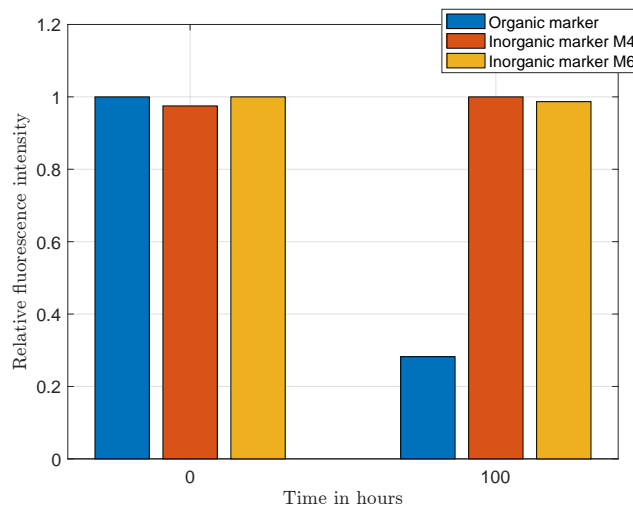
Figure 2.5: Photobleaching of 1 organic and 2 inorganic markers separately incorporated in white POM plastic. Fluorescence intensity of the organic marker decreases by about 70% while no changes with the inorganic markers after 100 h in a Suntest exposure chamber [38] (approx. 60 kWh/m² of insolation).
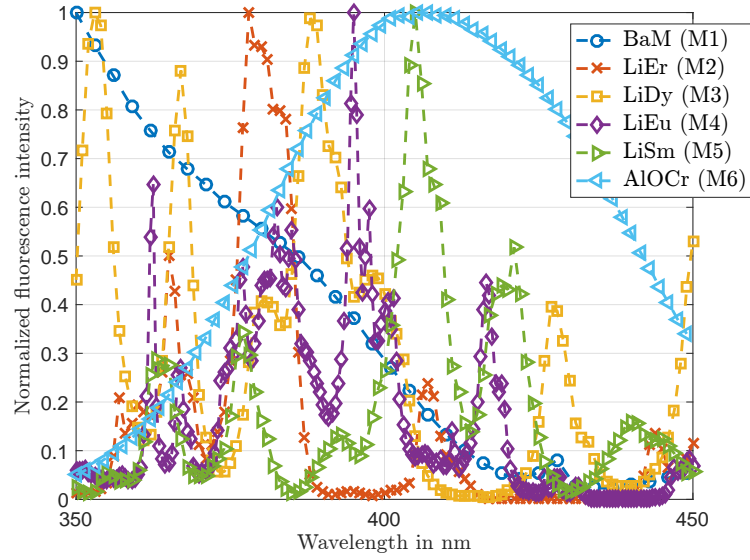
(a)
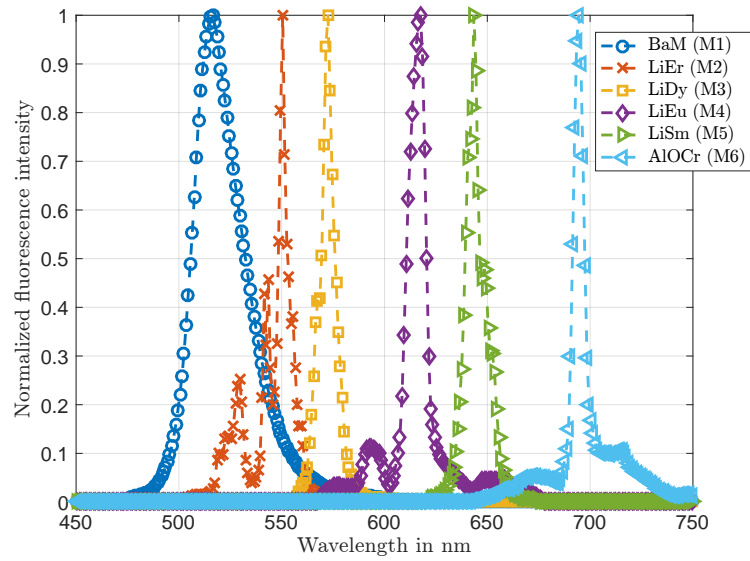
(b)

Figure 2.6: Excitation (a) and emission (b) spectra of the 6 selected inorganic markers (M1-M6).

"minimum excitation spectrum" of this group can be used (Fig. 2.7 blue curve with circles). For monochromatic excitation light, the minimum excitation spectrum of the group of 6 markers is given by:

$$E_{min}(\lambda_e) = \min\left(E_h(\lambda_e)\right), \text{ for all } \lambda_e \in (\lambda_{e_{lower}}; \lambda_{e_{upper}}) \text{ and } h = 1..M, \qquad (2.3)$$

where M is the number of markers in the group (here $M = 6$), and $\lambda_{e_{lower}}$ and $\lambda_{e_{upper}}$ denote the lower and upper limits of the wavelength range where the 6 markers can be excited in terms of the design of the overall measurement system (here $\lambda_{e_{lower}} = 350$ nm and $\lambda_{e_{upper}} = 450$ nm, see Fig. 2.6a).

The minimum excitation spectrum shows the emission intensity provided by the weakest marker in the group when excited with monochromatic light of a certain wavelength of λ_e. For the given group of 6 markers, the minimum excitation spectrum reaches its maximum at approx. 378 nm, which is thus the best wavelength for a monochromatic excitation light to excite all markers in the group.

For a non-monochromatic light source such as an LED, the minimum excitation spectrum is the result of the convolution of the emission spectrum of this light source with the minimum excitation spectrum for monochromatic light $E_{min}^{LED}(\lambda_e) = E_{min}(\lambda_e) * I_e^{LED}(\lambda_e)$. In Fig. 2.7, the yellow curve with crosses depicts the convolution result of the minimum excitation spectrum for monochromatic light with the modeled Gaussian bell-shaped emission spectrum of an LED with 15 nm full width at half maximum (FWHM). With this LED, the maximum of the minimum excitation spectrum (and the best central wavelength of the LED) shifts to approx. 368 nm, whereas approx. 25% of the maximum is still achieved with an LED with a central wavelength between approx. 390 nm and 400 nm. Assuming the same excitation light intensity $I_e(\lambda_e)$ per nm for monochromatic and non-monochromatic light sources, a much stronger fluorescence emission can be achieved with the latter if the same excitation light source is used for all 6 markers. As can be seen in Fig. 2.7, the maximum of the excitation spectrum $E_{min}^{LED}(\lambda_e)$ of an LED is approx. 3.7 times larger than the maximum of the excitation spectrum $E_{min}(\lambda_e)$ of the monochromatic light.

2.5   Incorporation of markers into plastics

Special attention should be paid to the incorporation process and thus the resulting labeled plastics. The quality of the incorporation process directly influences the achievable plastics' classification performance. In this section, the most significant aspects associated with the incorporation will be discussed. Their influence in terms of the classification performance will be quantified in detail in Chapter 4.

2.5.1   Change of the plastics' color

The incorporation of markers into (thermoplastic) polymers involves melting and subsequent compounding of the plastics with fluorescent markers. Depending on the polymer, temperatures of > 150 °C may be required [39]. During the processing at high temperatures, plastic resins may burn and change color. White plastics are particularly susceptible to high temperatures and may become yellow, brown, or even black. This change of color is not homogeneous but appears at sparse spots on the plastic's surface thus affecting the appearance of the resulting product. In this dissertation, such behavior was observed when
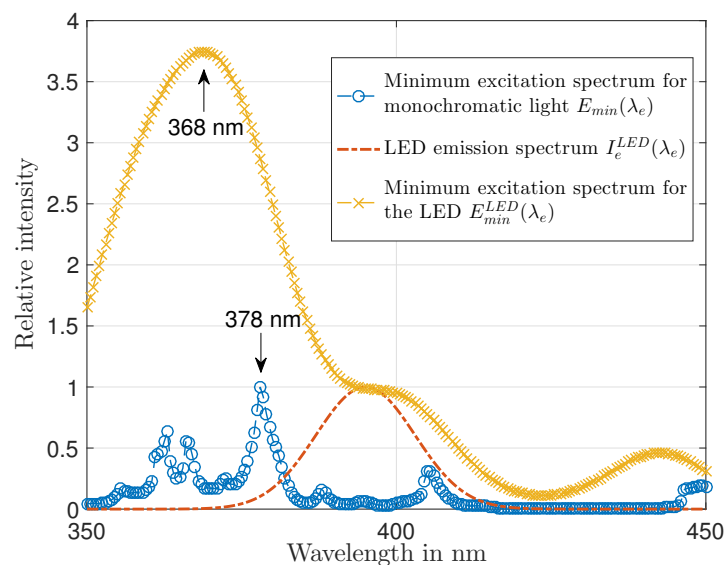
Figure 2.7: The "minimum excitation spectrum" for monochromatic light (blue curve with circles) for the group of 6 markers represents the emission intensity achieved by the marker with the weakest fluorescence emission in the group if excited with monochromatic light of a particular wavelength. If a non-monochromatic light source such as an LED (red broken curve) is used, the minimum excitation spectrum (yellow curve with crosses) is given by the convolution of the red curve with the blue curve.

laboratory-scale plastic kneading devices were used for marker incorporation. With professional industrial extruders, plastics are processed at lower temperatures and the change of color is thus avoided. Professional extruders, however, require larger amounts of plastic resins for one cycle of production and are thus more expensive to run.

2.5.2   Homogeneous marker distribution

Insufficient mixing of plastic resins and markers results in an inhomogeneous distribution of markers within the plastics. That, in turn, results in different fluorescence emission intensities at different spatial locations on the plastic sample.

What is more, when a combination of markers (i.e. more than one marker) is inhomogeneously incorporated into a plastic, the relation between individual marker concentrations of that combination may vary within the plastic. In that case, one marker with larger concentration and thus larger fluorescence emission intensity may mask the presence of other markers with smaller concentrations and intensities and the resulting overall emission spectrum may be misclassified [40]. Special attention should thus be paid to the spatial homogeneity of marker concentrations in the plastics.

The most homogeneous distribution of markers and thus low marker intensity fluctuations can be achieved when professional plastics extruding machinery is used. Figure 2.8 shows (peak) fluorescence emission intensity values measured at different locations on a
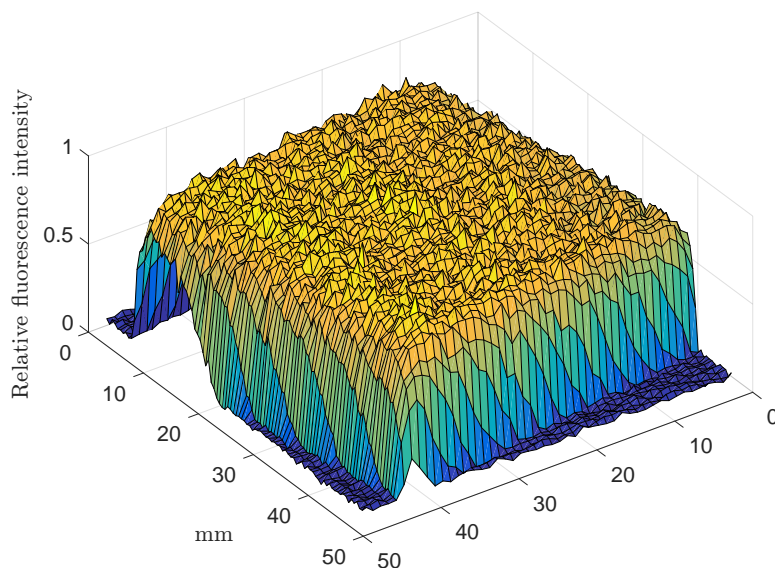
Figure 2.8: Fluorescence intensity of a POM sample (ca. $50\,\mathrm{mm}\times50\,\mathrm{mm}$) labeled with marker M4 measured at different spatial positions. The standard deviation of the marker fluorescence intensity does not exceed 5% ($\sigma < 5\%$).

POM sample labeled with marker M4 using a professional extruder. The POM sample (approx. $50\,\mathrm{mm}\times50\,\mathrm{mm}$) was placed on a non-fluorescent background, the measurement was carried out using components of the prototype system (see Chapter 6). The spectral camera's integration time was adjusted in order to achieve high S/N ratio (> 25 dB) of the acquired fluorescence emission spectra and reduce noise influence. In Fig. 2.8, fluorescence emission intensities are normalized to 1. Mainly two intensity levels can be seen: values around 0 correspond to the non-fluorescent background and values around 1 correspond to the marker fluorescence. At the edges of the sample, intermediate values occur due to the spatial resolution of the applied optics. Throughout the sample, however, the standard deviation of the marker fluorescence intensity does not exceed 5% ($\sigma < 5\%$), indicating the high spatial homogeneity of the marker concentration within the plastic.

2.5.3   Marker concentration

Apart from the factors mentioned in Section 2.2, the intensity of fluorescent light emitted from labeled plastics strongly depends on the marker concentration. In order to investigate this dependency in practice, marker M1 was incorporated into white POM plastics at 6 different concentrations between 10 ppm and 160 ppm, and its fluorescence emission intensity at each concentration was measured. In order to reduce the influence of the spatial inhomogeneity of the marker concentrations (see Section 2.5.2), the measurement of the fluorescence emission intensity for each concentration was repeated 5 times at different

spatial locations on the samples and the results were averaged.

Figure 2.9 shows the relative fluorescence emission intensity as function of the marker concentration in white POM. The marker fluorescence emission intensity is normalized on the emission intensity at concentration 10 ppm. According to this experiment, the increase of the marker concentration by a factor $160/10 = 16$ results in an intensity increase by approx. a factor 15.5. Hence, an almost linear 1:1 dependency can be expected in practice.
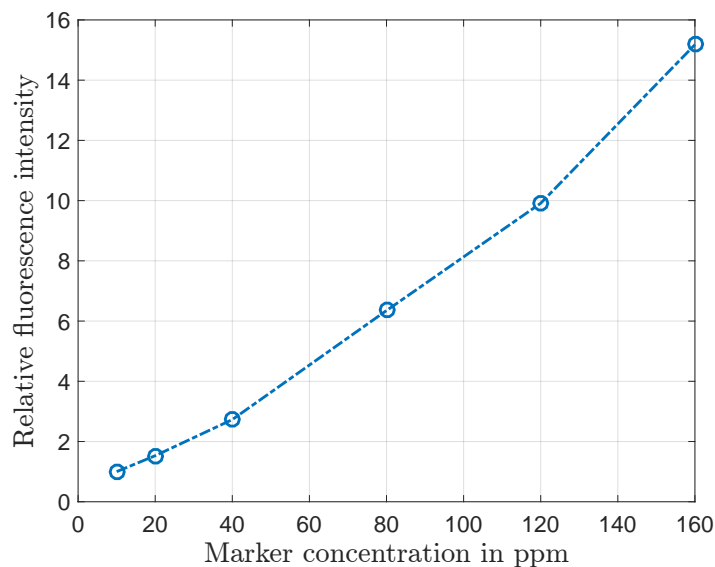
Figure 2.9: Relative fluorescence intensity of POM samples labeled with marker M1 as function of the marker concentration.

2.5.4 Autofluorescence of plastics

The biggest problem that occurs once markers have been successfully incorporated into plastics is the interference of marker fluorescence with the plastics' autofluorescence (AF). AF is the intrinsic fluorescence of plastics due to their chemical structure and/or various additives such as brightening agents, UV-protection, etc. [41] White or light-colored plastics may exhibit particularly strong AF in the visible wavelength range. Strong AF in comparison with the marker fluorescence can severely change the emitted (overall) spectrum making correct classification of marker combinations difficult or even impossible [34]. Figure 2.10a depicts the measured spectrum of marker M4 incorporated in white POM plastic at a concentration of 50 ppm. The measured spectrum consists of the marker's fluorescence spectrum (narrow spike at approx. 617 nm) and the broadband AF spectrum. AF with such intensity may easily be mistaken for a marker (in this case most probably for marker M1) and produce a misclassification. If the marker concentration was further reduced for economic reasons, the presence of AF in the overall spectrum would become even

(a)   (b)
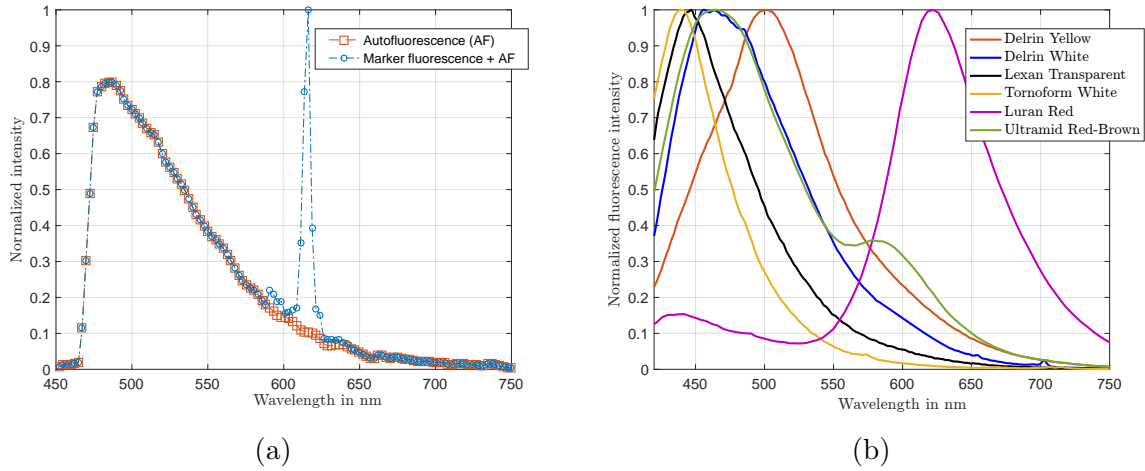
Figure 2.10: (a) The emission spectrum of white POM plastics labeled with M4 at 50 ppm concentration consists of the autofluorescence (AF) of the plastic and the marker fluorescence. (b) Typical AF spectra of different plastics.

more dominant and result in more misclassifications. This effect is especially noticeable at low S/N ratios (i.e. here at high measurement and classification rates).

Similar to the well-known parameter S/N ratio (see Section 3.4.1), a measure called signal-to-autofluorescence ratio (S/AF ratio) can be defined:

$$S/AF = \frac{P_s}{P_{AF}}, \tag{2.4}$$

where P_s and P_{AF} denote the power of the marker fluorescence spectrum and the power of the AF spectrum, respectively. Similarly to the S/N ratio, both P_s and P_{AF} are calculated in the respective marker wavelength bands (see Eqn. 3.4 and 3.5). In order to avoid confusion with the S/N ratio defined with a logarithm in dB (see Section 3.4.1), the signal-to-autofluorescence ratio (S/AF ratio) is defined as a linear measure in this dissertation. The S/AF ratio is used in Chapter 4 to quantify the amount of AF in the simulated fluorescence spectra.

There are several ways to deal with the AF problem. One is to increase the marker concentration in order to increase the marker fluorescence compared to the AF. This would, however, inevitably increase the price of the labeled plastics. A change of the plastics' mechanical and/or optical (coloring) properties might also occur.

Another way to decrease the influence of the AF is to "pre-bleach" the labeled plastics before classification. AF is usually not photostable and decreases when the plastics are exposed to UV light (similar to organic markers) [41]. This approach is thus applicable only with inorganic markers. The downside of this approach is that after pre-photobleaching, the AF tends to somewhat recover within several hours (fluorescence molecules do not get completely destroyed) [41]. Thus, pre-bleaching of plastics should ideally take place right before classification, and before AF has had the chance to partially recover. What is

more, pre-bleaching only works in regions of the plastic flakes that were directly exposed to UV-light.

Yet another way to tackle the AF problem is to apply an extended form of the linear mixture analysis to the acquired spectra in order to partially "unmix" the AF from the overall spectrum [35, 42].

In this dissertation, the most promising approach to suppress the negative influence of the AF – time-gated fluorescence spectroscopy (TGFS) – is pursued. TGFS builds upon the difference of the decay time constants of marker fluorescence and AF by using time-gated excitation and acquisition. It is capable of (almost) completely suppressing the plastics AF in the measured spectrum. Implementation of TGFS in an industrial environment is a challenging task. Chapter 5 explains TGFS in detail and discusses its usability in an industrially viable system.

Chapter 3

Hyperspectral imaging

In this chapter, the principles of hyperspectral imaging are briefly discussed. The hyperspectral data format is explained in Section 3.1. Different approaches to hyperspectral image generation are presented in Section 3.2. The composition of the hyperspectral camera used in this dissertation is described in Section 3.3.

3.1 Hyperspectral imaging basics

A two-dimensional (2D) gray value digital image is a rectangular array of X rows and Y columns made of quantized intensities (or gray values), also called pixels. In this context, a pixel is an entry in the digital image with a certain location and corresponding intensity value. The third dimension λ is introduced when more than one gray value layer is needed. For example, for color imaging on computer screens or TVs three image layers are used and contain red, green, and blue information needed to create the illusion of a color image to the human eye (RGB image), as shown in Fig. 3.1. The intensity values in each of the layers are digitized and are expressed as integers. For example, in an 8-bit image, $2^8 = 256$ digital intensity levels (gray values) from 0 to 255 can be contained, whereas e.g. 0 usually represents black and 255 is white. In advanced imaging systems 12 bits ($2^{12} = 4096$ intensity levels), 14 bits ($2^{14} = 16384$) or 16 bits ($2^{16} = 65536$) are used.

The concept of the 3 layers RGB image can be extended to multivariate images. Multivariate images contain $\Lambda > 1$ 2D X $\times$ Y layers, each of which corresponds to a certain wavelength band $\Delta\lambda_i$, $i = [1, 2, ..., \Lambda]$. In practice, the wavelength band $\Delta\lambda_i$ spans over a range of analog wavelengths $[\lambda_{lower}; \lambda_{upper}]$ depending on the optical resolution of the dispersive elements and optics (see Section 3.2.2). When the number of layers (or wavelength bands) Λ becomes large, starting from approx. 100, the resulting image is called hyperspectral image, or hypercube. Figure 3.2 depicts the structure of a three-dimensional (3D) hypercube. The coordinates x $= [1, 2, ..., X]$ and y $= [1, 2, ..., Y]$ in the X $\times$ Y $\times$ Λ hypercube correspond to the real world coordinates x and y in the object plane (i.e. plane where the imaged object is located; conveyor belt in this work, see Sections 3.3 and 6.1). The X $\times$ Y $\times$ Λ hypercube can be represented as a X $\times$ Y grid of 1 $\times$ Λ vectors. Each

Figure 3.1: Example of an RGB color image [43]. Three layers (red, green and blue, not to scale) are combined on a computer screen to create the illusion of a color image. The red, green and blue layers, or channels, roughly correspond to the colors seen by the human eye.

vector of length Λ at the coordinate $[x, y]$ is thus interpreted as a discretized spectrum $\boldsymbol{s}$. The spectrum $\boldsymbol{s}$ consists of digitized integer values s_i of light intensity I_i within a certain wavelength band $\Delta\lambda_i$, for $i = 1, 2, ..., \Lambda$. The unit of s_i is "digital counts", the conversion from light intensity I_i in W/m^2/nm to digital counts is carried out by a detector. In this work, it is denoted for simplicity that for any wavelength band $\Delta\lambda_i$, the value $s_i = a_i \cdot I_i$, where a_i is a proportionality constant with units m^2·nm/W which depends on the detector's quantum yield, photosensitive area and electronics. The light intensity value in digital counts at a certain location $[x, y]$ in the hypercube is denoted by $s_i[x, y, \lambda_i]$, where λ_i is the discrete wavelength that corresponds to the analog wavelength band $\Delta\lambda_i$. In practice, every optical instrument has a finite spatial resolution, therefore the spatial coordinates $[x,y]$ in the hypercube correspond to the range of real-world coordinates or in other words to an acquisition spot of a finite size $(\Delta x, \Delta y)$. Hence the digitized intensity value s_i is the result of the integration of the analog intensity I_i over the spatial acquisition spot and the wavelength band:

$$s_i[x, y, \lambda_i] = a_i \cdot \int_{\Delta x} \int_{\Delta y} \int_{\Delta\lambda_i} I_i(x, y, \lambda_i) \, dx \, dy \, d\lambda_i. \qquad (3.1)$$

In remote sensing applications, the intensity of light reflected by the Earth's surface is usually measured. Every material has a unique and characteristic reflectance spectrum $\boldsymbol{s}$ along the wavelength axis λ. These unique and characteristic spectra are often referred to as "spectral signature" of this material. By comparing the spectral signature of an unknown material with the spectral signatures of known materials one can identify the chemical components present in this object and identify what material it is.

This concept holds true when fluorescence emission spectra are considered in the fluorescent labeling of plastics (see Chapter 2) where incorporated fluorescent markers are used. Similarly to satellite remote sensing applications, measured fluorescence spectra of
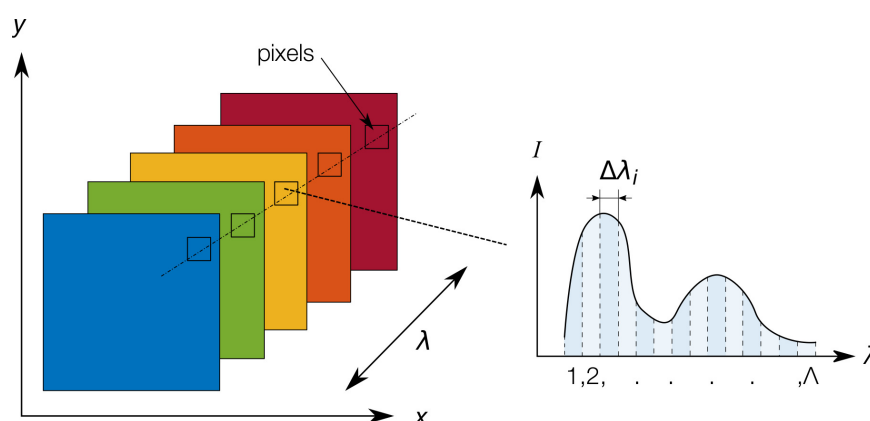
Figure 3.2: Hyperspectral image, or hypercube, consists of Λ 2D images each of size $X \times Y$ within the wavelength band $\Delta\lambda_i$. The 1D vectors $s[\lambda]$ in the hypercube represent the characteristic spectra of the material being investigated. "Spectrum" is the distribution of light intensity I over wavelengths λ.

unknown labeled plastics are compared with the known marker spectra for identification purposes.

3.2 Hyperspectral image acquisition

A measurement device for the acquisition of single spectra or hyperspectral images consists of several essential parts: 1.) an excitation light source, 2.) a dispersive optical element to select wavelength bands, and 3.) a detection system, which includes a light-sensitive sensor as well as control and digitization hardware and software [43]. In this section, first, a laboratory device for spectral characterization of materials – spectrofluorometer – is described; next, approaches to spectral and spatial scanning for fast and efficient acquisition of large objects or scenes are discussed.

3.2.1 Laboratory spectrofluorometer

The schematic diagram of a typical spectrofluorometer is shown in Fig. 3.3a [28]. In this instrument, a broadband excitation light source such as a xenon lamp is usually used. Xenon lamps provide high intensity over a broad wavelength range starting upward from approx. 250 nm. A dual grating excitation monochromator is used to produce monochromatic excitation light of a particular wavelength, which is then directed to the sample to stimulate fluorescence. The emitted fluorescence light is forwarded to the emission monochromator, which scans through wavelength bands. A sensitive photodetector such as a photomultiplier tube (PMT) is positioned after the emission monochromator to capture incoming fluorescence light. The sample presentation chamber may also contain optional optical elements such as shutters to block excitation or emission light, filters, polarizers, and a

beam splitter. The beam splitter is used to direct part of the excitation light onto a reference object with known and very stable fluorescence, which is captured by a second PMT. Changes in intensity of the excitation lamp due to e.g. aging can thus be corrected for using this reference measurement.

Acquisition of fluorescence excitation and emission spectra (see Section 2.1) is carried out as follows: to measure the fluorescence emission spectrum of a sample, the excitation monochromator is set to select the desired wavelength band $\Delta\lambda_i$ from the excitation light and the emission monochromator scans through the desired wavelength bands. The detector measures fluorescence emission intensity at different wavelength bands with fixed excitation wavelength band thus building up the fluorescence emission spectrum. In the excitation spectrum measurement, the emission monochromator is fixed at a certain wavelength band (typically at one of the emission spectrum maxima) and the detector measures fluorescence emission intensity at this wavelength band while the excitation monochromator scans through the desired excitation wavelength bands.

The spectral resolution of the acquired fluorescence spectra is determined by the slit width of both excitation and emission monochromator as well as by the sensor pixel resolution. Typical monochromators have slit width in the 10^{-5} m range, which provides nm spectral resolution. Typical sensors are capable to sample incident light with a sub-nm sampling rate.

Monochromators, however, are complicated and thus expensive devices. Additionally, their mechanical (scanning) parts are wear-prone. For this reason, instead of the xenon lamp and the monochromator, LEDs or laser diodes of certain wavelengths can be employed for excitation of the sample's fluorescence. This, of course, reduces the flexibility of selecting an arbitrary excitation wavelength band, which makes the acquisition of excitation spectra using LED or laser diodes is problematic. Also, optical low-, high- or bandpass filters in combination with broadband light sources (such as xenon lamps) can be used to shape the desired excitation light. Optical filters with passbands of several nm can also be used instead of the emission and/or excitation monochromator when a high spectral resolution is not necessary.

The functionality of a spectrofluorometer can be extended to permit time-resolved measurements (see Chapter 5). For example, a pulsed excitation light source (xenon lamp, LED, laser diode, etc.) can be installed instead of the time-constant excitation light source and a dedicated detector electronics is necessary to carry out time-correlated single photon counting (TCSPC) [28].

3.2.2 Spectral scanning

Data acquisition in the spectral dimension λ of the hypercube requires the utilization of techniques called spectral scanning. Ultimately, the goal is to split light into different wavelengths and acquire those separately. Several approaches currently exist:

1. Filter wheels consist of several optical bandpass filters with different cut-on and cut-off wavelengths. The wheel is rotated to switch from filter to filter and thus change
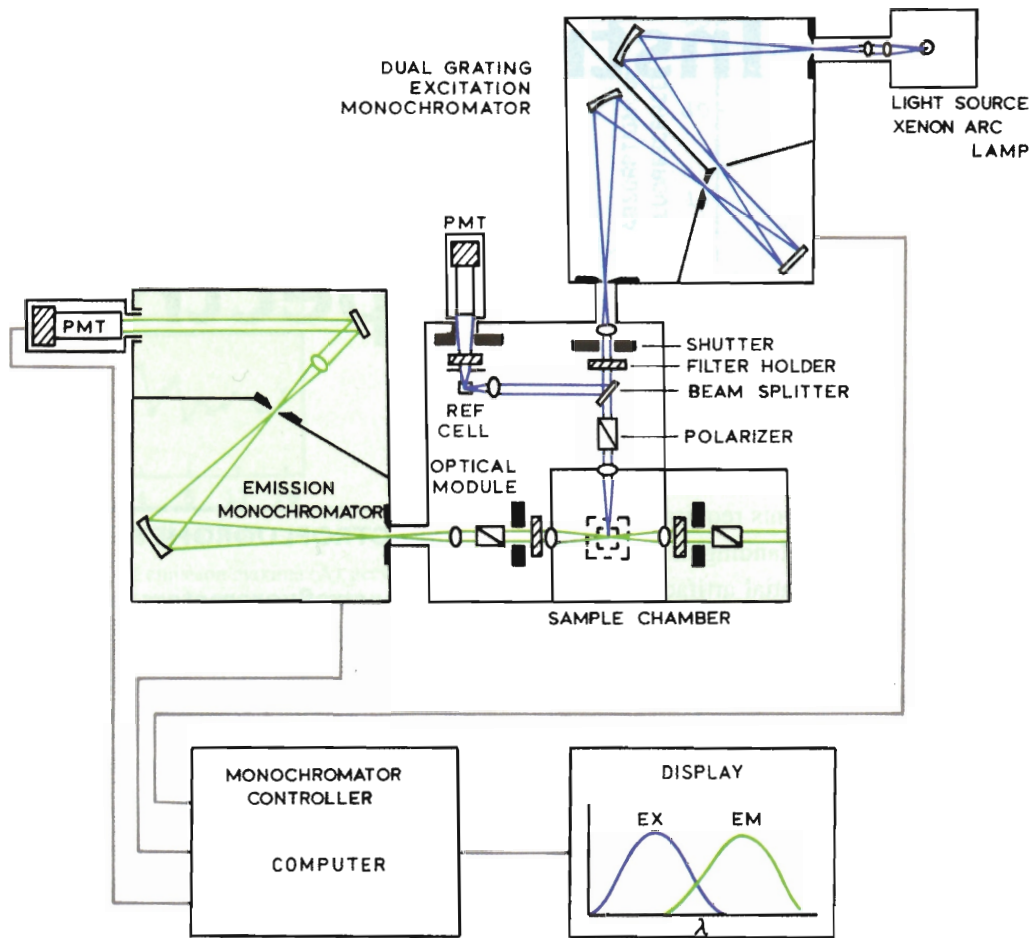
(a)
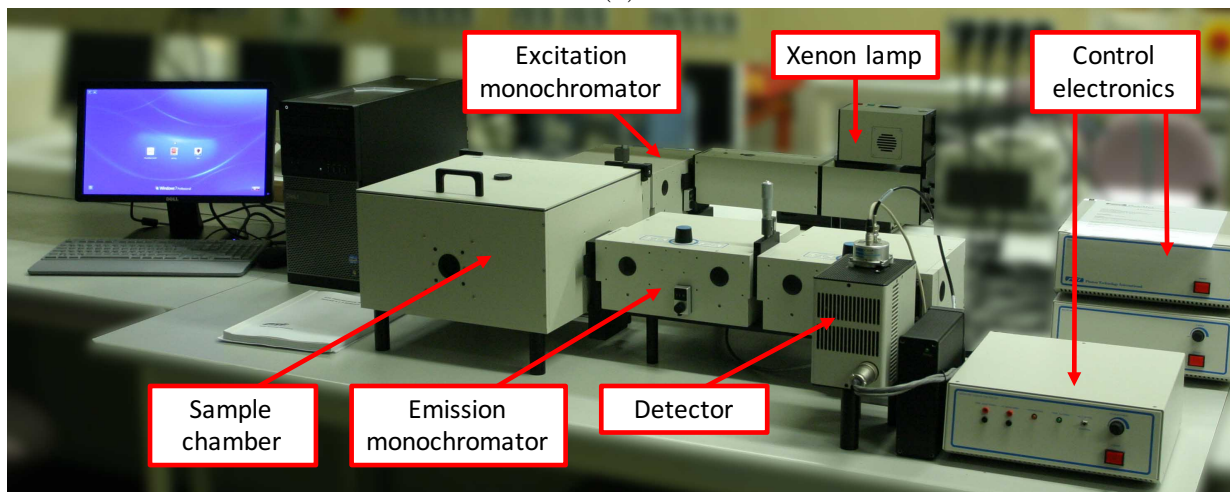
(b)

Figure 3.3: (a) Schematic diagram of a typical laboratory spectrofluorometer [28]. (b) Picture of the modular PTI Quantamaster 40 spectrofluorometer used for the investigation of fluorescent markers.

the wavelength band $\Delta\lambda_i$ acquired by the sensor. Filter wheels are typically used in multispectral imaging.

2. Acusto-optical tunable filters (AOTF) employ the principle of selective transmission of light wavelength bands $\Delta\lambda_i$ through a specialized material penetrated by acoustic waves. The optical passband is determined by characteristics of the material and the acoustic wave and can be varied over time. Similarly, liquid-crystal tunable filters (LCTF) have variable light transmission depending on the applied voltage. Both devices allow fast selection of wavelengths, but generally suffer from low optical throughput, limited angular fields of view [44] and are expensive [45].

3. Interferometer collects the so-called interferogram by splitting the investigated light into two beams, introducing a temporal delay in one of them and directing both beams onto the sensor [46]. The temporal delay is varied over phase shift $[0; 2\pi]$, which changes the interference of the two beams, the interferogram is thus built up. An inverse Fourier transform is usually used to extract the light spectrum from the interferogram, this technique is thus often referred to as Fourier transform spectroscopy. This approach is rather sophisticated with a fragile device and thus not suitable for industrial environments.

4. Prisms are optical components that refract incident light in different directions depending on its wavelength [46]. With a detector placed at the back of a prism, the intensity of the incident light at different wavelengths (i.e. the spectrum of the incident light) can be acquired.

5. Reflection gratings are optical components with a periodic structure of equally spaced grooves of a certain width that split incident light into beams of different wavelengths by diffraction [46]. Thus angle-dependent dispersion of light is achieved.

6. Transmission gratings are similar to reflection gratings but have slits instead of grooves [46]. Upon passing through the slits, the passing light is directed to different angles depending on the wavelength. The dispersion of light is also achieved by diffraction.

In approaches 1, 2, and 3 the acquisition of spectral information is carried out over time, i.e. wavelength bands are acquired one after another. This may be time-consuming and is therefore not suitable if a fast measurement rate is required. In contrast, in approaches 4, 5, and 6 wavelength bands are acquired simultaneously allowing fast measurements.

3.2.3 Spatial scanning

The spectrofluorometer described in Section 3.2.1 is a precise measurement instrument suited for laboratory investigations. It is best used in situations when the duration of the characterization of a material is more or less irrelevant. The measurement can take up to several minutes with commercial instruments of this type. In applications, however, where

a large scenery or many objects need to be investigated quickly and at a high rate, different measurement approaches are needed. Specifically, spatial scanning techniques can be employed. Three main approaches to spatial scanning exist: 1.) snapshot, 2.) whiskbroom scanning, and 3.) pushbroom scanning.

1. Snapshot means capturing the entire object or scene spatially at once using a 2D sensor and acquiring spectral information with a set of optical bandpass filters. The detector therefore acquires one X × Y layer of the hypercube at a time. In order to build up the spectral dimension λ of the hyperspectral cube, the object or scene has to be (spatially) captured multiple (Λ) times using filters with different passbands. This approach traditionally was used in multispectral imaging. Its main advantage is longer dwell time available for each pixel of the 2D sensor in comparison to whiskbroom or pushbroom scanning, which results in brighter images and less measurement noise. In the case of hyperspectral imaging, however, snapshot acquisition quickly becomes impractical: when the number of wavelength bands is increased, acquisition of the entire hypercube takes more and more time.

2. In whiskbroom scanning, the light from all object or scene points is sequentially directed to a single detector by a mirror. The mirror is mechanically rotated to move the acquisition point/spot back and forth along the spatial dimension y thus spatially building up one 1 × Y line of the image pixel by pixel. The spectral information is acquired by dispersed light coming from each pixel and projecting it on the single 1D detector. Hence, the imaging system captures one $1 \times \Lambda$ spectral vector (spectrum) $\boldsymbol{s}$ of the hypercube at a time, and the spatial dimension y of the hypercube arises from moving the imaging spot. After one 1 × Y line of the hypercube is captured, either the imaging system (e.g. a satellite in remote sensing applications) or the scene (e.g. conveyor belt in industrial monitoring applications) is moved one line forward in the scanning direction along the spatial dimension x and the acquisition of the next 1 × Y line of the hypercube begins. The third, x dimension of the hypercube thus arises from the movement along the scanning track.

   The main advantage of whiskbroom scanning is that all points/spots on the object or scene are captured by the same sensor, which means that there is no variance from spectrum to spectrum due to different sensors. The main disadvantage is that the dwell time (time available for integrating the light) for each pixel is relatively short, which reduces the signal-to-noise ratio (S/N ratio). Moreover, distortions resulting from the forward direction of the scenery during the acquisition of one line (motion blur) may occur. Finally, the mechanical moving parts make this type of scanner expensive and prone to wear [47].

3. In pushbroom scanning, similarly to whiskbroom scanning, the camera spatially captures the scene line by line. But in contrast, the acquisition of all spots in a line is carried out simultaneously: the 1D imaging line is dispersed into wavelength bands, and the resulting 2D image $s\,[\mathrm{y}, \lambda]$ is captured by a dedicated 2D sensor. For each

spot in the line, a corresponding spectrum is projected onto one dimension of the 2D sensor. The data read-out from the sensor at a time thus contains one $Y \times \Lambda$ slice of the hypercube. As in whiskbroom scanning, the third, x dimension of the hypercube arises from the scene movement. The complete spectral information of a spatial line is acquired simultaneously with the spatial information, providing higher measurement rates. Since the pushbroom scanner acquires all pixels in a line simultaneously, the dwell time for each pixel in this line is much longer in comparison to the whiskbroom scanner, provided both have the same measurement rate. This results in higher S/N ratios of the resulting images and spectra, which may be crucial in low-light fluorescence applications. Additionally, the lack of mechanical parts makes this type of scanners attractive for harsh environments.

The most critical drawback of pushbroom scanning in comparison to whiskbroom scanning is that different pixels in 2D sensors always have slightly different photosensitivity. Therefore, two equal spectra collected from two different locations on the same (identical) material may look different in the final digital image when acquired by two different pixel columns of the sensor. These distortions can be compensated for, but since the sensitivity of the pixels may change with time, it is necessary to carry out such compensation periodically.

For the application at hand, where small plastic flakes are delivered on a moving conveyor belt in an industrial environment (see Chapter 6), the pushbroom scanning approach is naturally the most suitable due to significant S/N ratio advantages and high robustness. As it will be shown in Chapter 4, noise is the main limiting factor for the reliable classification of fluorescence spectra, whereas some minor spectral shape changes can be tolerated by the classification algorithm, be it due to the poor quality of the fluorescent markers incorporation process, or to the spatially inhomogeneous sensitivity of the sensor pixels. Additionally, pushbroom scanning allows a reduction of illumination requirement: only one line across the object needs to be illuminated. This reduces the electrical power consumption and the heat load on the objects, as compared to the snapshot imaging and whiskbroom scanning.

3.3   Hyperspectral camera

The concept of the plastics classification and sorting system (described in detail in Chapter 6) inherits its composition from industrial monitoring systems and implies scanning a stream of plastic (waste) flakes delivered on a conveyor belt. The most important part of the measurement system is a linescan hyperspectral camera, that together with the conveyor belt implements the pushbroom approach to spatial scanning (see Section 3.2.3). This solution is advantageous because of its simplicity, robustness, relatively low price, and yet good imaging quality due to the prism-grating-prism (PGP) imaging spectrograph used in the spectral camera [48].

The overall arrangement of image acquisition with the spectral camera is illustrated in Fig. 3.4. In general, a pushbroom spectral camera consists of an objective lens, an imaging spectrograph, and a 2D detector. The objective lens gathers light emitted by or reflected off the object on the conveyor belt and directs it to the entrance slit of the imaging spectrograph. The slit is positioned perpendicular to the conveyor belt's movement direction x such that its width and length determine the camera's field of view in spatial directions x and y, respectively. Due to its geometry, from the 2D scenery captured by the objective lens, the slit selects only one narrow rectangular region of interest (ROI) across the conveyor belt, which corresponds to the y dimension of the hypercube. The light from the slit is collimated and dispersed by the PGP element producing the spectral dimension of the hypercube λ (see also Fig. 3.5). Therefore every spot of the rectangular ROI on the conveyor belt is represented by a 1D spectrum. The resulting 2D image $s\,[\mathrm{y}, \lambda]$ is projected on the 2D monochrome detector.

In this arrangement, spatial information is assigned to the horizontal axis of the 2D detector, parallel to the longer dimension of the entrance slit, and spectral information is assigned to the vertical axis, perpendicular to the entrance slit. Thus, the imaging spectrograph allows a 2D (monochrome) detector to sample the spectral dimension (λ) and one spatial dimension (y) of the 3D hypercube at a time. The second spatial dimension (x) results from the movement of the conveyor belt along the spatial direction x. Both spectral and spatial resolution of the resulting images are determined by characteristics of the objective lens and the spectrograph's slit dimensions, especially its width. In addition, the spectral resolution depends on the dispersion performance of the PGP element, especially on the quality of the grating [49].

The most important advantage of the utilized PGP imaging spectrograph is its straight optical path. The diagram in Fig. 3.5 depicts the light path through the PGP imaging spectrograph. In comparison to the usual dispersive elements that use arrangements of prisms and/or reflection gratings, the compact PGP element enables lightweight, robust, and thus industrially viable design of the spectral camera. Additionally, the optical throughput of the PGP spectrograph is usually 4 times better than that of an equivalent spectrograph that uses reflection gratings [49]. Overall, the PGP spectrograph provides very good optical and dispersive performance in comparison to other dispersive elements [50].

3.4   Imaging sensor

The 2D sensor (or detector) plays an important role in the acquisition of spectral and spatial information in the hyperspectral camera. In a simplified representation, the sensor and its electronics are responsible for: (1) converting the energy of the incident photons into electrical charges, (2) converting electrical charges into voltage signals, and (3) digitizing the voltage signal. On the output there is a digital "light intensity" value s in "digital counts" that corresponds to the physical light intensity I in $\mathrm{W/m^2/nm}$ (see Section 3.1).

The quality of the resulting (hyperspectral) image highly depends on the sensitivity of the sensor, which is determined by its quantum efficiency and photo-active area. The latter
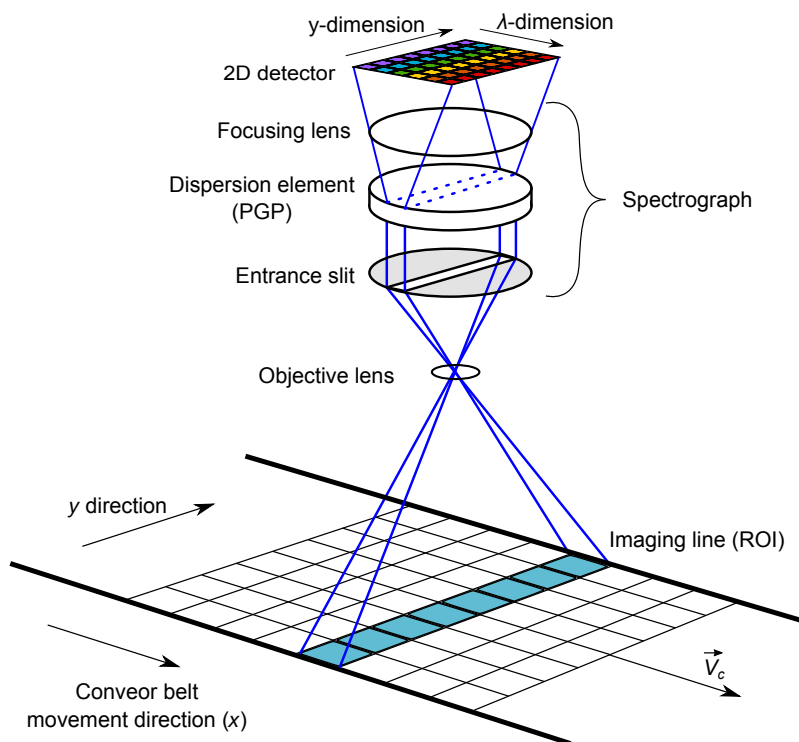
Figure 3.4: Pushbroom scanning implemented in the hyperspectral camera used in this work. The camera acquires a single line (ROI) across the conveyor belt in y direction at a time. The PGP spectrograph disperses the line in spectral components λ producing a 2D $Y \times \Lambda$ image, which is captured by a 2D grayscale sensor. The second spatial dimension x of the hypercube arises from the movement of the conveyor belt along the x direction.
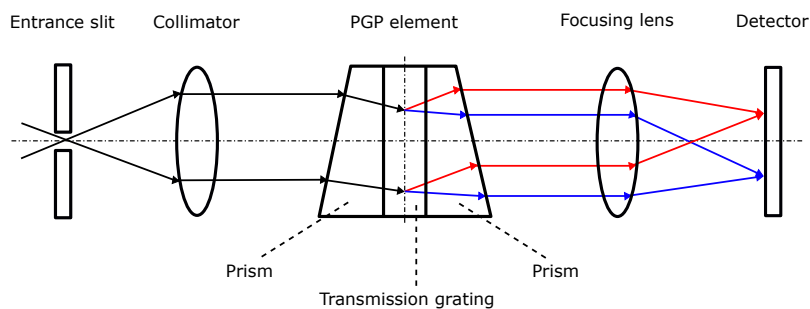
Figure 3.5: Optical arrangement of the PGP element. The main advantage of PGP is its straight optical path.

depends on the size of the pixels – bigger pixels of the same sensor type provide higher sensitivity. Quantum efficiency is a ratio of the number of electrons generated inside a pixel to the number of photons incident on that pixel. Two types of sensors are mainly used in industrial applications: complementary metal-oxide-semiconductor (CMOS) based and charge-coupled device (CCD) based sensors. Although both technologies rely on similar semiconductor photosensitive elements to convert the energy of incident photons into electrical charges, they are very different with regard to how these charges are transformed into a digital signal, which produces significant differences in the quality of images they produce. Also, different architectures of CCD and CMOS sensors result in different active areas and fill factors (see also Fig. 3.6).

CCD sensors use a structure of interconnected (charge-coupled) pixels (analogue "shift registers") to move electrical charges to a single output node (see Fig. 3.6a). At the output node, electrical charges are converted into a voltage signal, amplitude digitized, and read-out. The repeated shift of charges naturally creates a bandwidth bottleneck and essentially limits the sensor's frame rate. In contrast, CMOS sensors utilize "active" pixels that in addition to photosensitive elements also incorporate electronic circuitry to convert generated electrical charges into voltages (see Fig. 3.6c). These voltages from all pixels are then digitized and transferred to corresponding output nodes in a highly parallel fashion. The obvious advantage of this structure is the high frame rate, which can be further increased if only a certain ROI and thus fewer pixels need to be read out.

However, the parallel structure of "active" pixels introduces certain compromises that may not be suitable for a low-light application such as the measurement of fluorescence emission spectra. First, additional circuitry built upon each pixel reduces the photosensitive area and thus the pixel's sensitivity, resulting in dimmer images and in view of the S/N ratio in smaller dynamic range [51]. Second, uniformity, i.e. the consistency of the response signal of different pixels under equal illumination conditions is inherently worse with CMOS than with CCD where only a single amplifier and analog-to-digital converter (ADC) are employed. The non-uniformity is especially noticeable at low light levels. Finally, the "rolling shutter" typically used in CMOS sensors may introduce additional distortions in the image due to movements in the acquired scene. Implementation of a global shutter in CMOS sensors is possible, but requires additional electrical components built into each pixel, which decreases the pixel sensitivity even further [52]. CCD sensors do not have these drawbacks. Additionally, CCDs usually have better sensitivity in UV and IR light, which makes them a better choice for hyperspectral image acquisition [53].

Interline CCDs possess another useful feature, which is particularly interesting for the application at hand with regard to the autofluorescence (AF) problem described in Section 2.5.4. In interline CCDs, each photosensitive pixel is accompanied by an additional "storage" pixel, the so-called shift register, which is covered by an opaque shell to protect them from incident radiation (see Fig. 3.6b). After each acquisition frame (image), electrical charges generated in the photosensitive pixels are immediately transferred to the shift registers, which forward them to the output using the charge-coupled mechanism. While charges are being transferred by the shift registers, the photosensitive pixels can begin acquisition of a new frame; because read-out and exposure can happen in parallel, the overall
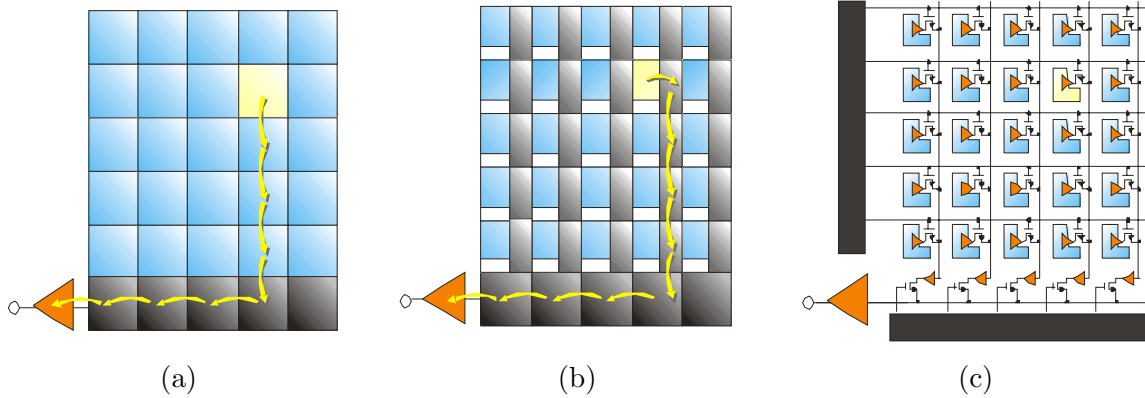
Figure 3.6: Architecture of (a) full-frame CCD, (b) interline CCD and (c) CMOS sensors. Blue (bright) squares represent photosensitive pixels, gray (dark) squares represent non-photosensitive "storage" pixels. Arrows represent the path along which generated electrical charges are transferred to the output amplifier in CCD sensors (a) and (b). In (c) CMOS sensors, charges are converted into voltage directly on the "active pixels" and voltages are transferred to the output. (Source: Dalsa [54])

frame rate is increased. Most importantly, storage pixels enable the so-called "frame accumulation" acquisition mode, where each frame consists of several subframes individually acquired by the photosensitive pixels at subsequent time slots and accumulated in the storage pixels. Charges generated during the acquisition of multiple subframes are stored and accumulated in the storage pixels; accumulated charges are not transferred to the output until a specified number of subframes has been accumulated. This "frame accumulation" facilitates the TGFS measurement approach and the suppression of the autofluorescence (AF) described in detail in Chapter 5.

CCDs also provide a method of operation that significantly increases their sensitivity – pixel binning. In binning mode, adjacent pixels are organized in groups of 2^n, electrical charges generated by the pixels in each group are added and the sum is transferred to the output node. As a result, the effective photosensitive area of binned pixels is doubled. Additionally, since the summation of charges is carried out in the analog domain, the noise associated with the conversion from charge to voltage, A-D-conversion, and read-out occurs only once per pixel group. Provided the intensity of light incident on the binned pixels is equal and the read-out noise generated in single pixels is uncorrelated, the S/N ratio can be increased by (almost) a factor of 2^n. Binning is also possible with CMOS sensors, but there noise coming from the amplifiers is inevitably added to the signals of every single pixel and therefore a binning of 2^n yields an increase of the S/N ratio of $\sqrt{2^n}$ at most (since read-out noise follows Gaussian statistics, see Section 3.4.1) [53].

Pixels in both horizontal and vertical directions can be binned. Binning in the vertical direction (i.e. direction parallel to the shift registers' transfer direction) also decreases the number of transfer steps in the CCD shift registers, therefore less time is needed for the transfer and the (overall) sensor frame rate can be increased. Since in the hyperspectral

camera used in this work the spectral dimension (λ) of the hypercube is projected on the vertical axis of the CCD sensor, an increase of the frame rate can only be achieved by binning in the spectral domain.

The trade-off for the increased sensitivity achieved through binning is a reduced spectral and/or spatial sampling of the resulting image (hypercube). However, especially in low light applications such as measuring subtle fluorescence emissions, an improved image S/N ratio outweighs the loss of spectral sampling.

3.4.1   Sensor noise

The quality of the image (hypercube) produced by the sensor is negatively affected by the noise of different types and origins. Understanding the origins of noise helps optimize the design of the spectroscopic system and improve the quality of the resulting images.

For the classification of fluorescence spectra as in this dissertation, especially noise in the spectral dimension of the hyperspectral cube is critical. Moreover, marker fluorescence spectra are processed separately from the spatial content. For this reason, image quality degradation due to (spatial) non-uniformity effects is not considered here.

There are four main sources of noise that need to be considered in the context of designing a spectroscopic measurement system [55, 56, 57]:

- Photon noise (or shot noise) arises from the fundamental property of the quantum nature of light, which is that the rate of photons emitted by a steady light source is not constant and varies over time according to the Poisson distribution. Therefore, the photon arrival rate at the CCD surface and the number of electrons generated in the photosensitive pixels also vary with Poisson statistics. The resulting photon noise is proportional to the square root of the number of incident photons that generate electrons and, equivalently, to the square root of intensity of the generated signal (voltage). The photon noise is multiplicative and has Poisson statistics.

- Dark current noise (or offset fixed pattern noise, FPN) comes from the variations in dark currents of different pixels due to the inequalities of their structures. Dark current noise depends on the temperature of the sensor pixels and can be virtually eliminated in cooled sensors at temperatures below approx. $-100\,^{\circ}$C. In room temperature sensors, dark current noise can be very distinctive especially in low-light conditions. Dark current noise is additive, it is not dependent on illumination and is relatively constant. It can be hence rather effectively suppressed by measuring and subtracting a dark frame from each acquired frame (i.e. here the $s\,[\mathrm{y}, \lambda]$ layer of the hypercube) [58]; the dark frame is to be acquired under the same conditions (temperature, acquisition time, etc.) as the frame that needs to be corrected.

- Dark current *shot* noise is of the same nature as photon noise but results from the fluctuations of the number of dark current electrons produced in the pixels. Dark current *shot* noise also follows Poisson statistics and is proportional to the square root of the number of dark current electrons.

- Read-out noise is a combination of noise produced by the electronics for amplification and conversion of electrical charges into voltage signals. This type of noise is additive and has Gaussian statistics. Read-out noise ultimately limits the S/N ratio of the sensor, but its influence can be reduced by averaging or filtering (e.g. in binning mode and/or in "frame accumulation" mode).

Under the assumption that the dark current noise can be effectively suppressed, the measured spectrum $\tilde{\boldsymbol{s}}$ (in digital counts) that represents the analog spectrum of the emitted fluorescence light (in W/m^2/nm) is thus corrupted by three most prominent noise types and is given by:

$$\tilde{\boldsymbol{s}} = \boldsymbol{s} \cdot \boldsymbol{n}_p(\boldsymbol{s}) + \boldsymbol{n}_d + \boldsymbol{n}_r, \tag{3.2}$$

where $\boldsymbol{s}$ is the (digital) spectrum without noise, $\boldsymbol{n}_p$, and $\boldsymbol{n}_d$ and $\boldsymbol{n}_r$ are photon, dark current shot and read-out noise, respectively, whereas the standard deviation of the photon noise is $\sigma_{\boldsymbol{n}_p} = \sqrt{\boldsymbol{s}}$.

3.4.2 Signal-to-noise ratio (S/N ratio)

As a measure of the amount of noise present in the measured spectrum $\tilde{\boldsymbol{s}}$, the signal-to-noise ratio (S/N ratio) is used:

$$\text{S/N} = 10 \cdot \log_{10}\left(\frac{P_s}{P_n}\right), \tag{3.3}$$

where P_s denotes the power of the spectrum $\boldsymbol{s}$ and P_n the power of the overall noise $\boldsymbol{n}$. For discrete $\boldsymbol{s}$ and $\boldsymbol{n}$, P_s and P_n are given by:

$$P_s = \frac{1}{\Lambda_s}\sum_{i=1}^{\Lambda_s} s_i^2, \tag{3.4}$$

$$P_n = \frac{1}{\Lambda_s}\sum_{i=1}^{\Lambda_s} n_i^2, \tag{3.5}$$

where s_i is the digitized value that represents the light intensity I_i within a certain wavelength band $\Delta\lambda_i$ as defined in Section 3.1, n_i is the overall noise component within the same wavelength band $\Delta\lambda_i$, and Λ_s denotes the number of (discrete) wavelengths where the spectrum $\boldsymbol{s}$ of the marker or marker combination is present. Since the marker spectra are situated in their individual wavelength ranges (see Fig. 2.6b) that do not cover the entire wavelength range of the sensor, calculating P_s and P_n within the entire sensor's wavelength range would artificially decrease the S/N ratio of marker combinations with few markers in comparison to those with many markers. To avoid this, both P_s and P_n are calculated only for the wavelengths where the (known) markers of each particular marker combination are present. Since in the laboratory measurements the class (i.e. the binary code) of the measured noisy spectrum is typically known a priori, it is also known what

markers are present in the spectrum and thus the wavelength bands $\Delta\lambda_i$ in Eqn. 3.4 and 3.5 can be easily specified. This also holds true for the simulations in Chapter 4 and experiments in Chapter 7.

Minimization of noise is one of the primary concerns in sensor design. As already mentioned, cooling is usually used to reduce the dark current noise and its dark current photon noise component. To reduce read-out noise, specialized electronics designs, digital filters, etc. are utilized [56, 59]. Photon noise, however, is a natural property of light itself and cannot be reduced by sensor design. Therefore, photon noise is essentially the minimum achievable noise level. When the intensity of the photon noise is significantly larger than the intensity of the read-out noise, the system is said to be photon noise limited, which represents the desired mode of operation. In low-light conditions as in the application in this work, when signal intensity and therefore photon noise intensity is low, read-out noise becomes dominant and the imaging system is said to be read-out noise limited.

The goal of this dissertation is to develop a system optimized in terms of minimal marker concentrations, large mass throughput, and highest possible measurement rate, while at the same time achieving good performance of classification of fluorescently labeled plastics. This results in a system that works close to the read-out noise limit (see also Chapter 6) and delivers spectra with relatively low S/N ratio. Several options to decrease the amount of noise in the measured spectra and increase their S/N ratio are available.

A simple way to decrease the amount of noise in the measured spectra is the averaging of several acquired spectra. For example, several spectra can be acquired from different locations on a plastic flake if it is larger than the camera's spatial sampling (spatial averaging) or from the same location one after another (temporal averaging). If the noise from different pixels is uncorrelated, averaging N spectra results in a decrease of both the Gaussian distributed and Poisson distributed noise components and thus in an increase of the S/N ratio by $\sqrt{N}$ (i.e. $20 \log_{10}(\sqrt{N})$ dB according to Eqn. 3.3).

The CCD pixel binning operation mode mentioned in Section 3.4 reduces only the read-out noise. With CCD pixel binning the summation of electrons generated by "binned" pixels is carried out in the analog domain and the read-noise is added after that only once. Hence in a read-out noise limited system, where the photon noise and the dark current shot noise are small (i.e. $n_p \ll n_r$ and $n_d \ll n_r$) and can be neglected, binning with a factor of N increases the S/N ratio of the acquired spectrum by a factor of N (i.e. $20 \log_{10} N$ dB):

$$\text{S/N}_N = 10 \cdot \log_{10}\left(\frac{P_{s_N}}{P_{n_N}}\right) = 10 \cdot \log_{10}\left(\frac{\sum_{i=1}^{\Lambda_s} s_{Ni}^2}{\sum_{i=1}^{\Lambda_s} n_{Ni}^2}\right) =$$

$$= 10 \cdot \log_{10}\left(\frac{\sum_{i=1}^{\Lambda_s}(N \cdot s_i)^2}{\sum_{i=1}^{\Lambda_s}(N \cdot n_{pi} + N \cdot n_{di} + n_{ri})^2}\right) \approx$$

$$\approx 10 \cdot \log_{10}\left(N^2 \cdot \frac{\sum_{i=1}^{\Lambda_s} s_i^2}{\sum_{i=1}^{\Lambda_s} n_{ri}^2}\right) =$$

$$= 20 \cdot \log_{10} N + 10 \cdot \log_{10} \left(\frac{\sum_{i=1}^{\Lambda_s} s_i^2}{\sum_{i=1}^{\Lambda_s} n_{ri}^2} \right) =$$

$$= 20 \cdot \log_{10} N + 10 \cdot \log_{10} \left(\frac{P_s}{P_n} \right) =$$

$$= 20 \cdot \log_{10} N + \text{S/N}, \tag{3.6}$$

where S/N_N stands for the S/N ratio of the spectrum acquired with a binning factor of N, P_{s_N} and P_{n_N} denote the power of the spectrum and the power of the noise in the "binned" spectrum, respectively, s_{Ni} and n_{Ni} are the spectrum and noise in the "binned" spectrum, respectively, s_i, n_{pi} and n_{di} are the spectrum, photon noise and dark current shot noise components in the individual (not "binned") pixels, and n_{ri} is the read-out noise added only once after the analog binning has been carried out.

Since despite binning the photon noise is added to each pixel, its component in the resulting "binned" spectrum is increased in comparison to the read-out noise component. Thus photon noise limited conditions can be potentially achieved even in low-light applications. If the photon noise n_p and dark current shot noise n_d cannot be neglected, the increase of the S/N ratio due to pixel binning is smaller than N, but is at least $\sqrt{N}$ (similar to the averaging).

It should be mentioned, that the above holds true when binned pixels contain identical copies of the spectrum $\boldsymbol{s}$, which is normally the case when binning is carried out in the spatial domain (x and y axes of the 3D hypercube, see Section 3.1). When binning is carried out in the spectral domain (λ axis of the 3D hypercube), each of the binned pixels contains digitized fluorescence intensity at a certain wavelength band. Thus, binned pixels contain non-identical, though correlated values, and binning N pixels results in the increase of the S/N ratio smaller than N.

In the "frame accumulation" mode of the interline CCD sensors mentioned in Section 3.4, the read-out noise is also added only once when a specified number N of subframes are acquired. Hence, similarly to binning, the S/N ratio is increased by (almost) a factor of N (i.e. $20 \log_{10} N$ dB) in a read-out noise limited system. In contrast to binning, signals are accumulated over time, thus the acquired scene (i.e. fluorescence light) must be temporally constant.

Chapter 4

Hyperspectral signal classification

The objective of hyperspectral signal classification in this dissertation is to automatically categorize different plastic types based on the fluorescence spectra acquired from fluorescently labeled plastic flakes. In this work, a class denotes a particular plastic labeled with a unique binary combination of fluorescent markers. "Better" classification leads to smaller classification errors and provides a higher quality of the recycled plastics. Naturally, there is no universal classification approach that suits every application. The selection of a classifier for a specific problem is often an iterative process. The goal of this chapter is to find the best approach to the problem at hand. In Sections 4.1-4.7 an overview of relevant classification techniques is given. Section 4.8 introduces different metrics to evaluate classification performance. In Section 4.9 computer simulations are employed to investigate the ability of different classifiers to deal with fluorescence spectra disturbances most relevant here: sensor noise, relative intensity fluctuations (i.e. fluctuations of the relation between fluorescence intensities of individual markers in marker combinations), and autofluorescence (AF).

4.1 Classification basics

Based on the availability of prior knowledge about investigated objects (here plastics and their emitted fluorescence spectra), all classification techniques can be divided in two broad groups: unsupervised and supervised classification. When absolutely no or very little prior knowledge about the objects is available, unsupervised classification methods can automatically group object features (here fluorescence spectra) in classes based on similarities between them, i.e. identifying "natural" structures within the available data. Unsupervised classification is usually followed by an expert a-posteriori analysis, when identified "natural" classes are assigned to the known objects or materials (here plastic types).

When prior knowledge about the investigated objects is available (or has been acquired during unsupervised classification), supervised classification can be carried out. In supervised classification, knowledge derived from examples (i.e. objects) of known identity (here plastic type) is used to assign novel (unseen) unclassified examples to one of the existing

classes. In the application at hand, plastic types and marker fluorescence emission spectra are known and thus the corresponding classes can be easily defined. Therefore, the main focus of this chapter lies in supervised classification methods.

Figure 4.1 shows the general structure of a supervised classification system. It consists of 5 stages: (1) data acquisition; (2) data pre-processing and enhancement; (3) feature extraction; (4) training; (5) classification. Stage (1) corresponds to the hyperspectral data acquisition discussed in Chapter 3. Stage (2) is responsible for data preparation which may include noise suppression, filtering, selection of relevant datasets, grouping data based on a priori knowledge, etc. The preprocessing stage is not explicitly described here. In the simulations in Section 4.9 (almost) no preprocessing is carried out in order to compare classifiers in equal (worst case) conditions. The data preparation carried out in the experiments in Chapter 7 is described there. Stage (3), feature extraction, aims at two goals: first, to reduce the dimensionality of the data and thus facilitate the use of complex classifiers; and second, to improve the interpretability and/or discriminability of the data to aid classification. At stage (4), a training algorithm is used to derive knowledge about existing classes from available (known) training data. Once this knowledge is derived, the classification of novel (previously unseen) data can be carried out at stage (5).

4.2   Spectral similarity measures

Even when high-dimensional data as in hyperspectral imaging needs to be classified, it is not always necessary to use traditional feature extraction approaches if numerically simple classification algorithms are employed. Rather, it may be advantageous to directly classify the acquired spectra.

The so-called spectral similarity measures utilize all Λ acquired discrete wavelength bands (spectral samples) of the spectrum to estimate the similarity between the unknown acquired spectra and the reference spectra of known classes. The acquired spectrum is then assigned to the class with the most similar value of the applied similarity measure. With regard to the structure of a supervised classification shown in Fig. 4.1, stage (4), training, is represented by deriving the reference spectra of known classes from the training data, and stage (5), classification, is carried out by assigning the unknown acquired spectra to the known classes, which reference spectra they are most similar to (in terms of the applied similarity measure).

Below is a short overview of the similarity measures used in this work.

4.2.1   Euclidean distance (ED)

Euclidean distance (ED) is a geometric measure that determines the spatial distance between two spectra in the Λ-dimensional space. Let $\boldsymbol{s} = [s_1, s_2, ..., s_\Lambda]^T$ be the acquired fluorescence spectrum to be classified, and $\boldsymbol{r_i} = [r_{i1}, r_{i2}, ..., r_{i\Lambda}]^T$ be the known reference spectrum of class ω_i, where Λ is the number of (discrete) wavelength bands (i.e. spectral
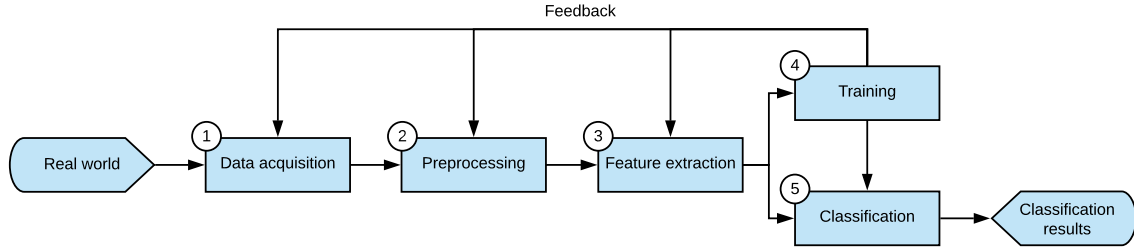
Figure 4.1: Flowchart of a typical classification system includes 5 stages.

samples). ED between these two spectra is then given by [60]:

$$\text{ED}_i(\boldsymbol{s}, \boldsymbol{r_i}) = \sqrt{\sum_{\lambda=1}^{\Lambda} (s_\lambda - r_{i\lambda})^2}, \tag{4.1}$$

where λ denotes the discrete wavelength band (spectral sample) and i indicates the membership of class ω_i. Provided both $\boldsymbol{s}$ and $\boldsymbol{r_i}$ are normalized (have the same peak intensity), small ED_i values mean high similarity between the unknown spectrum $\boldsymbol{s}$ and the reference spectrum $\boldsymbol{r_i}$. When ED_i values of all $i = 1..C$ classes have been calculated, the unknown spectrum $\boldsymbol{s}$ is assigned to the class with the smallest ED_i.

ED is very sensitive to the magnitude (i.e. the digitized value of the fluorescence intensity $s[\lambda]$) of compared spectra, hence, for proper classification all spectra need to be normalized [61]. In this work, normalization of the magnitude is carried out for all spectra, so that $\max(s_j) = 1$ for all $j = 1, 2, ..., \Lambda$.

4.2.2 Sum of absolute differences (SAD)

The sum of absolute differences (SAD) is a numerically more efficient variation of ED:

$$\text{SAD}(\boldsymbol{s}, \boldsymbol{r_i}) = \mid \boldsymbol{s} - \boldsymbol{r_i} \mid = \sum_{\lambda=1}^{\Lambda} \mid s_\lambda - r_{i\lambda} \mid . \tag{4.2}$$

Similarly to ED, SAD requires normalization of $\boldsymbol{s}$ and $\boldsymbol{r_i}$ for correct classification.

4.2.3 Spectral cross correlation (SCC)

The cross correlation approach used in many signal and image processing applications measures the linear dependence of two (vector) patterns. Here, the spectral cross correlation (SCC) measures the degree of linear dependence (and hence similarity) between two fluorescence spectra. For two spectra $\boldsymbol{s}$ and $\boldsymbol{r_i}$ ($i = 1, 2..C$), SCC is defined by [62]:

$$\text{SCC}_i(\boldsymbol{s}, \boldsymbol{r_i}) = \frac{\sum_{\lambda=1}^{\Lambda} [(s_\lambda - \overline{s}) \cdot (r_{i\lambda} - \overline{r_i})]}{\sqrt{\sum_{\lambda=1}^{\Lambda} (s_\lambda - \overline{s})^2 \cdot \sum_{\lambda=1}^{\Lambda} (r_{i\lambda} - \overline{r_i})^2}}, \tag{4.3}$$

where $\overline{s}$ and $\overline{r_i}$ are the mean values of the two spectra. SCC is equal to 1 when the spectra are equal or scaled versions of each other and 0 when they are uncorrelated. The acquired spectrum $\boldsymbol{s}$ is assigned to the class ω_i with the highest SCC_i value.

SCC is primarily sensitive to the shape differences of the compared spectra and insensitive to magnitude differences, which may be advantageous if a proper scaling/normalization of spectra is not possible due to e.g. noise.

4.2.4   Differential spectral cross correlation (DSCC)

The differential spectral cross correlation (DSCC) is the SCC (Eqn. 4.3) calculated using first derivatives of the fluorescence spectra with respect to the wavelength λ:

$$\text{DSCC}_i = \text{SCC}_i(\frac{\mathrm{d}\boldsymbol{s}}{\mathrm{d}\lambda}, \frac{\mathrm{d}\boldsymbol{r_i}}{\mathrm{d}\lambda}). \tag{4.4}$$

In Eqn. 4.4 the formula of the derivative for the continuous space is shown, in practice it is replaced by the discrete derivative, e.g. $\Delta\boldsymbol{s}/\Delta\lambda$. DSCC values are interpreted similar to SCC values (1 and 0 mean good bad similarity, respectively) and the acquired spectrum is assigned to the class with the highest DSCC_i value. DSCC can be useful for fluorescence spectra with sharp peaks but is inherently prone to noise.

4.2.5   Spectral angle mapper (SAM)

The spectral angle mapper (SAM) is an extension of the two-dimensional space angle to the Λ-dimensional spectral space. SAM estimates the similarity between two spectra $\boldsymbol{s}$ and $\boldsymbol{r_i}$, $i = 1, 2, .., C$, by measuring the "angle" between them given by [60]:

$$\text{SAM}_i(\boldsymbol{s}, \boldsymbol{r_i}) = \arccos(\frac{\boldsymbol{s}^T \cdot \boldsymbol{r_i}}{\|\boldsymbol{s}\| \cdot \|\boldsymbol{r_i}\|}), \tag{4.5}$$

where $\|\boldsymbol{s}\|$ and $\|\boldsymbol{r_i}\|$ denote the euclidean norm of $\boldsymbol{s}$ and $\boldsymbol{r_i}$, respectively. Smaller angles (i.e. smaller SAM_i values) mean higher similarity between compared spectra.

Similar to SCC, SAM is primarily sensitive to shape differences of the compared spectra and insensitive to magnitude differences [61]. In contrast to SCC, SAM does not centralize the data in the mean and introduces a non-linearity due to the arccosine function.

4.3   Feature extraction

Feature extraction is the process of finding characteristic components – features f – that describe information as unambiguously and compact as possible. Good features allow the explicit definition of classes and avoid misinterpretation of one class for another. Furthermore, feature extraction usually reduces the dimensionality of the raw data thus keeping computational costs of further processing (classification) low(-er). The vector $\boldsymbol{f}$ which elements are features f is called the feature vector.

The most straightforward type of features is the so-called expert features, which are a set of logical rules derived from expert knowledge about the objects and applied for classification. For example, in the application at hand, such expert features could be the (known) positions of peaks in the fluorescent marker spectra. A classification algorithm based on this idea of a single data point is, however, very susceptible to sensor noise [32]. A less straightforward way to define distinctive features is to apply an algebraic transformation to the data. Three such techniques of most interest for the problem here, principal component analysis (PCA), linear discriminant analysis (LDA) and least-squares mixture analysis (LSMA) are discussed below.

4.3.1 Principal component analysis (PCA)

Principal component analysis (PCA) is one of the main methods of data dimensionality reduction with loss of information and is a common technique for feature extraction in high dimensional data. The main idea is to convert the multivariate, possibly correlated data into a smaller set of linearly uncorrelated values, which are called principal components.

Let $\boldsymbol{S} = [\boldsymbol{s}_1, \boldsymbol{s}_2, ..., \boldsymbol{s}_J]$ be the initial dataset consisting of J unknown fluorescence spectra $\boldsymbol{s}_j = [s_{j1}, s_{j2}, ..., s_{j\Lambda}]^T$, where $j = 1..J$ and Λ is the number of discrete wavelength bands in the spectrum (i.e. spectral samples). PCA transformation is built up of eigenvectors of the data covariance matrix, sorted in descending order according to the corresponding eigenvalue. The following eigenvector decomposition of the covariance matrix is used in order to find these eigenvectors [63]:

$$\boldsymbol{\Sigma} = \boldsymbol{E}\boldsymbol{D}\boldsymbol{E}^T, \tag{4.6}$$

where $\boldsymbol{\Sigma} = \mathrm{cov}(\boldsymbol{S})$ is the covariance matrix of $\boldsymbol{S}$, $\boldsymbol{E} = [\boldsymbol{e}_1, \boldsymbol{e}_2, ..., \boldsymbol{e}_\Lambda]$ is the matrix composed of the eigenvectors $\boldsymbol{e}_j$ of $\boldsymbol{\Sigma}$ and $\boldsymbol{D}$ is the diagonal matrix composed of the eigenvalues e corresponding to the eigenvectors $\boldsymbol{e}_j$. For large matrices finding eigenvalues and eigenvectors is usually carried out using numerical algorithms [64] implemented in many software packages.

The PCA is defined as a linear transformation:

$$\widetilde{\boldsymbol{s}}_j = \boldsymbol{E}^T \boldsymbol{s}_j \text{ for } j = 1, 2, ..., J. \tag{4.7}$$

Vectors $\widetilde{\boldsymbol{s}}_j$ form the transformed matrix $\widetilde{\boldsymbol{S}} = [\widetilde{\boldsymbol{s}}_1, \widetilde{\boldsymbol{s}}_2, ..., \widetilde{\boldsymbol{s}}_J]$ of the PCA coefficients (i.e. principal components) of the original data $\boldsymbol{S}$. The number of principal components after transformation is equal to the number of variables (here Λ, number of discrete wavelength bands) in the initial dataset, but since principal components in transformed data are arranged according to the variance in the eigenvectors/eigenvalues and thus according to the amount of "information" they contain, reducing the dataset $\widetilde{\boldsymbol{S}}$ to only the first several principal components usually results in a marginal loss of information.

For example, 63 binary combinations of 6 fluorescent markers are normally characterized by their 63 fluorescence emission spectra each with $\Lambda = 350$ discrete wavelength bands (spectral samples), resulting in a 350×63 matrix. However, with PCA each of the 63

spectra can be reduced to e.g. a 6-dimensional vector by taking only the first 6 principal components. Figure 4.2a depicts the Pareto chart of the variance of the first 6 principal components of the dataset $\boldsymbol{S}$. It can be seen, that these first 6 principal components contain more than 99% of the variance in the data, which is essentially the information carried by these data.

PCA can also improve the interpretability of the data, i.e. the degree to which a human observer can understand the structure of the data. Figure 4.2b shows the 3D plot of the first 3 principal components of the first 7 of 63 fluorescence spectra of the binary marker combinations corrupted with 10 dB noise, grouped according to their class label. It is easy to see that all 7 classes make up 7 well-separated regions in the 3-dimensional PCA feature space. Similarly, 63 classes are grouped in separated regions in the 6-dimensional PCA feature space (not shown here for obvious reasons).

4.3.2 Linear discriminant analysis (LDA)

Linear discriminant analysis (LDA) is very similar to PCA, but instead of searching for a geometrical transformation that ranks components according to their variance (i.e. carried information) and thus maximizes interpretability of the data, LDA maximizes discriminability of multiple classes in the data, i.e. the capability of different classes in the data to be distinguished from one another. As illustrated in Fig. 4.3, LDA searches for a projection of data such that examples from the same class are located close to one another, and at the same time far from examples from other classes.

Mathematically this criterion can be expressed in terms of within and between class scatter matrices. Let $\boldsymbol{S}_i = [\boldsymbol{s}_{i1}, \boldsymbol{s}_{i2}, ..., \boldsymbol{s}_{iJ_i}]$ be the dataset consisting of J_i spectra belonging to the class ω_i, for $i = 1, 2, ..., C$. The within class and between class scatter matrices are then defined as follows [65]:

$$\boldsymbol{S_W} = \sum_{i=1}^{C} \sum_{j=1}^{J_i} (\boldsymbol{s}_{ij} - \boldsymbol{\mu}_i)(\boldsymbol{s}_{ij} - \boldsymbol{\mu}_i)^T, \quad \boldsymbol{S_B} = \sum_{i=1}^{C} (\boldsymbol{\mu}_i - \overline{\boldsymbol{\mu}})(\boldsymbol{\mu}_i - \overline{\boldsymbol{\mu}})^T, \quad (4.8)$$

where $\boldsymbol{\mu}_i$ is the mean spectrum of class ω_i and $\overline{\boldsymbol{\mu}}$ is the overall (global) mean spectrum:

$$\boldsymbol{\mu}_i = \frac{1}{J_i} \sum_{j=1}^{J_i} \boldsymbol{s}_{ij}, \quad \overline{\boldsymbol{\mu}} = \frac{1}{C} \sum_{i=1}^{C} \boldsymbol{\mu}_i. \quad (4.9)$$

The objective of LDA is to maximize the following function:

$$\mathrm{L}(\mathbf{W}) = \frac{\mathbf{W}^T \boldsymbol{S_B} \mathbf{W}}{\mathbf{W}^T \boldsymbol{S_W} \mathbf{W}}, \quad (4.10)$$

where $\mathbf{W}$ is the LDA transformation operator:

$$\widetilde{\boldsymbol{s}}_{ij} = \mathbf{W}^T \boldsymbol{s}_{ij}, \quad (4.11)$$
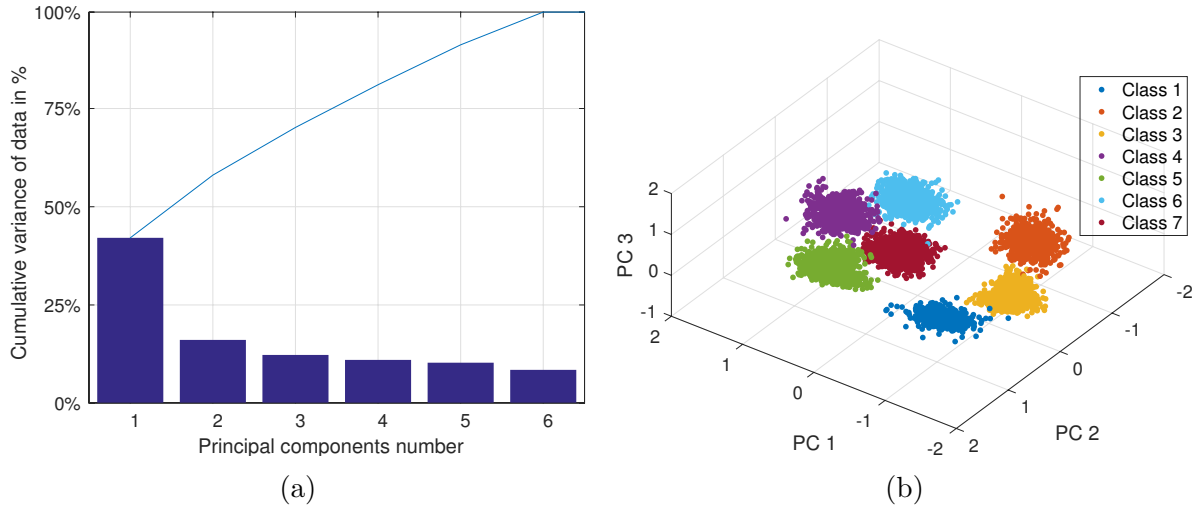
Figure 4.2: (a) Cumulative variance of the first 6 principal components of fluorescence spectra of 63 binary marker combinations. The first 6 of 63 principal components contain more than 99% of the overall variance and thus information. (b) The first 3 principal components of fluorescence spectra of the first 7 of 63 binary marker combinations (classes). Spectra were first corrupted with noise to achieve an average S/N ratio of 10 dB. 7 separated regions correspond to the 7 binary marker combinations.

where $\widetilde{\boldsymbol{s}}_{ij}$ denotes the projection of vector $\boldsymbol{s}_{ij}$ onto the LDA feature space. By maximizing $\mathrm{L}(\mathbf{W})$, good separability of the classes is achieved: small within-class scatter means that classes are compact, whereas large between-class scatter indicates at a large distance between classes in the feature space.

The optimal matrix $\mathbf{W}$ consists of eigenvectors that correspond to the eigenvalues in the following generalized eigenvector problem:

$$\boldsymbol{S_B}\mathbf{w}_i = q_i \boldsymbol{S_W}\mathbf{w}_i, \tag{4.12}$$

where q_i is the i-th eigenvalue. Eigenvalues q_i can be found as roots of the polynomial:

$$|\boldsymbol{S_B} - q_i\,\boldsymbol{S_W}| = 0, \tag{4.13}$$

and then eigenvectors $\mathbf{w}_i$ can be found from:

$$(\boldsymbol{S_B} - q_i\,\boldsymbol{S_W})\mathbf{w}_i = 0. \tag{4.14}$$

Similar to PCA, most often only the first several LDA features carry the majority of information. Since by definition better class discriminability can be achieved with LDA than with PCA, better classification results can be expected with the former. However, when an accurate estimation of class statistics (its location, size, and shape in the multi-dimensional feature space) is not possible due to e.g. a small training dataset, PCA may still achieve better results [66].
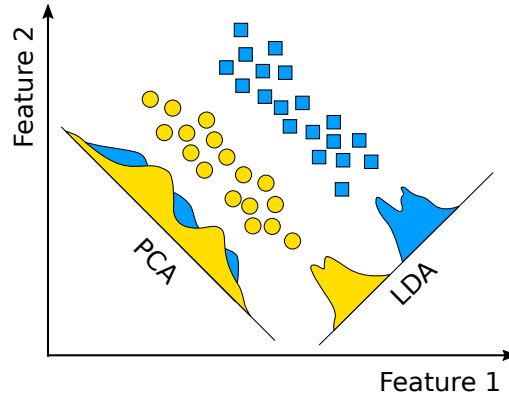
Figure 4.3: Comparison of PCA and LDA projections of 2-dimensional data. Yellow circles and blue squares represent examples belonging to arbitrary classes 1 and 2, respectively. Whereas PCA provides better data interpretability, LDA results in better discrimination of classes.

4.3.3   Least squares mixture analysis (LSMA)

Least-squares mixture analysis (LSMA) is a widely used group of techniques to determine and quantify materials in hyperspectral imagery, mostly in geoscience and remote sensing [67]. LSMA is based on the linear mixture model (LMM), which assumes that any (unknown) spectrum $\boldsymbol{s}$ can be represented as a linear mixture, or superposition, of several target (marker) spectra $\boldsymbol{m}_h$. Suppose that $\boldsymbol{M} = [\boldsymbol{m}_1, \boldsymbol{m}_2, ..., \boldsymbol{m}_M]$ is the matrix of target marker fluorescence spectra, where $\boldsymbol{m}_h = [m_{h1}, m_h2, ..., m_{h\Lambda}]^T$ is the $\Lambda \times 1$ spectrum of fluorescent marker M_h and M is the overall number of fluorescent markers. Let $\boldsymbol{\alpha} = [\alpha_1, \alpha_2, ..., \alpha_M]^T$ be a $M \times 1$ column vector associated with the (unknown) spectrum $\boldsymbol{s}$, where α_h denotes the abundance fraction of the marker fluorescence spectrum $\boldsymbol{m}_h$ present in the spectrum $\boldsymbol{s}$. The spectrum $\boldsymbol{s}$ can thus be represented by the following linear mixture model [68]:

$$\boldsymbol{s} = \boldsymbol{M}\boldsymbol{\alpha} + \boldsymbol{n}, \tag{4.15}$$

where $\boldsymbol{n}$ is the measurement noise. The goal of the mixture analysis is to estimate the unknown abundance fractions α_h of markers $\boldsymbol{m}_h$ in Eqn. 4.15. The least-squares (LS) error as the optimality criterion ("best fit") yields the following approximation $\widehat{\boldsymbol{\alpha}}_{LS}$ of the abundance vector $\boldsymbol{\alpha}$ [68]:

$$\widehat{\boldsymbol{\alpha}}_{LS}(\boldsymbol{s}) = (\boldsymbol{M}^T\boldsymbol{M})^{-1}\boldsymbol{M}^T\boldsymbol{s}, \tag{4.16}$$

where $(\boldsymbol{M}^T\boldsymbol{M})^{-1}\boldsymbol{M}^T$ is the Moore-Penrose pseudoinverse of marker spectra matrix $\boldsymbol{M}$ [69]. This is the most simple, unconstrained solution to Eqn. 4.15 for the case when all spectra in $\boldsymbol{M}$ are known. Unconstrained LSMA is useful when the goal is to only determine the

presence or absence of marker spectra $\boldsymbol{m}_h$ in the unknown spectrum $\boldsymbol{s}$. When the amount of the markers in the unknown spectrum needs to be determined, two constraints can be imposed: the sum-to-one constraint, $\sum_{h=1}^{M} \alpha_h = 1$, and the non-negativity constraint, $\alpha_h \geq 0$ for all $h = 1, 2, ..., M$.

Sum-to-one constrained least squares (SCLS) mixture analysis

Imposing the sum-to-one constraint on abundance fractions $\boldsymbol{\alpha}$ results in the following optimization problem:

$$\min_{\boldsymbol{\alpha} \in \Delta} \{ (\boldsymbol{s} - \boldsymbol{M}\boldsymbol{\alpha})^T (\boldsymbol{s} - \boldsymbol{M}\boldsymbol{\alpha}) \} \quad \text{subject to} \quad \Delta = \{ \boldsymbol{\alpha} | \sum_{h=1}^{M} \alpha_h = 1 \}. \tag{4.17}$$

The solution to this problem is given by [68]:

$$\widehat{\boldsymbol{\alpha}}_{SCLS} = \boldsymbol{P}\,\widehat{\boldsymbol{\alpha}}_{LS} + (\boldsymbol{M}^T\boldsymbol{M})^{-1}\mathbf{1}[\mathbf{1}^T(\boldsymbol{M}^T\boldsymbol{M})^{-1}\mathbf{1}]^{-1}, \tag{4.18}$$

where $\widehat{\boldsymbol{\alpha}}_{LS}$ is given by Eqn. 4.16, $\mathbf{1} = [1, 1, ..., 1]^T$ is an $M \times 1$ unity column vector and $\boldsymbol{P}$ is given by:

$$\boldsymbol{P} = \boldsymbol{U} - (\boldsymbol{M}^T\boldsymbol{M})^{-1}\mathbf{1}[\mathbf{1}^T(\boldsymbol{M}^T\boldsymbol{M})^{-1}\mathbf{1}]^{-1}\mathbf{1}^T, \tag{4.19}$$

where $\boldsymbol{U}$ is the identity matrix.

According to [68] and [60], the SCLS method provides more accurate quantification of materials present in the measured spectrum $\boldsymbol{s}$.

Non-negatively constrained least squares (NCLS) mixture analysis

The non-negatively constrained least squares (NCLS) problem can be formally stated as follows [70]:

$$\min_{\boldsymbol{\alpha} \in \Delta} \{ (\boldsymbol{s} - \boldsymbol{M}\boldsymbol{\alpha})^T (\boldsymbol{s} - \boldsymbol{M}\boldsymbol{\alpha}) \} \quad \text{subject to} \quad \Delta = \{ \boldsymbol{\alpha} | \alpha_h \geq 0, h \in [1, M] \}. \tag{4.20}$$

Finding a closed-form algebraic solution to the set of inequalities in Eqn. 4.20 is not always possible. In [70] an iterative algorithm that uses the following two equations was proposed:

$$\widehat{\boldsymbol{\alpha}}_{NCLS} = \boldsymbol{M}^T\boldsymbol{M}^{-1}\boldsymbol{M}^T\boldsymbol{s} - (\boldsymbol{M}^T\boldsymbol{M})^{-1}k = \widehat{\boldsymbol{\alpha}}_{LS} - (\boldsymbol{M}^T\boldsymbol{M})^{-1}k \tag{4.21}$$

and

$$k = \boldsymbol{M}^T(\boldsymbol{s} - \boldsymbol{M}\widehat{\boldsymbol{\alpha}}_{NCLS}). \tag{4.22}$$

where $\widehat{\boldsymbol{\alpha}}_{LS}$ is given by Eqn. 4.16. Equations 4.21 and 4.22 are iterated until the non-negativity constraint is not satisfied.

Although NCLS cannot accurately quantify the amount of materials present in the example (object), sometimes it may be advantageous over the unconstrained LSMA and SCLS for materials detection [60, 68].

Fully constrained least squares (FCLS) mixture analysis

The fully constrained least squares (FCLS) mixture analysis satisfies both the sum-to-one and non-negativity constraints in order to achieve good target detection and quantification performance. In order to accommodate the sum-to-one constraint, the target spectra matrix $\boldsymbol{M}$ and the measured spectrum $\boldsymbol{s}$ are modified as follows:

$$\widetilde{\boldsymbol{M}} = \begin{bmatrix} \delta\boldsymbol{M} \\ \boldsymbol{1}^T \end{bmatrix}, \quad \widetilde{\boldsymbol{s}} = \begin{bmatrix} \delta\boldsymbol{s} \\ 1 \end{bmatrix} \tag{4.23}$$

where δ is a constant, which controls the impact of the sum-to-one constraint [68]. Using $\widetilde{\boldsymbol{M}}$ and $\widetilde{\boldsymbol{s}}$ from Eqn. 4.23 in Eqn. 4.21 and 4.22 imposes both sum-to-one and non-negativity constraint on the LSMA problem.

4.4   Naive Bayes classification

The naive Bayes classifier is one of the most fundamental statistical approaches to classification. It encompasses a group of statistical classification methods based on the "naive" Bayes' assumption, that all elements in the feature vector $\boldsymbol{f}$ are independent. The main principle is to assess the probability of a correct classification of an example (i.e. an unknown object) given its feature vector by minimizing the cost of failure. The idea can be best explained for a 1-dimensional classification problem.

Let f denote a feature value in a one-dimensional feature space. In general, any discrete sample of the fluorescence spectrum $\boldsymbol{s}$, any PCA or LDA components, or any abundance fractions α_j can be taken as the feature f. The decision to be made is whether f indicates the membership in any of the classes ω_i, for $i = 1, 2, ..., C$. The probability of class ω_i given the feature value f, also called the posterior probability, or in other words, the probability that the feature value f belongs to the class ω_i, is given by the Bayes' formula [65]:

$$\rho(\omega_i|f) = \frac{\rho(f|\omega_i)\,\rho(\omega_i)}{\rho(f)}, \tag{4.24}$$

where $\rho(\omega_i)$ is the a-priori probability of class ω_i, $\rho(f|\omega_i)$ is the class-conditional probability density function of f (i.e. the probability density function of f given that the class is ω_i) and $\rho(f)$ is the so-called evidence, i.e. the probability of f belonging to any class at all. The evidence $\rho(f)$ is basically a normalization constant which scales all $\rho(\omega_i|f)$ to sum to one, denoted by:

$$\rho(f) = \sum_{i=1}^{C} \rho(f|\omega_i)\,\rho(\omega_i), \tag{4.25}$$

where C is the number of existing classes. The ideal (optimal) naive Bayes classifier supposes complete and absolute knowledge of probabilities in Eqn. 4.24. Thus, given $\rho(\omega_i|f)$, the intuitive decision rule is to select ω_i if $\rho(\omega_i|f) > \rho(\omega_j|f)$ for all $j \neq i$. Interestingly, the evidence value $\rho(f)$ is the same for all classes and thus does not influence the decision.

However, this simple decision rule does not consider the penalty for picking the wrong class, or more precisely, it assumes that the penalty for taking any action (choosing or not choosing any class) is always the same. In practice, however, this is not always the case. For this reason, the concept of the cost function and the risk was introduced [71].

Let $\boldsymbol{z} = [z_1, z_2, ..., z_Z]$ be the finite set of Z possible actions given the feature f, such as choosing class ω_i or not choosing any class at all. If $\xi(z_j|\omega_i)$ is the penalty or the cost of performing action z_j if f belongs to the class ω_i, the risk of taking action z_j is given by:

$$R(z_j|f) = \sum_{i=1}^{C} \xi(z_j|\omega_i) \cdot \rho(\omega_i|f). \tag{4.26}$$

The decision rule is formally defined as a function $z(f)$ that chooses one of the actions z for any given f. The overall risk associated with a given decision rule $z(f)$ is denoted by:

$$R = \int R(z(f)|f)\, \rho(f)\, df, \tag{4.27}$$

where integration is performed over the entire feature space. The Bayes decision rule aims to minimize the risk R and is thus stated as follows: to minimize the overall risk R, compute the conditional risk $R(z_j|f)$ for all possible z_j and select z_j for which $R(z_j|f)$ is minimal. The resulting minimal risk is called the Bayes risk. Provided that the posterior probabilities $\rho(\omega_i|f)$ are perfectly known, the Bayes decision rule gives the optimal classification result.

The Bayes decision rule is easily extended to a multidimensional case: instead of only one feature value f, a K-dimensional feature vector $\boldsymbol{f} = [f_1, f_2, ..., f_K]^T$ is used in the above equations.

4.4.1 Maximum-a-posteriori (MAP) and maximum-likelihood (MLC) classifiers

Despite its simplicity and strength, the Bayes decision rule can only serve as a theoretical foundation and guideline for the development of real-life classifiers. This is because in practice none of the probabilities $\rho(\omega_i|\boldsymbol{f})$, $\rho(\omega_i)$ or $\rho(\boldsymbol{f}|\omega_i)$ are usually known, which makes the use of an optimal naive Bayes classifier impossible. An approximation can be made by estimating these probabilities where the accuracy of such estimation highly depends on the available training data.

Under certain assumptions, it is sometimes possible to simplify the Bayes decision rule. Two of the most common variations of the Bayes decision rule are the maximum-a-posteriori criterion (MAP) and the maximum likelihood criterion. MAP assumes a zero (or symmetrical, i.e. when all actions have equal costs) cost function ξ and instead of minimizing the overall risk R, it maximizes the posterior probability $\rho(\omega_i|\boldsymbol{f})$ according to Eqn. 4.24. Thus, MAP decides in favor of the most probable class given a feature vector $\boldsymbol{f}$.

The maximum-likelihood classifier (MLC) further simplifies the Bayes decision rule by assuming equal prior probabilities $\rho(\omega_i)$ of all classes in addition to the zero cost function thus maximizing only the likelihood $\rho(\boldsymbol{f}|\omega_i)$. The likelihood is usually approximated by a normal distribution model [71]:

$$\rho(\boldsymbol{f}|\omega_i) = (2\pi)^{-K/2} \, |\boldsymbol{\Sigma}_i|^{-1/2} \exp(-\frac{1}{2}(\boldsymbol{f} - \overline{\boldsymbol{f}}_i)^T \, \boldsymbol{\Sigma}_i^{-1} \, (\boldsymbol{f} - \overline{\boldsymbol{f}}_i)), \tag{4.28}$$

where $\overline{\boldsymbol{f}}_i$ and $\boldsymbol{\Sigma}_i$ denote the mean feature vector and covariance matrix of class ω_i. MLC assigns the feature vector $\boldsymbol{f}$ to the class with the highest likelihood $\rho(\boldsymbol{f}|\omega_i)$.

Both MAP and MLC assign an example to a class independently of the absolute value of the posterior probability or the likelihood. Hence, even examples that do not belong to any of the known classes and thus have very low posterior probability or likelihood are assigned to one of the classes ω_i. In order to avoid this, a threshold on the posterior probability or the likelihood value can be introduced: examples with values lower than the threshold are not classified.

It should be noted that the calculation of the covariance matrix $\boldsymbol{\Sigma}_i$ and especially of its inverse as needed in Eqn. 4.28 for each class is a computationally costly task. Therefore, applying MLC directly to the fluorescence spectra, i.e. when $\boldsymbol{f} = \boldsymbol{s}$, might not be reasonable in a real-time application.

4.4.2 Mahalanobis distance (MD) and Euclidean distance (ED) classifiers

A further simplification of the Bayes decision rule presumes that all C classes have equal covariance matrices: $\boldsymbol{\Sigma}_i = \boldsymbol{\Sigma}$ for all i. A metric derived from this assumption and Eqn. 4.28 is called Mahalanobis distance [71]:

$$\mathrm{MD}_i = \sqrt{(\boldsymbol{f} - \overline{\boldsymbol{f}}_i)^T \, \boldsymbol{\Sigma}^{-1} \, (\boldsymbol{f} - \overline{\boldsymbol{f}}_i)}. \tag{4.29}$$

Geometrically the Mahalanobis distance classifier represents all classes as multidimensional ellipsoids of equal size and shape defined by the same $\boldsymbol{\Sigma}$. The Mahalanobis distance classifier assigns the feature vector $\boldsymbol{f}$ to the class with the smallest MD_i.

The Euclidean distance classifier further assumes $\boldsymbol{\Sigma} = \boldsymbol{U}$:

$$\mathrm{ED}_i = \sqrt{(\boldsymbol{f} - \overline{\boldsymbol{f}}_i)^T \, \boldsymbol{U}^{-1} \, (\boldsymbol{f} - \overline{\boldsymbol{f}}_i)}, \tag{4.30}$$

where $\boldsymbol{U}$ is the identity matrix. Therefore, geometrically ED represents all classes as points in the multidimensional space. The Euclidean distance classifier assigns the feature vector $\boldsymbol{f}$ to the closest class, i.e. to the class with the smallest ED_i.

4.5   Random forest (RF)

One of the most natural types of classifiers is the decision tree. A decision tree is a set of "if-then-else" rules arranged as a flowchart, each node of which represents a test of a certain attribute (feature f) of the input feature vector $\boldsymbol{f}$ and makes a classification decision based on the output of this test. For each such node, decision tree training algorithms try to find a feature and a threshold that achieves the best separation of the classes, whereas different metrics for the separation quality can be used [72].

The main downside of decision trees is that they tend to overfit the training data and do not generalize, i.e. perform poorly on novel data. To combat this downside, ensemble techniques are usually employed: the initial training dataset is split into smaller subsets, for each of which a separate decision tree is built; the ensemble of trees is then used to classify unknown data, whereas the final classification decision is carried out either by averaging the decisions of all trees or by the voting principle [72]. The random forest (RF) classifier is an ensemble of decision trees, each of which is trained on a random subset of the training dataset and, additionally, each node in the tree is trained on a random subset of available features, i.e. on a random feature subspace [73, 74]. The latter, although being counterintuitive, helps achieve better generalization [75].

Implementation of the random forest (RF) classifier used in this work is based on the original algorithm proposed in [75] and its MATLAB implementation by [76].

4.6   Support vector machine (SVM)

The support vector machine (SVM) is a relatively simple, yet powerful classification approach that requires little tuning and is thus suitable for problems where little or no prior knowledge about the nature of the data is available [77]. Initially, support vector machine (SVM) was defined only for linear binary classification, but extensions for multiclass non-linear problems make it suitable for a variety of scenarios.

Suppose a dataset $\boldsymbol{F} = [\boldsymbol{f}_1, \boldsymbol{f}_2, ..., \boldsymbol{f}_J]$ containing $j = 1, .., J$ K-dimensional feature vectors $\boldsymbol{f}_j = [f_{j1}, f_{j2}, ..., f_{jK}]^T$ ("examples") with respective class labels g_j so that $g_j = 1$ for class ω_1 and $g_j = -1$ for class ω_2, for all $j = 1, 2, .., J$. Two classes defined by these vectors are linearly separable if there exists a hyperplane that separates all feature vectors belonging to class ω_1 from vectors belonging to class ω_2. Figure 4.4 illustrates the 2-dimensional case with circles and squares belonging to classes ω_1 and ω_2, respectively.

Mathematically, any hyperplane in the feature space is defined as a set of points $\boldsymbol{f}_j$ satisfying $\boldsymbol{h}^T \cdot \boldsymbol{f}_j + h_0 = 0$, where $\boldsymbol{h}$ is the normal vector to the hyperplane and h_0 is the offset from the origin. In Fig. 4.4 two parallel hyperplanes $\boldsymbol{h}^T \cdot \boldsymbol{f}_j + h_0 = 1$ and $\boldsymbol{h}^T \cdot \boldsymbol{f}_j + h_0 = -1$ going through the closest to each other feature vectors from ω_1 and ω_2, respectively, define the margin between two classes. Feature vectors through which the hyperplanes are drawn, are called support vectors. The distance between two hyperplanes – the margin – is given by $2/\|\boldsymbol{h}\|$, where $\|\boldsymbol{h}\|$ is the euclidean norm of the vector $\boldsymbol{h}$. Intuitively, a hyperplane that maximizes this distance achieves the best separation of the classes. Thus, the problem of
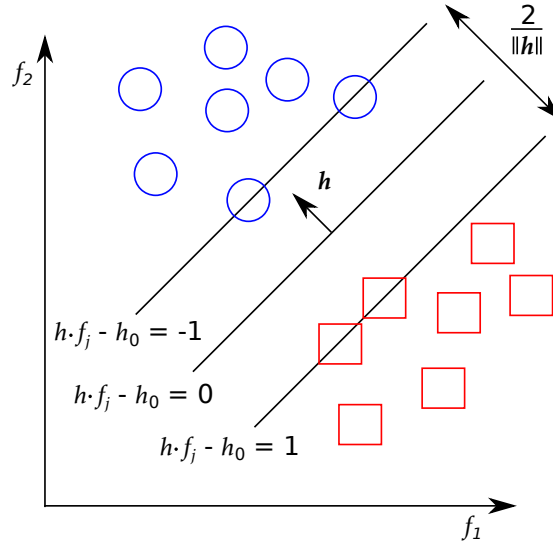
Figure 4.4: 2-dimensional geometrical illustration of an optimal hyperplane (line in 2D) in the feature space separating two classes represented by squares and circles.

finding the optimal hyperplane can be formally stated as follows:

$$\text{minimize } \|\boldsymbol{h}\|, \text{ subject to: } g_j\left(\boldsymbol{h}^T \cdot \boldsymbol{f}_j - h_0\right) \geq 1, \text{ for all } j = 1, 2, .., J. \tag{4.31}$$

The problem is usually arithmetically solved using quadratic programming algorithms [78].

When the given data is not linearly separable, the usual approach is to use a convenient function $\Phi(\boldsymbol{f}_j)$ to transform the low-dimensional raw data to a high-dimensional space where it becomes linearly separable and then apply SVM. However, for complex problems, too many dimensions in the new feature space would slow down the training of an optimal SVM. In order to bypass this problem, a technique called kernel trick is used [77]. The trick is to replace all vector dot products in the new feature space by a kernel function: $\Psi(\boldsymbol{f}_{j1}, \boldsymbol{f}_{j2}) = \Phi(\boldsymbol{f}_{j1}) \cdot \Phi(\boldsymbol{f}_{j2})$. Thus the kernel function uses low-dimensional representation of the feature vectors to calculate the result of their dot product in the high-dimensional space. Usual kernel functions include polynomials, Gaussian radial basis function and sigmoid function [77].

Multiclass SVM deal with the multiclass problem by splitting it into a set of binary problems. This is usually done by employing either the one-versus-all or the one-versus-one paradigm [79]. The former trains an individual SVM for each class so that feature vectors belonging to this class are treated with a positive label and feature vectors from all other classes have negative labels. In the end, the "winner takes all" principle selects the class with the highest SVM output. In the one-versus-one paradigm SVMs are trained to decide between pairs of classes. The decision made by each SVM is counted as a vote for a particular class. The unknown feature vector is then assigned to the class with the most votes.

4.7 Neural networks

Due to their nonlinear structure and flexibility, neural networks (NN) are very well suited for the situation, when the organization of the problem is not known and no assumptions about it can be made. Given the training data $\boldsymbol{F} = [\boldsymbol{f}_1, \boldsymbol{f}_2, ..., \boldsymbol{f}_J]$ containing $j = 1, .., J$ K-dimensional training feature vectors $\boldsymbol{f}_j = [f_{j1}, f_{j2}, ..., f_{jK}]^T$ ("examples") with respective class labels vectors (so-called "target" vectors) $\boldsymbol{g}_j = [g_{j1}, g_{j2}, ..., g_{jC}]^T$ so that $g_{ji} = 1$ if $\boldsymbol{f}_j$ belongs to class ω_i and $g_{ji} = 0$ otherwise, for all $j = 1, 2, .., J$ and $i = 1, 2, .., C$, neural networks (NNs) attempt to find the best "fit" for the data, i.e. derive the so-called decision boundaries that best separate all C classes in the K-dimensional feature space, and use this "fit" to classify the novel (i.e. unknown, previously unseen) data. Different NN architectures were developed for many applications including pattern recognition, clustering, function approximation, etc. [80]. Below is a brief overview of the most important concepts of NNs.

4.7.1 Neuron model

In order to achieve high numerical performance, NNs employ a highly interconnected structure of simple computing cells referred to as neurons. The diagram in Fig. 4.5a depicts the model of a neuron. Each neuron performs a relatively simple calculation: the elements f_k of the input feature vector $\boldsymbol{f} = [f_1, f_2, ..., f_K]^T$ are multiplied by the weights w_k of corresponding synapses, i.e. connecting links, the result is summed with the bias b and passed to the activation function φ, which calculates the output $\hat{g}$. Thus, the output of the neuron is given by:

$$\hat{g} = \varphi(v) = \varphi(u + b), \quad \text{with} \quad u = \sum_{k=1}^{K} w_k f_k, \tag{4.32}$$

where $v = u + b$.

Two types of activation functions are most often used for classification: the threshold function and the sigmoid function [80]. The threshold function, also known as the Heaviside function, is shown in Fig. 4.5b. A neuron with the threshold activation function is called McCulloch-Pitts neuron [81] and it models the behavior of a single neuron in a biological nervous system. The neuron employs the so-called all-or-none principle, which means that just like the biological neuron, the artificial neuron can either be activated (1) or not (0).

The sigmoid function is one of the most common activation functions used in NN architectures. The sigmoid function is an S-shaped, strictly increasing function and it maps the interval $(-\infty, +\infty)$ onto $(0, 1)$. Two most popular examples of sigmoid functions are the hyperbolic tangent function $\varphi(v) = \tanh(v)$ depicted in Fig. 4.5c and the logistic sigmoid function denoted by:

$$\varphi(v) = \frac{1}{1 + \exp(-av)}, \tag{4.33}$$
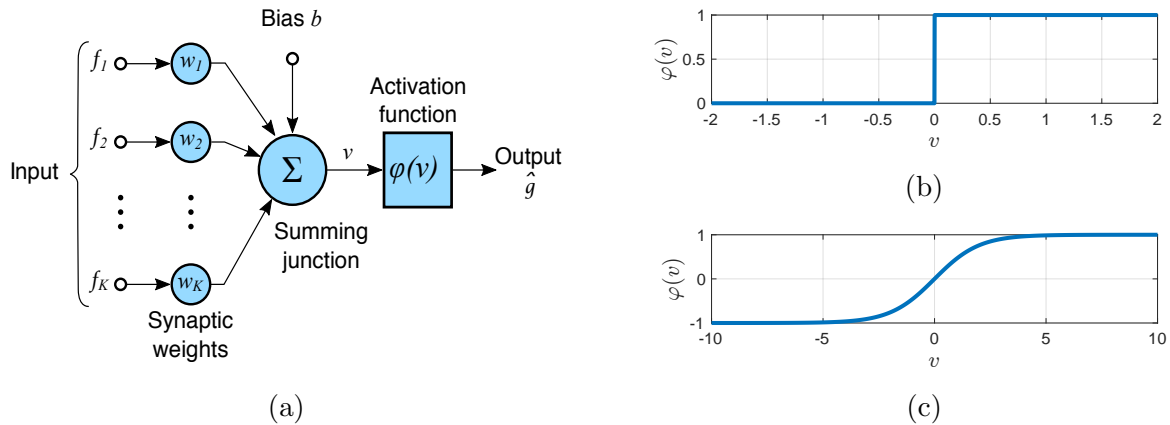
Figure 4.5: (a) The model of a neuron; (b) Heaviside and (c) sigmoid neuron activation functions (Source: Haykin [80]).

where a is the slope parameter.

4.7.2   Pattern recognition neural networks

The way neurons are connected with each other within one NN is referred to as the network topology or network architecture and along with the neurons' activation functions it defines the performance and functionality of the NN. The network architecture specifies the number of neuron layers, the size of these layers, and the types of interconnections between them. The more complicated the architecture of the NN is, the more sophisticated problems it can solve. On the other hand, a large number of layers and neurons in those layers increases the computational cost of training the network and may result in overfitting [82].

In practice, most of the pattern recognition and classification problems can be efficiently solved using relatively simple multilayer NN with only feed-forward interconnections. The single-layer perceptron is probably the simplest NN type used for classification and the first algorithmically described NN [80]. It has only one processing layer (Fig. 4.6a) – the output layer – consisting of McCulloch-Pitts neurons. It is a fully connected feed-forward NN, i.e. all nodes (neurons) of the input layer are connected with all neurons of the output layer. Although being simple, the single-layer perceptron is still a very powerful tool for the classification of linearly separable data [81].

The extension of the single-layer perceptron is the multi-layer perceptron, which is also a fully connected feed-forward neural network, but has at least one hidden layer of neurons (see Fig. 4.6b). Additionally, in comparison to the single-layer perceptron, neurons of the multi-layer perceptron use non-linear sigmoid activation functions. Having hidden layers and non-linear activation functions permits the classification of not linearly separable data. In fact, networks with only one hidden layer and non-linear activation functions are able to build decision boundaries that surround convex regions in the feature space, whereas three-layer networks (2 hidden layers) can create arbitrary decision boundaries [83].
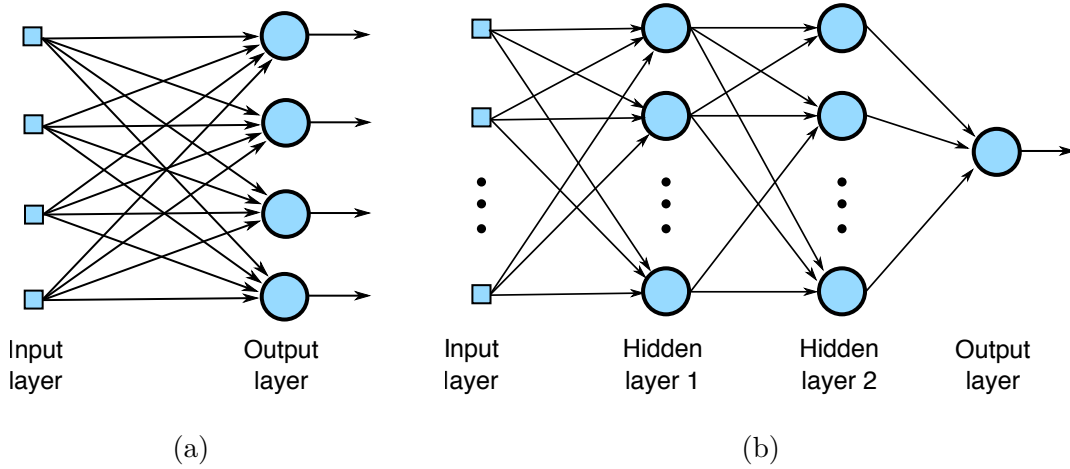
Figure 4.6: Architectures of (a) a single-layer and (b) a three-layer feed-forward neural network (Source: Haykin [80]).

4.7.3 Neural networks training

Neural networks training is an iterative process of adjusting the weights w_k and biases b of all neurons according to a certain training criterion. Training of a multilayer feed-forward network consists of two steps: (1) evaluation of the gradient of the training function (or error function) ϵ (see Eqn. 4.34) in the weight space, which is usually accomplished using the error back-propagation algorithm; and (2) modification (update) of the weights w_k to minimize the error function ϵ.

A variety of training functions ϵ can be used for neural network training. The least-squares criterion is an example of a training function used for regression analysis problems, where the output of the neural network is a continuous real number [81]. In classification problems the output layer of the neural network consists of C (equal to the number of classes in the problem) output neurons, whereas the "activated" output neuron has a value of $\hat{g}_i = 1$ representing the classification decision in favor of class ω_i, and all other output neurons are not "activated" and have a value of 0. The output of a classification neural network is therefore the vector $\hat{\boldsymbol{g}} = [\hat{g}_1, \hat{g}_2, ..., \hat{g}_C]^T$. For classification problems, the cross-entropy criterion is usually used, which is denoted by [81]:

$$\epsilon = -\sum_{j=1}^{J} \sum_{i=1}^{C} g_{ji} \log(\hat{g}_i(\boldsymbol{f}_j)), \tag{4.34}$$

where J is the overall number of training input feature vectors $\boldsymbol{f}_j$ in the training dataset $\boldsymbol{F}$, C is the size of the target output vector $\boldsymbol{g}_j$ and the corresponding NN output vector $\hat{\boldsymbol{g}}_j$ (which is equal to the number of classes ω_i), g_{ji} is the i-th element of the target output vector $\boldsymbol{g}_j$ corresponding to the training input feature vector $\boldsymbol{f}_j$ and $\hat{g}_i$ is the output of the i-th neuron in the output layer of the NN.

From a mathematical point of view, the goal of the neural network training is to minimize the training function ϵ using the training dataset, such that the trained neural network can be used to classify novel (i.e. previously unseen) data with small ϵ. The minimization of ϵ is usually done by the computationally efficient gradient descend method and the error back-propagation algorithm. A detailed explanation of both the error back-propagation algorithm and the gradient descend method can be found in [81].

4.8 Classification performance metrics

In order to choose the best classification method for a particular problem, a measure for the classification performance must be specified. The two most important characteristics of a classifier are the correctness of classification and computational cost. Whereas the latter can be easily measured, the definition of "correctness" can be ambiguous. Usually, correctness is evaluated using the following 4 counts:

- true positives (TP): the number of correctly recognized class examples, i.e. when an example that belongs to the class was correctly recognized as such.

- true negatives (TN): the number of correctly recognized examples that do not belong to the class, i.e. when an example not belonging to the class was correctly recognized as such. This case corresponds to correct rejection.

- false positives (FP): the number of examples incorrectly assigned to the class. This case corresponds to the false alarm or type I error [84].

- false negatives (FN): the number of examples that actually belong to the class but were not recognized as such. This case corresponds to a miss, or type II error [84].

In a multiclass problem, i.e. when more than one class needs to be recognized, the counts above are specified for each class ω_i individually: TP_i, TN_i, FP_i and FN_i. Depending on the application, the counts can be more or less important. In the application at hand, "positive" class examples correspond to the labeled plastic flakes that need to be sorted (recycled), and "negative" class examples are represented by either unlabeled plastic flakes or plastic flakes with an unknown fluorescence emission, e.g. labeled with counterfeit fluorescent markers. In any case, as long as no "negative" class examples get into the respective containers with "positive" class examples, the quality (purity) of the recycled plastics is intact. This means in particular, that the number of correct rejections TN is less important.

These 4 counts can be combined to calculate classification performance metrics. A thorough overview of classification performance metrics can be found in [84]. For the application at hand, two performance metrics are of most importance: the true positive rate (TPR), also known as recall or sensitivity:

$$\text{TPR}_i = \frac{\text{TP}_i}{\text{TP}_i + \text{FN}_i} \cdot 100\%, \tag{4.35}$$

and the positive predictive value (PPV), also known as precision:

$$\mathrm{PPV}_i = \frac{\mathrm{TP}_i}{\mathrm{TP}_i + \mathrm{FP}_i} \cdot 100\%, \tag{4.36}$$

where index i indicates class ω_i.

Both of these metrics are important for the assessment of the classification performance. TPR_i indicates what percentage of all examples that belong to class ω_i was actually assigned to this class. In plastics sorting that corresponds to the recovery rate of a particular plastic type ω_i. However, TPR_i alone does not unveil the full picture. For example, in a binary decision problem, a classifier that always returns positive decisions (i.e. classifies all examples as belonging to the class) would have TPR=100%, even though all negative examples (not belonging to the class) would be incorrectly classified as positive, i.e. FP would be high. In plastics sorting that would mean that many unlabeled plastic flakes would get into the container(s) with labeled plastic flakes, decreasing the purity (and quality) of the recycled product. In order to avoid this, one also needs to consider the PPV_i values which indicate what percentage of positively classified examples was actually positive.

For a more compact representation of classifier performance in multiclass decision problems, averaged versions of TPR and PPV are typically used. Two types of averaging exist: micro-averaging and macro-averaging. The former is given by:

$$\mathrm{TPR}_\mu = \frac{\sum_{i=1}^{C} \mathrm{TP}_i}{\sum_{i=1}^{C} \mathrm{TP}_i + \sum_{i=1}^{C} \mathrm{FN}_i} \cdot 100\%, \tag{4.37}$$

$$\mathrm{PPV}_\mu = \frac{\sum_{i=1}^{C} \mathrm{TP}_i}{\sum_{i=1}^{C} \mathrm{TP}_i + \sum_{i=1}^{C} \mathrm{FP}_i} \cdot 100\%, \tag{4.38}$$

where $i = 1, ..., C$ is the number of classes. If the class sizes in the dataset used for testing the classifier are unbalanced, i.e. some classes have more examples than others, large classes will have higher impact on the micro-averaged TPR_μ and PPV_μ values, which might be unwanted. Micro-averaging can be useful when the class sizes in the dataset are representative and important for classification, and a similar relation between classes is expected to hold in practice. For all other cases, macro-averaging is preferable. Macro-averaging treats all classes equally, independently of their sizes:

$$\mathrm{TPR}_M = \frac{\sum_{i=1}^{C} \mathrm{TPR}_i}{C}, \tag{4.39}$$

$$\mathrm{PPV}_M = \frac{\sum_{i=1}^{C} \mathrm{PPV}_i}{C}, \tag{4.40}$$

In order to evaluate the classification performance based on a single metric, TPR and PPV can be combined as follows:

$$\mathrm{F}_\beta\text{-score}_i = \frac{(\beta^2 + 1)\mathrm{PPV}_i \cdot \mathrm{TPR}_i}{\beta^2 \mathrm{PPV}_i + \mathrm{TPR}_i}, \tag{4.41}$$

$$\text{F}_\beta\text{-score}_M = \frac{(\beta^2 + 1)\text{PPV}_M \cdot \text{TPR}_M}{\beta^2 \text{PPV}_M + \text{TPR}_M}, \tag{4.42}$$

where $\text{F}_\beta\text{-score}_i$ and $\text{F}_\beta\text{-score}_M$ represent the individual score of class ω_i and the macro-averaged score, respectively, and β is a weight factor. For $\beta = 1$, the F_1-score becomes the harmonic mean of TPR and PPV. An important property of the F_1-score is that it has a high value only if both TPR and PPV have high values.

In a multiclass problem as in this dissertation, it is implicit, that if a spectrum that belongs to class ω_i is falsely assigned to class ω_j, for $i \neq j$, it generates a miss FN_i for class ω_i and a false alarm FP_j for class ω_j. Therefore, if as in the simulations in Section 4.9 the macro-averaged metrics TPR_M and PPV_M are calculated for all *existing* classes $i = 1, 2, ..., C$, their values are always equal and therefore $\text{TPR}_M = \text{PPV}_M = \text{F}_1\text{-score}_M$. In the simulations in Section 4.9 only the $\text{F}_1\text{-score}_M$ is thus used as the main classification performance metric.

In the experiments in Chapter 7, TPR_M and PPV_M are calculated only for a subset of all existing classes, and therefore they are not necessarily equal. There, it is thus important to look at all 3 metrics TPR, PPV and the F_1-score (both macro-averaged and individual per-class values) separately in order to understand the full picture.

4.9 Simulations

From the classification approaches described above, a classifier that provides the best performance for given marker fluorescence spectra under specific measurement conditions must be found. Furthermore, for the development of the measurement system prototype, it is necessary to quantify the worst situation in which the classification of marker fluorescence spectra can still be reliably carried out and what (spectral) disturbances of the marker fluorescence spectra can occur without a significant decrease of the classification performance. To answer these questions, computer simulations were carried out before experimental measurements were made.

Figure 4.7 shows the block diagram of the developed simulation framework in MATLAB. There are 2 modules: spectra modeling and spectra classification. In the spectra modeling module, emission spectra of the 6 fluorescent markers were first combined according to the binary coding scheme. The binary codes of the $2^6 - 1 = 63$ marker combinations can be found in Table A.1 in Appendix A. Fluorescence marker spectra acquired with the spectral camera (see Section 6.1.2) with an optical spectral resolution of approx. 2.8 nm and spectral sampling of approx. 1 nm were used. The spectra had $\Lambda = 350$ discrete wavelength bands (spectral samples) from 450 nm to 800 nm. The individual marker spectra and the marker combination spectra were saved in the reference library for classification purposes. Next, spectra of the 63 marker combinations were corrupted by one or more of 3 disturbances: (A) sensor noise, (B) relative intensity fluctuations, and (C) AF (will be referred to as scenarios A, B, and C, respectively). In all investigations in this section, 1000 spectra per disturbance factor and per class (i.e. marker combinations) were modeled resulting
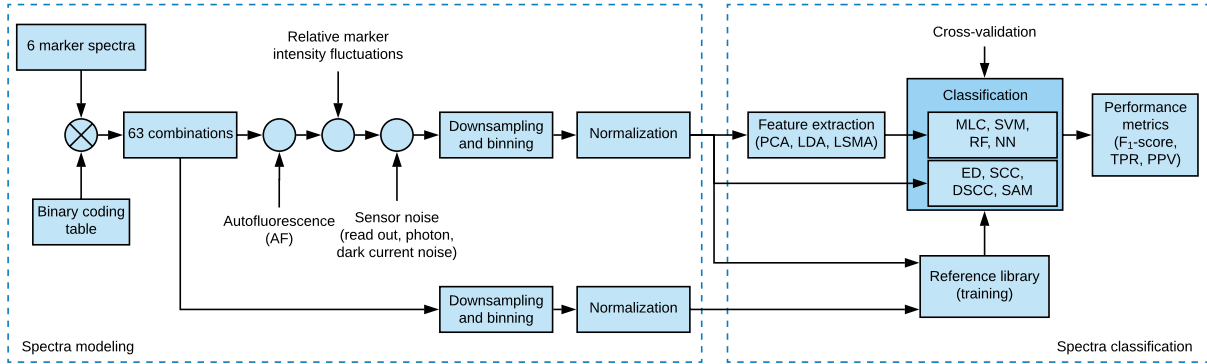
Figure 4.7: Block diagram of the simulation framework developed in MATLAB. The simulation framework consists of two separate modules for spectra modeling and spectra classification (see text).

in $63\,000$ spectra per one F_1-score$_M$ value, in order to ensure a small margin of error (see Section 7.1.1) in the resulting estimation of the classification performance and facilitate the comparison of different classifiers. Before classification, the modeled spectra were intensity-normalized, so that the maximum intensity s_j of every spectrum is equal to 1.

The modeled spectra were passed to the classification module. In order to ensure equal conditions for all classifiers, no pre-processing of the modeled spectra was carried out. The classification performance was quantified with F_1-score$_M$. Due to their relatively low computational complexity, the spectral similarity measures ED, SAM, SCC, DSCC were applied directly to the spectra, the more complex classifiers MLC, RF, SVM and NN were used in combination with the feature extraction algorithms PCA, LDA and LSMA. With PCA and LDA only the first 6 of 350 features (i.e. features bearing approx. 99% of the variance in the data, see Sections 4.3.1 and 4.3.2) were used. With the LSMA feature extraction methods (i.e. the unconstrained LSMA and constrained SCLS, NCLS and NCLS) all 6 marker abundance fractions were used as features.

For NN and RF the "size" of the classifier is very important. For NN the "size" here stands for the number of neurons in the hidden layer (i.e. hidden neurons), and for the RF classifier it is the number of trained decision trees. In both approaches larger size means potentially better classification performance, but brings a risk of overfitting training data and results in higher computational costs. For each problem the size of the classifier should be found empirically, therefore NNs and RFs of different sizes were investigated.

Since both NN and RF were always randomly initialized before training, different iterations of the training-test could result in slightly different results. In order to achieve more meaningful results, 10 training-test iterations with different initializations of NN and RF were carried out and their individual results were averaged.

In order to avoid overfitting, k-fold cross-validation was used with all classifiers [65]. In this approach, the modeled spectra are randomly split into two groups: the training set and the test set. All spectra in the training set were accompanied with a class label (i.e. target output vectors $\boldsymbol{g}$) and were used to derive model parameters for each classifier

and thus teach it to recognize spectra of the existing classes. The test set is then used to evaluate the performance of the classifier under test using TPR, PPV and F_1-score. The entire process, i.e. random split, training, and test, is carried out k times. After k repetitions, k values of TPR, PPV and F_1-score are averaged.

Classification results achieved in 3 scenarios – A (sensor noise), B (relative intensity fluctuations) and C (AF) – are presented below. All results shown were achieved with 10-fold cross-validation (k = 10).

4.9.1   Scenario A – sensor noise

Sensor noise is present in more or less any measurement system and can be very pronounced in a low-light fluorescence application, especially when the TGFS measurement approach is used (see Chapter 5). In the simulation framework, the CCD sensor noise was modeled with three primary types of noise: photon noise, dark current shot noise, and read-out noise (see Section 3.4.1). The model allowed the corruption of an arbitrary fluorescence spectrum with a realistic, CCD-typical noise of proper power to achieve the required S/N ratio.

The read-out noise and dark current shot noise are independent of the measured fluorescence intensity and are determined by the intrinsic parameters of the imaging sensor. The read-out noise was modeled as a random Gaussian process with zero mean and specified standard deviation using MATLAB's `randn(.)` function. The generated read-out noise was added to the marker combination spectrum. The seed of the (pseudo-)random process was specified in the program in order to achieve reproducible noise realizations.

In order to model the dark current *shot* noise, a two-step procedure was used: first, the dark current noise (offset fixed pattern noise, FPN, see Section 3.4.1) was modeled as a random Gaussian process and corrupted with a Poisson-distributed shot noise using MATLAB's `poissrnd(.)` function; next, the Gaussian dark current noise (FPN) was subtracted from the resulting noise in order to extract the dark current *shot* noise. The result was then added to the marker combination spectrum.

Since the amount of read-out noise and dark current shot noise is constant for a particular imaging system and specific measurement parameters (measurement rate, etc.), a change of the S/N ratio in the simulated spectrum is only possible by adjusting the amount of photon noise. However, because photon noise is proportional to the square root of the signal (spectrum) intensity at a particular wavelength (i.e. $n_{pi} = \sqrt{s_i}$ for each element in the vector $\boldsymbol{n}$, see Section 3.4.1), generating a proper amount of photon noise requires the scaling of the spectrum $k \cdot \boldsymbol{s}$. Assuming that both the power P_s of the spectrum $\boldsymbol{s}$, and the power P_n of the combined read-out and dark current shot noise ($\boldsymbol{n}_r + \boldsymbol{n}_d$) are known, the S/N ratio is given by:

$$\text{S/N} = 10 \cdot \log_{10}\left(\frac{k^2 \cdot P_s}{P_n}\right), \tag{4.43}$$

where the signal (amplitude) scaling factor k is squared (see also Eqn. 3.4 and 3.5). Solving

Eqn. 4.43 with respect to the scaling factor k results in:

$$k = \sqrt{10^{\frac{S/N}{10}} \cdot \frac{P_n}{P_s}}. \tag{4.44}$$

The spectrum $\boldsymbol{s}$ was multiplied by the scaling factor k and photon noise was applied to it using the MATLAB's Poisson random generator `poissrnd(.)`. Finally, the photon noise-corrupted spectrum was summed with read-out noise and dark current shot noise generated at the previous step.

Since all generated noise realizations are essentially (pseudo-)random values and the number Λ of elements (i.e. spectral samples) of the noise vector and of the spectrum is finite, the S/N ratio of the simulated spectrum cannot achieve any desired value with infinite precision. However, the S/N ratio values of an ensemble of such spectra will have a mean value converging the required S/N ratio.

Figure 4.8 compares the fluorescence spectra of marker M1 with and without noise at 4 different S/N ratios. At an S/N ratio of 20 dB, marker M1 is clearly distinguishable; it is intuitive that such a spectrum can be easily classified. However, with increasing noise, it becomes increasingly difficult to recognize the spectrum of marker M1 which leads to a more complicated classification.

Figure 4.9 shows the noise components of the simulated spectra from Fig. 4.8. At high S/N ratios (large fluorescence intensity), the photon noise is large (see Fig. 4.8a and 4.9a). At low S/N ratios (small fluorescence intensity), the photon noise is small, and the read-out noise and dark current shot noise are dominant (see Fig. 4.8d and 4.9d).

Size of the neural network and the random forest

The classification performance of NN and RF strongly depends on the "size" of the classifier, i.e. the number of neurons in the hidden NN layer and the number of decision trees in RF. Before NN and RF can be compared with other classifiers, it is necessary to find their suitable sizes. Although a rule of thumb exists for determining the suitable size, a better estimation can be achieved by employing computer simulations and investigating different sizes. Additionally, in order to determine whether the S/N ratio of the modeled fluorescence spectra or the feature extraction algorithm influence the optimal size, classification performance as a function of the classifier size was evaluated with different S/N ratios and different feature extraction algorithms.

Figure 4.10 shows the classification performance (F_1-score$_M$ macro-averaged over all 63 classes, see Section 4.8) of (a), (b) NN and (c), (d) RF of various sizes, achieved using LDA and LSMA features extracted from the simulated spectra corrupted with noise with S/N ratios of 0 dB, -5 dB and -10 dB. As explained in Section 4.8, the F_1-score$_M$ is high (100%) only if both TPR$_M$ and PPV$_M$ are high. With 63 existing classes, an F_1-score$_M$ of $1/63 \cdot 100\% = 1.59\%$ is achieved by "pure guessing", which can be considered as the lower bound for all investigated classifiers.

NNs with the hidden layer size between 1 and 30 neurons were investigated. As can be seen in Fig. 4.10a and 4.10b (subplots on the left), when LDA features are used, NNs

(a) S/N ratio 20 dB.

(b) S/N ratio 10 dB.

(c) S/N ratio 5 dB.

(d) S/N ratio 0 dB.
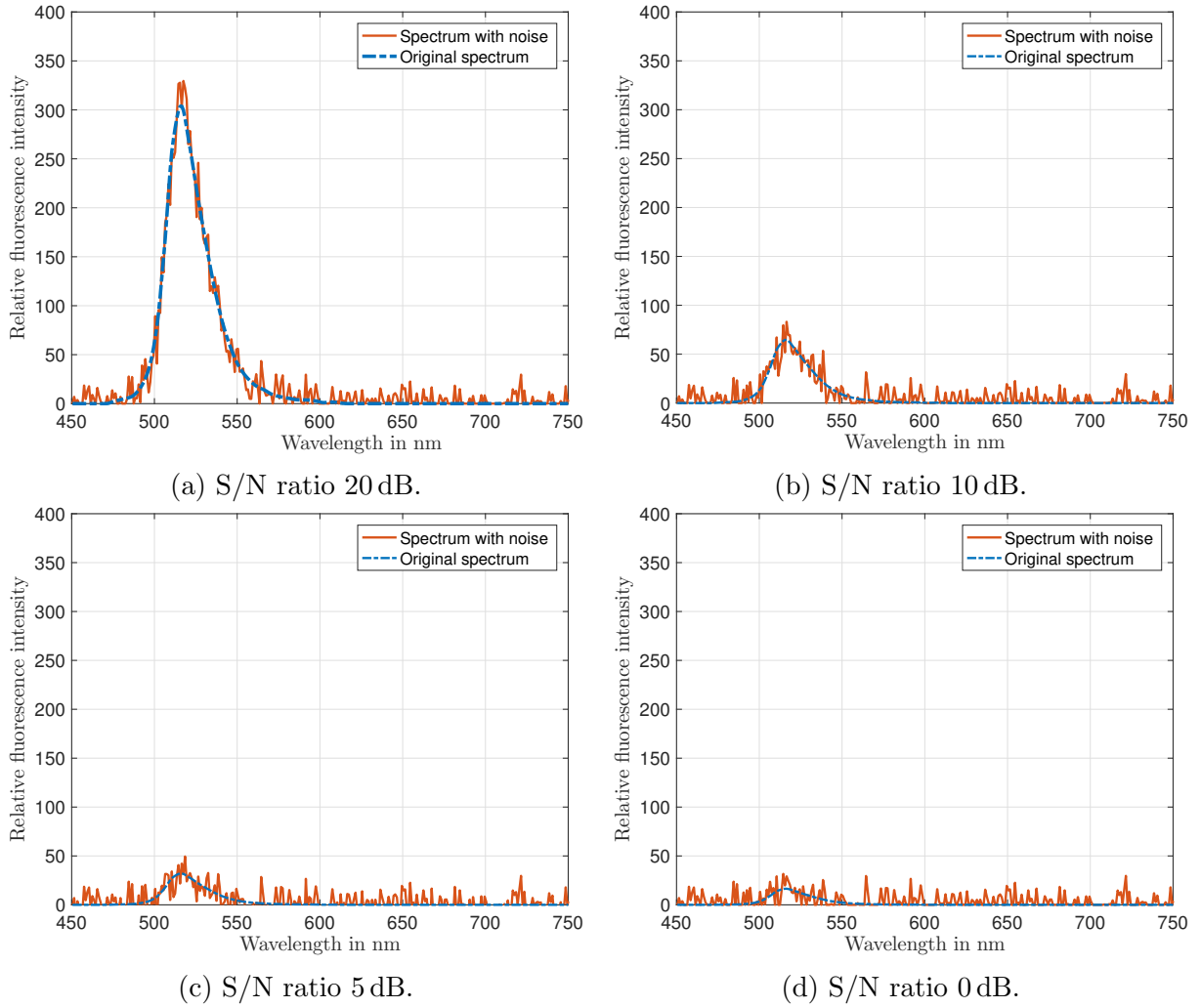
Figure 4.8: Comparison of the fluorescence spectrum of marker M1 corrupted with sensor noise at different S/N ratios. In order to change the S/N ratio in simulations, the spectrum s is multiplied by the scaling factor k to change the signal power and thus the amount of photon noise. (a) S/N ratio is 20 dB. With decreasing S/N ratios the marker fluorescence spectrum becomes more obscured in (b) with S/N ratio of 10 dB and (c) with S/N ratio of 5 dB, and is almost completely buried in noise in (d) when the S/N ratio is 0 dB.

even with a large number of neurons only achieve an F_1-score$_M$ of approx. 87.17% when the S/N ratio of the spectra is -5 dB and an F_1-score$_M$ of approx. 53.57% when the S/N ratio is -10 dB. This is not surprising since with S/N ratios this low the marker spectra get completely buried in noise. When the S/N ratio of the spectra is 0 dB, NNs with approx. 9 hidden neurons provide an F_1-score$_M$ of approx. 98.88% with LDA features. With LSMA features (Fig. 4.10b) extracted from spectra with an S/N ratio of 0 dB, NNs only achieve an F_1-score$_M$ of approx. 90.09% even with a large number of hidden neurons. At the S/N ratios of -5 dB and -10 dB, NNs with LSMA features achieve an F_1-score$_M$ of

(a) S/N ratio 20 dB.

(b) S/N ratio 10 dB.

(c) S/N ratio 5 dB.

(d) S/N ratio 0 dB.
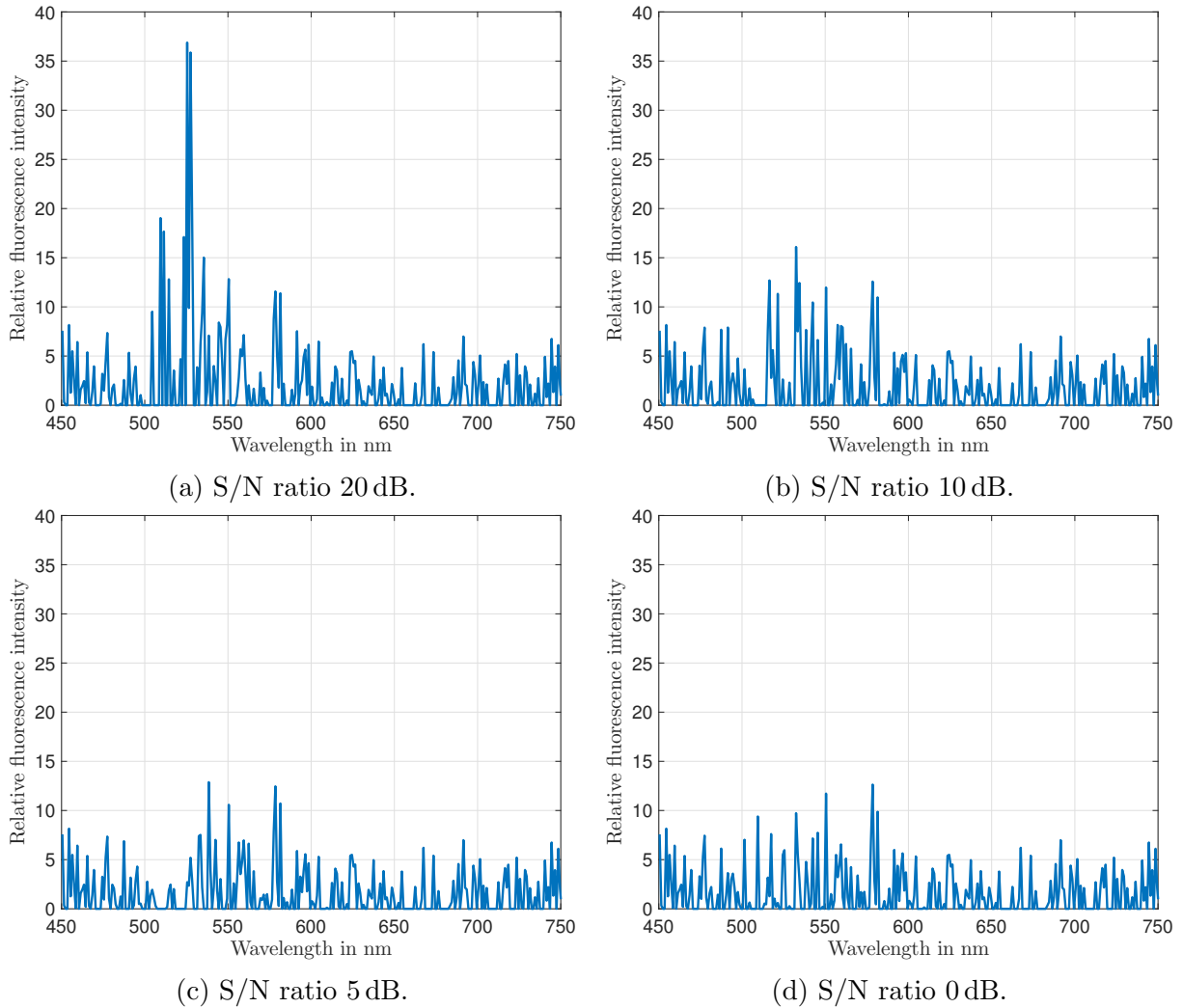
Figure 4.9: Comparison of the noise component in the spectrum of marker M1 (see Fig. 4.8) at different S/N ratios: (a) 20 dB, (b) 10 dB, (c) 5 dB and (d) 0 dB. In (a) the strong photon noise in the wavelength range between approx. 500 nm and 550 nm can be seen. The photon noise is smaller in (b) and (c), whereas in (d) there is only read-out and dark current shot noise.

approx. 55.35% and 20.53%, respectively.

However, the goal of this investigation was to find the optimal number of hidden neurons in NN in given conditions. It is easy to see in Fig. 4.10a and 4.10b, NNs with 8 or 9 neurons in the hidden layer bring the F_1-score$_M$ in saturation with both feature extraction algorithms at all investigated S/N ratios. This number is only a bit larger than the number of input nodes of the network, which here is 6 (equal to the number of elements in the input feature vector $\boldsymbol{f}$). Simulations with other features and other S/N ratios have shown similar results. In scenario A, NNs with 9 neurons were thus used in this dissertation.
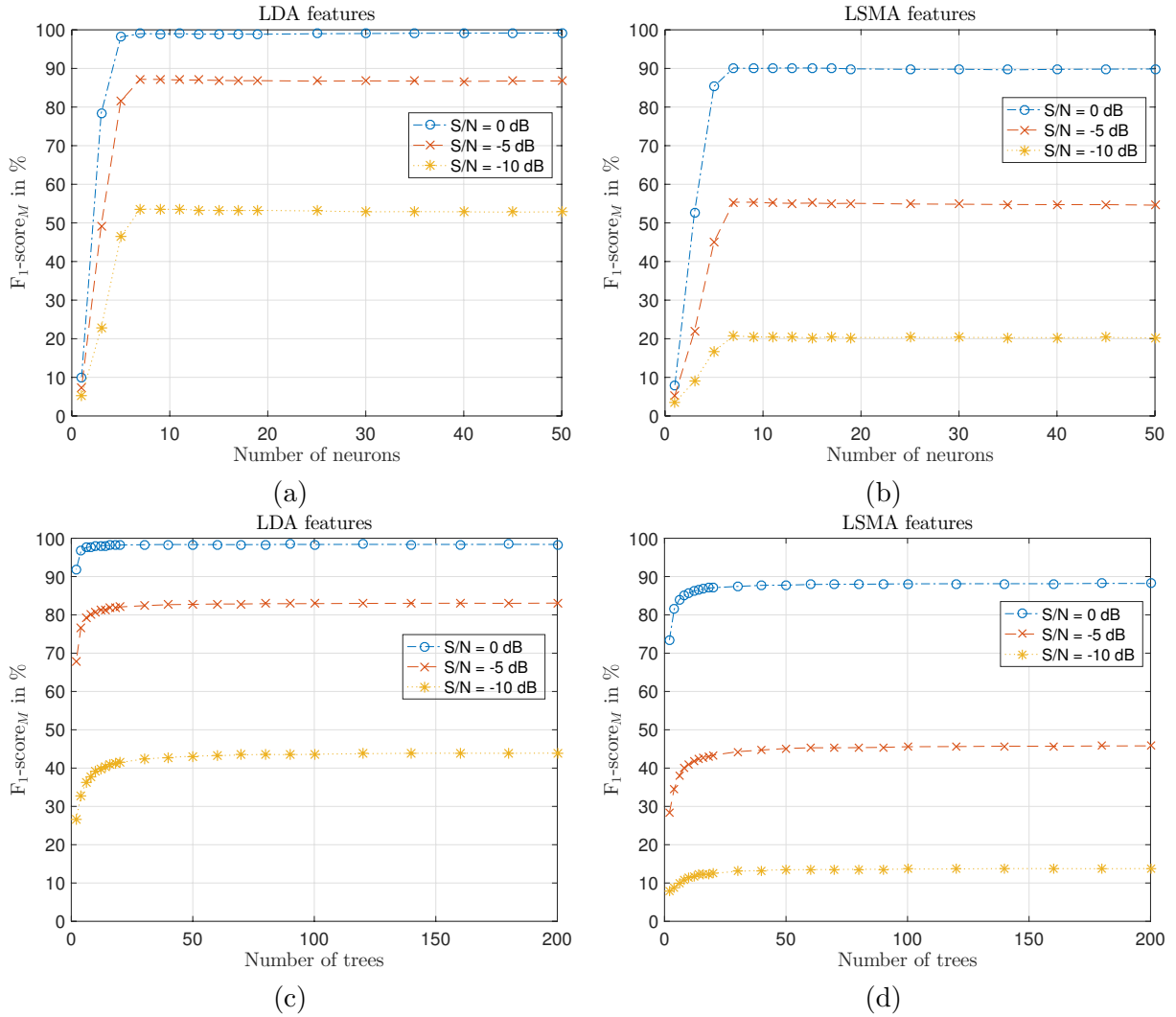
Figure 4.10: F_1-score$_M$ achieved with (a), (b) NNs with different numbers of hidden neurons and (c), (d) RFs with different numbers of decision trees with LDA and LSMA features in the situation where sensor noise is the only present disturbance.

Figures 4.10c and 4.10d show the classification performance achieved with RFs with 1 to 200 decision trees using the same simulated spectra with S/N ratios of 0 dB, -5 dB and -10 dB, and LDA and LSMA feature extraction algorithms, respectively. As can be seen, the results are very similar to those achieved with NNs shown in Fig. 4.10a and 4.10b. The F_1-score$_M$ saturation can be clearly seen for RF with more than approx. 100 decision trees. Similar results were achieved with other features. RF with 100 trees was thus used for further simulations in this dissertation.

Classification results

In order to determine the performance of all investigated classifiers, a rather broad range of S/N ratios was evaluated. The spectra were corrupted with the noise of overall 16 S/N ratios between -50 dB and +40 dB. 1000 independent noise realizations were applied to the spectra of the 63 marker combinations (classes) resulting in 63 000 noisy spectra per S/N ratio to determine the F_1-score$_M$.

Figure 4.11 shows the F_1-score$_M$ values achieved with different classifiers as function of the S/N ratio. Classifier names and feature extraction methods are abbreviated as defined in Sections 4.3-4.7. SVMlin and SVMrbf stand for the linear SVM and the SVM with a (Gaussian) radial basis kernel function (see Section 4.6), respectively. The classification performance values F_1-score$_M$ for only S/N ratios -5 dB, 0 dB, 5 dB and 10 dB are shown here. The values for other S/N ratios can be found in Appendix B in Table B.1. Both in Fig. 4.11 and in Table B.1, classifiers are ranked in descending order of the achieved F_1-score$_M$ at an S/N ratio of 0 dB. Strictly speaking, feature extraction methods reduce the noise in the input spectra and thus increase the S/N ratio. However, for simplicity and a better comparison, the S/N ratio values in Fig. 4.11 and in Table B.1 correspond to the S/N ratios of the "raw" simulated spectra (i.e. noise reduction due to the feature extraction is not considered).

As can be seen, RF, NN, SVMlin, SVMrbf and MLC with LDA features comprise a group with the highest F_1-score over all S/N ratios as compared to other classifiers. Moreover, the subtle difference in their F_1-score values over all S/N ratios leads to the conclusion that the feature extraction algorithm – LDA – was mostly responsible for the high(er) classification performance, whereas the choice of the classifier was not crucial. For the application at hand, F_1-score$_M$ higher than 95% should be achieved in order to ensure a high purity of the sorted plastics. The 95% F_1-score$_M$ level is shown in Fig. 4.11 by the dashed red line. Remarkably, even at an S/N ratio of 0 dB, i.e. when the power of the noise is equal to the power of the marker fluorescence spectrum, all 5 classifiers from this group provide an F_1-score$_M > 95\%$.

Even though being much less complex in comparison to RF, NN, SVM and MLC, the SCC algorithm that uses the "raw" spectra without prior feature extraction has provided results only slightly worse. At an S/N ratio of 0 dB, the SCC achieved an F_1-score$_M$ of 96.53%.

RF, NN, SVMlin, SVMrbf and MLC with PCA and LSMA features are the second group of classifiers that achieved F_1-score$_M$ around 90% at an S/N ratio of 0 dB. As with LDA, the PCA and LSMA features were mostly responsible for the achieved F_1-score$_M$. As expected, LDA which is designed to improve class separability, outperformed PCA which is good for dimensionality reduction. The unconstrained LSMA performed very similar to PCA.

SAM performed similarly to PCA and LSMA achieving an F_1-score$_M = 90.6\%$ at 0 dB S/N ratio.

Contrary to the expectations, imposing constraints on LSMA did not improve the classification. All 5 classifiers RF, NN, SVMlin, SVMrbf and MLC achieved lower performance
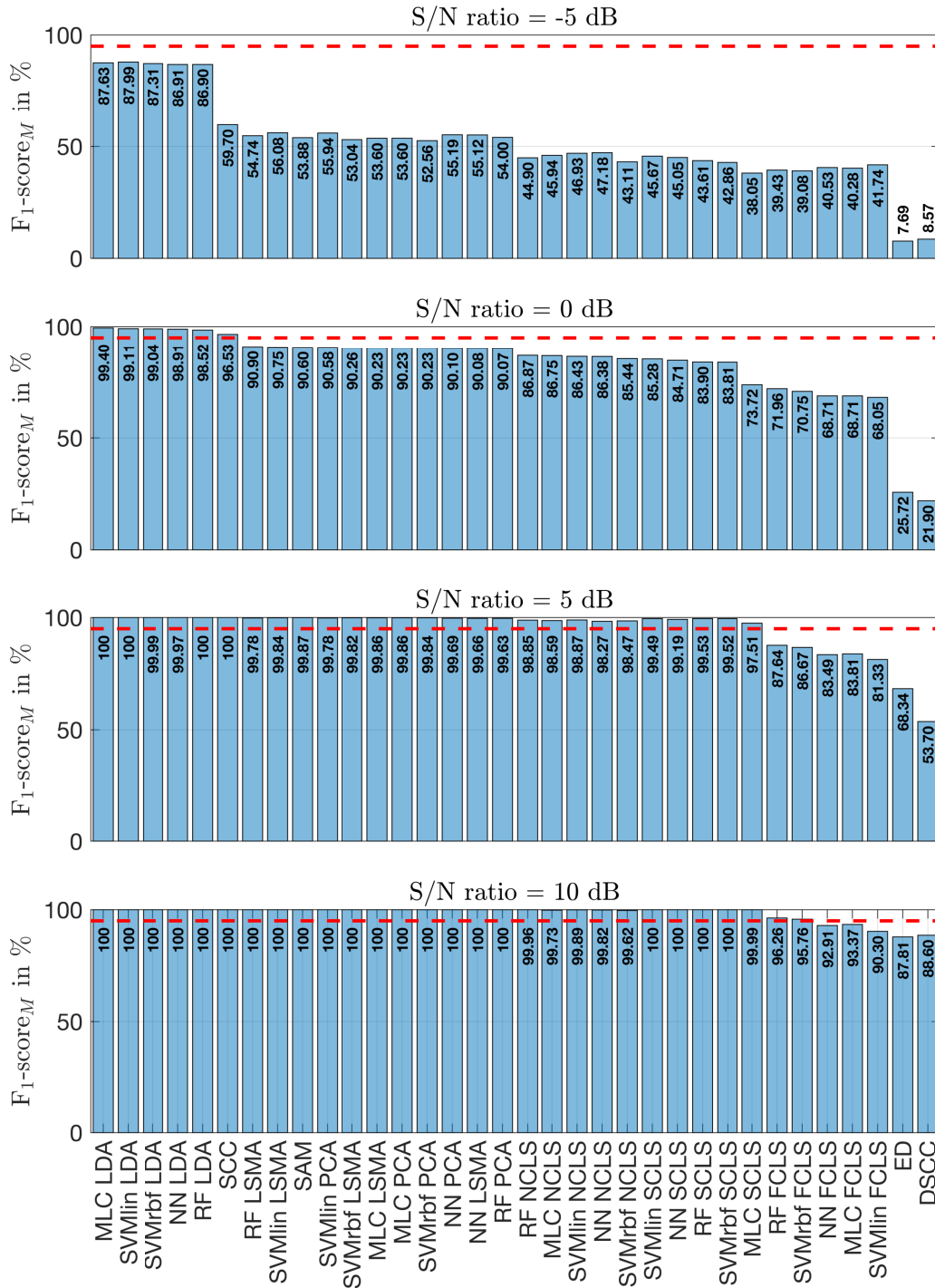
Figure 4.11: Classification performance (F_1-score$_M$) for the 34 investigated algorithms in scenario A. Classifiers are ranked by their F_1-score$_M$ values with S/N ratio of 0 dB. The red dashed lines indicate the 95% level. The macro-averaged F_1-score$_M$ is calculated using TPR$_M$ and PPV$_M$ (see Eqn. 4.42).

with NCLS than with LSMA: F_1-score$_M$ range between 86.38% for RF and 85.44% for SVMrbf. Even worse results were achieved with SCLS and FCLS: 83.81% and 68.05% at an S/N ratio of 0 dB, respectively.

Nevertheless, already at S/N ratio 5 dB, which is a more realistic and practical value, LSMA, PCA, NCLS, SCLS with RF, NN, SVMlin, SVMrbf and MLC, as well as SAM achieve F_1-score$_M$ > 97%, where LSMA, PCA and SAM achieve F_1-scores > 99%. FCLS with RF and SVMrbf achieve F_1-scores > 95% at an S/N ratio of 10 dB, whereas FCLS with NN, MLC and SVMlin achieve F_1-score$_M$ > 95% at an S/N ratio of 15 dB.

The ED and DSCC classifiers showed by far the worst results. At an S/N ratio of 0 dB, the former only achieved an F_1-score of 25.72% and the latter 21.90%. Both classifiers need S/N ratios of at least 15 dB in order to achieve F_1-score$_M$ > 95%. The ED is a simplified version of the MLC, which does not consider the classes' covariance matrices (see Section 4.4.2).

Since most of the investigated algorithms achieve an F_1-score$_M$ of 100% already at an S/N ratio between 5 dB and 10 dB, it is reasonable to select a computationally efficient classifier. The selection of classifiers is thus reduced to the computationally efficient SCC and SAM that showed good results in comparison to the other classifiers, but since SCC performs significantly better than SAM at lower S/N ratios, it is the obvious choice when sensor noise is the only present disturbance.

4.9.2 Scenario B – relative marker intensity fluctuations

The (peak) intensities of markers incorporated into plastics can fluctuate relative to one another from plastic flake to plastic flake due to an imperfect marker incorporation process (e.g. insufficient mixing of markers, fluctuations of marker concentrations, inhomogeneous incorporation, etc.) and due to the unpredictable chemical interactions between the marker molecules and hosting plastics (see Section 2.5). Such fluctuations may negatively influence the classification performance. The aim of this section is to estimate the magnitude of this effect using computer simulations.

The intensity fluctuations were modeled separately for each marker in the marker combination as a uniform random process with upper and lower limits defined in percent of the marker's intensity. The uniform random process was chosen as a process with maximum entropy [85] to model the worst-case scenario for the intensity fluctuations. The probability density function of the uniform distribution is given by:

$$f(p) = \begin{cases} 0, & \text{for } x < (1 - p/100) \\ \frac{1}{2p/100}, & \text{for } (1 - p/100) \leq x \leq (1 + p/100) \\ 0, & \text{for } x > (1 + p/100) \end{cases} \quad , \tag{4.45}$$

where p is the parameter defining the limits of the uniform distribution in percent of the marker's intensity, and $x \subset \mathbf{R}^1 \mid x > 0$. If the scaling factor k is a random variable with the probability density function $f(p)$, then the resulting spectrum $\tilde{\boldsymbol{m}}_h$ of marker M$_h$ is

given by:

$$\tilde{\boldsymbol{m}}_h = \boldsymbol{m}_h \cdot k. \tag{4.46}$$

For example, if the (peak) intensities of all 6 markers in the marker combination are equalized so that $\max(\boldsymbol{m}_1) = ... = \max(\boldsymbol{m}_6) = 1$, fluctuations of $p = \pm 20\%$ mean that each marker's peak intensity can fluctuate within the interval $[80\%; 120\%]$ following the uniform distribution. Therefore, the peak intensity of one marker can be 80%, yet that of another marker in the same flake 120% at the same time. In order to investigate the worst-case scenario, the peak intensities of all 6 markers are allowed to fluctuate simultaneously.

Figure 4.12 depicts an example of the modeled spectrum of class 7 (code "000111") with 20% relative intensity fluctuations (solid line) as well as the spectrum of class 7 without intensity fluctuations (broken line), i.e. the peak intensities of M4, M5 and M6 are equal. The peak intensity of marker M5 (peak at approx. 650 nm) is only 80% of the peak intensity of marker M4 (left peak), and 120% for M6 (right peak). Naturally, the probability of this particular situation is quite low, it is shown here as one of the extreme cases for $p = \pm 20\%$.

Size of the neural network and the random forest

In order to find the optimal number of neurons in NN and the number of trees in RF, simulations with NN and RF of different sizes were carried out. Figure 4.13 depicts the F_1-score$_M$ achieved with NN and RF for rather large relative marker intensity fluctuations of $\pm 50\%$, $\pm 60\%$ and $\pm 70\%$. As can be seen, similarly to scenario A, NN with 8 or 9 neurons in the hidden layer and RF with approx. 100 decision trees bring the F_1-score$_M$ in saturation, i.e. a further increase of the size of the classifier does not increase the F_1-score$_M$. Similar behavior was observed with other features. For the further simulations in this dissertation, NN with 9 hidden neurons and RF with 100 trees were used.

Classification results

To investigate the influence of marker intensity fluctuations on the classification performance, spectra with uniformly distributed intensity fluctuations in the range of $\pm 0\%$ to $\pm 100\%$ were modeled: overall 11 p-levels in 10% steps. 1000 random realizations of intensity fluctuations were produced for each intensity fluctuation p-level, and for each of 63 marker combinations (classes). For each realization and each marker in the class, the scaling factor k_h was randomly generated according to the probability density function defined in Eqn. 4.45 and the marker spectrum was multiplied by the scaling factor k_h. Next, the scaled spectra of all markers were combined according to the binary coding scheme in order to produce the spectrum of the specific class with unequal marker intensities. Thus, overall 63 000 spectra were generated per intensity fluctuation p-level to determine the F_1-score$_M$. All spectra were noise-free for this investigation of scenario B.

Figure 4.14 shows the results achieved with intensity fluctuations $\pm 100\%$, $\pm 90\%$, $\pm 80\%$ and $\pm 70\%$. Results for other intensity fluctuation levels can be found in Appendix B in
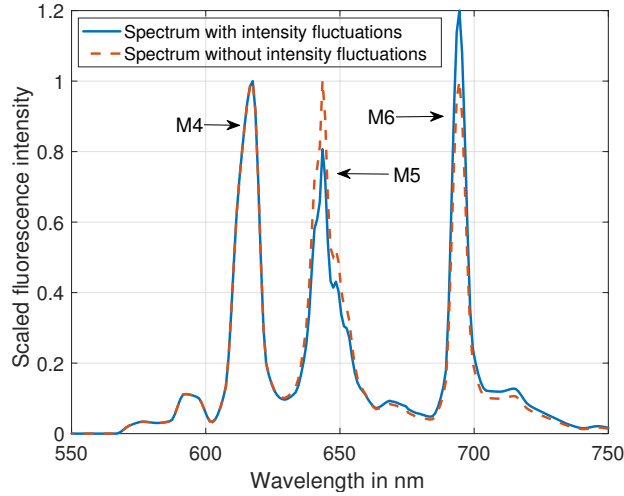
Figure 4.12: The spectrum of class 7 (code "000111", the combination of markers M4, M5, and M6). The broken line corresponds to the situation when the marker peak intensities are equal. The solid line depicts one possible realization of the spectrum with $p = \pm 20\%$ relative marker intensity fluctuations such that the peak intensities of marker M5 and M6 are 80% and 120%, respectively, of the peak intensity of marker M4.

Table B.2. Both in the figure and in the table, the classifiers are ranked according to their F_1-scores with intensity fluctuations of $\pm 100\%$.

Interestingly, the LDA features which showed good results in scenario A (sensor noise) perform rather poorly in scenario B. On the contrary, the SCLS features, which demonstrated a below-average performance in the presence of noise independently of the classifier, show good results with intensity fluctuations.

The best performance was achieved by RF with LSMA features: F_1-score$_M = 97.98\%$ with intensity fluctuations of $\pm 100\%$ and F_1-score$_M = 100\%$ with smaller intensity fluctuations. Then the MLC follows, which achieved an F_1-score$_M > 97\%$ with PCA, LSMA and SCLS features with intensity fluctuations of $\pm 100\%$, but showed an F_1-score$_M < 100\%$ with intensity fluctuations $\pm 70\%$ and $\pm 80\%$. MLC with NCLS failed to achieve an F_1-score of 100% with intensity fluctuations even as low as $\pm 20\%$.

NN with PCA, LSMA and SCLS had also shown a performance above average with F_1-score$_M > 96\%$ even with intensity fluctuations as high as $\pm 100\%$.

Both linear and radial-basis function SVM delivered an F_1-score$_M \leq 90\%$ for intensity fluctuations of $\pm 100\%$.

In contrast to scenario A (see Table B.1), all spectral similarity measures perform poorly in comparison to the classifiers RF, NN, SVM and MLC: As can be seen in Table B.1, SAM, SCC and DSCC can tolerate intensity fluctuations of up to about $\pm 40\%$ without significant loss of classification performance (F_1-score$_M > 99\%$), but fail with intensity fluctuations larger than $\pm 50\%$ and only provide an F_1-score$_M$ of approx. 44% for $\pm 100\%$ intensity fluctuations; the F_1-score$_M$ of ED drops below 99% with intensity fluctuations of only $\pm 30\%$ and decreases gradually to 31.44% for intensity fluctuations of $\pm 100\%$.
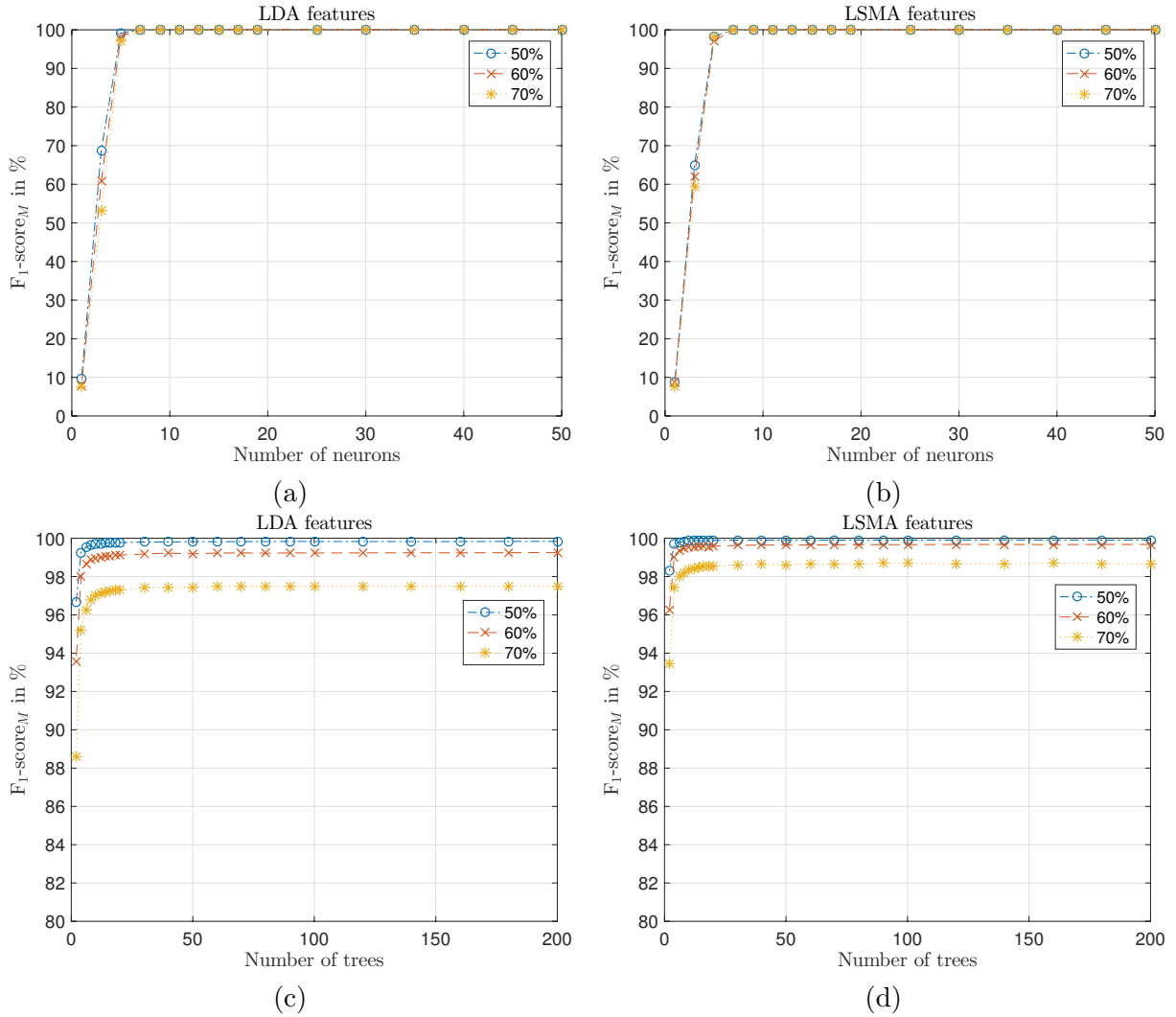
Figure 4.13: F_1-score achieved with (a), (b) NNs as a function of the number of hidden neurons and (c),(d) RFs as a function of the number of decision trees with LDA and LSMA features for intensity fluctuations of 50%, 60% and 70%.

Comparable results were achieved by RF, NN, SVM and MLC with FCLS features: for intensity fluctuations larger than ±20%, the F_1-score$_M$ drops below 99%. However, with increased intensity fluctuations the further decrease of the F_1-score$_M$ is not as steep as with similarity measures: for intensity fluctuations of ±100%, SVMrbf, RF and MLC achieve an F_1-score$_M$ of approx. 70%, and NN and SVMlin achieve F_1-score$_M$ > 50%.

The main reason for the high performance of the classification algorithms RF, NN, SVM and MLC in comparison to the similarity measures ED, SCC, DSCC and SAM is that they consider class variances (or scatter), which in this scenario are caused by intensity fluctuations.

However, it needs to be pointed out that according to the findings in this work, in
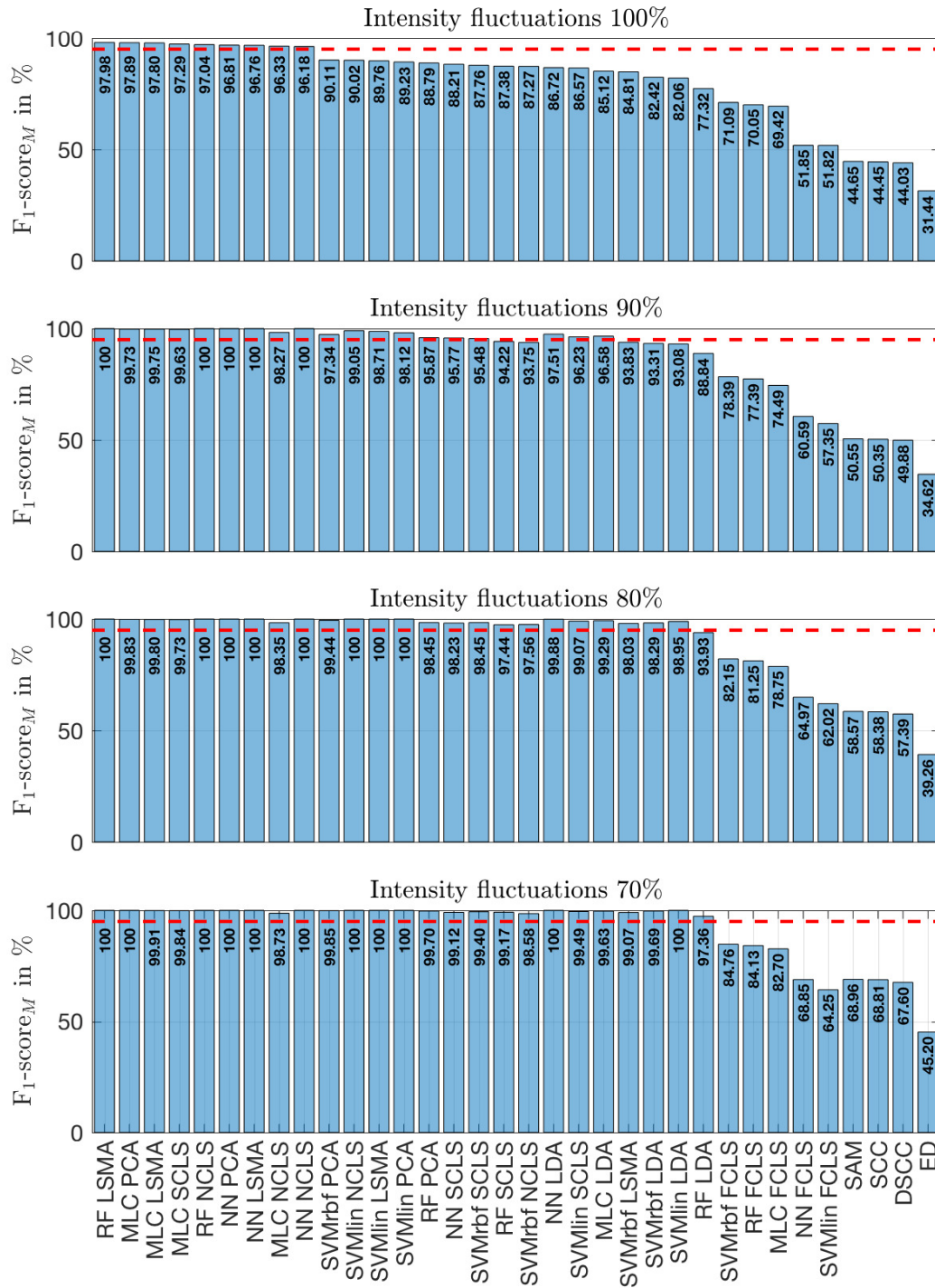
Figure 4.14: Classification results (F_1-score$_M$) for the 34 investigated algorithms in scenario B. Classifiers are ranked by their F_1-score$_M$ for intensity fluctuations of $\pm 100\%$. The red dashed lines indicate the 95% level.

practice less than about $\pm 10\%$ intensity fluctuations are to be expected if professional plastics extruders are used for the incorporation of the markers into plastics (see Chapter 2). Therefore, the influence of relative marker intensity fluctuations in practice seems not as critical as that from sensor noise or AF (see Section 4.9.3). Since almost all of the investigated classifiers provide the highest possible performance (F_1-score$_M = 100\%$) for intensity fluctuations up to approx. $\pm 30\%$, the choice of the classifier is not critical with regard to intensity fluctuations that occur in practice.

4.9.3 Scenario C – autofluorescence of the hosting plastics

As explained in Chapter 2, autofluorescence (AF) is inherently present in many plastics. By overlapping with the markers' fluorescence spectra, AF can make plastics that are labeled with different marker combinations indistinguishable from one another and thus degrades the classification performance. In this section, the influence of AF on the classification performance is quantified using computer simulations.

Figure 4.15 depicts the modeled spectrum of marker M4 overlapped with AF of a white POM with S/AF ratios (see Eqn. 2.4) ranging from 0.001 to 10, and the spectrum of marker M4 with no AF (S/AF ratio $= \infty$). An S/AF ratio of 10 means that the marker fluorescence power is 10 times higher than the AF power (in the wavelength range where the markers are present). With an S/AF ratio of about 10 the marker fluorescence is highly distinguishable and the classification probably would not be (much) affected by AF. This is clearly not the case for an S/AF ratio 0.01 or 0.001. Especially in the presence of sensor noise, AF this high may obstruct marker fluorescence and result in misclassification. Yet, a high AF can easily occur with many plastics. For example, the S/AF ratio achieved with the POM "Delrin 500NC010 White" and incorporated marker M4 (50 ppm) is approx. 0.01.

Size of the neural network and the random forest

In order to find the best size of NN and RF, simulations with different S/AF ratios were carried out. Figure 4.16 shows the F_1-score$_M$ achieved using LDA and LSMA features with NN and RF. Similarly to Fig. 4.10, the best classifier size in terms of the achieved F_1-score$_M$ versus classifier complexity is easily seen. For NN it is approx. 8 or 9 hidden neurons and for RF it is approx. 100 trained trees. These values are similar to those found in Sections 4.9.1 and 4.9.2. NN with 9 neurons in the hidden layer and RF with 100 decision trees were used in the simulations below.

Classification results

In the simulations in this section, fluorescence spectra of 63 combinations of 6 markers were superposed with different AF measured from 10 different plastics. In order to prevent classifiers from taking advantage of distinctive spectral shapes of different AF, all 63 combinations were "incorporated" into each of the 10 plastics thus resulting in 10 spectra per marker combination (class). Having a dataset with only 10 spectra per class can be
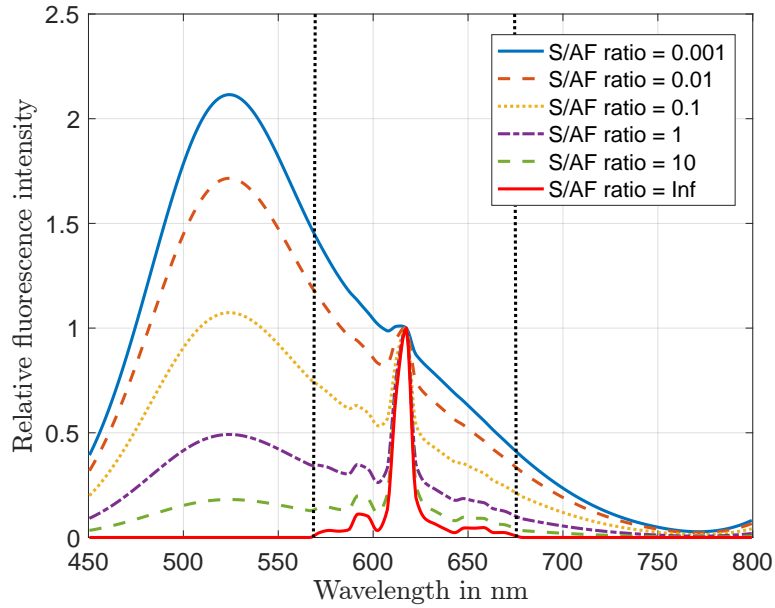
Figure 4.15: Fluorescence spectrum of marker M4 overlapped with AF of a white POM polymer at different S/AF ratios. The rather narrow spike at approx. 614 nm corresponds to the marker fluorescence and the broadband component between 450 nm and 700 nm is the AF. Spectra were normalized by the peak intensity of marker M4. The wavelength range between the dotted vertical lines was used to calculate the S/AF ratio (see Section 2.5.4).

very disadvantageous for classification algorithms that derive information about classes from the data and need prior training. Algorithms such as e.g. NN might not be able to successfully and efficiently train using only 10 spectra per class, especially if the class members are very different from each other as was the case here due to the different shapes of the AF spectra. To avoid these problems, all 10 spectra of each class were corrupted with random realizations of sensor noise of 20 dB (see Section 3.4.1), which is the noise level that can be expected in practice (see Section 7.2). 1000 random realizations of noise were used for each of $63 \times 10 = 630$ combinations resulting in 630 000 spectra per S/AF ratio level and per F_1-score$_M$ value. Overall 23 S/AF ratio levels between 10^{-4} and 10^2 were investigated, which results in $630 \times 23 \times 1000 = 13\,230\,000$ spectra to be processed by each of the classifiers and feature extraction algorithms.

Classification results achieved with all investigated classifiers and feature extraction algorithms are shown in Fig. 4.17. Only the F_1-score$_M$ values for the S/AF ratios 0.01, 0.05, 0.1 and 0.2 are shown. The F_1-score$_M$ for the other S/AF ratios can be found in Appendix B in Table B.3. Both in the figure and in the table, classifiers are ranked according to their F_1-scores for the S/AF ratio of 0.05, i.e. S/AF ratio where the best classifiers achieve an F_1-score$_M > 95\%$.

Similarly to scenario A, classifiers can be grouped in the following way. The best results were achieved with LDA features almost independently from the actual classifier: the
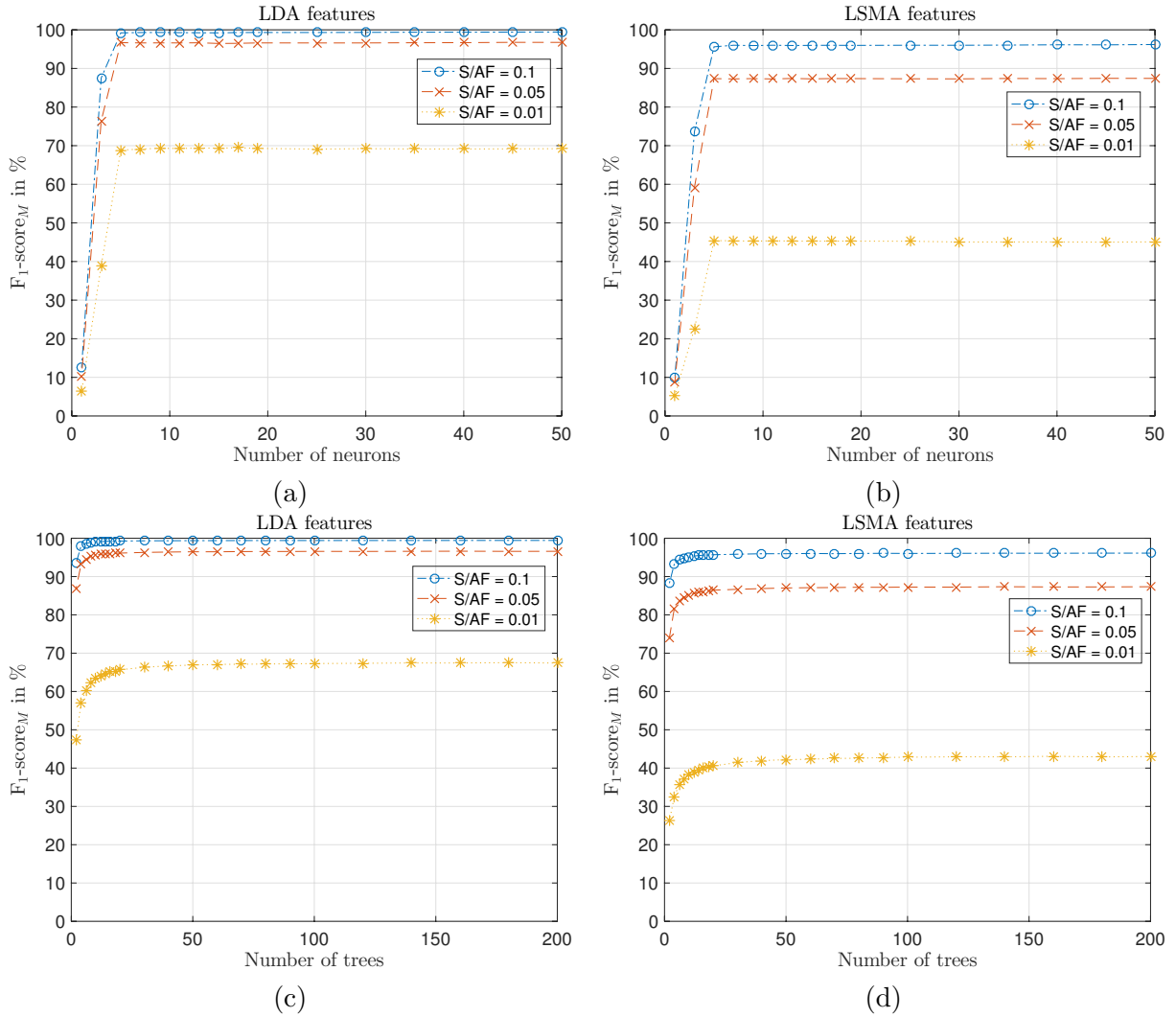
Figure 4.16: F_1-score achieved with (a), (b) NNs with different number of hidden neurons and (c), (d) RFs with different number of decision trees with LDA and LSMA features and the autofluorescence scenario C.

difference between the F_1-score$_M$ achieved by MLC, SVMlin, NN, RF and SVMrbf is below 1%, the F_1-score$_M$ values lie between 96.31% and 97.07%. An ideal F_1-score$_M = 100\%$ is achieved for an S/AF ratio of 0.2 or even 0.4 (see Table B.3) with these 5 classifiers using LDA features.

In contrast, the performance of the SCC, which achieves an F_1-score$_M = 93.09\%$ at S/AF=0.05, rapidly grows to 100% already at S/AF=0.1.

SCC is followed by SAM and MLC, SVMlin, NN, RF and SVMrbf with PCA, LSMA and NCLS features, all of which achieve an F_1-score$_M$ between 89.44% and 85.91% at S/AF=0.05. As with LDA, the further classification performance increase is rather slow and F_1-score$_M = 100\%$ is reached at S/AF ratios of 0.6 to 1. In contrast to scenario A,
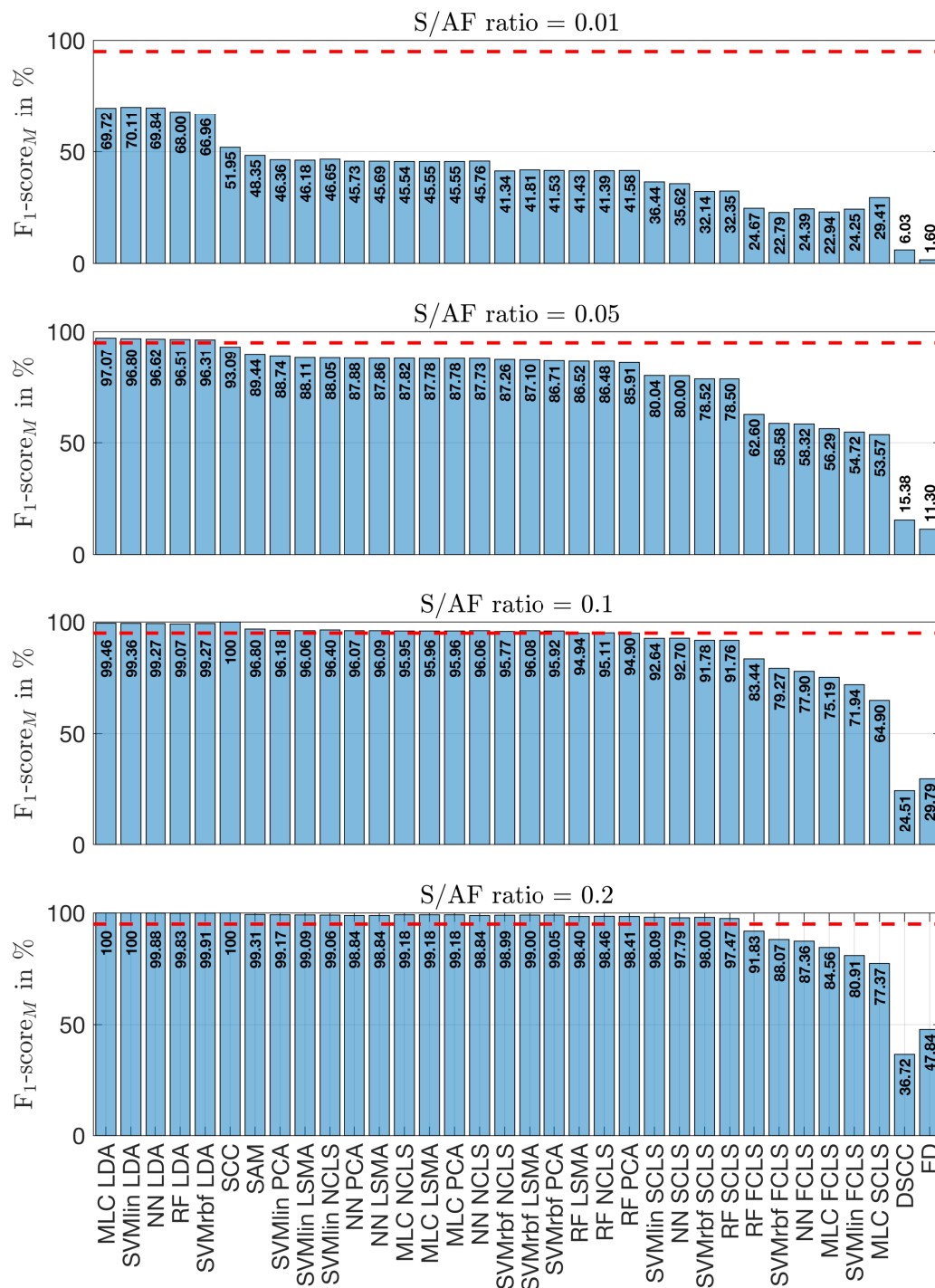
Figure 4.17: Classification results (F_1-score$_M$) for the 34 investigated algorithms in scenario C. Classifiers are sorted by their F_1-score$_M$ for S/AF ratio of 0.05. The red dashed lines indicate the 95% level.

where NCLS performed noticeably worse than both PCA and LSMA, here it achieves results comparable with the latter. Apparently, the NCLS model is slightly advantageous over unconstrained LSMA when "wanted signals" (i.e. marker spectra) need to be unmixed from the "unwanted background" (i.e. AF).

With SCLS, classifiers MLC, SVMlin, NN, RF and SVMrbf achieve on average approx. 5% smaller F_1-score$_M$ than with PCA, LSMA and NCLS. The F_1-score$_M$ values range between 78.50% and 80.04% at S/AF=0.05 and increase to 99.99% at S/AF=1 for the mentioned algorithms.

The last group encompasses FCLS features with the F_1-score$_M$ between 54.72% and 62.60% at S/AF=0.05. Even at S/AF=1 none of the classifiers provides perfect classification and only achieves F_1-score$_M$ values between 91.04% (SVMlin) and 96.73% (RF). The worst classification results were provided by DSCC and ED. At S/AF=0.05 they achieved an F_1-score$_M$ of 15.38% and 11.30%, respectively. For the DSCC the presence of even a small amount of noise (S/N ratio is 20 dB here) appears to be critical. Since in practice the presence of some amount of noise is inevitable, the use of DSCC is not advisable.

In contrast to scenario A where only sensor noise was present and all investigated classifiers provided perfect classification performance (F_1-score$_M$ = 100%) at an S/N ratio of 20 dB, here in the presence of AF and 20 dB noise simultaneously the F_1-score$_M$ of all investigated classifiers starts rapidly decrease for S/AF ratios below approx. 0.2 - 0.1. Such values of both S/N ratio and AF can be expected in practice. Avoiding the presence of the plastics' AF is thus important for classification performance.

4.9.4 Equalized marker fluorescence peak intensities

In sections 4.9.1 - 4.9.3, the marker fluorescence peak intensities were equal for all markers in all combinations. Random relative marker intensity fluctuations investigated in Section 4.9.2 represented the situation when individual marker intensities *randomly* varied from one realization of the marker combination spectrum to another. Thus relative marker peak intensities within individual realizations of such spectra could have been unequal, but the mean peak intensities of all markers were equalized. In practice, equalizing the (mean) marker fluorescence intensities requires recursive chemical fine-tuning of marker concentrations. Due to unpredictable interactions of the marker molecules with the hosting plastics, higher or lower marker concentrations might be necessary to achieve the desired marker fluorescence intensity. This is a time-consuming and costly procedure. However, it will be demonstrated in this section that despite the associated practical difficulties, the equalization of the marker fluorescence peak intensities helps improve the classification performance.

It was shown in Section 2.4.2 that an LED with 368 nm central wavelength and 15 nm FWHM provides good excitation for the 6 markers used in terms of the maximization of their fluorescence intensities. Using Eqn. 2.2 the relation between the intensities of all 6 markers can be calculated for this particular excitation light source. When equal marker concentrations are used, the marker peak intensities are unequal as can be seen in Fig. 4.18a. A comparison with Fig. 4.18b, where markers with equal peak intensities (i.e.
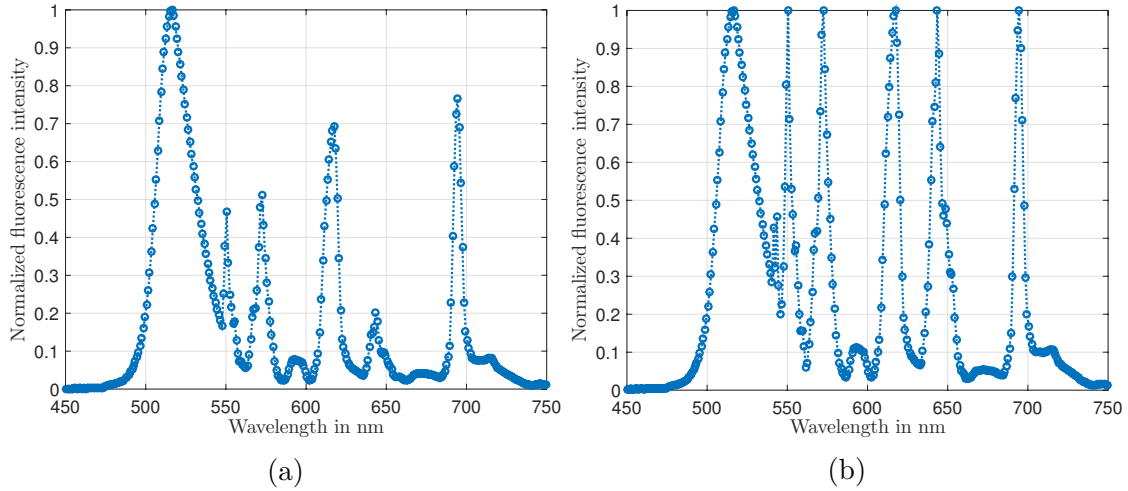
Figure 4.18: Normalized fluorescence spectrum of class 63 (code "111111") with unequal (left) and equalized (right) marker peak intensities achieved by accordingly adjusted concentrations for each marker.

accordingly adjusted marker concentrations) are shown, intuitively suggests that these are better distinguishable and thus must be easier to classify.

Classification results

Figure 4.19 compares results achieved with equalized and unequal marker fluorescence peak intensities in the 3 scenarios: A (sensor noise), B (relative intensity fluctuations) and C (AF). For presentation purposes, only the results achieved using those 2 classifiers – MLC with LDA features and SCC – which have shown the best performance in previous simulations (see Sections 4.9.1, 4.9.2 and 4.9.3), are depicted here. In each scenario, 1000 realizations of spectra for each of 63 classes were generated resulting in overall 63 000 spectra per F_1-score$_M$ value.

As expected, equalized marker fluorescence peak intensities result in a better classification performance in all 3 scenarios. For example, at an S/N ratio of 0 dB, SCC with equalized marker intensities achieves an F_1-score$_M = 96.53\%$, while unequal marker intensities result in an F_1-score$_M = 59.32\%$ (see Fig. 4.19a). Similarly, MLC with LDA features achieves 99.40% and 80.08% at an S/N ratio of 0 dB with equalized and unequal marker intensities, respectively (see Fig. 4.19b). For S/N ratios above approx. 15 dB both classifiers achieve equal performance of F_1-score$_M = 100\%$ with equalized and unequal marker intensities.

In the relative marker intensity fluctuations scenario B, the decrease of the classification performance produced by unequal (mean) marker intensities in comparison to equalized (mean) marker intensities is less drastic, but still noticeable. The F_1-score$_M$ for SCC drops from 99.8% to 97.75% with ±40% fluctuations (Fig. 4.19c). MLC being less prone to intensity fluctuations, shows almost no performance decrease with ±40% fluctuations,
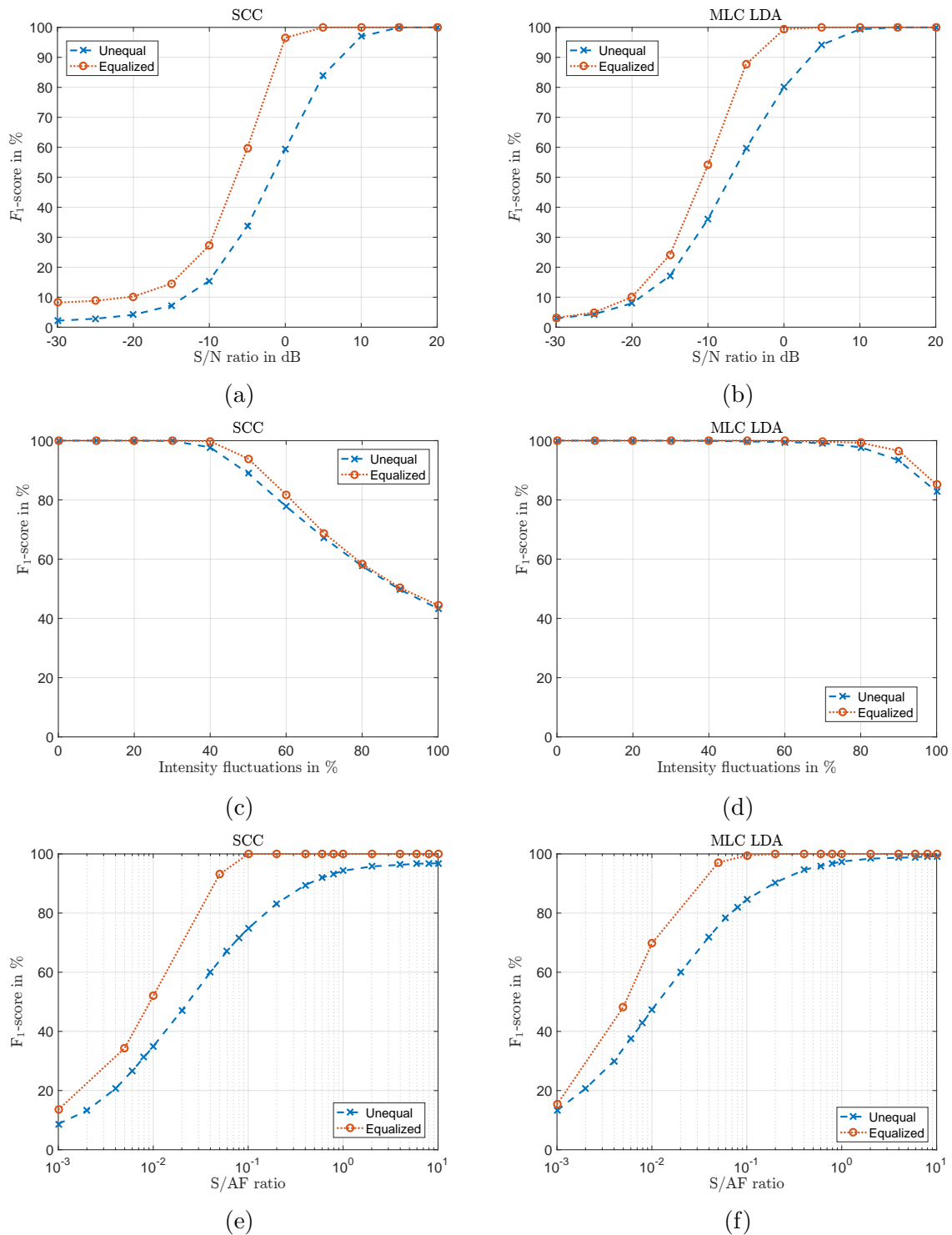
Figure 4.19: Comparison of the classification performance achieved by MLC with LDA features and SCC in situations with equalized and unequal relative marker fluorescence intensities within marker combinations in (a, b) scenario A (sensor noise), (c, d) scenario B (intensity fluctuations) and (e, f) scenario C (autofluorescence).

but also performs worse with unequal marker intensities than with equalized ones when fluctuations are $\pm 80\%$ and larger (Fig. 4.19d). Both classifiers have perfect performance (F_1-score$_M$ = 100%) with equalized and unequal marker intensities for intensity fluctuations below $\pm 30\%$.

In the AF scenario C, both SCC and MLC show a significant decrease of the F_1-score$_M$ with unequal marker intensities for S/AF ratio < 1 (Fig. 4.19e and 4.19f). Moreover, SCC fails to reach the F_1-score$_M$ = 100% even at an S/AF ratio as high as 10, if marker intensities are unequal. At the same time, if marker intensities are equalized, SCC reaches an F_1-score$_M$ = 100% with an S/AF ratio as low as 0.1. Similar situation is with MLC: it reaches an F_1-score$_M$ = 100% at S/AF ratio > 6 with unequal and at S/AF ratio > 0.1 with equalized marker intensities.

For all 3 scenarios, the same trends were found with all other investigated classifiers.

4.9.5 Spectral sampling

In all previous simulations in this dissertation, the fluorescence spectra had a spectral sampling of 1 nm. Thus, 300 samples cover the wavelength range between 450 nm and 750 nm. One way to increase the sensor's (see Section 3.4) measurement rate and also speed up the classification calculations is to reduce the number of samples.

There are several ways of changing the sampling of the fluorescence spectra. The software methods include downsampling, decimation, spectral averaging, etc. Downsampling simply takes every N-th spectral sample and discards the others. It can be useful to reduce the processing time of the classification algorithms and has the advantage of being computationally fast. However, one has to be careful with respect to aliasing [86]. Decimation introduces an additional step – low-pass filtering of the spectra – prior to downsampling. The low-pass filtering is employed to increase the S/N ratio of the spectra, which may compensate for the loss of spectral resolution with respect to classification performance. Averaging adjacent spectral samples before downsampling serves the same purpose, but depending on the particular implementation may be computationally faster than the low-pass filtering.

The hardware method called pixel binning is available in CCD cameras and allows the integration of the electrical charges of groups of 2^n adjacent pixels thus imitating a larger pixel (see Section 3.4). For example, binning with a factor of 2 would sum the charges of a pair of pixels. In addition to reducing spectral sampling by a factor of 2, with CCD binning the read-out time is reduced and the measurement rate is increased. Another important advantage of binning over the software methods is that since the integration of charges is carried out physically, the amplitude of the acquired signal is increased, whereas the read-out noise stays the same; thus the S/N ratio of the measured spectrum is increased. However, the binning capabilities of CCD sensors are limited, and usually binning factors larger than 8 are not used. If a further reduction of the number of spectral samples is necessary, software methods can be used.

In order to understand how much the sampling can be reduced, the Fourier transforms (FFTs) of the marker fluorescence spectra can be consulted [86]. Figure 4.20 depicts the

(normalized) magnitudes of the Fourier transforms of the fluorescence spectra of markers M1-M6. In the figure, the x-axis has "pseudo-frequency" units of nm^{-1}, so that for example $0.1\ nm^{-1}$ corresponds to a sampling of 10 nm. According to the Nyquist criterion, in order to avoid aliasing, the sampling frequency must be at least twice as high as the maximum frequency present in the signal. As can be seen in Fig. 4.20, most of the Fourier transform of marker M1 is situated below $0.05\ nm^{-1}$. Thus the sampling "frequency" must be at least $0.1\ nm^{-1}$, which corresponds to a sampling of 10 nm. The Fourier transforms of the other 5 markers are broader, but mostly lie below approx. $0.15\ nm^{-1}$. Therefore sampling "frequency" must be at least $0.3\ nm^{-1}$ and the sampling approx. 3.33 nm. Hence, in order to be able to acquire spectra of all 6 markers and their combinations, spectral sampling of at least 3.33 nm should be used.

The Nyquist criterion provides the hard limit about the minimum necessary sampling for signals that are indefinitely long and sampled with ideal sampling impulses. To determine the influence of the spectral sampling on the classification performance in the application at hand, simulations were carried out. In the simulations, downsampling and binning were investigated. The former represents the "worst" case with respect to the S/N ratio and thus classification performance, but is computationally faster than the other software methods. The latter is the realistic case, that theoretically provides the best S/N ratio improvement (up to the factor of N, see Section 3.4.2) and is thus advantageous for classification. The other software methods such as decimation and spectral averaging provide an S/N ratio improvement better than the simple downsampling, but worse than binning and therefore represent the "middle" case and are not further discussed here.

In the simulations, downsampling was implemented by simply keeping every N-th sample in the spectrum. In order to properly model binning, the following procedure was used. For a binning factor of 2^n, 2^n spectra of the same marker combination were first scaled to achieve the necessary photon noise level for a particular S/N ratio as described in Section 4.9.1. Next, individual photon noise and dark current shot noise realizations were applied to each of the scaled spectra:

$$\tilde{\boldsymbol{s}}_i = \boldsymbol{s} + \boldsymbol{n}_p(\boldsymbol{s}_i) + \boldsymbol{n}_{di}, \tag{4.47}$$

where $\boldsymbol{s}$ is the scaled version of the original marker combination spectrum, $\boldsymbol{n}_p(\boldsymbol{s}_i)$ and $\boldsymbol{n}_{di}$ are individual realizations of photon noise and dark current shot noise, respectively, and $i = 1, ..., 2^n$. The noisy spectra $\tilde{\boldsymbol{s}}_i$ were then summed and corrupted by additive Gaussian read-out noise:

$$\tilde{\boldsymbol{s}} = \sum_{i=1}^{2^n} \tilde{\boldsymbol{s}}_i + \boldsymbol{n}_r \tag{4.48}$$

In the CCD sensor employed in the prototype system in this work, binning factors 2, 4, and 8 can be used (see Section 6.1). Therefore, these factors were investigated in the simulations below.

If spectra with an original sampling of 1 nm that were used in all previous simulations are downsampled or binned by a factor of 8, a sampling with 8 nm results. Figure 4.21
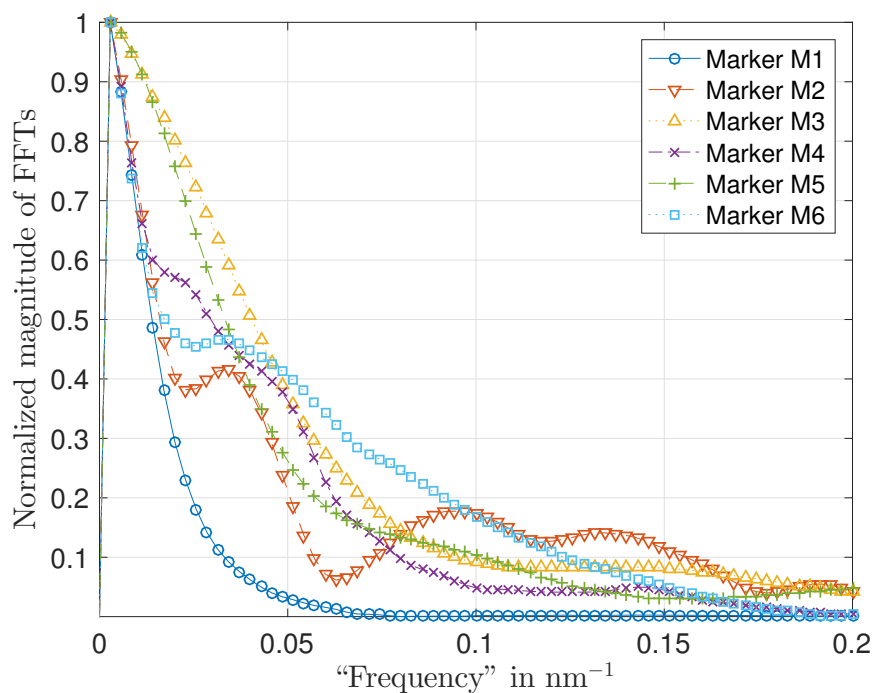
Figure 4.20: Normalized magnitudes of the Fourier transforms of the fluorescence spectra of markers M1-M6.

compares spectra of markers M1 and M6 with a sampling of 1 nm and 8 nm (achieved with both downsampling and binning). In the figure, all spectra are normalized to the maximum of the spectra with a sampling of 1 nm. As can be seen, marker M1 is very well distinguishable even with the sampling of 8 nm with both downsampling and binning (8 nm is better than the Nyquist sampling of 10 nm for this marker, see Fig. 4.20). The situation is different with marker M6, for which the Nyquist sampling is approx. 3.33 nm. If the spectrum is downsampled to 8 nm and the samples are not optimally chosen, the peak of the marker M6 may be (almost) absent in the spectrum (as shown in Fig. 4.21b) or the spectral shape of the marker may look different and not as expected by the classification algorithms. In contrast, although intensity-reduced, the peak of marker M6 is still present in the spectrum and the original spectral shape is better preserved with the sampling of 8 nm when binning is used.

Classification results

Figure 4.22 shows results achieved by MLC with LDA features and SCC for the scenarios A (sensor noise), B (relative marker intensity fluctuations) and C (autofluorescence), for different sampling when downsampling was used. It is easy to see that compared to the reference sampling of 1 nm, the larger sampling increments provide worse classification performances in all 3 scenarios.

For the scenario A (see Fig. 4.22a and 4.22b), decreasing the sampling from 1 nm to
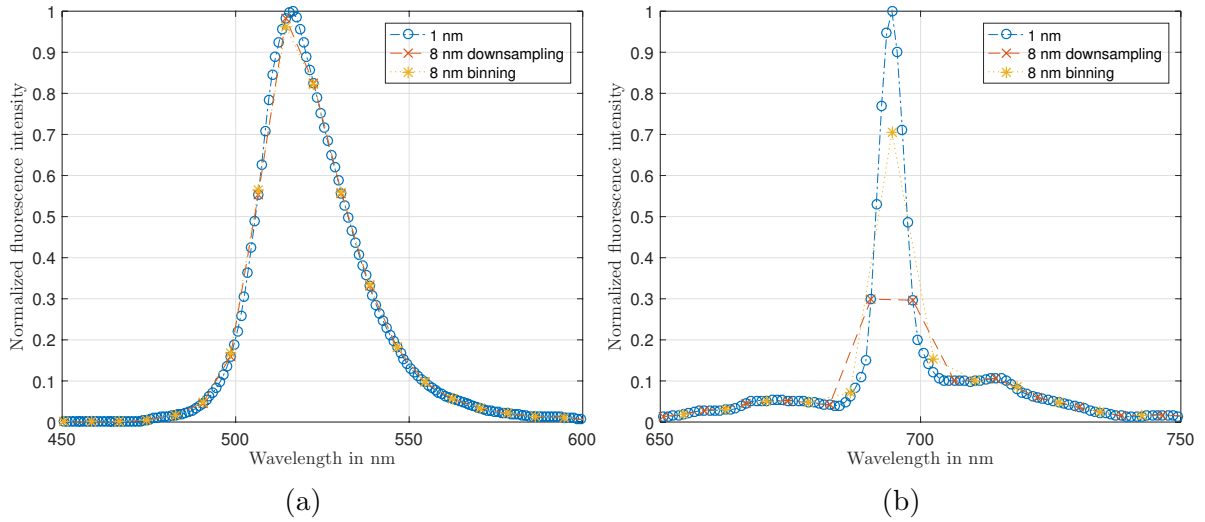
Figure 4.21: Spectra of (a) marker M1 and (b) marker M6 with the original sampling of 1 nm compared to the spectra with 8 nm sampling when downsampling and binning are used. The fluorescence intensities of all spectra are normalized to the maximum of the spectra with 1 nm sampling.

2 nm results in the decrease of the F_1-score$_M$ of SCC from 100% to 97.19% and of MLC from 100% to 98.53% at S/N ratio = 5 dB. At lower S/N ratios the decrease of the F_1-score$_M$ is even more noticeable. For example at S/N ratio = 0 dB, the F_1-score$_M$ of SCC decreases from 96.53% to 68.84% and of MLC from 99.40% to 80.95%. The further increase of the sampling increments results in even worse classification performance. SCC achieves F_1-score$_M$ of 83.91% with sampling 4 nm and 48.80% with sampling 8 nm at an S/N ratio of 5 dB, and F_1-score$_M$ of 45.44% with sampling 4 nm and 20.50% with sampling 8 nm at an S/N ratio of 0 dB. The F_1-score$_M$ of MLC decreases to 86.76% (4 nm) and 49.66% (8 nm) at an S/N ratio of 5 dB, and to 50.10% (4 nm) and 22.3% (8 nm) at S/N ratio of 0 dB. It should be noted, that at S/N ratio of 20 dB, which is the realistic value achieved in the experiments (see Chapter 7), both SCC and MLC achieve a perfect F_1-score$_M$ = 100% even with the 8 nm sampling.

For the scenario B, the change of sampling is less dramatic in terms of the classification performance (see Fig. 4.22c and 4.22d). With intensity fluctuations of ±40%, the F_1-score$_M$ of SCC decreases from 100% with the sampling of 1 nm to 98.53%, 97.10% and 92.02% with the samplings of 2 nm, 4 nm and 8 nm, respectively. With intensity fluctuations of ±60% the decrease of the F_1-score$_M$ of SCC is even smaller: from 81.77% with the sampling of 1 nm to 80.61%, 79.45%, and 75.45% with the samplings of 2 nm, 4 nm, and 8 nm, respectively. With larger intensity fluctuations of ±80% and ±100%, the already low classification performance of SCC with 1 nm (F_1-score$_M$ of 58.38% and 44.45%, respectively) does not significantly decrease with the samplings of 2 nm, 4 nm, and 8 nm.

The change of sampling from 1 nm to 2 nm and 4 nm with intensity fluctuations of
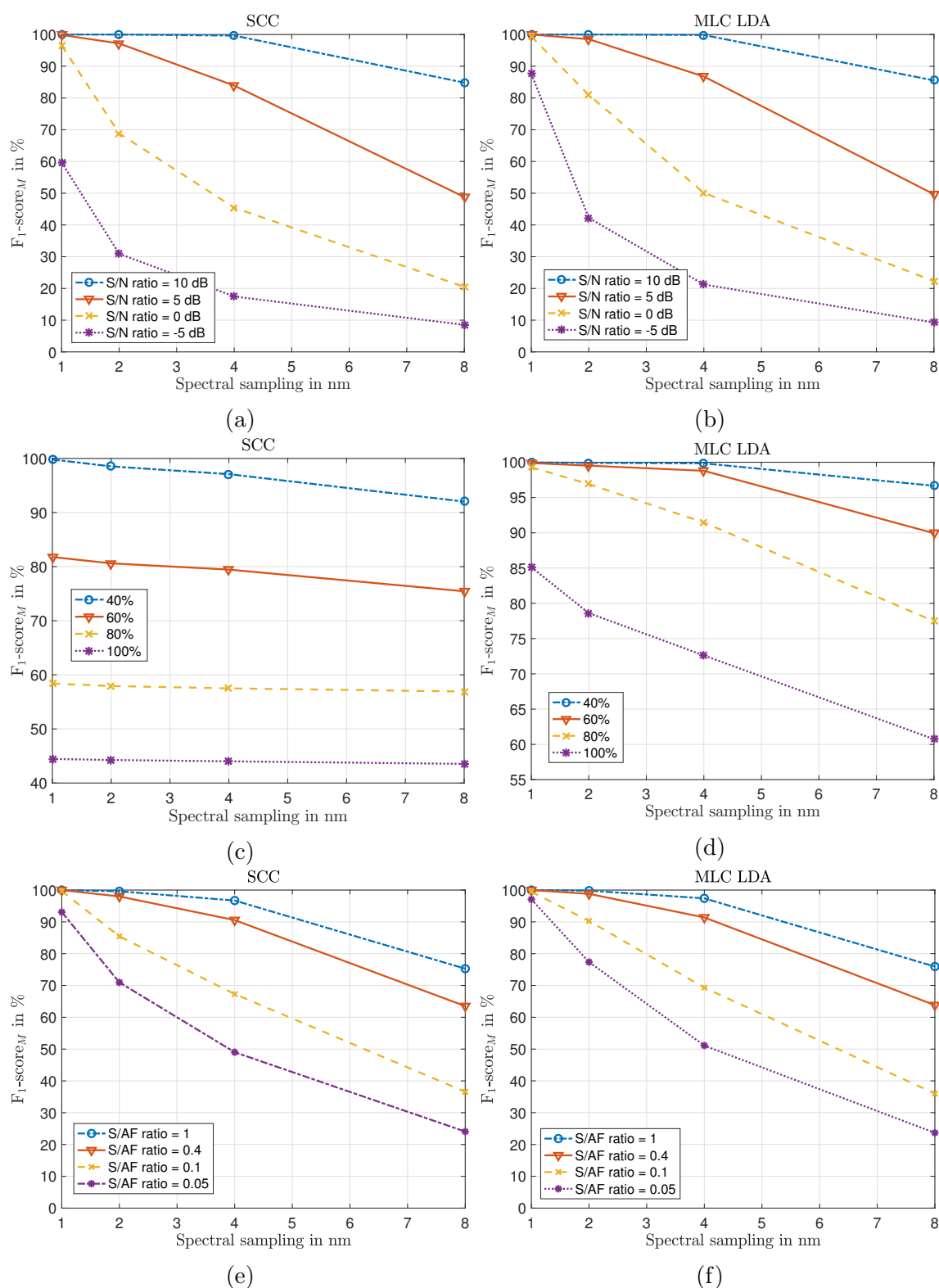
Figure 4.22: Comparison of classification performance achieved by the MLC with LDA features and SCC with different spectral sampling rates when downsampling was used in (a, b) scenario A (sensor noise), (c, d) scenario B (intensity fluctuations) and (e, f) scenario C (autofluorescence).

$\pm 40\%$ results in a marginal decrease of the F_1-score$_M$ of MLC from 100% to 99.92% and 99.85%, respectively. The use of 8 nm sampling, however, degrades the F_1-score$_M$ of MLC to 96.67% with the same intensity fluctuations. With intensity fluctuations of $\pm 60\%$ the F_1-score$_M$ of MLC changes from 99.89% with the sampling of 1 nm to 99.52%, 98.79% and 89.94% with the samplings of 2 nm, 4 nm and 8 nm, respectively. With larger intensity fluctuations the change of the sampling results in a steeper decrease of the F_1-score$_M$ of MLC: with $\pm 80\%$ it goes from 99.29% with 1 nm through 96.91% and 91.47% with 2 nm and 4 nm, respectively, down to 77.46% with 8 nm. With $\pm 100\%$ MLC achieves F_1-score$_M$ of 85.12%, 78.62%, 72.62% and 60.74% with samplings of 1 nm, 2 nm, 4 nm and 8 nm, respectively.

For the scenario C (see Fig. 4.22e and 4.22f), the change of the sampling at an S/AF ratio of 1 brings the decrease of the F_1-score$_M$ of SCC from 100% with 1 nm to 99.62% with 2 nm, 96.71% with 4 nm and 75.28% with 8 nm, and that of MLC from 100% with 1 nm to 99.82%, 97.40% and 75.95% with 2 nm, 4 nm and 8 nm, respectively. An even more significant decrease can be seen at S/AF ratio = 0.1: the F_1-score$_M$ of SCC decreases from 100% with the sampling of 1 nm to 85.45%, 67.31% and 36.57% with the samplings of 2 nm, 4 nm and 8 nm, respectively; the F_1-score$_M$ of MLC decreases from 99.46% with 1 nm to 90.28% with 2 nm, 69.31% with 4 nm and 36.02% with 8 nm.

Obviously, the simple downsampling has negative influences on the classification performance. In contrast, the influence of binning on the classification performance is far less severe. Figure 4.23 shows classification results achieved by SCC and MLC with LDA features for the scenarios A, B and C, for different samplings when binning was used. As mentioned before (see also Section 3.4), pixel binning in CCD sensors reduces the read-out noise component in the resulting spectra, thus effectively increasing the actual S/N ratio and (partly) compensating the loss of spectral resolution. This is especially important in scenario A, but since noise is inevitably present in any measurement system, this quality of binning becomes vital.

For presentation purposes, the S/N ratios given in the Fig. 4.23a and 4.23b correspond to the S/N ratios of the spectra before binning (i.e. with the sampling of 1 nm). For example, the S/N ratio of 0 dB for spectra with a sampling of 2 nm, 4 nm, and 8 nm corresponds to the S/N ratio of the original spectra with no binning (i.e. 1 nm sampling). The actual S/N ratio of spectra with binning is in fact higher (see below).

In scenario A, the blue and the red curves in Fig. 4.23a, which correspond to the S/N ratios before binning of 10 dB and 5 dB, respectively, show that SCC achieves an F_1-score$_M$ of 100% even with the sampling of 8 nm. This is due to the fact that the actual S/N ratio of the spectra is increased from 10 dB and 5 dB to 19 dB and 13.5 dB, respectively, when binning with the factor of 8 was applied. This corresponds to the S/N ratio increase in a photon noise-limited measurement system (see Section 3.4.2). With the S/N ratio before binning of 0 dB (yellow curve in Fig. 4.23a), the F_1-score$_M$ decreases from 96.53% with the sampling of 1 nm to 90.45%, 88.75% and 86.43% with the samplings of 2 nm, 4 nm and 8 nm. The decrease of more than 10% (absolute value) with the sampling of 8 nm in comparison to 1 nm is noticeable here but is far smaller than that with the simple downsampling (see Fig. 4.22a). The actual S/N ratio is approx. 11 dB with the sampling

of 8 nm here. MLC shows a similar behavior with respect to binning in scenario A (see Fig. 4.23b).

Due to the fact that binning physically summarizes charges from adjacent pixels, narrow spectral peaks of markers are still present in the resulting spectrum even if the sampling of 8 nm formally violates the Nyquist criterion (see Fig. 4.21). Additionally, the physical summation of charges introduces the low-pass filtering effect in the spectral domain, which reduces the relative intensity fluctuations of markers in marker combinations thus compensating the loss of spectral resolution in scenario B (see Fig. 4.23c and 4.23d). The most noticeable decrease of the F_1-score$_M$ in scenario B is with MLC with the intensity fluctuations of $\pm100\%$: from 85% with 1 nm to 82.48% with 8 nm. However, even with the sampling of 8 nm, MLC achieves F_1-score$_M$ = 99.99% with intensity fluctuations of $\pm40\%$ and F_1-score$_M$ = 99.5% with intensity fluctuations of $\pm60\%$. The SCC classification algorithms shows only a small decrease of F_1-score$_M$ of only about 1% with intensity fluctuations up to $\pm100\%$ with all samplings.

In scenario C (see Fig. 4.23e and 4.23f), both SCC and MLC provide an excellent classification performance with S/AF ratio = 1 with the samplings of up to 8 nm with binning. With S/AF ratio = 0.1, the F_1-score$_M$ of SCC and MLC decreases from 99.67% with 1 nm to 94.32% with 8 nm and from 99.46% with 1 nm to 94.73% with 8 nm, respectively. With S/AF ratio = 0.05, the F_1-score$_M$ of SCC and MLC decreases from 93.09% with 1 nm to 84.91% with 8 nm and from 97.07% with 1 nm to 86.18% with 8 nm, respectively.

Overall, as simulations have shown, binning up to the factor of 8 (sampling of 8 nm) can be used with the 6 investigated markers without a severe loss of classification performance. A small F_1-score$_M$ tends to decrease more in comparison to a large F_1-score$_M$ if sampling increments are increased. In contrast, downsampling should be used only if absolutely necessary and high S/N ratio, S/AF ratio, and low relative marker intensity fluctuations can be ensured. The spectral sampling is very important for the classification performance in practice and should be paid attention to.
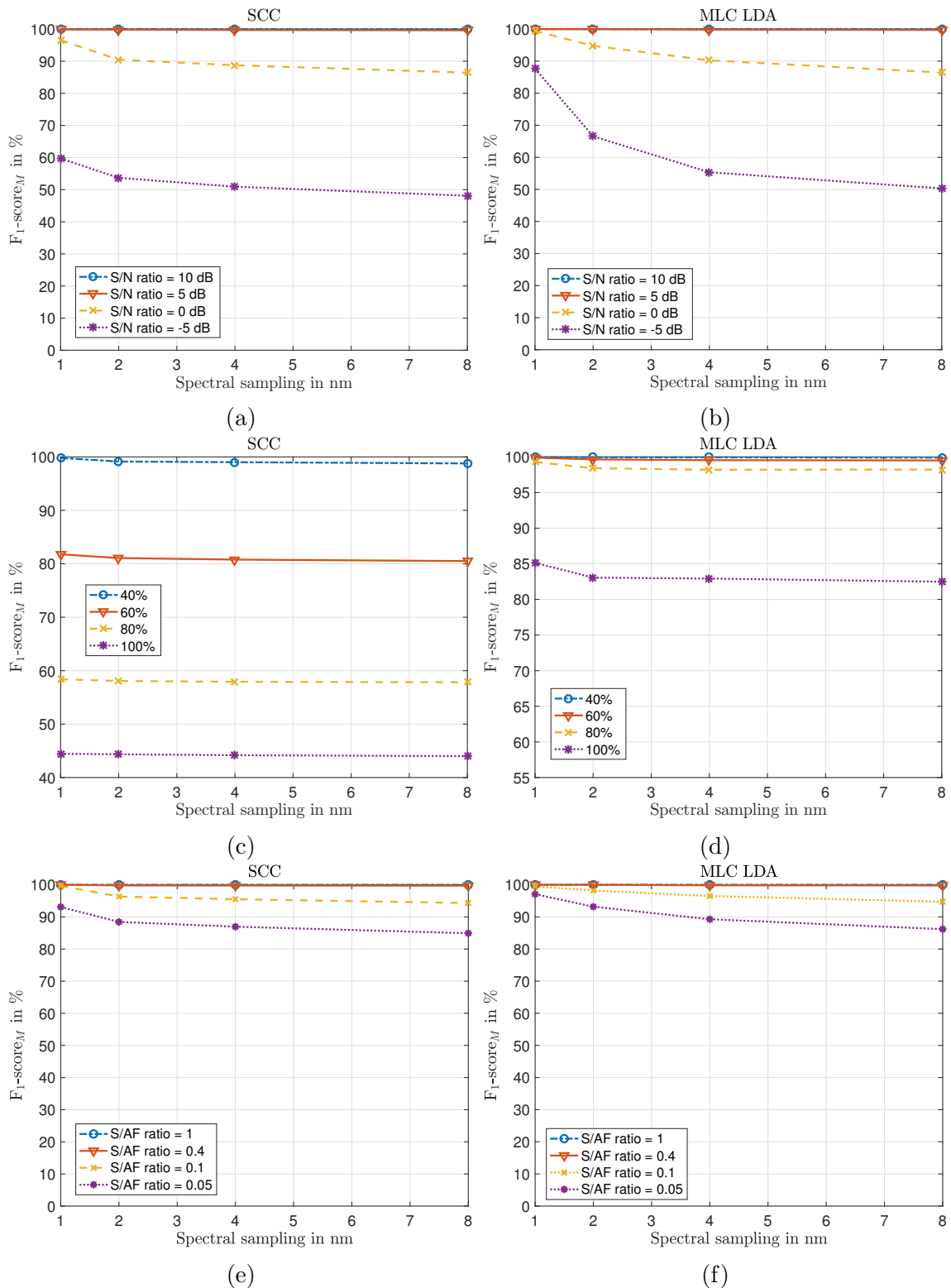
Figure 4.23: Comparison of classification performance achieved by the MLC with LDA features and SCC with different spectral sampling rates when binning was used in (a, b) scenario A (sensor noise), (c, d) scenario B (intensity fluctuations) and (e, f) scenario C (autofluorescence).

Chapter 5

Time-gated fluorescence spectroscopy

As already discussed in Chapters 2 and 4, intrinsic autofluorescence (AF) of plastics can pose a significant problem to the classification of fluorescently labeled plastics. When AF spectrally overlaps with the emission spectra of fluorescent markers and the signal-to-autofluorescence ratio (S/AF ratio) is low, a reliable classification of the measured spectra is very difficult [34]. Time-gated fluorescence spectroscopy (TGFS) is a measurement approach that suppresses AF in the measured spectra. It makes use of the fact, that upon excitation with a short light impulse, the fluorescence of appropriate markers lasts orders of magnitude longer than the AF. Therefore, it is possible to time-gate the acquisition by accumulating the fluorescence emissions only between excitation light impulses during suitable time periods when AF has significantly decayed but marker fluorescence is still present with large intensity. The idea of TGFS arises from the concept of time-resolved fluorescence measurements. In this chapter, the basic principle of two classical time-resolved fluorescence measurements – the time-domain and frequency-domain – as well as the fluorescence decay are discussed, before the principle of TGFS is introduced in detail. Furthermore, possible hardware options for the implementation of TGFS, its advantages and disadvantages as well as the optimization of TGFS measurements are discussed.

5.1   Time-resolved fluorescence measurements

Time-resolved fluorescence measurements are widely used, especially in studies of biological macromolecules and for cellular imaging [28]. In the traditional steady-state measurement approach, fluorescence emission spectra are acquired in conditions where excitation light and thus fluorescence emission are constantly present. If an investigated sample contains a mixture of fluorophores, it is not always possible to resolve emissions of the individual fluorophores using steady-state measurements. In contrast, time-resolved measurements may reveal distinctive fluorescence decay characteristics of individual fluorophores and help resolve the mixture. Before discussing the two dominant methods for time-resolved fluorescence measurements, it is important to briefly review the basics of fluorescence decay.

5.1.1   Fluorescence decay

Upon exposure to a sharp impulse of light, the initial population ν_0 of fluorophores in an investigated sample turns into the excited state. As discussed in Chapter 2, these excited-state fluorophores decay with a rate $\Gamma + k_{nr}$:

$$\frac{\mathrm{d}\nu(t)}{\mathrm{d}t} = (\Gamma + k_{nr})\,\nu(t), \tag{5.1}$$

where $\nu(t)$ is the number of excited fluorophores at time t after excitation, Γ is the emissive decay rate and k_{nr} is the non-radiative decay rate [28]. Since fluorescence emission is a random process, all excited fluorophores have equal probabilities of emitting photons in a given period of time. This results in an exponential decay of the excited population of fluorophores (see Fig. 5.1):

$$\nu(t) = \nu_0 \, \exp(-t/\tau_d), \tag{5.2}$$

where the decay time constant $\tau_d = (\Gamma + k_{nr})^{-1}$ is the inverse of the total decay rate. However, not the number of excited fluorophores is observed, but rather the also time-dependent intensity of the emitted fluorescence light. Fluorescence emission intensity I at a certain wavelength band $\Delta\lambda$ and a certain moment of time t is proportional to the number of photons emitted by the sample at this wavelength band, which in turn is proportional to the number of excited fluorophores ν at this moment of time t. Hence, Eqn. 5.2 can be rewritten in terms of fluorescence emission intensity I:

$$I(t) = I_0 \, \exp(-t/\tau_d), \tag{5.3}$$

where I_0 is the intensity at time 0 after the excitation light impulse.

Following the exponential decay law, a large number of the fluorophores emit photons quickly after the excitation, and some emit with a longer delay. The time distribution of emitted photons forms the fluorescence intensity decay curve, and according to Eqn. 5.3, the fluorescence decay time constant τ_d indicates the moment when $1/\mathrm{e}$ (approx. 37%) of all fluorophores are still in the excited state (have not emitted photons yet). The goal of time-resolved measurements is to determine τ_d.

5.1.2   Time-domain fluorescence measurements

In time-domain fluorescence measurements (also called pulse fluorometry [28]), the sample is excited with a light impulse to invoke time-dependent fluorescence decay, which is then measured. The duration of the impulse is made as short as possible, much shorter than the fluorescence decay time constant of the investigated sample. After the light impulse, the fluorescence intensity decay curve $I(t)$ is measured and the decay time constant τ_d is derived from $\log(I(t))$.

The most straightforward way to acquire the fluorescence decay curve would be to time-sample the fluorescence emission using an extremely fast detector. However, typical (organic) fluorophores have decay time constants of several hundreds of picoseconds
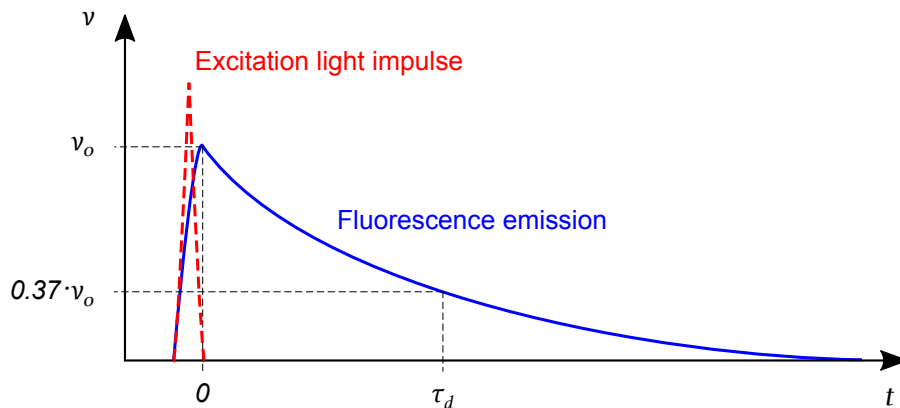
Figure 5.1: Timing diagram of the fluorescence decay process. The initial population of fluorophores ν_0 is excited with a short impulse of light (dashed line). The number of excited fluorophores ν then decays (solid line), the rate of the decay is determined by the time constant τ_d. The goal of time-resolved fluorescence measurements is to determine the fluorescence decay time constant τ_d.

to tens of nanoseconds [28]. Measuring such fast decay processes would require ultrafast (and very expensive) detectors and electronics. For this reason, a somewhat more sophisticated method called the time-correlated single photon counting (TCSPC) is in widespread use [87]. Most of the TCSPC instruments use a high repetition rate laser as excitation light source and a photomultiplier tube (PMT) detect the fluorescence photons. For economic reasons, lasers are often replaced with fast laser diodes or even LEDs. A laser-light pulse train is used to repetitively excite the fluorophores and invoke their time-dependent exponential decay. Instead of acquiring the entire fluorescence decay process, the PMT registers only the first incident photon. The time delay Δt between the end of the excitation impulse and the detection of the first incident photon is measured a large number of times and stored in a histogram. The resulting histogram represents an estimate of the probability density function of photon emission at a particular time delay after excitation. The shape of the histogram is equal to the fluorescence decay curve and can be used to derive the decay time constant τ_d.

Because of imperfections in the detector's electronics (e.g. dead time, jitter, etc.), the measurement conditions are usually adjusted in such a way that only 1 photon per approx. 50 to 100 excitation pulses arrives at and is detected by the PMT. If more than 1 photon per excitation pulse would arrive at the PMT, only the first one would be detected and all following photons would be missed. This would result in a histogram of time delays Δt shifted to shorter times and would distort the derived fluorescence decay time constant τ_d.

A specific measurement set-up is necessary to measure the time delay Δt (see Fig. 5.2). The measurement begins with the excitation impulse which is detected by the constant function discriminator (CFD) and the exact time of the pulse start is registered. The start
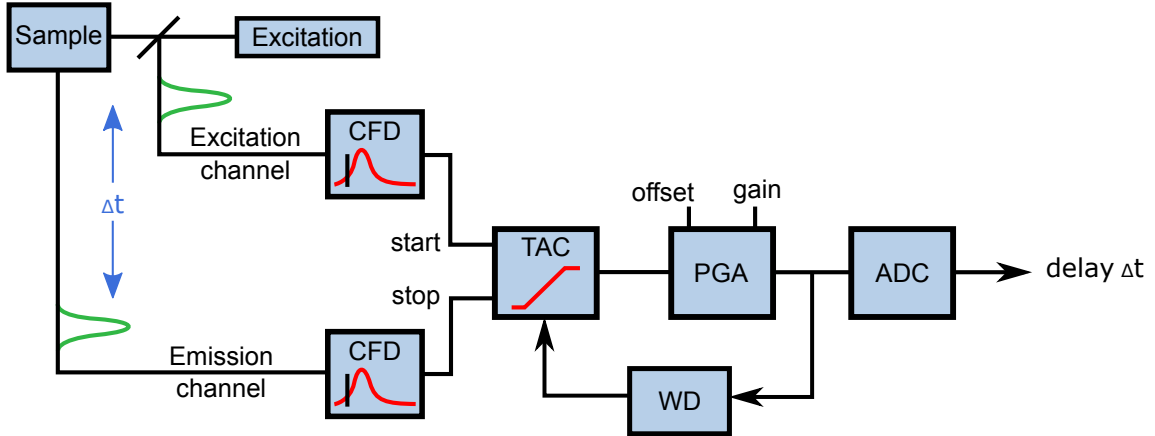
Figure 5.2: Block diagram of TCSPC measurements. (Source: J.R.Lakowicz [28]).

signal is passed from the CFD to the time-to-amplitude converter (TAC) which begins generating a linear voltage ramp. After the time delay Δt, the arrival of the first photon is registered by the second CFD in the emission channel. Upon registering the first photon, the second CFD sends the stop signal to the TAC to end generating the voltage ramp. Thus, the TAC has generated a voltage proportional to the time delay Δt. This voltage is then amplified by the programmable gain amplifier (PGA) and converted to a numerical value by the analog-to-digital converter (ADC). A window discriminator (WD) is used to restrict the generated voltage to a certain range in order to avoid false readings. The resulting digital value (delay time Δt) is stored. The histogram of Δt values is acquired by repeating the described process many times. The histogram is then used to derive the fluorescence decay time constant τ_d as described above [28].

5.1.3   Frequency-domain fluorescence measurements

Another way to determine the fluorescence decay time constant is frequency-domain fluorescence measurements, also called phase-modulated measurements, which are based on the fact that harmonically amplitude-modulated excitation light invokes a phase-shifted, amplitude-modulated fluorescence emission (see Fig. 5.3). The time lag (and phase angle ϕ_ω) between the excitation light and the fluorescence emission as well as the modulation m_ω (see Eqn. 5.5) of the fluorescence emission depend on the sample's fluorescence decay time constant τ_d and the light modulation angular frequency ω.

The fluorescence emission modulation index $m_\omega = (B/A)/(b/a)$ can be derived from the known amplitude b and mean value a of the modulated excitation light (intensity), and the measured amplitude B and mean value A of the modulated emission light (intensity). The phase angle ϕ_ω and the modulation m are then used to calculate the fluorescence decay time constant τ_d of the investigated sample as follows [28]:

$$\tan \phi_\omega = \omega \tau_{d\phi} \quad \Rightarrow \quad \tau_{d\phi} = \omega^{-1} \tan \phi_\omega, \tag{5.4}$$
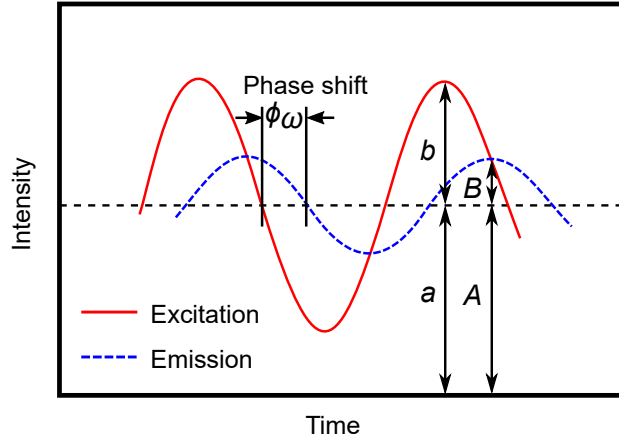
Figure 5.3: Frequency-domain measurements: sinusoidally modulated excitation light (solid line) invokes sinusoidally modulated, phase-shifted fluorescence emission (dashed line) of the sample. For representation purposes, the mean intensity a of the excitation light is equal to the mean intensity A of the emission light in the figure. (Source: J.R.Lakowicz [28]).

$$m_\omega = \frac{1}{\sqrt{1 + \omega^2 \tau_{dm}^2}} \quad \Rightarrow \quad \tau_{dm} = \frac{1}{\omega} \sqrt{\frac{1}{m_\omega^2} - 1}. \tag{5.5}$$

Equations 5.4 and 5.5 calculate the so-called apparent phase ($\tau_{d\phi}$) and apparent modulation (τ_{dm}) decay time constants of the sample. In case of a single-exponential decay function as in Eqn. 5.3, i.e. when only one type of fluorophores is present in the sample, phase and modulation decay time constants $\tau_{d\phi}$ and τ_{dm} are equal and can be interpreted as the fluorophore's actual decay time constant τ_d, as in time-domain measurements (see Section 5.1.2). However, investigated samples display multi-exponential or even non-exponential decay in many cases. Multi-exponential models are very powerful and can fit almost any fluorescence decay using the sum of several (i) exponentials:

$$I(t) = \sum_i I_{0i} \exp(-t/\tau_{di}). \tag{5.6}$$

However, in Eqn. 5.6 the values of I_{0i} and τ_{di} do not always have a physical meaning. The correct interpretation of these values highly depends on prior knowledge about the fluorophores present in the investigated sample and possible interactions between them. For multi-exponential decay, apparent phase and modulation decay time constants $\tau_{d\phi}$ and τ_{dm} measured at a single modulation angular frequency ω do not provide characteristics of the decay, but represent a weighted average of the decay times displayed by the sample. In order to find the actual fluorescence decay time constants τ_{di} in Eqn. 5.6, apparent decay time constants $\tau_{d\phi}$ and τ_{dm} need to be measured over a wide range of modulation

frequencies. The collected data $\tau_{d\phi}(\omega)$ and $\tau_{dm}(\omega)$ is called the frequency response of the sample. Typical frequency response curves of a sample containing a 50%:50% mixture of two fluorophores with decay time constants $\tau_{d1} = 2.5$ ns and $\tau_{d2} = 10$ ns are shown in Fig. 5.4 with modulation frequency $f = 2\pi/\omega$ on the x-axis and phase angle ϕ_ω and modulation m_ω on the y-axis. As it can be seen, with the increase of the excitation light modulation frequency the phase angle ϕ_ω increases from 0° to 90° (also see Eqn. 5.4). The modulation m_ω also depends on the excitation light modulation frequency: it decreases from 1 to 0 with increased modulation frequency (see Eqn. 5.5). The shape of the frequency response curve is determined by the decay time constants of all fluorophores present in the sample. One can find the underlying decay time constants τ_{di} by fitting the frequency response curve with the multi-exponential model in Eqn. 5.6 [28, 88].

5.2   Principle of time-gated fluorescence spectroscopy (TGFS)

Although the time-domain and frequency-domain measurements can help determine fluorescence decay time constants and give an insight or estimation of what fluorophores are present in the investigated sample, such measurements take much time and can barely be implemented in a fast industrial application. When fluorescence emissions of different fluorophores do not spectrally overlap with one another or the overlap is small, characterization of the sample is easier and faster carried out based on the fluorescence spectra rather than on the decay time constants. However, for the application at hand, the principles behind time-resolved measurements (Sections 5.1.2 and 5.1.3) can help separate autofluorescence (AF) of plastics from fluorescence of incorporated markers. When the fluorescence decay time constant of the AF is much (ideally orders of magnitude) shorter than that of the marker fluorescence, it is possible to resolve the AF and marker fluorescence in time using pulsed excitation and gated acquisition of the fluorescence emissions.

The main principle of time-gated fluorescence spectroscopy (TGFS) can be explained using the timing diagram in Fig. 5.5. When a plastic sample with incorporated fluorescent marker(s) is excited with a short light impulse ("1"), both AF and marker fluorescence are stimulated (see first row in Fig. 5.5). Once the excitation light is turned off ("0"), the AF of the plastics rapidly decays, usually within tens of nanoseconds (row 2 in Fig. 5.5), whereas the fluorescence afterglow of rare-earth-based markers can last up to several milliseconds (row 3). If the acquisition of the fluorescence emission only takes place at times between the light impulses (row 4), with appropriate pulsing frequency and duty cycle of the pulse train (see Section 5.4 for details), it is possible to achieve that virtually only marker fluorescence is present in the acquired spectrum. Accumulating fluorescence emissions over several such acquisition periods (or "subframes"), (row 5) helps achieve better S/N ratio of the acquired spectrum.
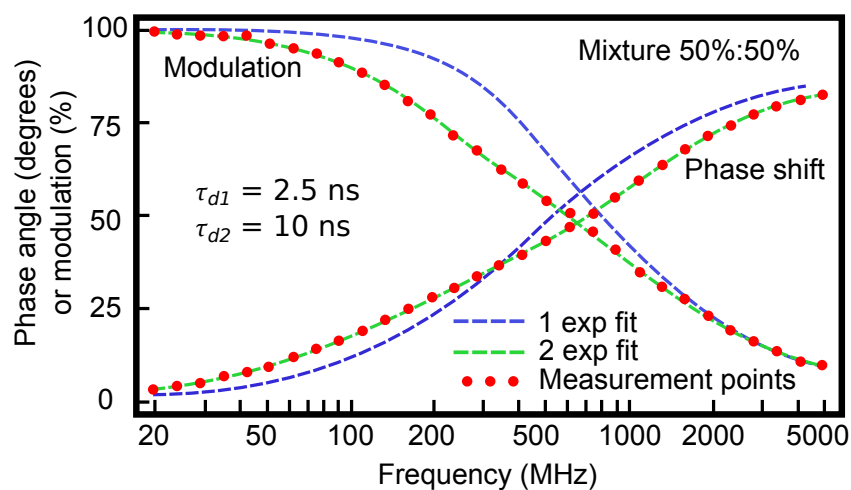
Figure 5.4: Frequency response curves of a sample with a 50%:50% mixture of two fluorophores with decay time constants $\tau_{d1} = 2.5$ ns and $\tau_{d2} = 10$ ns. A good least-squares fit is possible with two exponentials (source: Lakowicz [28]).
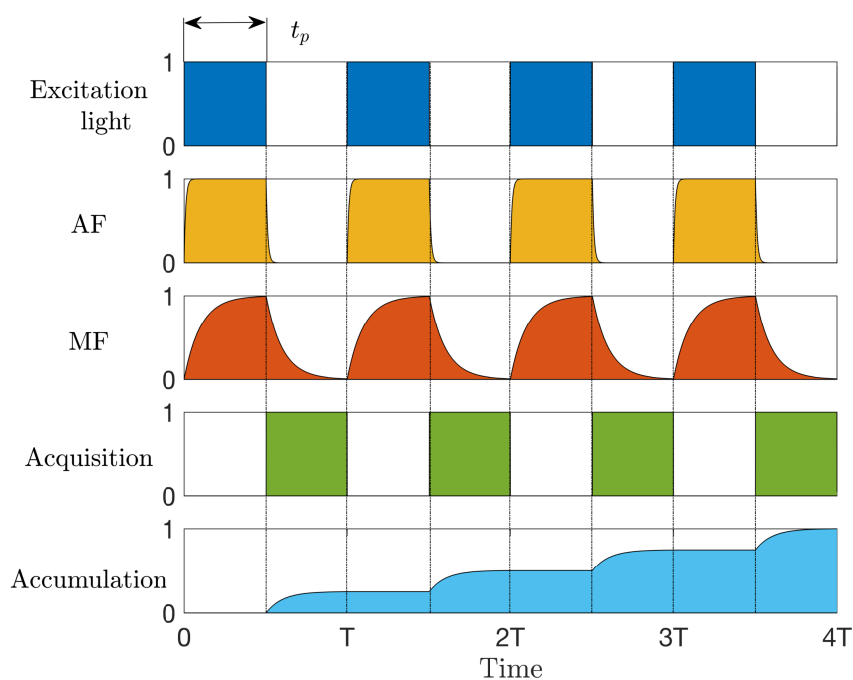
Figure 5.5: Timing diagram of TGFS with 4 acquisition periods ("subframes").

5.3   Implementation of TGFS

Implementation of TGFS in addition to the pulsed excitation requires a gated fluorescence emission acquisition system. Considering the large throughput and high sorting rates mandatory for an industrial plastics sorting system, this acquisition system needs to be very fast and robust. A rather low mass throughput of approx. 250 kg/h is specified for the prototype system developed in this work. In order to achieve it with plastic flake sizes in the range of 2-10 mm (typical for industrial plastic mills in widespread use), approx. 1500 plastic flakes per second need to be processed. With 50 parallel streams of plastic flakes on the conveyor belt, only approx. 10 ms are left for the measurement and classification of every single flake (see Chapter 6). When the measurement time is strictly limited, optimization of TGFS may require the acquisition of a large number of very short subframes (see next section). This reduces the number of options for the implementation of a TGFS system in practice.

Two approaches to gated acquisition exist: (1) to gate the emitted fluorescence light such that only light emitted within certain time frames arrives at the sensor, and (2) to gate the sensor itself. For option (1), mechanical choppers or filter wheels can be used. However, their mechanical parts are prone to wear and may be difficult to synchronize with the pulsed excitation light. The same applies to mechanical shutters. Another option could be acusto-optical tunable filters (AOTF) or liquid-crystal tunable filters (LCTF), which are also used for light modulation in frequency-domain measurements [45]. Yet, their prices rise dramatically with the increase of their aperture size, which would be necessary to gate excitation light that illuminates the entire acquisition scene (conveyor belt in this work). Furthermore, the tuning time usually lies in the milliseconds range for LCTF and in the hundreds of microseconds range for AOTF, which may be too long to implement optimized TGFS (see below).

Implementation of the option (2) requires a fast and, since in TGFS the acquisition takes place during fluorescence decay when emission intensity is low, very sensitive gated sensor. Recently, intensified CCD (ICCD) cameras have become more affordable and efficient. An ICCD camera essentially consist of a 2D CCD sensor and an image intensifier. The image intensifier is a very sensitive electro-optical device that captures incident photons, generates an electrical signal (electrons) proportional to the number of photons, amplifies this signal by a factor of several thousand, and converts it to a high-intensity digital image using a phosphor screen. The output of the image intensifier is coupled with the input of a CCD sensor such that the intensified image is directed onto the sensor. For the application at hand, ICCD cameras can greatly increase the S/N ratio of the measured marker fluorescence spectra and might be a good solution in general for a low-light TGFS measurement system. However, mostly due to the phosphor screen, at present (2018) the lifetime of ICCD cameras is limited to approx. 10 000 h (a little more than a year) [89], which does not seem long enough for an industrial application running 24/7. Replacing the ICCD camera after its lifetime would require disassembling and recalibration of the entire measurement system, which would heavily increase the costs of plastics recycling.

CMOS sensors are especially appreciated because of their fast frame rates which can

be even further increased when a smaller ROI is selected and the number of pixels used is reduced [54]. With some CMOS sensors, sparse selection of pixels is possible such that only certain regions in the spectral domain (wavelength bands corresponding to the fluorescent marker spectra) or spatial domain (direction across the conveyor belt) can be read out (see Chapter 3). Frame and measurement rates up to tens or even hundreds of kHz are not unusual in practice. Since in TGFS the fluorescence emission acquisition only takes place in the time periods when the excitation light is switched off, with an excitation light pulse duty cycle of 50% and 10 kHz measurement and excitation light pulse rate, up to 50 (sub)frames can be acquired during the duration of 10 ms available for the measurement. Signals from these 50 (sub)frames can be then averaged in order to increase the S/N ratio of the final frame. The main drawback of the CMOS-based implementation is that each subframe, no matter how short, must be read-out from the sensor immediately after its acquisition. This means that the electronic noise associated with the read-out is added to each subframe and thus if N subframes are averaged, the S/N ratio is increased by a factor of $\sqrt{N}$ at most (see Section 3.4).

Some CCD sensors provide the so-called "frame accumulation" triggering mode (see Section 3.4), which allows controlling the acquisition with an external trigger signal. The timing diagram of the "frame accumulation" is shown in Fig. 5.6. Upon receiving the first external trigger signal Trg.1, the camera clears its photosensitive pixel registers, starts exposure of the first subframe (Exp.1), completes the integration, transfers the information to the storage pixel registers, and waits for the next trigger signal Trg.2. With Trg.2, the next subframe is exposed and transferred to the sensor's storage pixel register. In other words, in "frame accumulation" mode the full frame is built up of several subframes, each of which is acquired at a certain time period specified by the trigger signal. The trigger signal can often be configured in a flexible way, allowing "accumulation windows" (subframes) of arbitrary length with arbitrary duty cycle. Once the specified number N of subframes is acquired, the full frame is read out. Thus, the accumulation of the subframes is done in the analog domain on the CCD chip. The read-out of the full frame is carried out at the very end of the (subframe) acquisition process and the electronic noise associated with it is added only once, which increases the overall S/N ratio by a factor of up to N in low-light applications (see Section 3.4).

The bottleneck of the "frame accumulation" mode is the time necessary for the read-out. In the normal acquisition mode, each frame is read out right after it is acquired. Therefore with interline CCD sensors, while frame k is being read out, acquisition of the frame $k+1$ can start. This is possible because once acquired, frame k is quickly transferred to the storage registers such that the photosensitive pixels can immediately be used for the acquisition of the subsequent frame $k+1$. In "frame accumulation" mode, however, the storage registers of the sensor are being accessed throughout the acquisition, since each new subframe is added to the previous ones. After all N subframes contributing to the full frame k are acquired, frame k needs to be read out from the storage registers before the acquisition of the next N subframes contributing to the full frame $k+1$ can take place. Thus, if the sensor's electronics needs T_R milliseconds to read-out one full frame, for the acquisition of all subframes only $(T_m - T_R)$ milliseconds are left, where T_m is the time
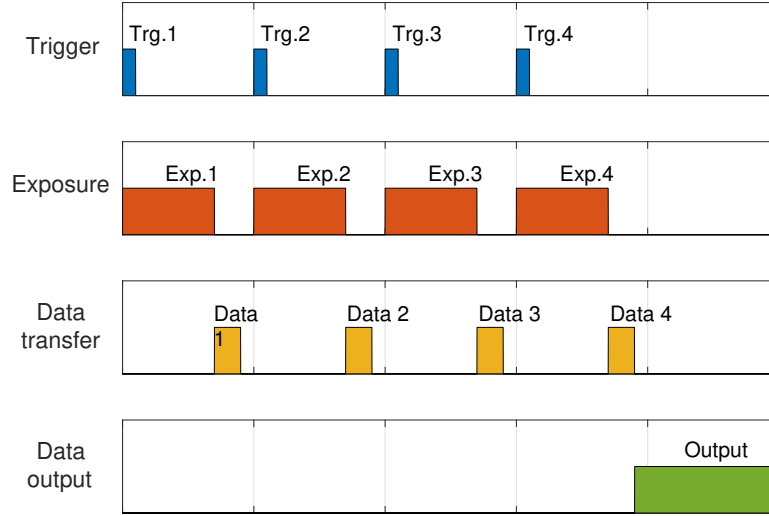
Figure 5.6: Timing diagram of the sensor's frame accumulation mode. 4 subframes accumulated, 1 frame output.

available for one measurement ($T_m = 1/$measurement rate). Even with fast CCD sensors, the read-out time T_R is usually in the milliseconds range and can thus significantly reduce the actual time available for the fluorescence emission acquisition.

This is the major disadvantage of the "frame accumulation" mode which limits the S/N ratio of the acquired marker fluorescence spectra if the time available for one measurement is limited. However, if compared to the other options described above in this section, the frame accumulation is more suitable for an industrial application for several reasons. First, the duration and number of subframes as well as the duty cycle of acquisition can be widely varied allowing a flexible optimization of the acquisition (see Section 5.4). Second, as already mentioned, read-out of the full frame takes place only once per one full frame providing analog summation of subframes on the CCD chip, which is advantageous in terms of S/N ratio (see Section 3.4). And finally, a CCD-based spectral camera is very robust, relatively inexpensive, has a long lifetime, and is thus suitable for an industrial environment. These are the reasons a CCD-based spectral camera with frame accumulation was selected for the measurement system prototype developed in this work (see Chapter 6).

5.4   Parameter optimization of TGFS

The main drawback of the TGFS in comparison to steady-state measurements is the low amplitude of the acquired spectrum. Given the duty cycle 50% as shown in Fig. 5.5, the exposure time for TGFS is decreased by a factor of 2 compared to the steady-state measurement. This reduces the amplitude of the resulting spectrum also by 50% in principle. The amplitude is reduced even more due to the exponential decay of the fluorescence. Figure 5.7a compares fluorescence spectra emitted from marker M4 incorporated into the
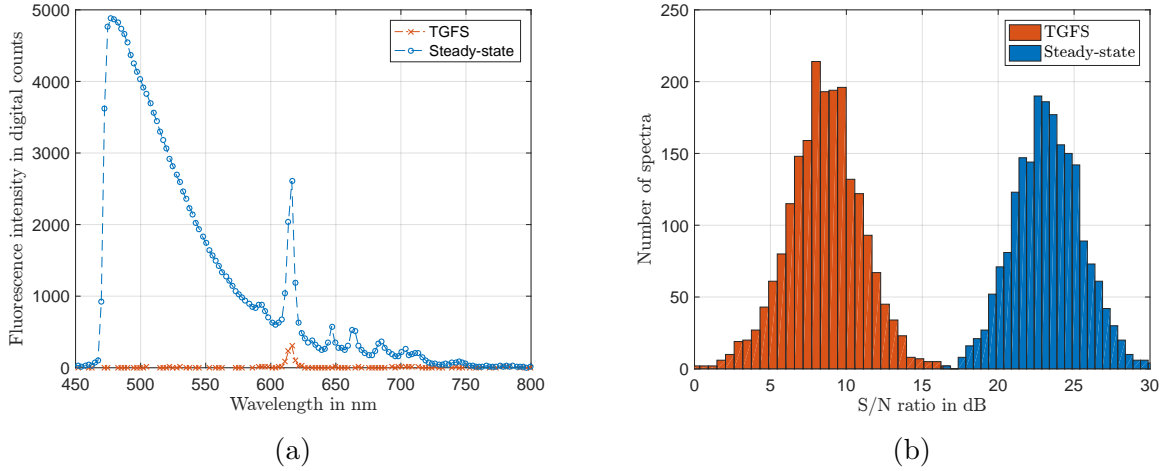
Figure 5.7: (a) Comparison of measured steady-state and TGFS spectra of marker M4 incorporated in a white POM plastic. (b) Histograms of the S/N ratios of 2000 steady-state (right) and 2000 TGFS (left) spectra.

white POM plastic "Delrin", measured using the traditional steady-state setup and TGFS. Both spectra in the figure were software-averaged over 50 acquisitions to reduce noise for further investigations. The part of the spectrum between 450 nm and 600 nm is the AF of the plastic and the spike at 615 nm is the fluorescence of marker M4. As can be seen, although the spectrum acquired with TGFS has no AF, its peak intensity value is approx. 8 times smaller than that of the steady-state spectrum. Furthermore, the S/N ratios of the TGFS spectra is smaller in comparison to the steady-state spectra. Figure 5.7b depicts S/N ratio histograms of approx. 2000 spectra acquired using the steady-state setup (right) and 2000 spectra acquired using TGFS (left). All spectra were acquired from several spots on the POM plastic sample labeled with the marker M4. The S/N ratio is defined within the wavelength band corresponding to the markers present in the sample (M4 in this case), as described in Section 3.4.1. As can be seen in Fig. 5.7b, the mean value of the S/N ratio for steady-state measurements is approx. 23 dB, whereas that of the TGFS measurements is only approx. 9 dB. The significantly decreased S/N ratio also decreases the achievable classification performance (see Chapter 4). Thus, the S/N ratio needs to be maximized using the best TGFS timing parameters. For this task, a model for the TGFS spectra is required as shown in the next section.

5.4.1 Model for TGFS spectra

Figure 5.8 demonstrates the timing diagram of the fluorescence rise and decay processes. In the figure and in the text below, the fluorescence rise process is assumed to start simultaneously with the excitation light impulse at the moment of time $t = 0$. The moment of time when the excitation light impulse is switched off is therefore $t = t_p - 0 = t_p$, where t_p is the duration of the impulse. For simplicity, in the text throughout this section, t_p
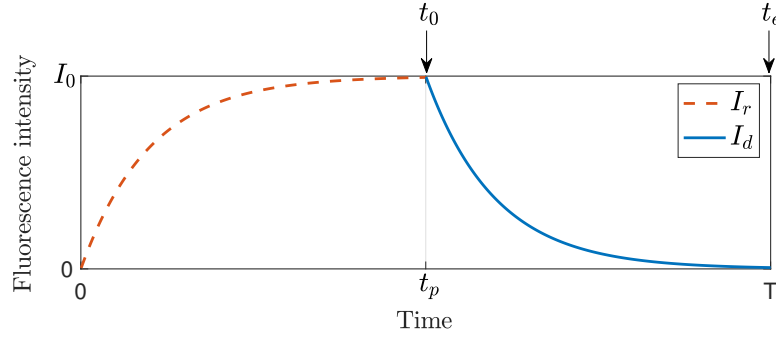
Figure 5.8: Rise $I_r(t)$ and decay $I_d(t)$ of the fluorescence intensity according to Eqn. 5.7 and 5.8. Integration in Eqn. 5.10 is carried out between time instants t_0 and t_e. Here, the case with $t_0 = t_p$ and $t_e = T$ is shown.

denotes both the excitation impulse duration and the moment of time when the impulse is switched off.

As already discussed in Section 5.1.1, the decaying intensity of a fluorescent emission after switching off the excitation light can be modeled as exponential decay. Assuming an excitation impulse duration t_p, Eqn. 5.3 can be rewritten:

$$I_d(t) = I_{d0} \cdot \exp(\frac{t - t_p}{\tau_d}), \tag{5.7}$$

where t is the time, I_{d0} the fluorescence intensity at time instant $t = t_p - 0 = t_p$, and τ_d the fluorescence decay time constant.

According to [88], the rise of the fluorescence intensity after the excitation light was switched on at time instant $t = 0$ can also be modeled as an exponential function:

$$I_r(t) = I_{r0} \cdot (1 - \exp(-\frac{t}{\tau_r})), \tag{5.8}$$

where τ_r is the fluorescence rise time constant and I_{r0} is the maximal fluorescence intensity that can be achieved (equal to the steady-state intensity).

As can be seen from Eqn. 5.8, the fluorescence emission intensity after excitation with a light impulse of duration t_p depends on the fluorescence rise time constant. Therefore, rare-earth elements based fluorescent markers which may have large decay and rise time constants may need excitation light pulses of longer duration in order to get "fluorescently charged". The value of $I_r(t_p)$ represents the initial fluorescence intensity I_{d0} of the decay process in Eqn. 5.7. Thus, the marker fluorescence intensity decay after an excitation pulse of duration t_p can be expressed by:

$$I_d(t) = I_{r0} \cdot (1 - \exp(-\frac{t_p}{\tau_r})) \cdot \exp(-\frac{t - t_p}{\tau_d}). \tag{5.9}$$

As explained in Section 5.2, in TGFS the acquisition of photons takes place only when the excitation light is switched off, i.e. at times between the light pulses when the AF

has sufficiently decayed but marker fluorescence is still present with large intensity. The associated digitized intensity value s generated by the CCD sensor (see Section 3.1) is thus proportional to the fluorescence emission intensity integrated on the sensor's photosensitive surface during the time period $(t_e - t_0)$ between excitation light pulses:

$$s = a \cdot \int_{t_0}^{t_e} I_d(t)\mathrm{d}t = a \cdot I_{r0} \cdot (1 - \exp(-\frac{t_p}{\tau_r})) \cdot \int_{t_0}^{t_e} \exp(-\frac{t - t_p}{\tau_d})\mathrm{d}t, \qquad (5.10)$$

where a is the proportionality constant defined in Section 3.1 and the integration limits t_0 and t_e correspond to the time instants when photon integration starts and stops, respectively. If the integration starts right after the excitation light has been switched off and stops right before the next excitation light impulse is switched on, then $t_0 = t_p$ and $t_e = T$, where T is the period of the excitation pulse. However, in this case, since the AF does not instantly decay to zero, it will still contribute to the resulting value of s, although in a highly reduced way. In principle, time instants t_0 and t_e can be adjusted in order to suppress the AF in the resulting spectrum most efficiently. However, it should be kept in mind, that choosing $t_0 > t_p$ also reduces s and hence the S/N ratio of the measured spectrum due to the exponential decay of the fluorescence light.

After integration with $t_0 = t_p$ and $t_e = T$ Eqn. 5.10 becomes:

$$s = a \cdot I_{r0} \cdot \tau_d \cdot (1 - \exp(-\frac{t_p}{\tau_r})) \cdot (1 - \exp(\frac{t_p(D - 1)}{D\tau_d})), \qquad (5.11)$$

where $D = t_p/T$ is the duty cycle of the excitation light pulse. Equation 5.11 represents the digitized intensity value generated by the sensor during one decay process and represents one subframe of the sensor's "frame accumulation" acquisition mode. In this mode, electrical charges generated by multiple (N) pulses (subframes) are coherently summed up in the sensor's storage pixel registers, resulting in a larger (full frame) digitized intensity value $s_N = N \cdot s$ and thus higher S/N ratio (provided the measurement noise is uncorrelated, see Section 3.4.1).

The resulting full frame value s_N depends on several parameters: fluorescence rise and decay time constants τ_r and τ_d, excitation light pulse duration t_p and duty cycle D, and the number N of accumulated subframes. The time constants τ_r and τ_d are intrinsic properties of the fluorescent markers and can be varied only within certain restricted chemical and physical limits. However, excitation light pulsing parameters t_p and D can be widely and easily varied in order to maximize s_N and thus the S/N ratio of the acquired spectrum. The possible number N of subframes depends on t_p and D, and is limited by the total time available for the measurement T_m: $N = T_m \cdot f_p = T_m \cdot D/t_p$, where f_p is the (switching) frequency of the excitation light pulse. With short light impulses and a high switching frequency, a large number N of subframes can be captured and accumulated during T_m. However, since fluorescence molecules (markers) need time to get "charged" (see Eqn. 5.8), it is not optimal to (simply) apply a large number of short light impulses. Instead, it is necessary to find the best compromise between excitation light pulse duration t_p, duty cycle D and number N of accumulated subframes for particular values of τ_r and τ_d. Before this optimization is explained in Section 5.4.2, one aspect should be pointed out:

In Eqn. 5.7-5.11 single-exponential fluorescence rise and decay processes are assumed. As was mentioned in Section 5.1.3, this is not always the case, and a multi-exponential model then needs to be employed. Equation 5.11 can easily be extended to the multi-exponential case. However, as measurements with a TCSPC spectrofluorometer have proven (not shown here), the rare-earth elements-based markers used in this work exhibit single-exponential decay and Eqn. 5.11 is appropriate.

5.4.2   Optimization of the TGFS timing parameters

The model for the TGFS digitized intensity value s_N derived in Section 5.4.1 was validated using 6 markers M1-M6 (see Chapter 2). In this section, the model is first validated using the marker M6 in pure form (powder), not incorporated into plastics, which represents "best case" conditions when no other chemical (fluorescent) agents other than the marker are present. Next, the model is compared to the measurements with all 6 markers M1-M6 (individually) incorporated into plastics, which corresponds to a realistic case.

Figure 5.9 compares the modeled and measured s_N as function of excitation light impulse duration t_p with duty cycle $D = 10\%$ for marker M4. In the figure, s_N represents the digitized value of the fluorescence emission intensity at the marker's peak wavelength 615 nm (see Fig. 5.9). The number N of subframes is varied depending on the switching frequency $f_p = D/t_p$ when $T_m = 11.9$ ms is constant (as explained in Section 6.2, $T_m = 11.9$ ms is the available measurement time with the prototype). In the model (Eqn. 5.11), the decay and rise time constants $\tau_r = \tau_d \approx 400$ μs were used, that had been measured for M4 (and the other markers) using a laboratory TCSPC device (see Chapter 3). $s_N(t_p)$ was measured utilizing the spectral camera of the developed prototype system (see Chapter 6) and a single high-power UV-LED. The dashed curve with circles (measured data) in Fig. 5.9 was acquired from the pure marker M4 in powder form, i.e. no possibly fluorescently active additives of the plastics could interfere. As can be seen, the modeled s_N (dashed curve) matches the measurement very well.

The next experiment was carried out with all 6 markers M1-M6 individually incorporated into the white POM polymer "Delrin". The comparison of modeled and measured $s_N(t_p)$ curves with constant duty cycle $D = 10\%$ is depicted in Fig. 5.10. In the figure, s_N represents the digitized value of the fluorescence emission intensity at the corresponding markers' peak wavelengths (see Table 2.1). As expected, when markers are incorporated in plastics, i.e. when not only the marker but other – unknown – (fluorescent) chemical components and additives may be also present in the sample, some deviations from the model (Eqn. 5.11) emerge. However, as can be seen, these deviations are not dramatic. As a result, optimal TGFS timing parameters derived using the model might differ a bit from those derived from measurements, but this would not significantly influence the optimization of the resulting (full frame) digitized intensity value s_N. For example, as can be seen in Fig. 5.10a for marker M1, the maximum of the modeled s_N is achieved with $t_p \approx 500$ μs, while the maximum derived from the measured curve is $t_p \approx 400$ μs. However, with pulse duration $t_p = 500$ μs the measured s_N is approx. 99.37% of the maximum achieved with $t_p = 400$ μs, which is a difference of not even 1%. The same is true for the
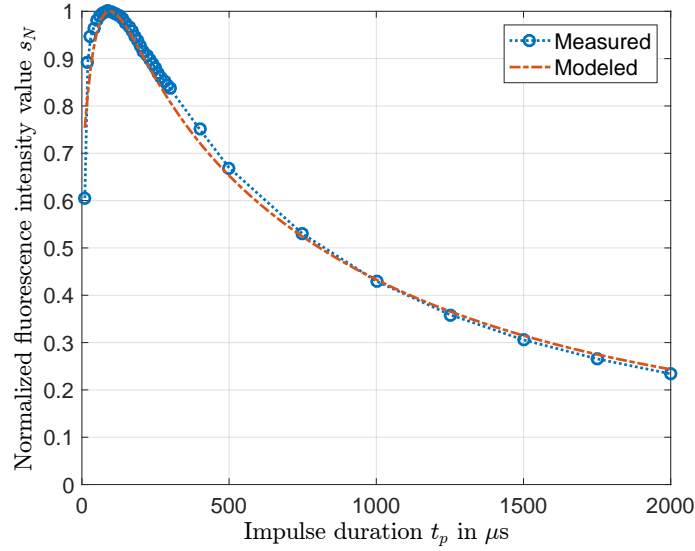
Figure 5.9: Comparison of the digitized fluorescence intensity value s_N for marker M4 ($\tau_r = \tau_d \approx 400~\mu$s): measured and modeled according to Eqn. 5.11 as a function of pulse width t_p. Here s_N represents the (normalized) digitized value of fluorescence emission intensity at the marker's emission peak wavelength 615 nm.

other 5 markers (Fig. 5.10b - 5.10f).

Not only can the model be used to vary the impulse duration t_p, but also the duty cycle D in order to find the parameter set (t_p, D) that maximizes s_N. Moreover, the optimal parameter set (t_p, D) can also be found algebraically. For the rare-earth based markers used in this work the individual rise and decay time constants are very similar, i.e. $\tau_r \approx \tau_d$ per marker. Therefore, τ_r and τ_d will be replaced with τ in the following in order to simplify algebraic derivations. By combining Eqn. 5.11, $s_N = N \cdot s$ and $N = T_m \cdot D/t_p$ one gets:

$$s_N = a \cdot T_m \cdot D/t_p \cdot I_{r0} \cdot \tau \cdot (1 - \exp(-\frac{t_p}{\tau})) \cdot (1 - \exp(\frac{t_p(D-1)}{D\tau})). \qquad (5.12)$$

As can be seen, s_N is a function of two variables t_p and D. Maximization of s_N requires finding its critical points and the second partial derivative test [90]. It is demonstrated in Appendix C, s_N in Eqn. 5.12 has only one maximum given by:

$$\begin{cases} t_p = 1.2564 \cdot \tau, \\ D = 0.5. \end{cases} \qquad (5.13)$$

Thus, for $\tau_r \approx \tau_d \approx \tau$, the optimal duty cycle is always D=0.5 (50%), whereas the optimal impulse duration t_p depends on the fluorescence decay/rise time constant τ of the markers. The optimal t_p values for all 6 markers derived using Eqn. 5.13 are listed in Table 5.1. As can be seen, even though the duty cycle $D = 0.5$ is optimal for all markers, different markers have different optimal impulse duration t_p that depends on
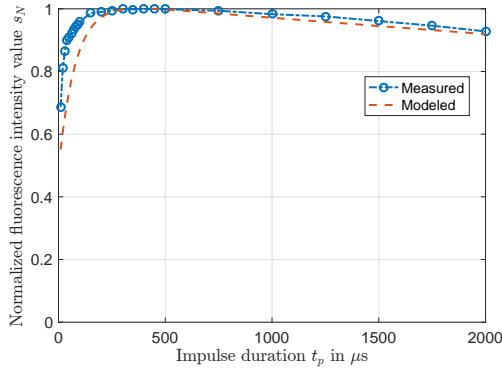
(a) Marker M1, $\tau_d \approx \tau_r = 4000$ μs
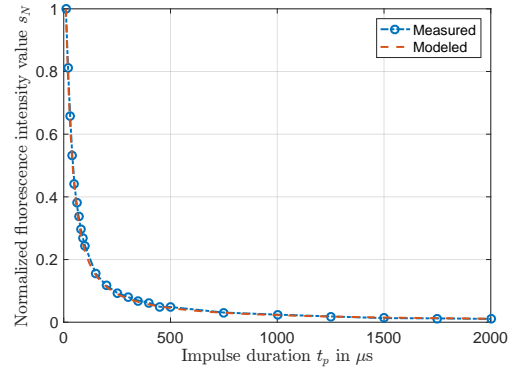
(b) Marker M2, $\tau_d \approx \tau_r = 25$ μs
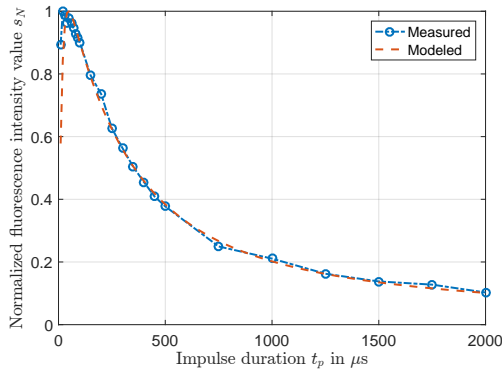
(c) Marker M3, $\tau_d \approx \tau_r = 180$ μs
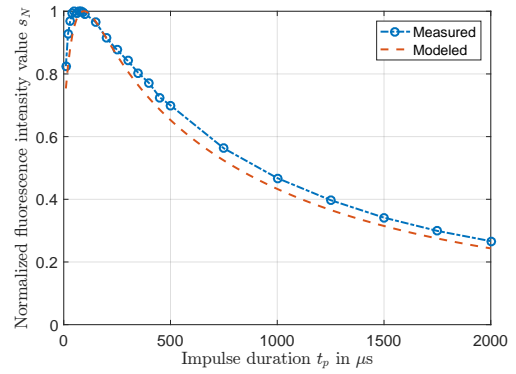
(d) Marker M4, $\tau_d \approx \tau_r = 400$ μs
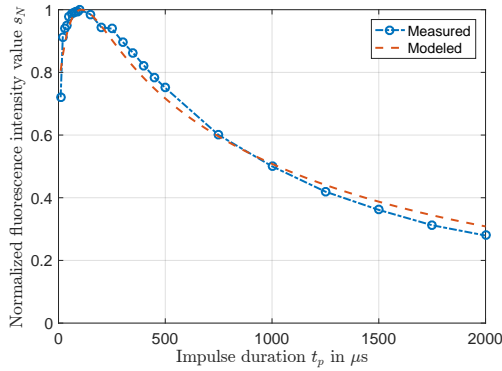
(e) Marker M5, $\tau_d \approx \tau_r = 450$ μs
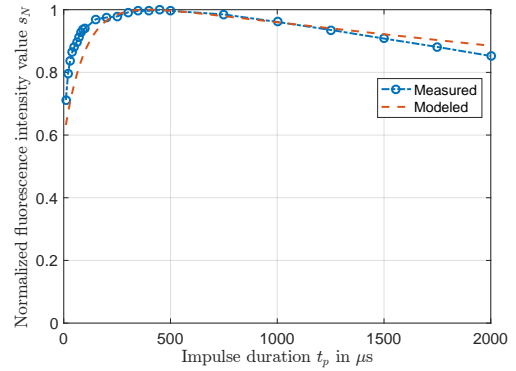
(f) Marker M6, $\tau_d \approx \tau_r = 2500$ μs

Figure 5.10: Digitized fluorescence intensity value s_N at the markers' individual emission peak wavelengths as function of the excitation impulse duration t_p with constant duty cycle $D = 10\%$. Comparison for all 6 markers M1-M6 incorporated into a white POM polymer: measured using the prototype system and modeled according to Eqn. 5.11.

their individual time constants τ. Hence, in order to maximize s_N for all 6 markers at the same time it would be necessary to have 6 different TGFS acquisition units each tuned

Table 5.1: Optimal excitation impulse duration t_p for the 6 investigated fluorescent markers M1-M6 according to Eqn. 5.13 provided that $\tau_d \approx \tau_r$ for all markers.

Marker	M1	M2	M3	M4	M5	M6
τ_d, τ_r in μs	4000	25	180	400	450	2500
Optimal t_p in μs	5030	31	230	500	570	3140

for a single marker. Clearly, the development and employment of fluorescent markers with similar time constants facilitate the system design from a practical point of view.

However, using the best parameters (t_p,D) for each marker may not be necessary. Figure 5.11 shows s_N in the neighborhood of the optimal parameter set (t_p,D) for each of the 6 markers M1-M6 is calculated using Eqn. 5.12. One can notice the relatively large plateau around the points optimal for every marker and that the function is convex. Therefore, taking parameter sets in the neighborhood of the optimal point will not result in a large decrease of s_N.

The selection of the best parameter set (t_p,D) to use in the measurement system should also be guided by the following considerations. First, since s_N of all markers (with different time constants τ) cannot simultaneously be maximized, (t_p,D) should be selected to maximize s_N of the most expensive marker(s). The emission of the less expensive markers can then be increased by increasing their concentrations in the plastics. Second, one can select the parameter set that maximizes s_N of the marker with the weakest fluorescence emission intensity. Third, when LEDs are used as excitation light sources. They usually can be overdriven in pulsed mode, i.e. supplied with a forward current several times higher than allowed in continuous mode, thus emitting more light and in turn increasing the intensity of the emitted marker fluorescence and the value of s_N. The main prerequisites for the overdrive are short pulses t_p and small duty cycles D. A significant overdrive of the LED using the markers' optimal pulsing parameters (e.g. marker M1: $t_p = 4000$ μs and $D = 50\%$) is thus not possible. However, for pulse durations and duty cycles smaller than the optimal values, the typical decrease of s_N (see Fig. 5.11) might be more than counterbalanced by an overdriven LED, depending on the overdrive factor.

In general, the shorter the pulses and the smaller the duty cycle, the higher the LED overdrive factor can be. At high overdrive factors, however, nonlinearities and saturations effects may occur. Theoretically, the forward current through an LED is limited by the maximum power dissipation this LED can withstand. For larger pulse durations (and thus larger average power dissipation) an overdriven LED will fail due to thermal damage in the die itself, typically at internal junction temperatures exceeding the allowed maximum [91]. At smaller pulse durations high current densities additionally heat the bonding wires which in turn raise their electrical resistance limiting the maximal sustainable current. Reducing the pulse duration even further while increasing the forward current leads to a melting of the bonding wires and LED failure. Another significant risk of pulsing is too short rise times of the forward current, which may damage the LED electronics.

Different commercially available LEDs have different overdrive capabilities. Thus, when

Table 5.2: Comparison of the TGFS intensity values s_N modeled with: (1) optimal (t_p, D) according to Eqn. 5.13 and no LED overdrive, and (2) $t_p = 10$ μs and $D = 10\%$ and forward current overdrive factor 10 (which causes an 8-fold increase of the excitation light intensity).

Marker	M1	M2	M3	M4	M5	M6
Maximum s_N in %	100	100	100	100	100	100
$s_N(10\,\mu\text{s}, 10\%)$, in % of s_N	33	45	43	38	38	34
Overdrive $8{\times}s_N$, in % of s_N	264	360	344	304	304	272

selecting the LEDs, attention must be paid to the allowed overdrive factors, pulse durations, and duty cycles. For a specific LED, the two-dimensional function $\eta(t_p, D)$, where η is the multiplicative overdrive factor, is to be multiplied with the two-dimensional function $s_N(t_p, D)$ in order to get the achievable "overdriven" digitized intensity value for different values of t_p and D. Such a function $\eta(t_p, D)$ is, however, barely practical, since it would require either an accurate physical/mathematical model of the particular LED, or extensive (and expensive) empirical tests with different t_p and D in order to figure out the damage thresholds of the LEDs. Such detailed information is usually not provided by the LED manufacturers. For the UV-LED used in this work (see Chapter 6), overdrive factors for a few specific values of t_p and D were provided by the manufacturer on request. A high (full frame) digitized intensity value s_N can be achieved using $t_p = 10$ μs and $D = 10\%$ and a forward current overdrive factor 10. A current overdrive factor $\eta(10\ \mu\text{s}, 10\%) = 10$ results in an excitation light intensity increased by approx. factor 8 (see Fig. 6.6).

For example, for marker M1 (which has the largest time constants $\tau_d \approx \tau_r \approx 4000$ μs), s_N achieved with $t_p = 10$ μs and $D = 10\%$ without LED overdrive is approx. 33% of the maximum value possible with the best parameters $t_p = 5030$ μs and $D = 50\%$ (according to Fig. 5.11). With the maximum LED current overdrive factor 10, the (full frame) digitized intensity value s_N becomes $8 \times 33\% = 264\%$ of the one that can be achieved with $t_p = 5030$ μs and $D = 50\%$ without overdrive. For the other markers M2-M6, s_N exhibits similar behavior (see Table 5.2): with $t_p = 10$ μs and $D = 10\%$ and the LED current overdrive factor 10, s_N is higher than with the best parameters (t_p, D) but no overdrive. For this reason, $t_p = 10$ μs and $D = 10\%$ with a current overdrive factor 10 was selected for the measurements carried out with the system prototype (Chapter 7).
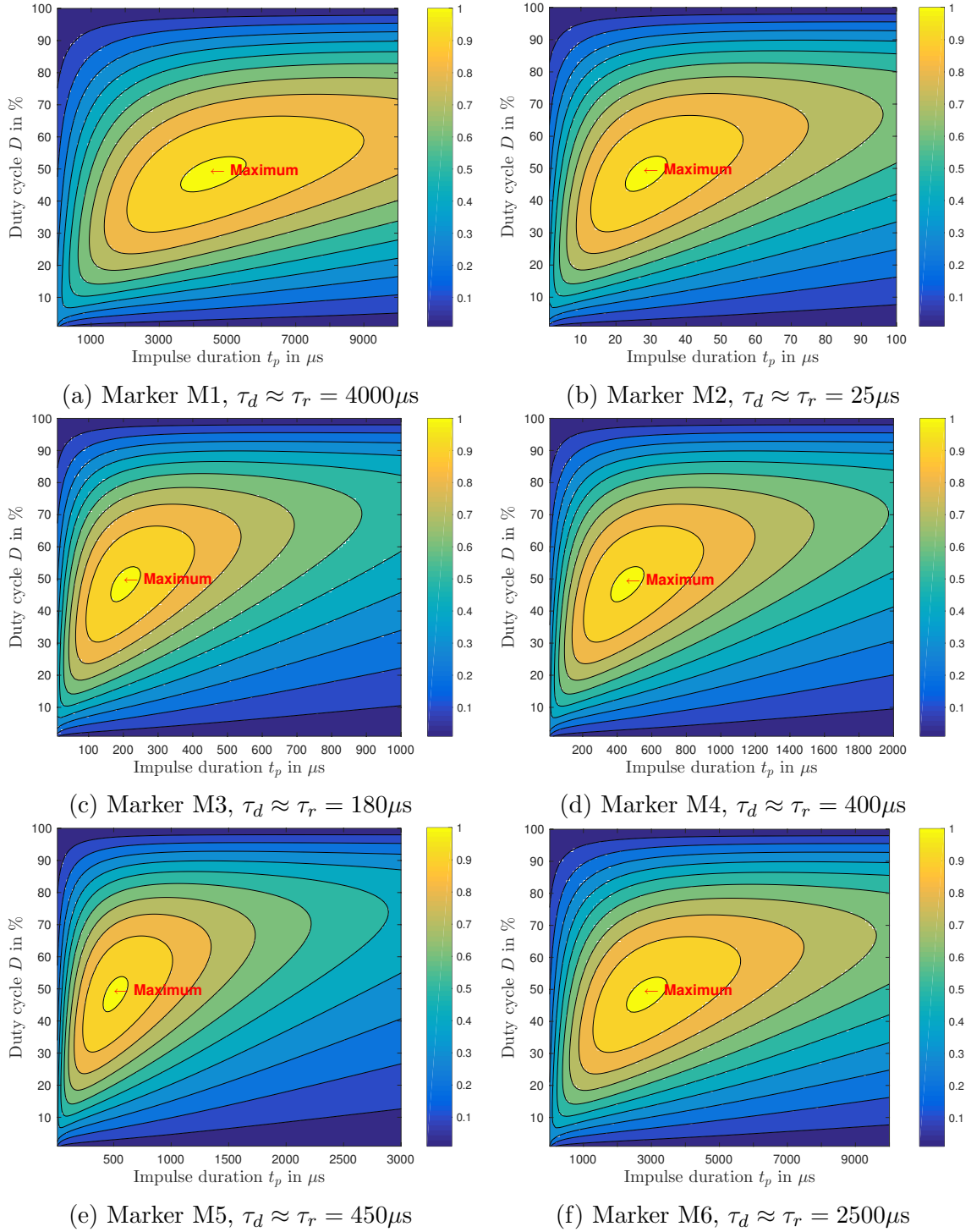
Figure 5.11: The digitized fluorescence intensity value s_N modeled according to Eqn. 5.12 as function of t_p and D for all 6 investigated fluorescence markers M1-M6. s_N of each marker is normalized to its individual maximum. The contour lines represent steps with 10% (95%, 85%, ... 5%).

Chapter 6

Measurement and classification system concept and prototype

In this chapter, the concept of the developed measurement and classification system prototype is outlined. The goal is to set up a system capable of classifying up to 63 different fluorescently labeled plastics and evaluate it in practice. The composition of the prototype encompasses hardware and software components. The former is outlined in Sections 6.1 and 6.2, whereas Section 6.3 presents the latter. Experimental measurements and results are presented in Chapter 7.

6.1 Hardware setup

The concept of the whole sorting approach consists of 3 functional parts: (1) plastic flakes feeding system with a singulation unit and a conveyor belt; (2) measurement and classification system; (3) plastic flakes sorting machinery. The design of the whole system is depicted in Fig. 6.1 and the actual prototype is shown in Fig. 6.2. The feeding system (1) and the sorting machinery (3) were developed by an external partner and are only briefly described here.

The purpose of the feeding system is to supply plastic flakes to the measurement and classification system. Investigation of flakes produced by typical industrial plastic waste mills has shown that their sizes vary between approx. 3 mm and 10 mm and follow almost a Gaussian size distribution around the mean value of approx. 5 mm. Some outliers were also present. Flakes smaller than approx. 3 mm and bigger than 10 mm are increasingly difficult to handle during the sorting phase. Additionally, small flakes contribute less to the overall mass throughput. Therefore, flakes are first separated into 3 groups: group 1 contains flakes with diameter 3 mm – 6 mm (small), group 2 contains flakes with diameter 6 mm – 8 mm (middle) and group 3 contains flakes with diameter 8 mm – 10 mm (big). The separation is achieved by passing all flakes through a system of mechanical filters, which sorts out flakes larger than 10 mm and smaller than 3 mm and groups the remaining flakes.
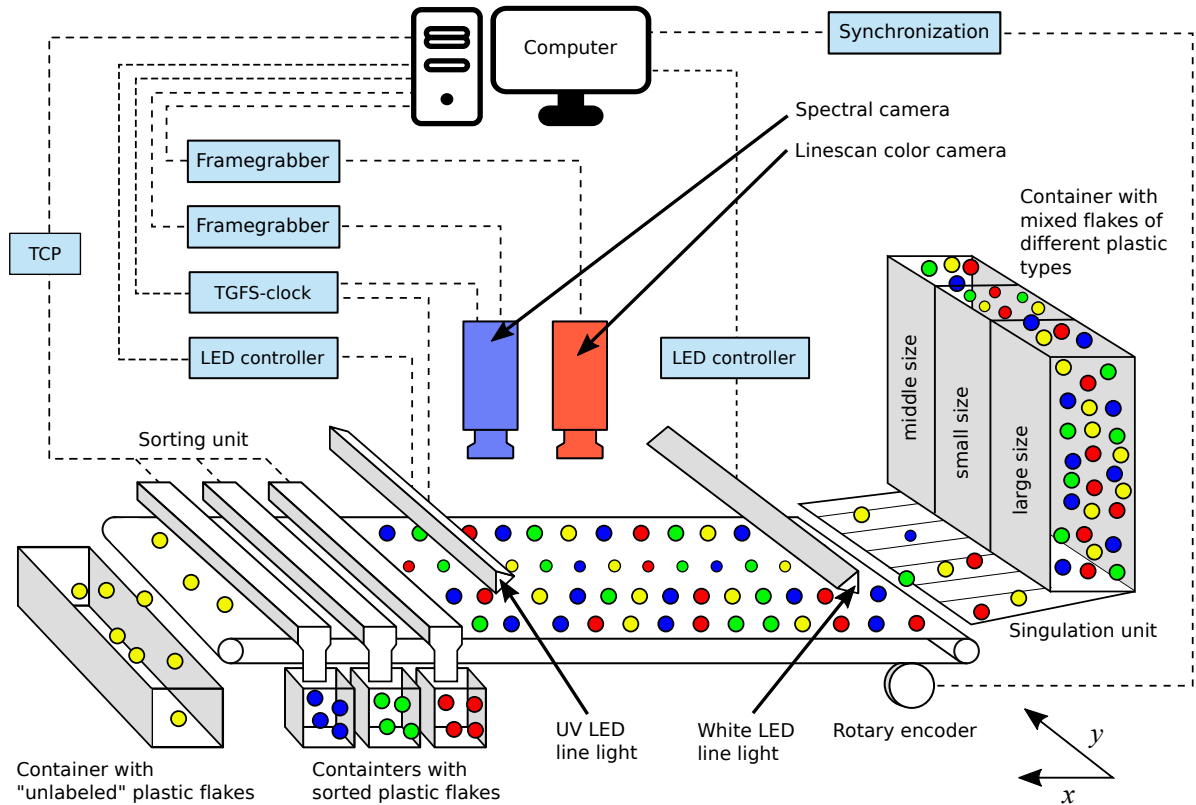
Figure 6.1: Design of the plastics classification and sorting system.

The plastic flakes are then passed through the singulation unit, whose purpose is to singulate and distribute flakes in parallel streams on the conveyor belt. The singulation unit consists of a shaker plate with overall 50 grooves for 50 channels (streams) of flakes. Processing plastic flakes in 50 parallel streams essentially increases the overall number of flakes processed by the system per unit time and thus helps increase the systems throughput a great deal (see Section 6.2). In order to improve the singulation performance, the width of the grooves in the shaker plate was adjusted to match the size of the flakes it should contain. Therefore, there are six 8 mm grooves for small flakes, twenty-two 9 mm grooves for middle flakes, and twenty-two 11 mm grooves for big flakes. The overall width of the singulation unit is 500 mm and equals the width of the conveyor belt. The small grooves are located in the middle of the plate and hence in the middle of the conveyor belt. Thus, when the smallest plastic flakes are delivered to the measurement system, they are positioned in the central region of the optical field of view (FOV) where the spatial resolution of both cameras is the highest. In order to prevent damage to the optical components of the measurement system due to the vibrations, the singulation unit is mechanically decoupled from the conveyor belt. Figure 6.3 depicts the system of mechanical filters and the singulation unit.

50 parallel streams of singulated plastic flakes are delivered on the conveyor belt to the measurement and classification system. A closed dark chamber shelters the measurement
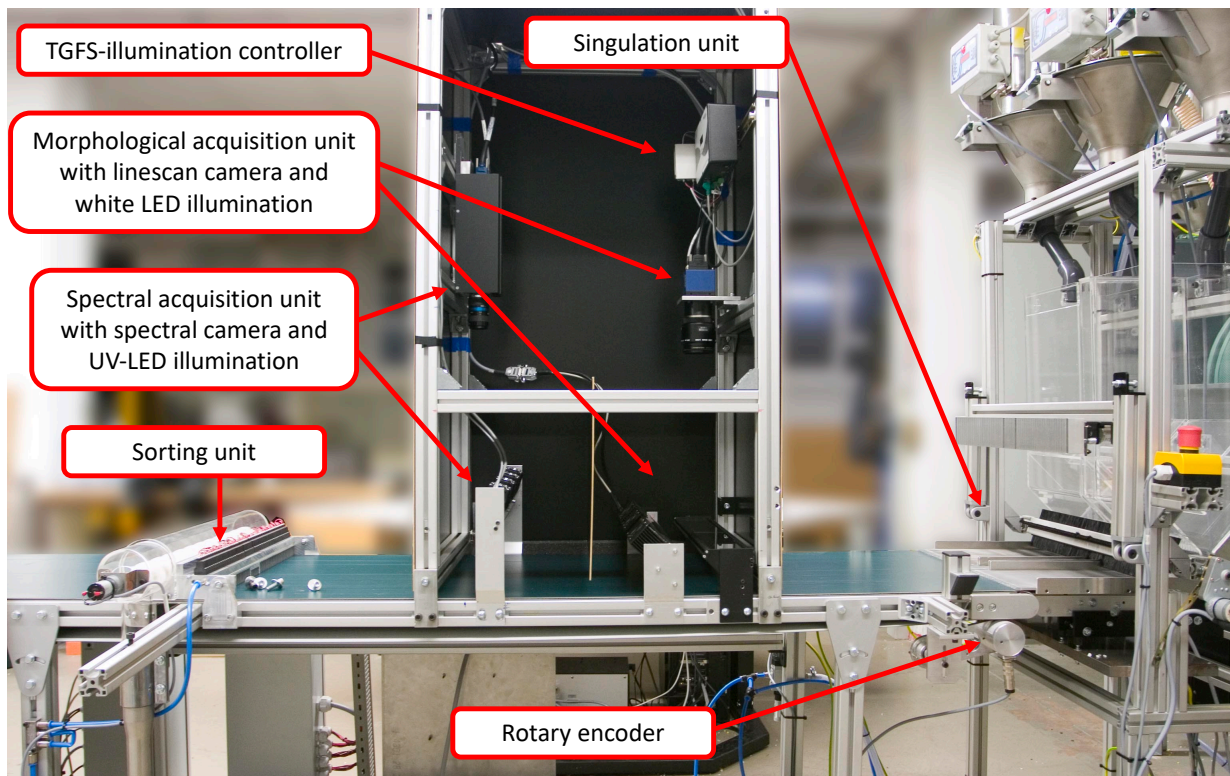
Figure 6.2: Prototype system. The singulation unit produces 50 parallel streams of singulated plastic flakes on the conveyor belt. The measurement and classification system consists of the morphological acquisition unit and the spectral classification unit. After passing the measurement and classification system, flakes are extracted from the conveyor belt by suction nozzles of the sorting unit according to their type (class).

system from surrounding (stray) light (see Fig. 6.2 where the chamber is opened for demonstration purposes). The inside of the chamber is painted black for maximum absorption of reflected excitation light.

The system consists of two main elements: the spectral acquisition unit for the measurement and classification of fluorescent spectra emitted from the plastic flakes and the morphological acquisition unit for the assessment of the geometrical properties of the plastic flakes such as size and position on the conveyor belt. The need for an auxiliary system for morphological data acquisition is dictated by the relatively low spatial resolution of the spectral acquisition unit, especially in the x-axis along the conveyor belt (see Section 6.2).

6.1.1 Morphological acquisition unit

Morphological data acquisition is carried out by a linescan color camera with 4096 pixels $10\,\mu\text{m}\times10\,\mu\text{m}$ across the conveyor belt (y-axis) and up to 9 kHz frame rate. The camera is mounted at 462 mm working distance over the conveyor belt in order to capture all 50 channels across the 500 mm wide conveyor belt using a 35 mm lens. With this configuration,

<div align="center">(a)   (b)</div>

Figure 6.3: Singulation unit of the prototype system. (a) The system of filters to group plastic flakes by size can be seen in the background; containers with already grouped flakes and the shaker plate are in the foreground. (b) A close-up of the shaker plate with 50 grooves to separate plastic flakes in 50 parallel streams (channels) on the conveyor belt. Plastic flakes are all yellow for demonstration purposes.

the optical resolution of the linescan camera is approx. 120 μm in both spatial directions, which allows capturing morphological information of the plastic flakes with great precision. The linescan camera provides a 2D image of the conveyor belt by scanning it line by line and combining those lines. The camera is triggered by the signal from the rotary encoder of the conveyor belt. The rotary encoder delivers a trigger signal every 100 μm of movement in x-direction, which allows the precise definition of the flakes x-position on the conveyor belt. Synchronization of the line acquisition with the movement of the conveyor belt helps achieve equidistant sampling in the x-direction and thus equal pixel size in the 2D image in the x-direction. Due to synchronization with the rotary encoder, the frame rate of the camera depends on the conveyor belt velocity.

A white LED line light focused on a line approx. 13 mm wide (FWHM) is used as a light source in the morphological data acquisition unit. In order to reduce shadows from the plastic flakes, which are highly disadvantageous for image processing and can affect the derived morphological information of the flakes, a mirror system guiding the light beam coaxially to the camera's field of view was set up. The schematics of the mirror system can be seen in Fig. 6.4. A half-transparent mirror is located at a 45 degree angle to the LED line light and to the conveyor belt, so that the illumination light reflected by the mirror falls normally to the conveyor belt illuminating the flakes from the top. The camera captures the reflected light through the half-transparent mirror and the optical window. Polarization filters are mounted in front of the LED line light and on the lens of the linescan camera. The polarization filter on the linescan camera can be rotated in order to tune polarization and increase the image contrast. With this setup shadows and direct light reflections from the conveyor belt can be reduced. The downside of the mirror system is that due to the half-transparent mirror, maximum 1/4 of the initial LED emission intensity reaches the

camera (provided 100% reflectance coefficient of the flakes). This disadvantage is, however, by far outweighed by the elimination of shadows, which can otherwise easily be mistaken as flakes.
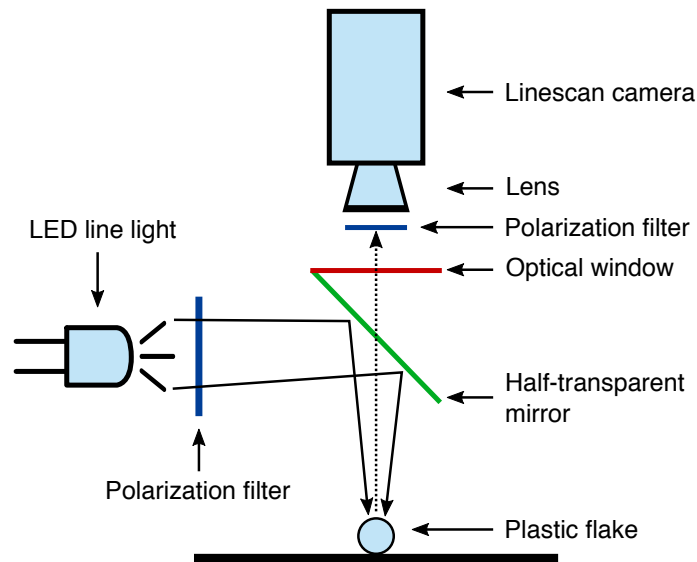
Figure 6.4: Mirror setup to direct the LED illumination coaxially to the camera's field of view. The setup consists of a half-transparent mirror mounted at 45 degree to the optical axis of the LED lamp and the conveyor belt and an optical window.

6.1.2 Spectroscopic acquisition unit

The spectroscopic acquisition unit consists of a custom-built spectral camera (Fig. 6.5) and a high-power pulsed UV-LED line light. The spectral camera was built for the application at hand and has the necessary TGFS frame accumulation mode (see Section 5.3). The principle of spectral cameras was discussed in Chapter 3. The applied camera uses a wide-angle lens with a 12 mm focal length to capture the fluorescence emissions across the conveyor belt line by line of the parallel plastic flakes streams. On the front end of the lens, an optical high-pass filter with cut-off wavelength 450 nm is mounted. The high-pass filter is used to suppress the UV excitation light, which is orders of magnitude stronger than the fluorescence emissions and might otherwise saturate the camera or disturb the marker fluorescence spectra. The high-pass filter is not absolutely necessary when TGFS measurements are carried out with excitation light that is always off during the image acquisition. However, some remnants of the excitation light (afterglow) might still be present during image acquisition due to the exponential decay of the LED emission in practice and/or imperfect timing of the TGFS process.

The lens of the camera focuses fluorescent emission light from the scan line across the conveyor belt on the entrance slit of the PGP imaging spectrograph. The spectrograph
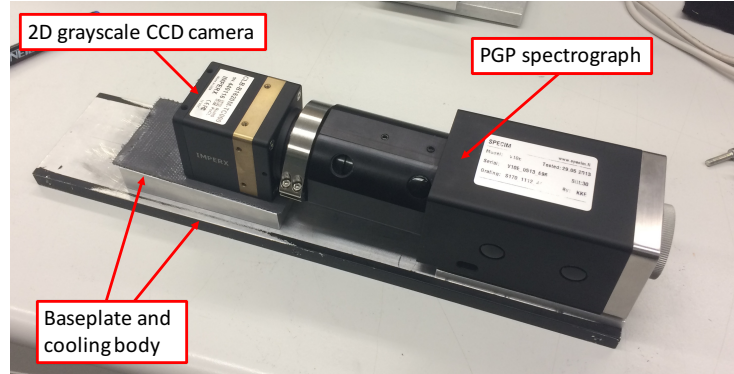
Figure 6.5: Custom-built spectral camera with removed protecting shell for demonstration purposes.

disperses the light of the visual and near-infrared (VNIR) wavelengths between 400 nm and 1000 nm and projects it onto the imaging sensor. The applied spectrograph achieves a spectral resolution of approx. 2.8 nm with an entrance slit width 30 μm, which is a good compromise when acquiring marker spectra with spectral bandwidth between approx. 10 nm and 20 nm (see Section 2.4.2).

The heart of the spectral camera is a grayscale CCD imaging sensor with 1600 (horizontal) $\times$ 1200 (vertical) pixels of $7.4 \, \mu\text{m} \times 7.4 \, \mu\text{m}$ size. The horizontal dimension of the sensor represents the imaged spatial line across the conveyor belt and the vertical dimension contains the spectral information of each pixel in that line. Thus, the camera allows simultaneous acquisition of 1200 spectral samples between 400 nm and 1000 nm across the 500 mm wide conveyor belt providing the spectral sampling of 0.5 nm. The camera supports vertical (i.e. spectral) and horizontal (i.e. spatial across the conveyor belt) binning up to factor 8 (see Section 3.4). For TGFS measurements the camera's frame rate and readout time are the most critical parameters. Short read out time T_R allows to accumulate a larger number N of subframes and results in a larger sensor signal s_N (see Chapter 5). As explained in Chapter 3, the frame rate of the CCD camera depends on the number of vertical lines (pixels) to read out. In the full frame mode, i.e. when all 1200 vertical pixels are used, the applied camera can only achieve a frame rate of 44 Hz. With vertical binning 8, the number of vertical lines is reduced to 150 and the corresponding frame rate is increased to approx. 170 Hz. A further increase of the frame rate can be achieved by selecting a vertical region of interest (ROI). The spectrograph's active wavelength band is 400 nm – 1000 nm; yet, in the application at hand, emission spectra of all 6 fluorescent markers are located in the wavelength band 450 nm – 750 nm (see Fig. 2.6b). Discarding wavelength bands below 450 nm and above 750 nm further reduces the number of relevant vertical pixels that need to be read out to 75 and increases the frame rate to approx. 225 Hz with corresponding $T_R \approx 4.4$ ms. With these parameters, the spectral camera can acquire up to 360 000 spectra per second. The spectral sampling becomes approx. 4 nm, which is worse than the spectrograph's spectral resolution, but is sufficient for a reliable classification according to the simulation results shown in Section 4.9.5 and is a good compromise

with respect to the S/N ratio, (low) marker concentrations and (high) measurement rates. Similarly to the morphological unit, the spectral camera is synchronized with the rotary encoder signal.

As fluorescence excitation light source a UV-LED line light with 395 nm central wavelength and approx. 10 nm FWHM is employed. The availability of high-power UV-LED line lights on the market is rather poor: the LED emission in the UV wavelength band is usually weak due to physical limitations. Although not optimal, sufficient excitation of all 6 markers simultaneously is possible with the selected LED with 395 nm central wavelength (see Section. 2.4.2). The selected LED line light produces an irradiance of approx. 650 W/m^2 with continuous forward current 0.6 A, i.e. with no overdrive. With forward current overdrive factor 10 (6 A) in pulsed operation mode, the irradiance of approx. 5200 W/m^2 is produced, which is an increase of factor 8. Figure 6.6 shows the measured irradiance produced by the LED line light as a function of the forward current in pulsed mode.

The UV LED line light is positioned vertically at a small angle to the spectral camera's viewing axis and is focused on a 4-mm wide line. In contrast to the morphological acquisition unit, where the loss of the intensity of the reflected light due to the double passing through the half-transparent mirror is justified by the reduction of unwanted shadows, utilizing a similar mirror system in the spectroscopic unit would reduce the intensity of already very weak fluorescence emissions too much. Additionally, shadows from the flakes on the conveyor belt (background) do not pose a significant problem for the acquisition of the fluorescence emission. The line light is pulsed by the dedicated controller, which is hardware-triggered by a custom-built electric circuit in order to synchronize the excitation light pulses with the acquisition times of the spectral camera and facilitate the TGFS measurement approach (see Section 5.3).

Once the measurement system had been mounted on the conveyor belt, necessary calibration procedures were carried out. First, both morphological and spectral acquisition units were spatially calibrated in order to accurately map the pixels of both cameras onto the real-world coordinates (x, y). Only with appropriate spatial calibration it is possible to determine the y-position (across the conveyor belt) of plastic flakes on the conveyor belt. Second, flat field correction was performed with both units. Flat field correction of the camera image is necessary to avoid distortions due to lens vignetting, sensor photo-response non-uniformity (PRNU), sensor dark current and fixed pattern noise (FPN) and the light source non-uniformity [56]. The applied linescan camera is supplied with built-in programmed routines for the flat field correction, which is carried out on-chip before the read-out. The spectral camera does not have built-in routines for flat field correction, therefore, the read out image had to be corrected in the software.

Additionally, the spectral camera was spectrally calibrated in order to account for the non-uniform spectral response of the camera pixels and spectrograph. Radiometric calibration was carried out using a calibrated broadband light source. The spectrum of its emission was measured with the spectral camera and the result was compared with the known spectral content of the light source. The radiometric correction was also carried out in the software.
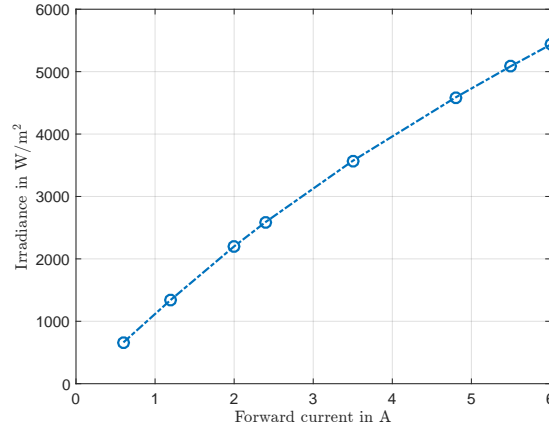
Figure 6.6: Irradiance of light emitted by the LED line light used in the prototype with different values of forward current in pulsed operation mode with $t_p = 10$ μs and $D = 10\%$.

Data streams from both linescan and spectral cameras were transferred via the Camera Link interface to the framegrabbers and processed by the developed software (described below). The software provides the location and class of all plastic flakes and passes these results onto the sorting unit via TCP.

6.1.3 Sorting unit

Based on the information received from the measurement and classification system, the sorting machinery selectively extracts plastic flakes from the conveyor belt according to their plastic types and stores them in separate containers. The sorting unit is set-up as a sequence of arrays with suction nozzles and a transport screw. Each array contains 50 suction nozzles of 3 different sizes according to the 3 size groups of plastic flakes (see Fig. 6.7). The air pressure in the nozzles is optimized to the size of the flakes the nozzle needs to extract. The transport screw is used to move extracted plastic flakes to the associated container. Each array can be programmed to sort out any of the plastic types known to the measurement system. However, each array can be programmed to sort out only a single plastic type at a time. Therefore, for 63 plastic types, 63 arrays are required. At the time of the experimental measurements (described in Chapter 7) only one array was available and therefore only one plastic type could be sorted out with one run-through. Unlabeled plastic flakes are not extracted by the sorting unit and fall off the conveyor belt at its end into a separate container.

6.2 System throughput

The overall mass of plastic flakes that can be processed per unit time, i.e. the mass throughput, depends on various parameters. Due to the low-light conditions of the TGFS
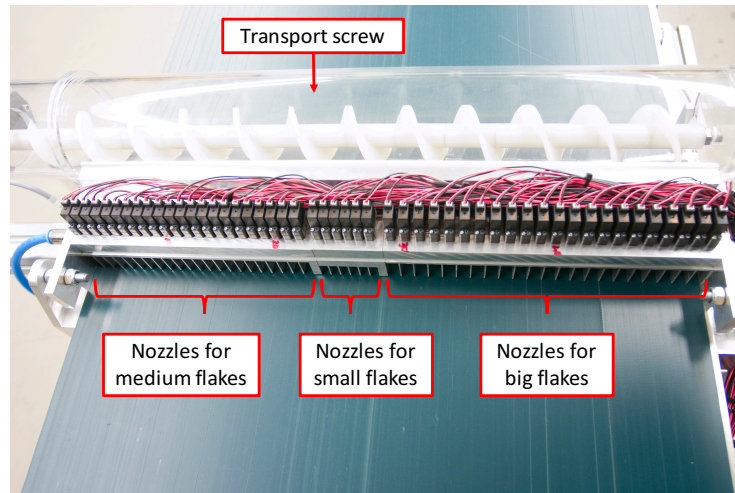
Figure 6.7: Sorting unit array with 50 suction nozzles to extract flakes of a particular plastic type from the conveyor belt. Suction nozzles are separated into groups of 3 different sizes to fit the flake sizes produced by usual industrial plastic mills. The transport screw moves the extracted flakes to the associated container.

fluorescence measurements, especially the measurement rate and thus the time available for the acquisition of the flakes' spectra is critical. Longer acquisition times result in higher S/N ratio of the measured signals, but in lower conveyor belt velocity and thus throughput. For a required mass throughput and for given system parameters, the maximal measurement rate and conveyor belt velocity can be estimated using simple considerations for a fixed focal length lens.

Figure 6.8b depicts the optical path of an ideal fixed focal length lens. The lens projects the object plane (rectangular area of the conveyor belt across its moving direction, see Fig. 3.4) on the image plane (sensor pixel array). Using the focal length F of the lens, all relevant parameters such as the working distance, image size, angular FOV, magnification, etc. can be calculated. F is the distance between the optical center of the lens and the focal point. Larger F results in a larger optical magnification and a smaller opening angle, small F represents wide angle lenses. The formulae used below are valid for a single convex lens. Since most real-life optical systems use a combination of several lenses in order to achieve high image quality, only approximate results can be achieved using the simple formulae for a single lens [46]. These simple formulae, however, allow calculating the working distance correct to several millimeters, which is sufficient here.

From the conveyor belt width and the focal length of the lens, the working distance d necessary to cover the entire width of the conveyor belt is calculated as follows [46]:

$$d = F \cdot (b/b' + 1), \tag{6.1}$$

where b is the object size (width of the conveyor belt) and b' is the image size (width of the imaging sensor), see Fig. 6.8a and 6.8b. With $b = 500$ mm, $b' = 1600 \cdot 7.4$ μm$= 11.84$ mm and $F = 12$ mm, the necessary working distance is thus $d \approx 520$ mm.

Having the necessary working distance d and the spectrograph slit width l' (see Section 3.3), one can find the resulting width l of the spectrograph's imaging line (i.e. the width of the spectrograph's rectangular ROI) on the conveyor belt by replacing b' with the slit width l' and rearranging Eqn. 6.1:

$$l = l' \cdot (d/F - 1). \tag{6.2}$$

With $l' = 30~\mu$m, the width of the spectrograph's imaging line hence is $l \approx 1.27$ mm.

Having the width of the imaging line l and (statistical) knowledge about the plastic flakes' sizes and masses (also see Section 7.1), the conveyor belt velocity and spectral camera's frame rate required for a particular mass throughput can be derived. In this work, relatively moderate mass throughput of 250 kg per hour was specified for the prototype. With the above-mentioned separation of flakes into 3 groups, the average weight of one flake in each group is 60 mg for the small flakes, 70 mg for the middle flakes, and 90 mg for the big flakes. To achieve the 250 kg/h overall throughput, it is, therefore, necessary to process approx. 1150/1050/750 – small/middle/big flakes per second, respectively. Although the size distribution is almost Gaussian, the following calculation will be carried out based upon small flakes since they represent the "worst case". To cover one small flake of size 4.5 mm with an imaging line width of 1.27 mm, $4.5/1.27 \approx 3.54$ lines should be acquired. However, in order to avoid acquiring fluorescence from two adjacent flakes, a minimal space Δl between flakes of one imaging line width should be kept. This means that to appropriately capture one such flake, $3.54 + 1 = 4.54$ acquired lines are necessary. It is easy to derive the required conveyor belt velocity:

$$v_c = 4.54 \cdot l \cdot n, \tag{6.3}$$

where n is the number of flakes to be processed per second. With $n = 1150$ and $l = 1.27$ mm: $v_c = 6630.67$ mm/s. Since plastic flakes are processed with the prototype system in 50 parallel channels, $v_c/50 \approx 132$ mm/s is required.

Knowing the conveyor belt velocity v_c and the width l of the imaging line of the spectral camera, one can calculate the required frame rate simply by: $v_c/l = 132/1.27 \approx 104$ Hz. The corresponding acquisition time is then given by $T_m = 1/104 \approx 9.6$ ms. Therefore, with the given read-out time $T_R \approx 4.4$ ms (see Section 6.1), there are $T_m - T_R = 5.2$ ms left for the required TGFS subframe accumulation. As described in Chapter 5, optimal TGFS parameters for all 6 utilized fluorescent markers are pulse width $t_p = 10~\mu$s, duty cycle $D = 10\%$ and hence the duration of one subframe is $t_p/D \cdot 100 = 100~\mu$s. With this setup, the accumulation of $N = 52$ subframes for TGFS measurements is thus possible.

6.3   Software setup

The software for data acquisition, storage, and processing was developed in National Instruments LabVIEW$^{©}$ with the Vision Acquisition [92], Vision Development [93, 94] and Multicore Analysis and Sparse Matrix toolkits [95, 96]. The software concept encompasses
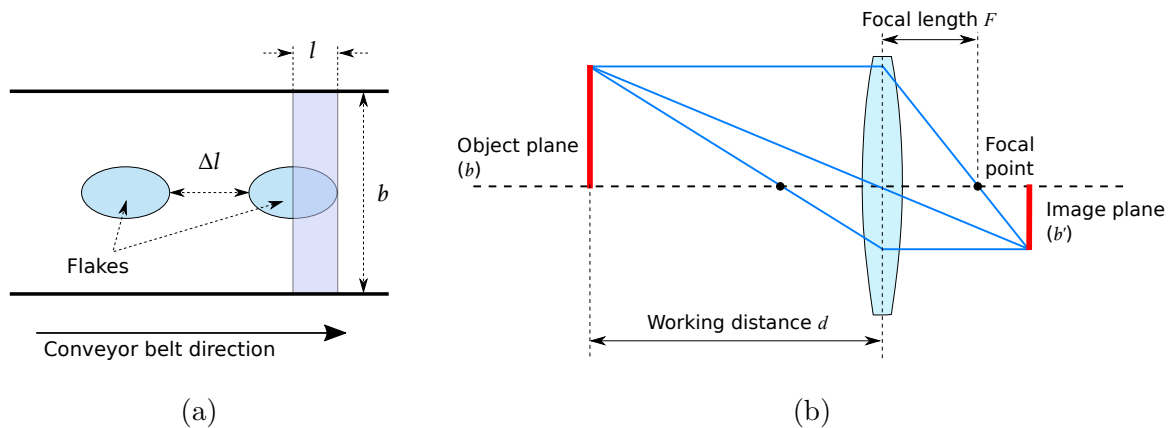
Figure 6.8: (a) Geometric parameters for spectral acquisition. The shaded rectangular area corresponds to the imaging line (ROI) of the spectral camera. (b) Optical paths of a convex lens. The object plane represents the conveyor belt and the image plane corresponds to the sensor pixel array.

a highly parallel structure of overall 7 separate low-level modules for hardware control, data acquisition, and processing (classification), plus 1 high-level module for user interaction. Communication between the modules is realized via the LabVIEW queue mechanism [97]. All modules are synchronized using the signal from the rotary encoder installed on the conveyor belt; the spectral acquisition module and the UV line light are additionally triggered by an external hardware clock to facilitate TGFS. Figure 6.9 illustrates the block diagram of the developed software modules.

Modules (1) and (2) are responsible for the morphological and spectral image acquisition, respectively. Calibration (see Section 6.1) and adjustment of camera-related parameters are also carried out in these modules. Additionally, modules include subroutines to control the illumination hardware. It should be noted that even with reduced spectral sampling due to binning 8, the spectral camera produces large amounts of data. One spectral image contains 1600×75 single-precision floating-point values and is thus approx. 469 kB large. Considering the necessary frame rate of 104 Hz, the spectral camera produces almost 48 MB/s. In order to avoid information loss due to inappropriate timing or OS events, the data from both cameras are first passed to the buffers of the data storage modules (3) and (4). There, it is extracted from the buffers and saved in binary format on the hard drive as a backup. These data can later be read by the acquisition modules and emulate the online mode for debugging.

Module (5) performs morphological image processing and analysis using the linescan camera data. The module detects plastic flakes on the conveyor belt and determines their sizes and positions. Particular care is taken with respect to the inhomogeneities of the conveyor belt, specifically scratches (can be seen in Fig. 6.3b and 6.7). Due to the movement of the conveyor belt, most of the scratches are oriented along the conveyor belt and can be identified using edge detection approaches. Derived morphological information
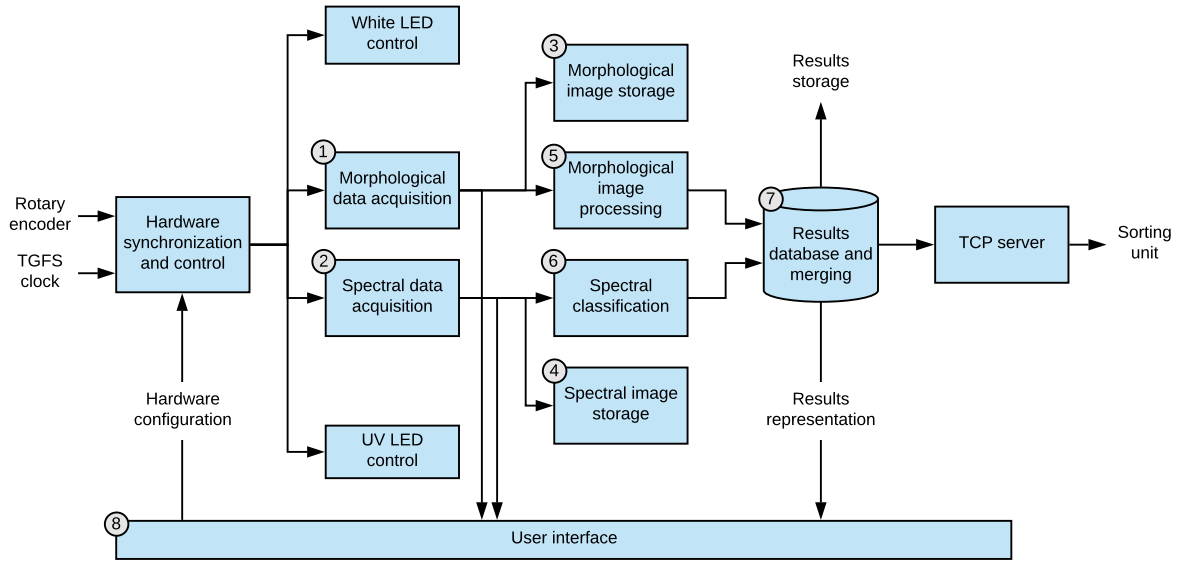
Figure 6.9: Block diagram of the software concept developed in LabVIEW. The software controls the entire hardware of the prototype, carries out data acquisition (modules (1) and (2)), storage (modules (3) and (4)), image processing (5), spectral classification (6), and functional and morphological information merging (7) in a parallel fashion. Classification results and morphological information are forwarded to the sorting unit via the TCP and stored on the hard drive for later analysis. The user interface module enables a live display of images from both morphological and spectral acquisition units as well as online monitoring of the classification. Adjustment of hardware parameters, calibration procedures, and control of the acquisition is also performed in the user interface module (8). Communication between modules is realized via the LabVIEW queue mechanism.

is passed to module (7), where it is stored in a dedicated database.

Module (6) carries out the classification of the acquired fluorescence spectra. The goal of this module is to assign each and every plastic flake delivered on the conveyor belt to one of the 63 known classes. The module implements several classification algorithms that were described in Chapter 4 including SCC, ED and MLC and feature extraction methods like PCA, LDA and unconstrained LSMA. In an online application, the numerical complexity of the algorithm plays a critical role. Since there are only $T_m \approx 9.6$ ms available for processing of 1600 spectra (i.e. 1600 pixels in the spatial domain across the conveyor belt), only 9.6 ms/1600 = 0.006 ms is left for the classification of each spectrum. If spectra are processed one by one (i.e. not in parallel), the classification algorithm should run very fast at a rate of larger than $1/0.006$ ms ≈ 166 kHz. Employing complex algorithms such as NN or SVM might thus be not affordable from the timing perspective. Utilizing the LabVIEW's Multicore Analysis and Sparse Matrix Toolkit together with numerically efficient algorithms helps accelerate the classification process.

The derived functional information (i.e. classes of the plastic flakes) is then sent to

the database in the module (7), where it is merged with the morphological information. The result is forwarded to the sorting unit via TCP. According to the class and position of the flake on the conveyor belt, the control software of the sorting unit activates the right suction nozzles at the required corresponding time instants.

For debugging purposes and offline classification with different algorithms as well as performance evaluations, the database is stored on the hard drive. The statistical evaluation of the acquired data and classification performance evaluation are carried out in MATLAB©.

The user interface module (8) provides the user with a means to interact with the hardware (configuration, calibration, control, etc.) and monitor the classification in real-time.

Chapter 7

Experiments and simulations

This chapter presents the results of test measurements and classification performance investigations for the developed system prototype and is organized as follows: in Section 7.1 the most important aspects of the measurement campaign are discussed; classification results achieved with the measured spectra of 14 fluorescently labeled plastics are presented in Section 7.2. In Section 7.3 simulations are employed to model spectra of additional 49 plastics and extend the classification performance investigations to the scenario with 63 plastics (i.e. 63 marker combinations, see Table A.1 in appendix A); Section 7.4 presents a special practical case when markers are split into two groups and investigates the idea of how to use one marker as a parity bit to increase the classification performance.

7.1 Experimental setup

For the experiments, 14 marker combinations were incorporated in 10 different plastics (also see Section 7.3). Table 7.1 shows the assignment of marker combinations to the plastics. The plastics are mostly POM and are of particular interest in the manufacturing of high-quality plastic parts. In order to experimentally investigate the possibility to encode additional information other than the plastics type using fluorescent markers (e.g. customer ID, production charge, etc.), four plastics (Delrin 500NC010 white, Hostaform C13031 white, Hostaform C13021 white, and Lexan LS2J-111 transparent) were used twice in this experiment and labeled with two different codes. In order to decrease re-absorption of the marker fluorescence by the hosting plastics and associated shape changes of the fluorescence spectra [40], markers were carefully assigned based on the color of the plastics. In order to ensure the production of plastics with representative mechanical and chemical properties, professional industry-scale extruders were used. Marker concentrations were adjusted in an attempt to equalize the fluorescence peak intensities of different markers within each marker combination and achieve comparable fluorescence intensities with all plastics (see Section 4.9.4). Concentrations between 500 ppm and 2000 ppm were used with markers M1, M4, and M6, whereas concentrations up to 4000 ppm were necessary with markers M2, M3, and M5 due to their lower fluorescence emission.

Table 7.1: Assignment of combinations of markers M1-M6 to the 14 plastics.

Decimal code/ Class	Markers/Binary code						Plastic		
	M1	M2	M3	M4	M5	M6	Name	Type	Color
1	0	0	0	0	0	1	Delrin 500NC010	POM	white
3	0	0	0	0	1	1	Duracon SW-01PS	POM	white
4	0	0	0	1	0	0	Hostaform C13021	POM	white
5	0	0	0	1	0	1	Delrin 500NC010	POM	brown
9	0	0	1	0	0	1	Tornoform T300MW4	POM	white
10	0	0	1	0	1	0	Hostaform C13031	POM	white
17	0	1	0	0	0	1	Lexan LS2J-111	PC	transparent
18	0	1	0	0	1	0	Hostaform C13021	POM	white
24	0	1	1	0	0	0	Hostaform C9021M	POM	white
27	0	1	1	0	1	1	Delrin 500NC010	POM	white
32	1	0	0	0	0	0	Hostaform C13031	POM	green
33	1	0	0	0	0	1	Hostaform C13031	POM	white
36	1	0	0	1	0	0	Delrin 500NC010	POM	yellow
37	1	0	0	1	0	1	Lexan LS2J-111	PC	transparent

Overall, approx. 5 kg of each of the 14 plastic types were produced, resulting in approx. 70 kg of fluorescently labeled plastics. To produce representative plastic flakes, extruded labeled plastics were first molded in solid objects and then ground using an industrial plastics mill. Figure 7.1 shows flakes of Delrin 500NC010 in brown labeled with the code "000101" (class 5) and of Hostaform C13010 in white labeled with the code "001010" (class 10). The size of the flakes typically varies between approx. 3 mm and 9 mm, as can be seen in the histograms in Fig. 7.2. A small number of outliers – dust or large plastic chunks – was discarded. In Fig. 7.3 plastics flakes can be seen on the conveyor belt in the measurement system (described in Chapter 6).

When carrying out a classification performance test, it is important to be able to verify decisions made by the system in order to accurately estimate the number of false decisions and thus the values of TPR and PPV (see Section 4.8). One necessary condition is that the plastic type of each and every measured flake is known a priori, otherwise, it becomes impossible to determine whether flakes assigned to a class by the system actually belonged to this class or not. Yet, this condition is difficult to achieve in practice: plastics of different types can have a virtually identical appearance and it is thus impossible for the experimenter to distinguish between them using e.g. a simple optical inspection procedure. Since for an extensive statistical evaluation thousands of flakes need to be investigated (see below), it is impossible to manually inspect and count every single flake. When a realistic

<table>
<tr><td>(a)</td><td>(b)</td></tr>
</table>

Figure 7.1: Typical plastic flakes produced by an industrial mill. (a) "Delrin 500NC010 Brown" labeled with the code "000101" (class 5). (b) "Hostaform C13031 White" labeled with the code "001010" (class 10).

mixture of flakes of all plastic types is delivered on a conveyor belt, the verification of the classification decision made by the system is thus not possible in practice.

This problem was solved here by measuring plastic types separately one after another instead of a mixture of different plastics. In this case, it is exactly known which type of plastic flakes are on the conveyor belt. However, two particular situations are not considered by this approach. First, in the case of the mixture of different plastics, the acquisition of the spectra of two or more adjacent flakes that belong to different plastics may occur due to the finite optical resolution of the spectral acquisition system. The measured fluorescence spectrum would contain a mixture of spectra of two or more different plastic types depending on how many plastic types were in the field of view (FOV). Such to the system unknown spectrum cannot be classified correctly, which leads to decreased TPR and PPV values. This effect can be decreased with a minimum distance Δl between adjacent flakes on the conveyor belt (see Section 6.1). In practice, however, it does not work 100% perfect.

Second, apart from the limitations due to the optical resolution, a similar effect may occur with two or more not properly singulated flakes of different plastic types. In this case, the measurement system will "see" one object consisting of different parts, each of which with its own fluorescence spectrum. The classification of such objects can be problematic.

Both described situations may occur if a mixture of different plastics is delivered on the conveyor belt since the singulation machinery does not work 100% perfect in practice. Clearly, neither of the situations is possible when only flakes of one plastic type are used. However, provided that flakes are correctly singulated, measuring one plastic type at a time is virtually identical to measuring their mixture.
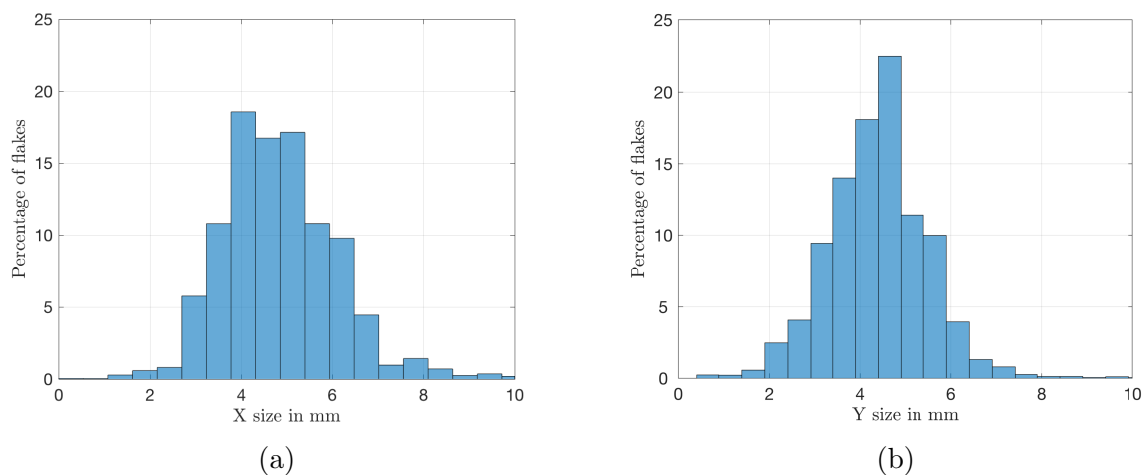
Figure 7.2: Histograms of the sizes of measured plastic flakes: (a) X (axis along the conveyor belt, see Fig. 6.1) and (b) Y (axis across the conveyor belt).
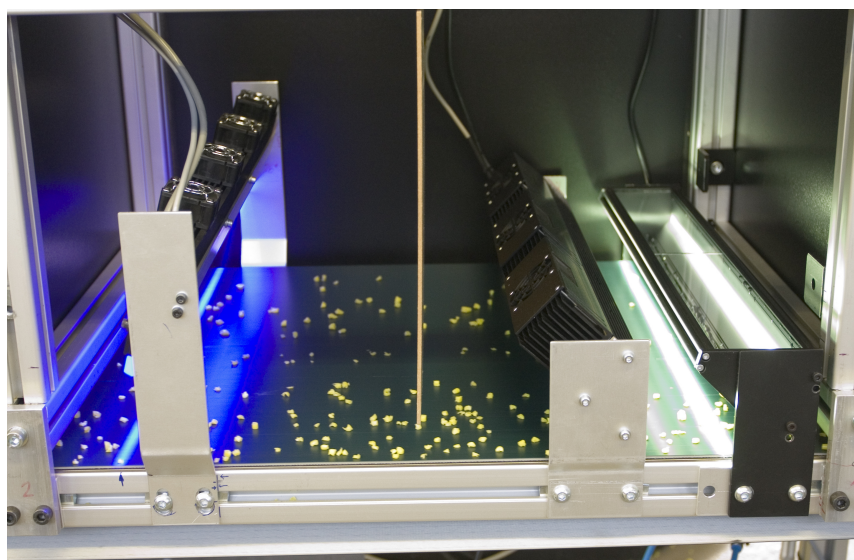
Figure 7.3: Flakes of Delrin 500NC010 in yellow labeled with the marker combination "100100" (class 36) being processed by the system prototype. The flakes enter from the right side where morphological data are acquired with the linescan camera under white LED illumination and leave the system on the left side where fluorescence spectra are acquired under UV LED illumination.

Proper singulation is mandatory for the sorting machinery as well: if two or more flakes of different plastic types are located too close to one another on the conveyor belt, even if the measurement system succeeds to correctly identify the "connected group" as separate flakes, an accurate physical sorting is impossible. In such a situation the sorting unit either would have to skip such group of flakes (which would decrease the plastics recovery

rate TPR), or attempt to sort such flakes (which inevitably would result in extracting several adjacent flakes of different plastics types from the conveyor belt and moving them to the same container, thus decreasing the plastics' purity PPV). Since correct singulation is crucial not only during the test phase but also under real-life sorting conditions, the classification of groups of flakes of mixed plastic types is irrelevant. Hence, measurement of plastics separately one after another, as carried out here, yields results very similar to those expected in industrial practice.

7.1.1 Statistical considerations

Assessing classification performance requires a blind and fair experiment. The most important part of such an experiment concerns data that should be unbiased, representative, and sufficient. The following conditions should be fulfilled:

1. Plastic flakes used in the experiment should be representative of the entire flakes' population (sample quality).

2. For 6 fluorescent markers, all $2^6 - 1 = 63$ possible marker combinations should be present in the experiment (sample quality) if all 63 marker combinations are expected to be present in practice.

3. The number of flakes of each plastic type should be equal or similar (sample size).

4. The number of flakes of each plastic type in the experiment should be sufficient (sample size).

The first condition implies that the performance assessment of the system prototype should be carried out using flakes very similar to those that are expected to be seen in practice. In other words, the portion of flakes used in the experiment (the sample) should be drawn randomly from the entire population of flakes.

The second condition is tightly linked to the first one and requires that flakes of all plastics expected to be seen in practice should be present in the experiment (representative data).

The third condition is necessary in order to avoid a bias towards any of the plastics. As Eqns. 4.36 and 4.35 suggest, this condition is not strictly necessary if the macro-averaged versions of TPR and PPV are used. However, having an equal number of flakes of each type simplifies the interpretation of the confusion matrices (see also appendix F) and helps achieve similar or at least comparable confidence intervals for all plastics (see below).

Condition number 4 must hold in order to achieve a statistically significant estimation of the classification performance. A common way to estimate statistical significance is to use confidence levels and confidence intervals. Having only a sample of limited size (limited number of flakes), one can only find an estimate $\hat{\theta}$ of the parameter of interest θ (such as the classification performance metrics TPR and PPV) of the entire population. Confidence levels tell how probable it is that the true value of parameter θ lies within the estimated

confidence interval $[\,\hat{\theta} - c;\ \hat{\theta} + c\,]$. The value c is called the margin of error and is calculated using the estimate $\hat{\sigma}^2$ of the population variance σ^2 [98]:

$$c = \frac{Z \cdot \hat{\sigma}}{\sqrt{n}}, \tag{7.1}$$

where Z is the fractile of the normal standard distribution corresponding to the desired confidence level, and n is the sample size (number of flakes in the experiment).

In case when the parameter θ is a real number, such as for example the average flake size, $\hat{\sigma}^2$ is usually approximated by the square of the empirical standard deviation s^2 of the sample data. However, the goal of the experiments described in this chapter is to estimate the classification performance metrics TPR and PPV, which both are in essence proportions of correctly classified flakes (TP) to either all flakes (TP+FN) in case of TPR, or to all detected flakes (including false alarms, TP+FP) in case of PPV. Furthermore, each member of the sample, i.e. each flake, can be considered as a dichotomous variable: the flake is classified either correctly (1) or incorrectly (0).[1] In this case, $\hat{\sigma}$ is approximated by [98]:

$$\hat{\sigma} = \sqrt{\hat{\theta} \cdot (1 - \hat{\theta})}. \tag{7.2}$$

Combining Eqns. 7.1 and 7.2 results in:

$$c = Z \cdot \sqrt{\frac{\hat{\theta} \cdot (1 - \hat{\theta})}{n}}. \tag{7.3}$$

Equation 7.3 gives the margin of error for a qualitative estimation of the population proportion [99]. If the margin of error is given, one can rewrite Eqn. 7.3 and find the sample size n (number of flakes) necessary to achieve this margin of error with the desired confidence level:

$$n = \frac{Z^2 \cdot \hat{\theta} \cdot (1 - \hat{\theta})}{c^2}. \tag{7.4}$$

According to Eqn. 7.4, the sample size n depends on the expected population parameter estimate $\hat{\theta}$ (i.e. expected TPR or PPV), the desired confidence level (Z-value) and the desired margin of error c. Generally, $\hat{\theta}$ (TPR or PPV) is unknown prior to the experiment. However, for a worst-case estimation, $\hat{\theta} = 0.5$ (50%) can be taken, since then $\hat{\theta} \cdot (1 - \hat{\theta})$ reaches its maximum thus maximizing n. Z depends on the desired confidence level and is taken from a table for the standard normal distribution [98]. Depending on the application, most commonly used confidence levels are 90%, 95% and 99%, with corresponding Z-values 1.64, 1.96 and 2.58. In the experiments described in this chapter, 95% confidence level with the maximum margin of error $c = 0.01$ (1%) is specified. This means, that in the worst-case scenario ($\hat{\theta} = 0.5$), the 95% confidence interval is 50% $\pm$ 1%. Substituting $\hat{\theta} = 0.5$, $c = 0.01$ and $Z = 1.96$ in Eqn. 7.4 gives $n = 9604$, which is thus the necessary minimum sample

---

[1]Incorrect classification includes overlooked or missed flakes as well as those falsely classified.

size (number of flakes) for the experiment. Clearly, as Eqn. 7.3 suggests, for other values of $\hat{\theta}$ the same sample size n will result in a smaller margin of error for the same confidence level. More realistic values required in practice should be larger than $TPR = 95\%$ and $PPV = 95\%$ and result in a margin of error $c = 0.0044$ (0.44%) with sample size $n = 9604$. For an almost perfect classification performance with $TPR = 99\%$ and $PPV = 99\%$, the margin of error becomes $c = 0.0020$ (0.20%).

In the experiments the rounded value $n=10\,000$ was used. With $TPR > 95\%$ and $PPV > 95\%$ the actual margin of error thus is $c \approx 0.43\%$. With $TPR = 99\%$ and $PPV = 99\%$ the actual margin of error is $c \approx 0.20\%$.

7.2 Experimental results

This section presents the results of the experiment carried out in this work. Section 7.2.1 shows the results of the measurement of spectra of the 14 labeled and 1 unlabeled plastics. Section 7.2.2 presents the classification performance investigation achieved with the measured spectra. Section 7.2.3 discusses the classification performance in black plastics.

7.2.1 Measurement results

Overall, more than 150 000 (10 000 × 14 fluorescently labeled and 10 000 unlabeled) flakes were investigated. In order to increase the measurement rate of the spectral camera and the S/N ratio of the measured spectra, spectral binning by a factor of 8 was used and only wavelengths between 450 nm and 750 nm were acquired. Thus, each measured discrete spectrum had $\Lambda = 75$ wavelength samples. Due to the binning and thus increased measurement rate of approx. 104 Hz and shorter camera's read-out time of $T_R \approx 4.4$ ms (see Section 6.2), $N = 52$ subframes could be acquired during each TGFS measurement with the pulsing parameter set to $t_p = 10$ μs and $D = 10\%$.

In the following, plastics labeled with marker combinations will be referred to as "classes", numbered according to the decimal code of the marker combinations given in Table 7.1. Figures 7.4 and 7.5 depict the average fluorescence emission spectra of the 14 investigated classes acquired with the measurement system prototype, the spectra are normalized for better presentation. Even though an effort was made to equalize the relative fluorescence emission peak intensities of the markers by adjusting their individual concentrations in the different plastics, in many cases the relative marker peak intensities still differ from one another. Especially marker M6 has at least 5 times higher peak intensity in comparison to the other markers in classes 3, 9, 17, 27, 33, and 37.

Mean values and standard deviations of the S/N ratio (see Eqn. 3.3) of the acquired spectra of the investigated flakes are shown in Table 7.2. As can be seen, the average S/N ratio of all classes is higher than 10 dB which is the minimum value derived in Chapter 4 required for highly reliable classification. However, as the standard deviations between 3 and 4 dB indicate, the S/N ratio of a small number of flakes actually drops below the 10 dB margin. Thus, the classification of those flakes can be problematic. The global average
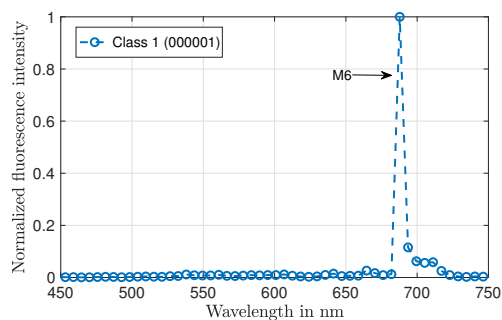
(a) Class 1 (code "000001").
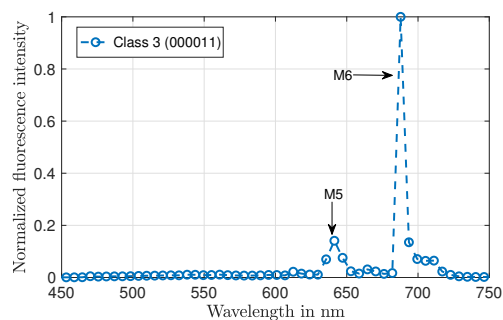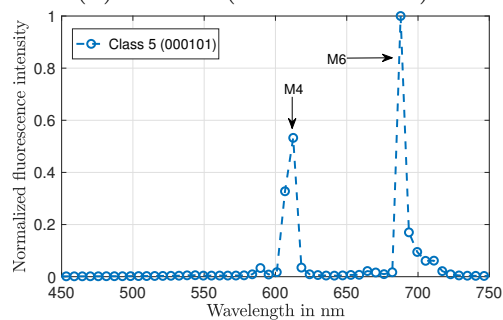
(b) Class 3 (code "000011").

(c) Class 4 (code "000100").

(d) Class 5 (code "000101").
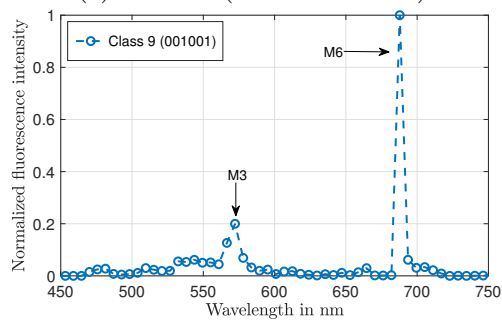
(e) Class 9 (code "001001").)
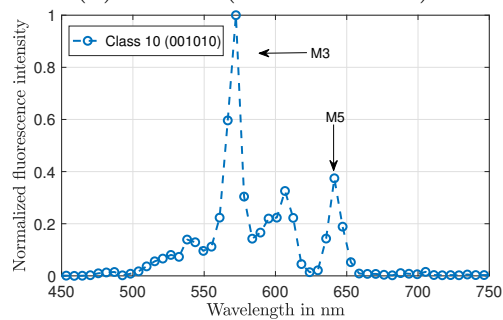
(f) Class 10 (code "001010").
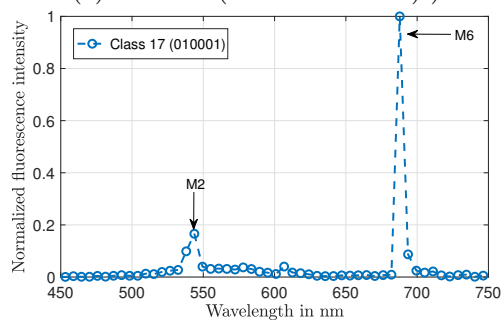
(g) Class 17 (code "010001").
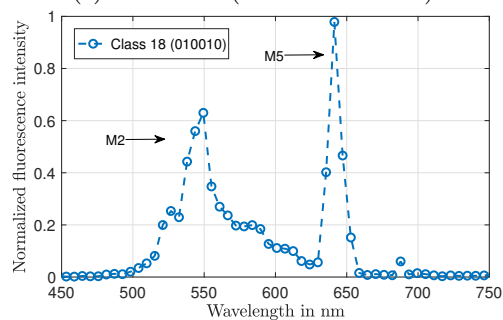
(h) Class 18 (code "010010").

Figure 7.4: Normalized measured emission spectra of fluorescently labeled plastics (classes 1 to 18, see Table 7.1). The shown spectra are averaged over all 10 000 flakes within each class.
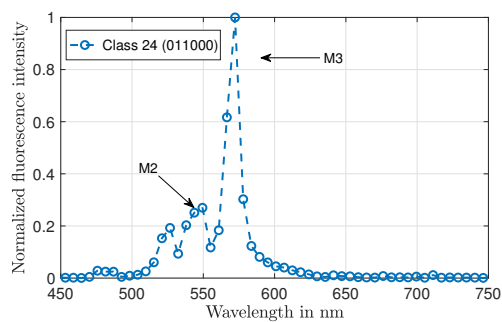
(a) Class 24 (code "011000").
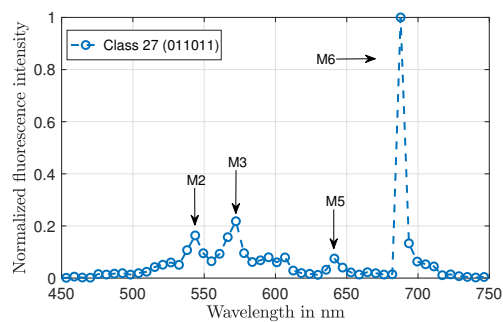
(b) Class 27 (code "011011".
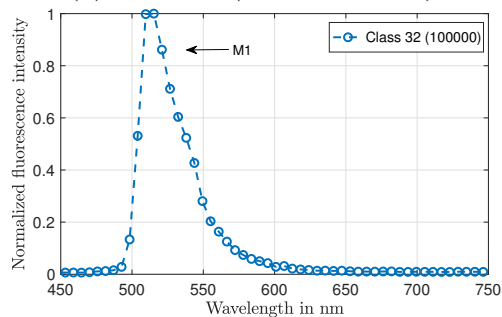
(c) Class 32 (code "100000").
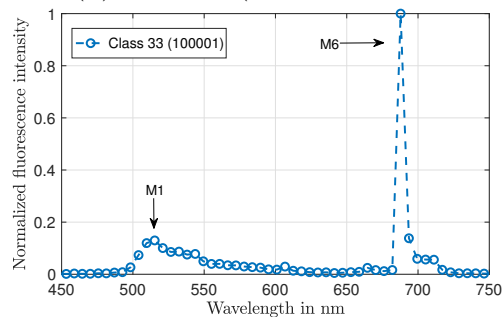
(d) Class 33 (code "100001").
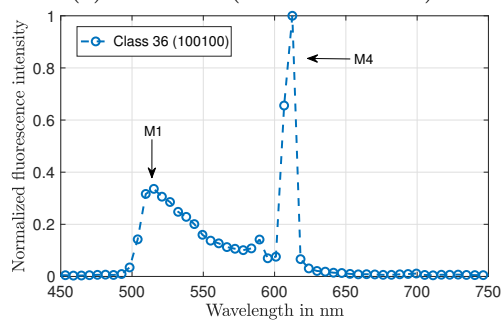
(e) Class 36 (code "100100").
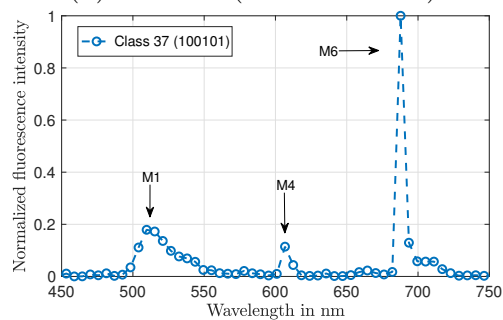
(f) and class 37 (code "100101").

Figure 7.5: Normalized measured emission spectra of fluorescently labeled plastics (classes 24 to 37, see Table 7.1). The shown spectra are averaged over all 10 000 flakes within each class.

Table 7.2: Mean values (S/N mean) and standard deviations (S/N SD) of the S/N ratio in dB of the acquired spectra of the investigated flakes.

Class	1	3	4	5	9	10	17	18	24	27	32	33	36	37
S/N mean	26.3	22.0	22.6	25.9	19.6	19.9	22.6	18.7	21.3	24.4	16.7	24.4	17.6	23.5
S/N SD	4.1	3.9	4.0	3.8	3.6	3.3	3.5	3.7	3.7	3.7	2.9	3.6	3.2	3.7

of the S/N ratio over all 14 classes is approx. 21.8 dB. Distributions of the S/N ratio of each class can be found in Fig. D.1 in Appendix D and provide a detailed insight into the situation.

The measurements also identified a practical problem: it turned out, despite using professional extruders, the relation between the peak intensities of the markers is not constant within each class and varies from flake to flake. Figure 7.6 shows the situation for class 27 (code "011011"). Histograms in Fig. 7.6a-7.6c show fluctuations of the intensities of markers M2, M3, and M5 relative to the intensity of marker M6 in the spectra of all 10 000 investigated flakes of class 27. In order to reduce the influence of noise, the intensity values in the histograms were averaged over two neighboring samples (discrete wavelengths) around the peak intensity wavelength. As can be seen, intensity fluctuations of roughly 5% occurred (SD value). This results in spectra that look different while they actually belong to the same class. The "minimum spectrum" and the "maximum spectrum" (in terms of the peak intensities of the individual markers) of class 27 are shown in Fig. 7.6d. In the minimum spectrum, the spikes corresponding to the markers M2, M3, and M5 are 20 to 30 times smaller than the spike of marker M6. Especially in the presence of noise, it is very problematic to distinguish such spectrum from the one belonging to class 1 (code "000001") with marker M6 only (compare with Fig. 7.4a). This problem can only occur with classes that contain two or more markers and is probably due to the marker incorporation process. Figure D.2 in Appendix D shows histograms of relative marker intensity fluctuations within other measured plastics. Intensity fluctuations of about 5-10% occurred in the other plastics.

7.2.2   Classification results with 14 measured classes

Classification of the measured fluorescently labeled plastic flakes was here carried out using the SCC algorithm (see Section 4.2.3) and the classification decision was made based on the maximum SCC_i value, where $i = 1, 2, ..., C$ is the class label. Since with 6 markers $C = 63$ classes exist, the classifier had to decide from 63 classes, i.e. each measured spectrum was compared with 63 reference spectra (see the binary coding scheme in Table A.1 in Appendix A). In order to improve the purity of the resulting material and sort out unlabeled plastics or those labeled with "wrong" (e.g. counterfeit) fluorescent markers, a threshold T was set for the SCC_i value. Flakes with SCC_i values less then T were assigned to class 64 "unlabeled". The value T was chosen according to the following considerations.

As mentioned in Section 4.8, two classification performance metrics are used in this
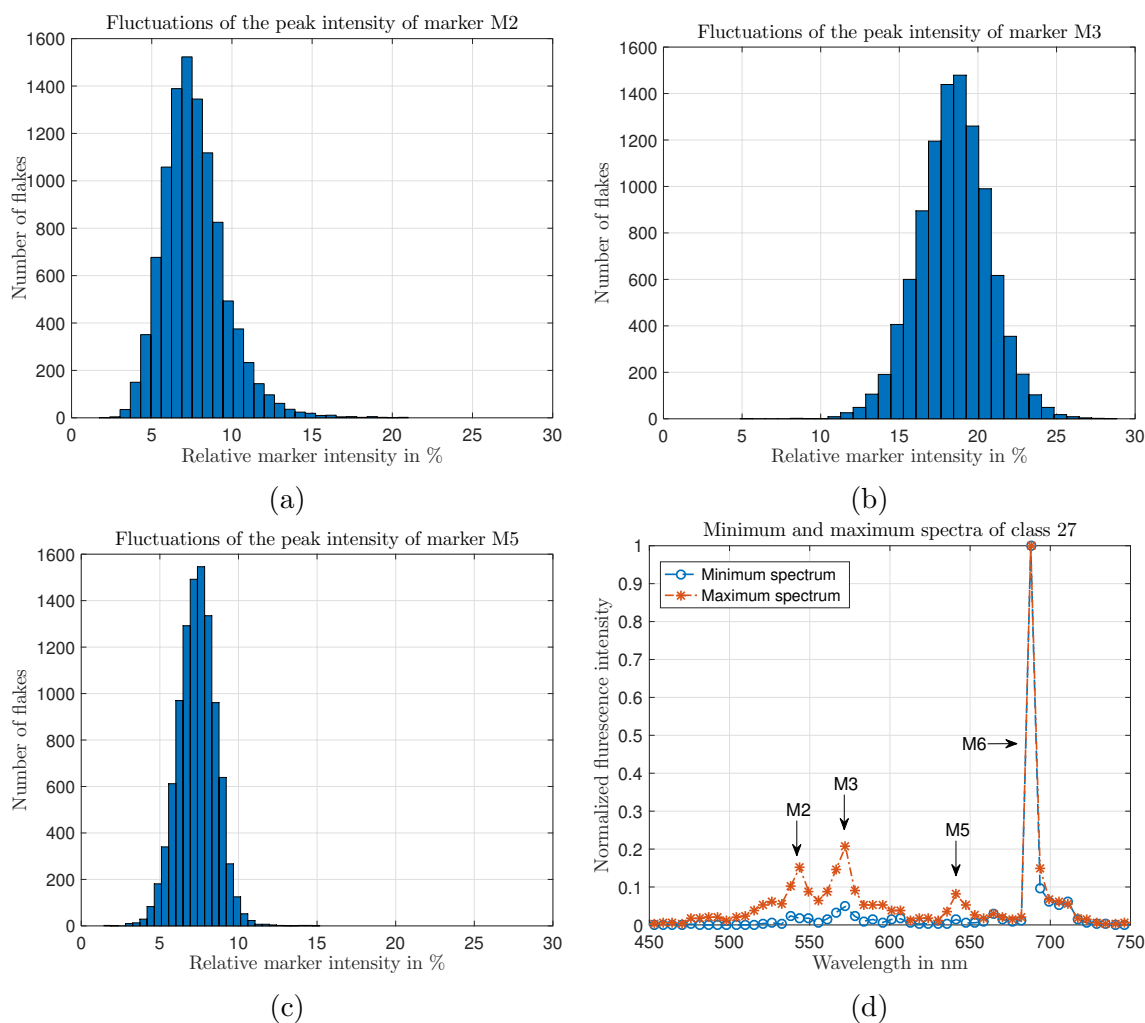
Figure 7.6: Histograms of the peak intensities of markers (a) M2, (b) M3, and (c) M5 relative to the peak intensity of marker M6 in the spectrum of class 27 (code "011011"). (d) Maximum and minimum spectra of class 27 in terms of the (peak) intensities of the individual markers.

study: TPR and PPV. In terms of plastics recycling, the former can be thought of as the recovery rate, i.e. percentage of the total amount of plastics correctly classified and sorted by the system; the latter represents the purity of the resulting recycled plastic material. Although different situations may require different priorities, it is reasonable to assume that purity of the resulting material is of utmost priority in plastics recycling, while recovery rate is secondary [4]. Under this assumption the choice of the threshold value T becomes straightforward: choose T to maximize PPV while keeping TPR at acceptable levels.

Figure 7.7 shows the mean TPR_M and PPV_M (macro-averaged) values derived from the 140 000 measured spectra of the 14 fluorescently labeled plastics flakes as function of the threshold T. As can be seen, T values between approx. 0.75 and 0.9 lead to large PPV
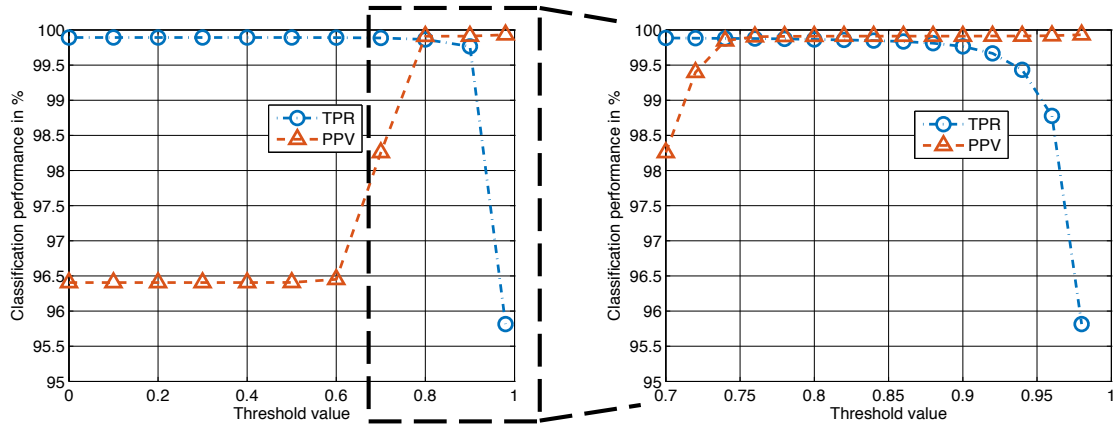
Figure 7.7: Classification performance (TPR_M and PPV_M macro-averaged over 14 classes) as function of the threshold value T.

values. In this range of T, TPR_M only changes by approx. 0.1%, which is less than the margin of error (approx. 0.20%, see Section 7.1.1). This behavior can be better understood using the histogram of the SCC_i values of the measured spectra of all 150 000 investigated flakes shown in Fig. 7.8. Most of the values lie between approx. 0.9 and 1, and apparently correspond to the labeled flakes (14 relevant classes). A small number of SCC_i values are distributed around $\text{SCC}_i = 0.7$, and mostly correspond to the unlabeled flakes (i.e. class 64). Hence choosing the threshold T between approx. 0.75 and 0.9 leads to large PPV. Since according to Fig. 7.7, TPR decreases above $T \approx 0.9$, $T = 0.85$ is used in the following.

Classification results of the 14 fluorescently labeled plus one unlabeled plastics are summarized in Fig. 7.9. The vertical bars depict individual TPR_i and PPV_i values of each class ω_i. TPR_i and PPV_i values of all classes except class 64 lie between 99% and 100%, which proves a really high performance, but still not all flakes were correctly classified. A deeper insight into the reasons for particular misclassifications can give the so-called confusion matrix, which not only shows what percentage of flakes belonging to a specific class were misclassified, but also what particular class those flakes were incorrectly assigned to. The confusion matrix of the results shown in Fig. 7.9 can be found in Tables F.1-F.2 in Appendix F.

Some particular cases of misclassification require a closer look. According to Fig. 7.9, class 17 (binary code "010001") had the lowest purity $\text{PPV}_{17} = 99.26\%$. As can be seen in Tables F.1-F.2, 12 flakes that belong to class 1 (code "000001"), 33 flakes of class 3 (code "000011"), 27 flakes of class 9 (code "001001") and 2 flakes of class 33 (code "100001") were incorrectly assigned to class 17. The reason for that can be seen in Fig. 7.4 and 7.5 where the fluorescence emission spectra of these classes are shown. All 5 classes have marker M6 in common (see Table 7.1), whereas class 17 additionally has marker M2, class 3 – marker M5, class 9 – marker M3, and class 33 – marker M1. However, those additional
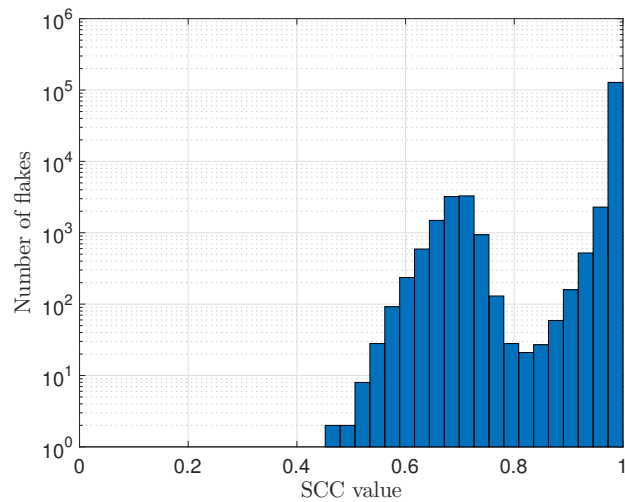
Figure 7.8: SCC values of the measured spectra of 150 000 flakes of 14 labeled and 1 unlabeled classes.
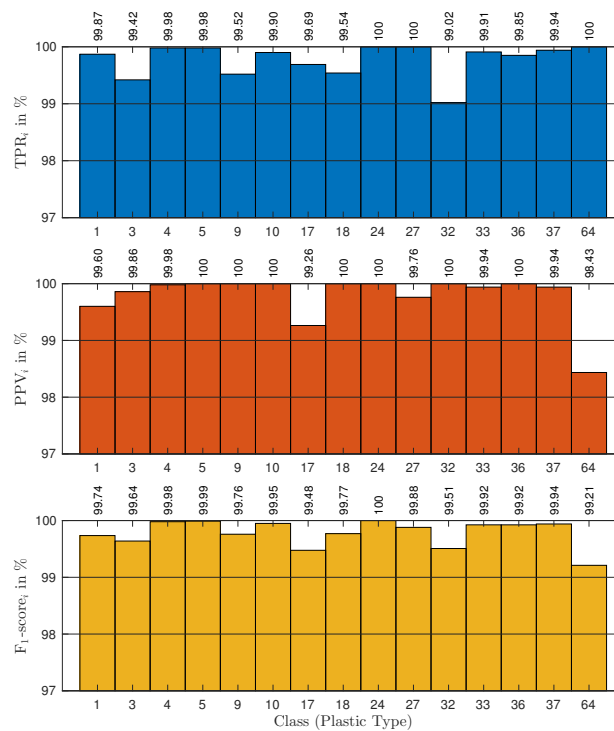
Figure 7.9: Classification performance per class (individual TPR_i and PPV_i) achieved with measured data (see text). Macro-averaged values are $TPR_M = 99.76\%$, $PPV_M = 99.88\%$ and $F_1\text{-score}_M = 99.82\%$.

markers have lower fluorescence emission intensities in comparison to marker M6. As already pointed out, the equalization of the (peak) intensities of different markers helps achieve better classification performance but is an empirical and iterative process. In this experiment, the peak intensity of marker M6 turned out to be about 5 to 7 times larger than the peak intensities of markers M1, M2, M3, and M5 in classes 3, 9, 17, and 33. This does not pose a problem for classification as long as the S/N ratio of the acquired spectra is sufficiently high. For some flakes, however, the marker fluorescence might be extra low, e.g. if the marker concentration of the flake is at its lower limit and/or the flake size is small and/or it is located on the conveyor belt such that a large portion of the excitation light is reflected of its surface. In such situations, the fluorescence of one or more markers might be partially or even fully buried in noise. Markers with larger fluorescence intensities (here M6) will be influenced less than markers with smaller intensities (M1, M2, M3, M5). In other words, in the multidimensional feature space spanned by the flakes' fluorescence spectra, the (spectral) feature vector points into the direction of marker M6 with only small variations due to the other less "strong" markers. Measurement noise might have the same effect and would provoke classification errors. Relative marker intensity fluctuations might aggravate the situation even further (see Fig. D.2).

The same explanations hold true for the 23 flakes actually belonging to class 3 (code "000011") and 17 flakes of class 17 (code "010001") that were falsely assigned to class 1 (code "000001") decreasing its purity to $PPV_1 = 99.60\%$; and 14 flakes that belong to class 17 were assigned to class 3 resulting in $PPV_3 = 99.98\%$. The intensities of both markers M2 and M5 are low compared with marker M6 in these classes.

Similarly, as Fig. 7.4e and 7.5b show, the difference between the emission spectra of classes 9 (code "001001") and 27 (code "011011) is rather subtle: intensities of markers M2 and M5 in class 27 are very low in comparison to the dominant marker M6. Insufficient class separation in the multidimensional (spectral) feature space and low S/N ratio were the reasons that 21 flakes belonging to class 9 were falsely classified as class 27 (see Tables F.1-F.2).

Similarly, spectra of classes 33 (code "100001") and 37 (code "100101") only differ in the small spike of marker M4 present in the latter (see Fig. 7.5d and 7.5f), which in 12 cases was insufficient to distinguish between them: 6 flakes that belong to class 33 were falsely classified as class 37 and 6 flakes that belong to class 37 were assigned to class 33.

An additional reason for the misclassification of some spectra of class 17 may be due to the fact that code 17 was incorporated into the transparent plastic (see Table 7.1). Due to lower absorption of the UV excitation light by the transparent plastic, fewer fluorescent marker molecules get excited and the resulting fluorescence emission is weaker compared to opaque plastics (leading to a small S/N ratio).

Class 32 (binary code "100000") has the lowest $TPR_{32} = 99.02\%$. As can be seen in Tables F.1-F.2, SCC_i values for 98 flakes were below the threshold T and were assigned to class 64. As it turned out, those flakes were smaller than 2 mm in size and thus had an S/N ratio lower than 10 dB. For the same reason 7 flakes from class 10 (code "001010"), 45 flakes from class 18 (code "010010"), and 8 flakes from class 36 (code "100100") were falsely classified as class 64, thus decreasing their individual TPR_i values to 99.90%, 99.54% and

99.85%, respectively.

As expected, due to the thresholded correlation coefficient, class 64 "unlabeled" has the lowest $PPV_{64} = 98.43\%$, which means that 1.57% of all flakes assigned to this class actually belonged to other classes. On the other hand, $TPR_{64} = 100\%$ indicates that each and every of the 10 000 actually unlabeled plastic flakes was correctly classified and therefore not a single unlabeled flake would "cross-contaminate" the labeled plastics.

TPR_M and PPV_M macro-averaged over 14 classes are 99.76% and 99.88%, respectively. Overall, out of 150 000 investigated plastic flakes only 338 were classified incorrectly, which is below 0.3%. What is important, the individual purity (PPV_i) of all 14 relevant classes (i.e. fluorescently labeled plastics) is well above 99%, which is sufficient for a good recycling quality.

These investigations provide valuable insight into the behavior of the measurement and classification system in practice. With regard to classification performance, two main problems with the acquired fluorescence spectra were identified. First, unequal relative peak intensities of the markers can degrade class separability therefore making classification more difficult. Adjusting marker concentrations for each marker-plastic combination (each class) can help reduce or overcome this problem. However, such adjustment is an iterative process requiring several repetitions of plastics labeling production per class (also see Section 2.5). This process might be costly though necessary if the highest possible classification performance needs to be achieved in practice. Another option could be to sacrifice one marker to be employed as a parity bit (see Section 7.4).

The second problem is associated with extra low S/N ratio, which can be the case if flakes are small (here approx. 2 mm) and/or the marker concentration is at its lower limit.

Overall, the experiments have proven that the TGFS measurement approach can successfully eliminate the influence of the AF and that a highly reliable classification of fluorescently labeled plastics is possible in practice.

7.2.3 Classification of black plastics

The classification performance of the developed measurement system had so far been investigated using uncolored or light-colored plastics labeled with fluorescent markers. However, dark colored or even black plastics are of high interest in certain industry fields such as the automotive industry. The main problem with fluorescence-based inspection of black plastics is that they highly absorb the excitation light and emit almost no fluorescence in the visible and NIR wavelength range. Moreover, black plastics absorb photons emitted by the markers such that only a small portion of the stimulated fluorescence emission leaves the surface of the plastics to be captured by the spectral sensor. As a result, the S/N ratios of the measured spectra are very low causing many misclassified or missed flakes. In order to investigate the performance of the developed system prototype with black plastics, marker M6 was incorporated into the commercial black plastic "Delrin 500NC010 Black" using industrial extruders as before. Labeling only with marker M6 corresponds to class 1 (code "000001") in the 6-bit binary coding scheme used here. Due to the high absorbance of the black dye, marker concentrations approx. 5 times higher than with light-colored

plastics were necessary in order to achieve fluorescence emission intensities comparable to those in light-colored plastics.

Since "Delrin 500NC010 Black" was labeled with the same marker M6 as "Delrin 500NC010 White" (see Table 7.1), and both plastics have flat reflectance spectra that do not change the spectral shape of the markers, their fluorescence emission spectra are very similar (see Fig. 7.10a). Therefore, the measured spectra of the black plastic were defined to be class 1 and classified along with the spectra of the 13 plastics of classes 3–37 (see Table 7.1).

Overall, approx. 10 000 flakes of the black plastic were processed. Despite the higher marker concentration, the average S/N ratio of the measured spectra was only approx. 8.6 dB, where spectra of 66 flakes had S/N ratios below 0 dB (see histogram in Fig. 7.10b). Nevertheless, successful classification was possible: only 24 flakes out of the 10 000 were incorrectly assigned to class 17 and the rest correctly to class 1, which corresponds to $TPR = 99.76\%$ and $PPV = 99.60\%$, which is basically equal to that achieved with "Delrin 500NC010 White" in the experiment in Section 7.2.2.

Overall, the successful classification of a black plastic was possible with the developed system prototype. Naturally, a higher marker concentration was necessary with black plastics in order to achieve a classification performance comparable with white plastics. The same results could be achieved for the same marker concentration and decreased measurement rate (lower conveyor belt velocity, longer measurement time, larger number N of accumulated subframes in the TGFS measurements), or increased intensity of the excitation light (see also Section 7.3.4).

7.3   Simulation results

The developed system is able to simultaneously identify up to 63 different plastics labeled with 63 binary combinations (classes) of 6 fluorescent markers. Therefore, in order to thoroughly evaluate the system performance, all 63 plastics should be present in the experiment. However, the production of such a large number of fluorescently labeled plastics in amounts and quality needed for a statistically significant experiment is problematic. Professional industrial plastics extruders that provide representative samples for the experiment can only operate with large amounts of raw material and are expensive to run. Producing plastics in small amounts using laboratory-scale equipment could reduce the costs, but would not guarantee a representative marker incorporation process with sufficient quality. For these reasons, in order to investigate the situation when all 63 plastics are present, simulations with regard to the additional $63 - 14 = 49$ plastics were performed. To achieve the most realistic practical conditions, the simulation parameters were derived from the experimental data of the 14 plastics. In particular, the same number of spectra per class with the same S/N ratios were used in the simulations. Additionally, relative marker intensities were modeled for each class exactly as they were in the experimental data (see Fig. 7.4 and 7.5). Simulations were set up such that the spectra of all markers were resampled in order to match the spectral sampling of the measured spectra (approx. 4 nm).

(a)   (b)
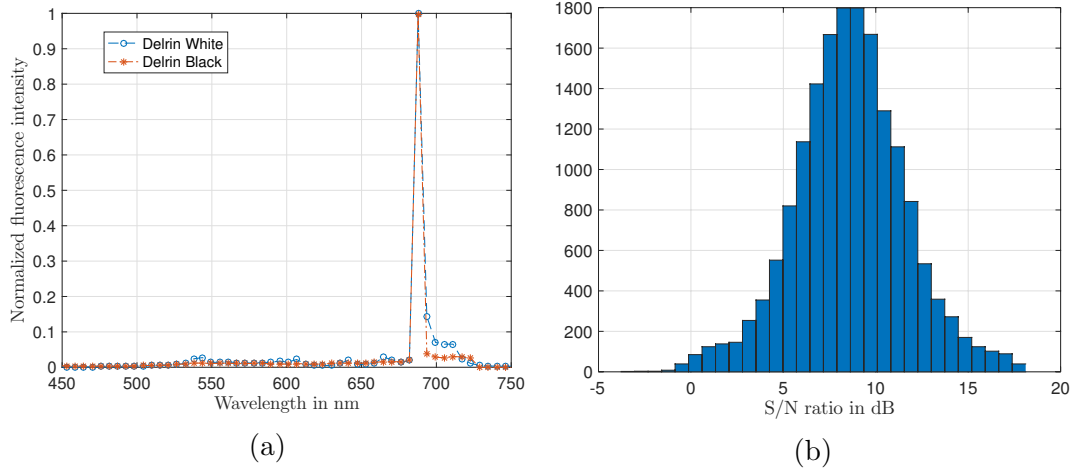
Figure 7.10: (a) Comparison of normalized fluorescence emission spectra of "Delrin 500NC010 White" and "Delrin 500NC010 Black" both labeled with marker M6. The marker concentration for the black plastics had to be 5 times higher compared to the white one. (b) S/N ratio of 10 000 measured spectra of "Delrin 500NC010 Black" labeled with marker M6.

7.3.1 Model validation

To validate the employed simulation model with experimental data, spectra of experimentally investigated 14 marker combinations were simulated as follows. First, all 14 marker combinations were "incorporated" into the plastics as in the experiment by multiplying their fluorescence spectra with the plastics' absorption spectra [40]. Next, the relative marker intensities were adjusted to match those measured in the experiment. In order to achieve the same confidence intervals (see Section 7.1.1) as in the experiment, the same sample size (10 000 flakes per class) was used in the simulations. Finally, the spectra were corrupted with noise most realistic for the prototype (see Section 6.1.2) in order to achieve the same S/N ratios as in the experiments. Examples of the resulting simulated spectra for classes 9 and 27 compared to the measured spectra of the same classes are shown in Fig. 7.11. As can be seen, apart from individual noise realizations, measured and simulated spectra of both classes are in good agreement. Comparison of measured and simulated spectra of all 14 classes can be found in Fig. E.1-E.3 in Appendix E. The measured and simulated spectra of the other classes are too in good agreement.

Figure 7.12a shows classification results achieved with the 14 simulated marker combinations. As can be seen, the results are in good agreement with those achieved in the experiments (see Fig. 7.9). Figure 7.12b depicts the ΔTPR_i, ΔPPV_i and $\Delta\text{F}_1\text{-score}_i$ values – the difference between results in the experiments and in the simulation. The individual TPR_i and PPV_i values of all classes except class 64 "unlabeled" do not differ by more than $\pm0.2\%$ (absolute value), which is equal to the margin of error (see Section 7.1.1). In fact, the difference in the PPV_i values of all classes except #17 and #64 is below $\pm0.1\%$. The biggest difference in the TPR_i and PPV_i values is with classes 17 and 18: in the
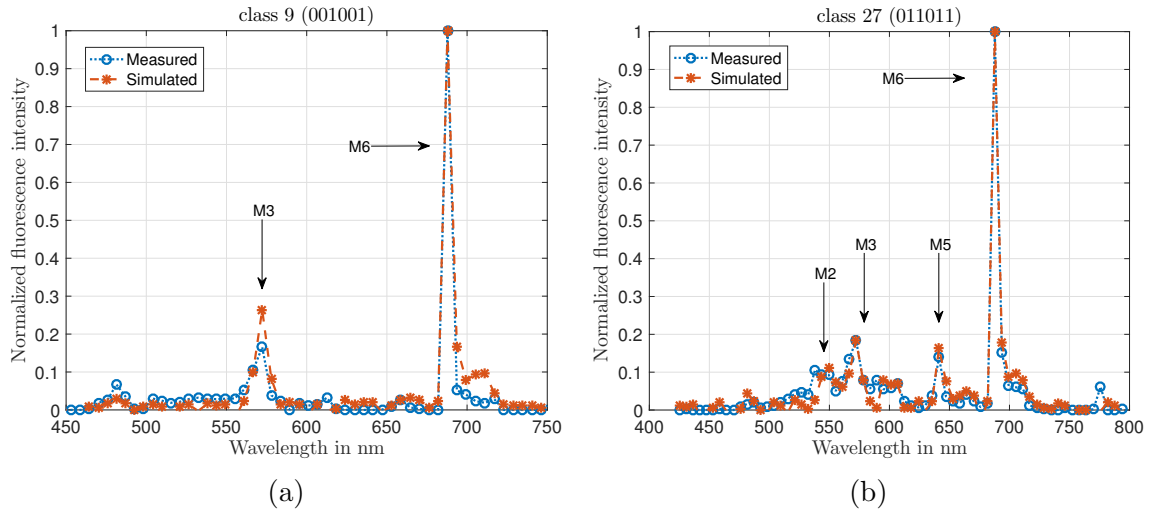
Figure 7.11: Comparison of measured and simulated spectra of (a) class 9 and (b) class 27. Apart from individual noise realizations, measured and simulated spectra are in good agreement.

simulations TPR_{17} is 0.17% smaller, PPV_{17} is 0.12% larger, and TPR_{18} is 0.18% smaller than in the experiment. The difference in the F_1-score$_i$ values of all classes except #64 is below 0.1%, and with the exception of classes 10, 18 and 33 it is below 0.05%.

One noticeable difference is that in the simulations the purity of class 64 $PPV_{64} = 97.46\%$ is lower by approx. 1% than in the measurements, which indicates that in the simulations more labeled flakes were sorted out as unlabeled. This can also be seen from the slightly lower TPR_i values of the 14 labeled plastics in Fig. 7.12 in comparison to Fig. 7.9.

The macro-averaged classification performance of the 14 classes in the simulations ($TPR_M = 99.62\%$, $PPV_M = 99.92\%$ and F_1-score$_M = 99.79\%$) almost does not differ from that in the experiment ($TPR_M = 99.76\%$, $PPV_M = 99.88\%$ and F_1-score$_M = 99.82\%$, see Fig. 7.9). Naturally, there are differences in the TPR and PPV values between simulations and the experiment, because in practice the incorporation of markers into plastics comes with some unpredictable influences. However, with the exception of class 64 "unlabeled" these differences are below the margin of error 0.2% and can thus be tolerated. Overall, the simulation models the reality very well and can thus be trusted.

7.3.2 Assignment of different codes to the same plastics type

In Section 7.3.1 the marker combinations were "incorporated" into plastics exactly as in the experiment in Section 7.2 (see Table 7.1). In the experiment, the assignment of markers and marker combinations to the plastics was carried out in such a way that absorption of marker fluorescence by the plastics due to their colors was (almost) avoided. However, such an assignment requires the measurement of the plastics' absorption/reflectance spec-
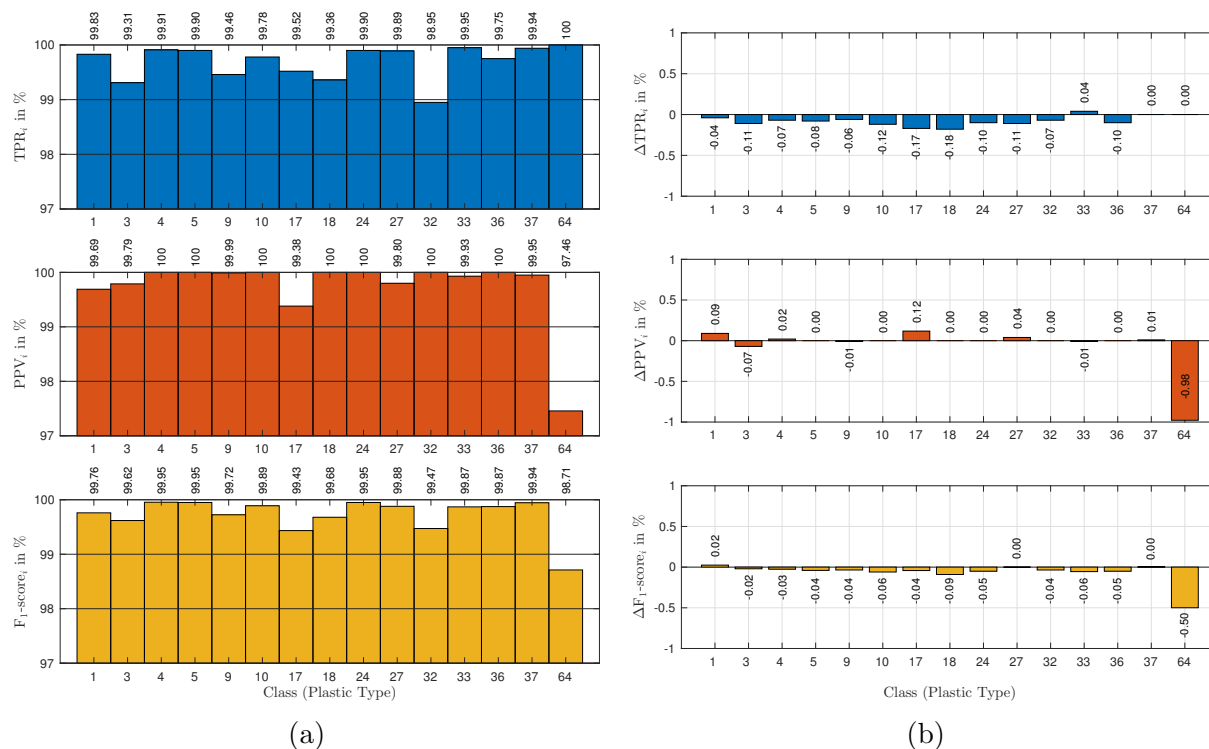
Figure 7.12: (a) Classification performance per class (individual TPR_i and PPV_i) achieved with simulated spectra of 14 classes. $TPR_M = 99.6\%$, $PPV_M = 99.9\%$ and $F_1\text{-score}_M = 99.79\%$. (b) The difference between classification performance achieved in the simulations and in the experiment in Section 7.2.2.

tra, which might not always be possible. Additionally, as already mentioned, the fluorescent labeling of plastics can be used not only for recycling purposes, but also to encode any desired information, for example, customer IDs, production charge numbers, or for counterfeit protection. It is thus important to know how the assignment of different marker combinations (classes) to the same plastic type influences the classification performance.

In this section, computer simulations are employed to investigate the different assignments of marker combinations (classes) to plastics: all 14 marker combinations were subsequently "incorporated" into the same plastic. This was repeated for the 10 plastics used in the experiment (see Table 7.1). The "incorporation" process was the same as that described in Section 7.3.1 and included (1) adjustment of the markers' individual fluorescence emission intensities due to the different marker concentrations, (2) multiplication of marker spectra with the absorption spectra of the corresponding plastics, and (3) corrupting spectra with a realistic noise of the same power as in the experiment to achieve the same S/N ratio of the 14 classes (see Table 7.2). For each class, 10 000 random noise realizations were generated.

The simulated spectra were again classified using the SCC algorithm with the threshold value $T = 0.85$. The classification results achieved with each of the 14 classes for all 10

plastics are summarized in Tables 7.3 (TPR_i values) and 7.4 (PPV_i values). The last column in both tables contains TPR_M and PPV_M values macro-averaged over the 14 (fluorescently labeled) classes. As can be seen, for most of the (white) plastics, there is not much difference in the classification performance when all 14 classes are incorporated into the same plastic type. In fact, the difference in the macro-averaged values is smaller than the margin of error 0.2% (see Section 7.1.1), thus no definite "best assignment" can be selected here. That is due to the fact that white and light-colored plastics usually have almost flat absorption/reflectance spectra, and almost no wavelength-dependent re-absorption of marker fluorescence emission by such plastics occurs and hence the spectral shape of the markers is not (significantly) changed.

In contrast, with colored plastics, some marker assignments can be very unfavorable for the classification. As can be seen in Tables 7.3 and 7.4, for example in Hostaform C13031 green a particularly bad recovery rate TPR_i was achieved with classes 4 (code "000100"), 18 (code "010010"), 27 (code "011011"), 36 (code "100100") and 37 (code "100101"), and a very low plastics purity PPV_i was attained with classes 27, 32 (code "100000"), 33 (code "100001") and 37. This can be explained using the reflectance spectrum of Hostaform C13031 green shown in Fig. 7.13. The reflectance spectrum shows the amount of light that gets reflected by the plastic as a function of the wavelength. Provided the plastic does not transmit light, the inverse of the reflectance spectrum shows what amount of light gets absorbed by the plastic as a function of the wavelength. For example, the reflectance coefficient of approx. 38% at 535 nm means that 38% of monochromatic light of wavelength 535 nm gets reflected by "Hostaform C13031 green", and 62% is absorbed (since "Hostaform C13031 green" is a non-transparent plastic its light transmittance coefficient is virtually zero). As the reflectance spectrum of "Hostaform C13031 green" shows, in the wavelength range between approx. 600 nm and 700 nm only approx. 15% of light gets reflected (i.e. 85% is absorbed), and in the wavelength range between 500 nm and 550 nm the reflectance coefficient is well above 30%. This means that the fluorescence emissions of markers M1 and M2 are less absorbed by this plastic than the emissions of markers M3, M4, M5, and M6 (see marker fluorescence emission spectra in Fig. 2.6b). As a result, Hostaform C13031 green, class 4 (code "000100") was in some cases misclassified as class 20 (code "010100"), class 27 (code "011011") was sometimes falsely classified as class 25 (code "011001"), class 36 (code "100100") was misclassified as class 32 (code "100000"), and class 37 (code "100101") was misclassified as class 33 (code "100001"), which reduced the individual TPR_i and PPV_i values of these classes. In fact, the value of PPV_{37} in "Hostaform C13031 green" could not be calculated, since not a single spectrum was classified as class 37 such that $TP_{37} = 0$ and $FP_{37} = 0$, and thus also $TPR_{37} = 0$.

Similar problems were identified with "Delrin 500NC010 brown". As can be seen in Fig. 7.13, "Delrin 500NC010 brown" reflects less light at wavelengths 450–570 nm (reflectance coefficient approx. 15%), where emission spectra of markers M1, M2, and M3 are located, than at wavelength 570–750 nm (reflectance of approx. 29%), where emission spectra of markers M4, M5 and M6 are situated. Therefore, for example the already "weak" intensity of marker M2 gets decreased compared to the already "strong" marker M6 (see Section 7.2.2) in "Delrin 500NC010" brown and the overall spectrum of class

Table 7.3: TPR_i values achieved with the SCC classification algorithm when the 14 classes are incorporated into the same plastics type, for each of the 10 plastics types used in the experiment. Per class and plastic, 10 000 random noise realizations were generated with the same S/N ratios as in the experiment (see Table 7.2). Values smaller than 98% are marked red.

| Plastic | | Class | | | | | | | | | | | | | | | Macro- |
Name	Color	1	3	4	5	9	10	17	18	24	27	32	33	36	37	64	averaged
Delrin 500NC010	white	99.93	98.93	99.52	99.65	98.65	99.78	99.08	99.36	99.90	99.89	99.01	99.81	99.72	99.46	100	99.48
Duracon SW-01PS	white	99.92	98.94	99.43	99.65	98.70	99.77	99.11	99.39	99.89	99.84	99.00	99.84	99.70	99.85	100	99.50
Hostaform C13021	white	99.93	98.85	99.47	99.73	98.65	99.79	99.14	99.37	99.90	99.87	99.02	99.90	99.69	99.85	100	99.51
Delrin 500NC010	brown	99.92	99.12	99.72	99.90	97.71	99.78	81.34	98.59	99.80	99.15	99.18	99.36	83.49	1.88	100	89.92
Tornoform T300MW4	white	99.93	98.96	99.54	99.70	98.55	99.75	98.70	99.34	99.90	99.85	99.02	99.84	99.71	99.60	100	99.46
Hostaform C13031	white	99.94	99.22	99.52	99.60	98.77	99.82	99.14	99.37	99.89	99.86	99.04	99.92	99.70	99.90	100	99.55
Lexan LS2J-111	transparent	99.93	99.19	99.51	99.60	98.74	99.77	99.25	99.35	99.89	99.86	99.01	99.90	99.69	99.92	100	99.54
Hostaform C9021M	white	99.93	98.93	99.47	99.73	98.66	99.78	99.09	99.36	99.90	99.89	99.02	99.90	99.69	99.85	100	99.51
Hostaform C13031	green	99.91	98.73	87.90	99.92	99.78	99.71	99.94	32.54	99.90	0.32	98.95	100	21.30	0	100	74.21
Delrin 500NC010	yellow	99.94	98.96	99.46	99.71	98.64	99.78	99.15	99.37	99.90	99.83	99.07	99.57	99.75	93.39	100	99.04

Table 7.4: PPV_i values achieved with the SCC classification algorithm when the 14 classes are incorporated into the same plastics type, for each of the 10 plastics types used in the experiment. Per class and plastic, 10 000 random noise realizations were generated with the same S/N ratios as in the experiment (see Table 7.2). Values smaller than 98% are marked red.

| Plastic | | Class | | | | | | | | | | | | | | | Macro- |
Name	Color	1	3	4	5	9	10	17	18	24	27	32	33	36	37	64	averaged
Delrin 500NC010	white	99.57	99.89	100	100	99.99	100	99.90	100	100	99.65	100	99.48	100	99.95	97.48	99.89
Duracon SW-01PS	white	99.67	99.92	100	100	99.99	100	99.86	100	100	99.61	100	99.86	100	99.95	97.48	99.92
Hostaform C13021	white	99.70	99.91	100	100	99.99	100	99.86	100	100	99.58	100	99.86	100	99.97	97.48	99.92
Delrin 500NC010	brown	86.41	97.84	100	100	99.47	100	99.85	100	100	99.36	100	50.48	100	99.47	96.53	95.21
Tornoform T300MW4	white	99.54	99.84	100	100	99.99	100	99.89	100	100	99.57	100	99.63	100	99.96	97.39	99.89
Hostaform C13031	white	99.76	99.92	100	100	100	100	99.94	100	100	99.67	100	99.90	100	99.98	97.57	99.94
Lexan LS2J-111	transparent	99.78	99.93	100	100	100	100	99.93	100	100	99.64	100	99.92	100	99.96	97.47	99.94
Hostaform C9021M	white	99.58	99.89	100	100	99.99	100	99.89	100	100	99.65	100	99.85	100	99.97	97.47	99.92
Hostaform C13031	green	99.89	100	100	100	100	100	99.87	100	100	84.21	78.46	50	100	–	45.33	93.26
Delrin 500NC010	yellow	99.68	99.90	100	100	100	100	99.89	100	100	99.60	100	93.79	100	99.98	97.57	99.49

17 (code "010001") becomes very similar to that of class 1 (code "000001") resulting in misclassifications and low $TPR_{17} = 81.34\%$ and $PPV_1 = 86.41\%$.

Nevertheless, as the experimental measurements in Section 7.2 confirmed, the problems with absorption of the marker emissions by colored plastics can be avoided if a careful assignment of markers to such plastics is carried out. For example, not assigning markers M3, M4, M5, and M6 to green plastics would help avoid many misclassifications of classes 4, 18, 27, 32, 33, 36, and 37, and not assigning markers M1, M2, and M3 to brown plastics would help avoid the decrease of classification performance with classes 1, 17, 36, 37, and 33. Therefore, paying attention to the plastics' color in the assignment of marker combinations is a necessary step for the fluorescent labeling of plastics.
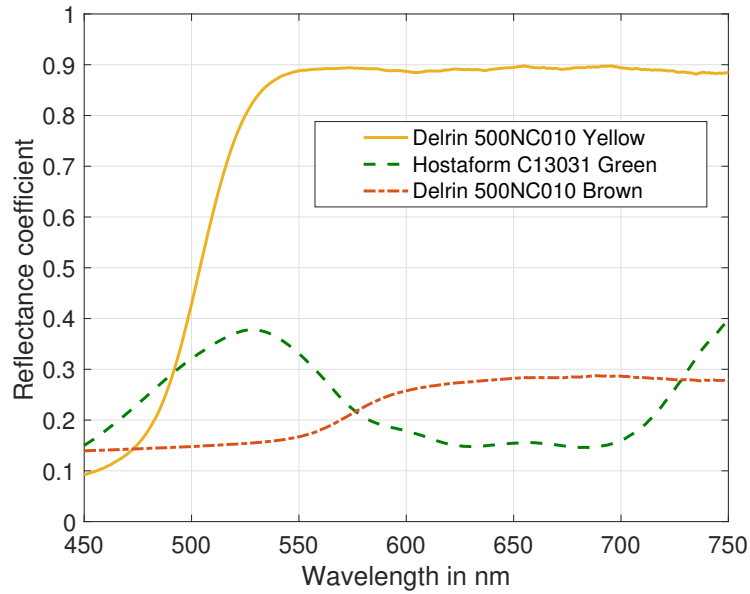
Figure 7.13: Measured reflectance spectra of 3 colored plastics: yellow, green and brown.

7.3.3　Classification results with 14 measured and 49 simulated classes

In order to model spectra of the additional $63-14=49$ classes in the most realistic way, the relative intensities of the markers within the classes were adjusted to match those achieved in the measurements (see Fig. 7.4 and 7.5). Per class $10\,000$ random noise realizations were generated in order to achieve the same confidence intervals as in the experiment in Section 7.2. The S/N ratio of the spectra of the additional 49 classes was 21.8 dB, which is the mean S/N ratio of the spectra of the 14 measured classes (see Table 7.2). The additional 49 classes were "incorporated" into the white "Delrin NC500NC010" using the procedure from Section 7.3.1.

Figure 7.14 shows the TPR_i and PPV_i values for all 64 classes (14 measured labeled plastics, 49 simulated labeled plastics and 1 measured unlabeled plastic). Despite the increased number of classes and hence the more complicated classification, the TPR_i and PPV_i values do not decrease below 99%. Moreover, the TPR_i and PPV_i values of the 14 measured plastics did not decrease in comparison to the case with only these 14 plastics present. The corresponding confusion matrix can be found in Appendix F in Tables F.3-F.4. In addition to the findings in Section 7.2, several cases of misclassification are worth noticing.

According to Tables F.3-F.4, 12 flakes that belong to class 23 (code "010111") were assigned to class 7 (code "000111"), whereas 10 flakes from class 7 were assigned to class 23. The only difference between classes 7 and 23 is marker M2. In fact, as can be seen in Tables F.3-F.4, classes that differ only in the presence or absence of marker M2 and additionally contain marker M6 can be mistaken for one another. The classes most affected
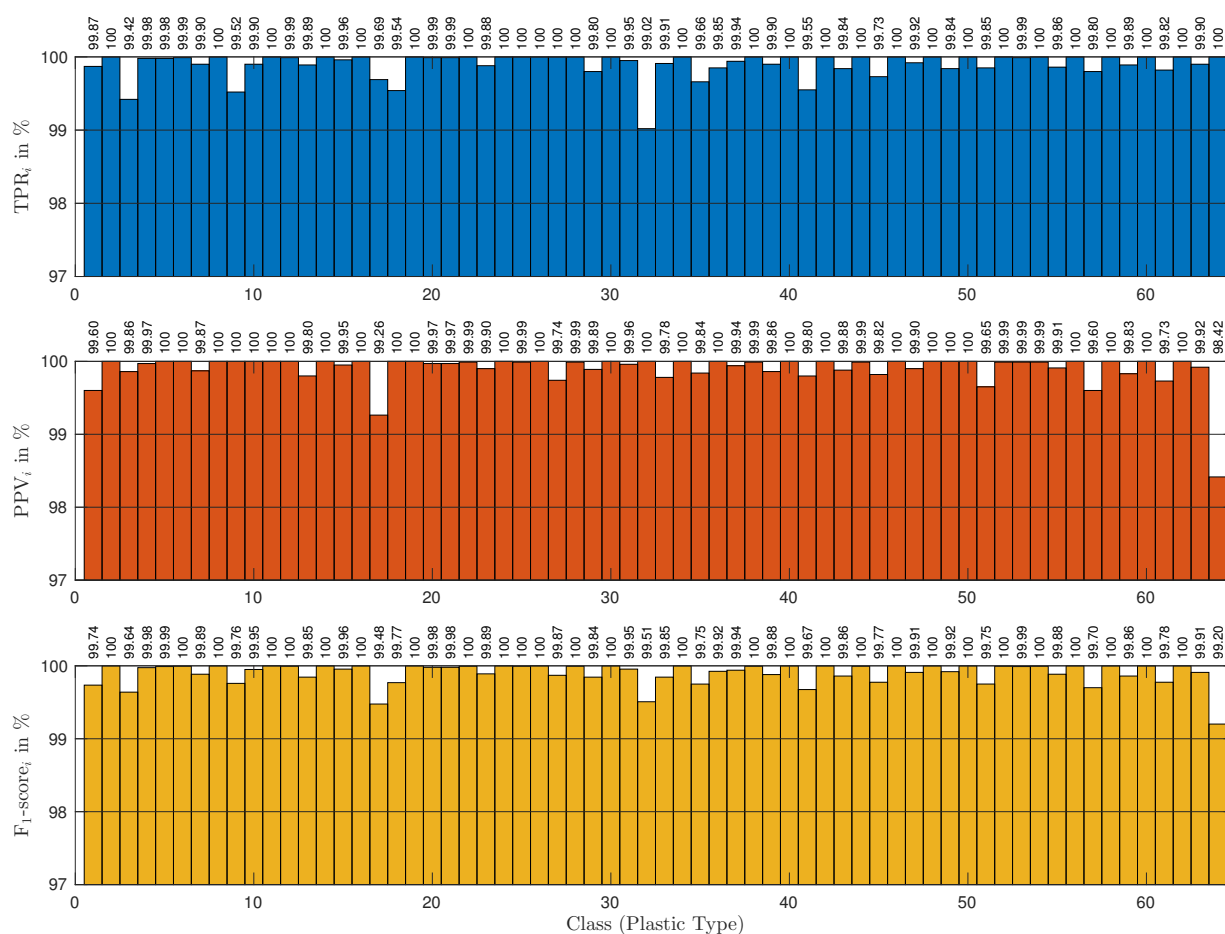
Figure 7.14: Classification performance per class (individual TPR_i and PPV_i) achieved with measured spectra of 14 labeled plastics and one unlabeled plastic, and simulated spectra of 49 labeled plastics. Macro-averaged values are $\text{TPR}_M = 99.76\%$, $\text{PPV}_M = 99.87\%$ and $\text{F}_1\text{-score}_M = 99.89\%$.

by this problem are the following pairs: 1 and 17, 7 and 23, 13 and 29, 15 and 31, 33 and 49, 35 and 51, 39 and 55, 41 and 57, 43 and 59, 45 and 61, 47 and 63. As the confusion matrix shows, overall 325 misclassifications occurred with these classes. Remarkably, pairs of classes which differ in marker M2, but do not contain marker M6, produce almost no errors. For example, classes 4 (code "000100") and 20 (code "010100") were mutually misclassified only 3 times. The explanation for this behavior is the large difference between the intensities of markers M6 and M2. The intensity of marker M6 is at least 5 times higher than the intensities of the other markers (see Fig. 7.4 and 7.5). In contrast, M2 is the weakest marker and has the lowest fluorescence intensity of all 6 markers. Therefore, the presence of the strong marker M6 suppresses the small feature introduced to the overall spectrum by marker M2. As a result, the spectra of classes with marker M2 and M6 become very similar to those without marker M2.

As expected, with the increased number of classes, the overall number of classification

errors also increases and some more misclassifications are produced. Nevertheless, very large macro-averaged values $\text{TPR}_M = 99.76\%$ and $\text{PPV}_M = 99.87\%$ were still achieved, which is comparable to the values achieved with the 14 measured plastics only ($\text{TPR}_M = 99.76\%$ and $\text{PPV}_M = 99.88\%$, see Section 7.2.2).

7.3.4 Influence of the measurement noise

The S/N ratio of the fluorescence spectra acquired from the plastic flakes is a critical parameter with respect to the classification performance. In the concrete situation in the experiment in Section 7.2.2, the average S/N ratio measured overall 140 000 spectra of the 14 labeled plastics was 21.8 dB. The goal of the simulations in Sections 7.3.1-7.3.3 was to model the practical situation, therefore the same S/N ratio as in the experiment was used. In order to predict the classification performance for other S/N ratios when the system is operated with different parameters (e.g. a larger or smaller measurement rate that would be necessary for a different throughput and thus speed of the conveyor belt, see also Section 6.2), additional computer simulations were carried out.

The spectra of the 63 classes were corrupted with the noise of different power such that different S/N ratios were achieved. Relative marker intensities in the simulated spectra were adjusted in order to match those in the experiment. The spectra were processed using the SCC classification algorithm with the threshold value T= 0.85 as in Section 7.2.2.

The macro-averaged TPR_M and PPV_M as function of the S/N ratio are shown in Fig. 7.15a. For S/N ratios below approx. -1 dB, a fraction of more than 99% of all SCC values lie below the threshold T= 0.85, so that these plastics are assigned to class 64 "unlabeled". Since class 64 is not included in the calculation of TPR_M and PPV_M for obvious reasons, the number of TP_i and FP_i values for S/N ratios below approx. -1 dB is insufficient to calculate PPV_M (see Eqn. 4.36, 4.35, 4.39 and 4.40). Thus there are no PPV_M values shown in the figure at S/N ratio below -1 dB, and consequently TPR_M is virtually zero in this region. Needless to say that this region is of no interest here since values of TPR_M and PPV_M below approx. 95% are irrelevant in practice.

It should be noted here, that the results shown in Fig. 7.15a are worse than those achieved in the simulations with unequal relative marker intensities in Section 4.9.4. This is due to the fact that here the relative marker intensities were adjusted to match the experimental results and thus the difference between the relative intensities of markers in the marker combinations is larger here than in the situation investigated in Section 4.9.4 (especially because of the "strong" marker M6, compare e.g. Fig. 7.4 and 7.5 with Fig. 4.18a).

According to the experimental results in Section 7.2.2, the values of both metrics for an S/N ratio of 21.8 dB is almost 100%. As can be seen in Fig. 7.15a, according to the simulations, perfect plastics purity ($\text{PPV}_M = 100\%$) can still be achieved at S/N ratios as low as approx. +5 dB, while for a perfect plastics recovery rate ($\text{TPR}_M = 100\%$), +8 dB or more are required. This opens up room for some optimization of the system and measurement parameters.

Figure 7.15b depicts the S/N ratio of the measured signals as a function of the fluorescence intensity [100]. Two particular S/N ratios are marked on the curve: 21.8 dB, i.e. the
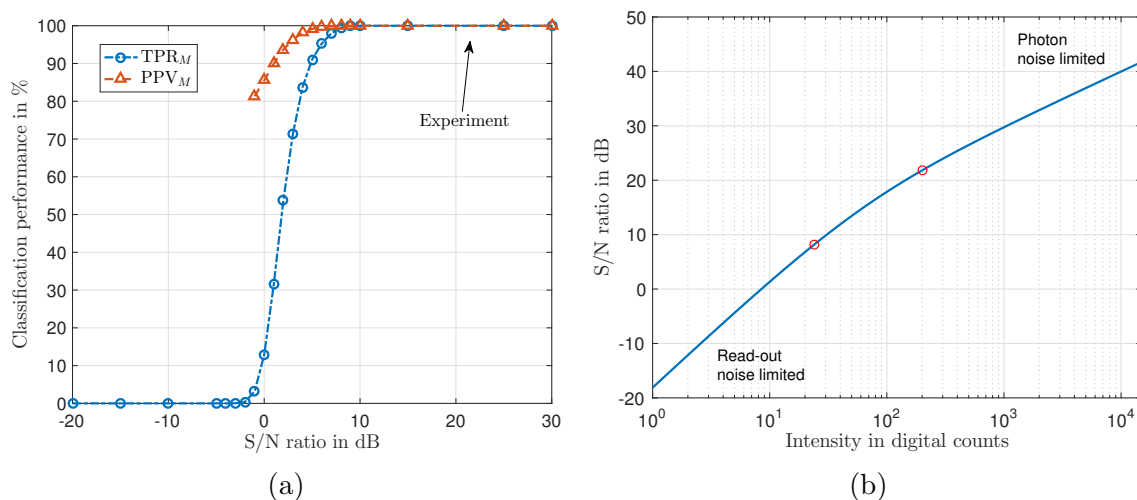
Figure 7.15: (a) Simulated classification performance of the prototype system with 63 classes individually "incorporated" into "Delrin 500NC010 white". (b) S/N ratio of the measured spectral camera signals as function of the (fluorescence) light intensity in the camera's unit "digital counts". The two circles indicate the S/N ratio in the experiment as in Section 7.2.2 and the one to achieve perfect plastics purity, respectively.

average S/N ratio of the spectra measured in the experiment, and 8 dB, i.e. the minimum S/N ratio necessary to achieve both perfect plastics purity and recovery rate according to Fig. 7.15a. For the decrease of the S/N ratio from 21.8 dB to 8 dB, the emitted fluorescence intensity can be decreased by a factor of approx. 8.

In order to take advantage of this, several options can be considered. Due to the linear relation between the exposure time of the spectral camera and the camera's output signal, the exposure time could be decreased by a factor of 8. This, in turn, would increase the camera's measurement rate, the conveyor belt velocity, and, as result, the system's overall mass throughput by a factor of 8.

Another option would be to decrease the marker concentrations by a factor of 8, which might be attractive from an economic point of view as it would decrease the costs of the labeled plastics. Yet another possibility is to decrease the excitation light intensity by a factor of 8. This might be an appealing option in order to lower electrical power consumption and heat dissipation.

7.4   Classification of small groups of plastics

In certain cases, it might not be necessary to employ all classes (here 63). If the origin of a particular plastics waste stream can be determined and it is known that there can be only a limited number of classes (plastic types), then the classification system has fewer options (classes) to choose from and hence classification errors decrease. For example, this may be the case when certain markers are assigned (sold) to a specific customer (e.g.

plastics production company) and plastics waste from this customer needs to be recycled. In this situation, it is known what markers or marker combinations can be present in the plastics and it is easier and more robust using the measurement system to consider only those markers during classification. Dividing markers into specific groups may also be useful when markers have different peak wavelength regions in their excitation spectra. Then excitation light sources with different peak wavelength regions for different groups of markers can be used and will increase the resulting emissions and S/N ratios and thus the classification performance.

In this section, a specific scenario is investigated where the 6 available fluorescent markers are split into two groups of 3 markers each. The first group consists of the "strong" markers M1, M4, and M6, which have high fluorescence intensities (see Chapter 2). The second group contains the other 3 "weak" markers M2, M3, and M5, which have lower fluorescence intensities. Splitting the markers into "strong" and "weak" groups has a practical meaning since as mentioned previously when "strong" and "weak" markers are combined together, the classification decision may be biased towards the "strong" markers and class separability gets worse. With 3 markers there are only $2^3 - 1 = 7$ binary marker combinations possible, which means 7 classes of fluorescently labeled plastics plus 1 class for "unlabeled" plastics exist in each of the two groups.

For the investigations in this section, the spectra measured in the experiment in Section 7.2 were used. The measured spectra, however, were split into two groups as explained above and processed separately by the SCC classification algorithm using threshold $T = 0.85$. The mean S/N ratio of group 1 was 22.43 dB and that of group 2 was 21.21 dB.

Table 7.5 shows the confusion matrix with classification results of group 1 with the "strong" markers M1, M4, and M6. Since in the previous experiments with 63 possible classes (see Section 7.2.2) most misclassifications occurred with spectra containing the "weak" markers M2, M3, and M5, it is not surprising that here very few misclassifications occurred in group 1 which does not contain these markers. Macro-averaged classification performance achieved with 7 classes of group 1 is $\text{TPR}_M = 99.96\%$ and $\text{PPV}_M = 99.98\%$.

The confusion matrix of group 2 with the "weak" markers M2, M3, and M5 can be found in Table 7.6 and requires a closer look. Due to the lower emission intensity of the "weak" markers and as a result of lower S/N ratios, more misclassifications occurred than in group 1. Class 4 (code "100") that contains only marker M2 has the lowest $\text{PPV}_4 = 99.13\%$: 34 flakes from class 1, 22 flakes from class 2, 22 flakes from class 5, 2 flakes from class 6 and 5 flakes from class 7 were incorrectly assigned to class 4. Similarly, $\text{PPV}_6 = 99.53\%$ because 32 flakes that belong to class 2 and 15 flakes from class 8 ("unlabeled") were assigned to class 6. Also $\text{PPV}_7 = 99.84\%$ is due to 14 unlabeled flakes (class 8) falsely assigned to class 7. The macro-averaged classification performance in group 2 is $\text{TPR}_M = 99.42\%$ and $PPV_M = 99.78\%$ and is slightly worse than in group 1.

If the classification performance with group 2 is to be improved, an additional fluorescent marker could be used as a parity bit in the coding scheme. This marker is added to the classes with either an even or odd number of actually present markers and should have an emission intensity sufficient for highly reliable detection. Marker M6, which here has the highest emission intensity of all 6 markers, was used as parity and added to plastics

Table 7.5: Confusion matrix of group 1 with markers M1, M4 and M6. $\text{TPR}_M = 99.96\%$, $\text{PPV}_M = 99.98\%$ and $\text{F}_1\text{-score}_M = 99.97\%$, macro-averaged over classes $1 - 7$, class 8 "unlabeled" not considered.

		Predicted class (output)								
		1	**2**	**3**	**4**	**5**	**6**	**7**	**8**	TPR_i
	1	9999	0	0	0	0	0	0	1	99.99
	2	5	9995	0	0	0	0	0	0	99.95
	3	0	0	10000	0	0	0	0	0	100
True class (target)	**4**	0	0	0	9990	0	0	0	10	99.90
	5	0	0	0	0	9995	0	5	0	99.95
	6	0	4	0	0	0	9994	0	2	99.94
	7	0	0	0	0	3	0	9997	0	99.97
	8	0	0	0	0	0	0	0	10000	100
	PPV_i	99.95	99.96	100	100	99.97	100	99.95	99.87	

Table 7.6: Confusion matrix of group 2 with markers M2, M3 and M5. $\text{TPR}_M = 99.42\%$, $\text{PPV}_M = 99.78\%$ and $\text{F}_1\text{-score}_M = 99.59\%$, macro-averaged over classes $1 - 7$, class 8 "unlabeled" not considered.

		Predicted class (output)								
		1	**2**	**3**	**4**	**5**	**6**	**7**	**8**	TPR_i
	1	9955	0	0	34	2	0	1	8	99.55
	2	0	9931	0	22	0	32	0	14	99.32
	3	0	0	9999	0	0	0	1	0	99.99
True class (target)	**4**	0	0	0	9740	0	0	0	260	97.40
	5	0	0	0	22	9823	0	0	2	99.76
	6	0	0	0	2	0	9992	0	0	99.98
	7	0	0	3	5	0	0	9991	1	99.91
	8	0	0	0	0	0	15	14	9971	99.71
	PPV_i	100	100	99.97	99.13	99.98	99.53	99.84	97.22	

of classes 1, 2, 4, and 7 from group 2 according to the coding scheme shown in Table 7.7. The decision procedure then has two steps:

1. Classification is carried out based on the 3 main markers M2, M3, M5. Since the presence of a strong peak of marker M6 may obstruct the other markers, only the part of the spectrum (wavelength range) with the 3 main markers is considered at this step.

2. Detection of the parity marker M6 (parity check):

Table 7.7: Binary coding scheme of group 2 with additional parity bit (M6).

Decimal code	Marker/Binary code			Parity bit
	M2	M3	M5	M6
1	0	0	1	1
2	0	1	0	1
3	0	1	1	0
4	1	0	0	1
5	1	0	1	0
6	1	1	0	0
7	1	1	1	1
8	0	0	0	0

– If the parity marker M6 is present and the classification result at step 1 was class 1, 2, 4, or 7, then no further action is required. Otherwise, the flake is assigned to class 8 "unlabeled".

– If the parity marker M6 is absent and the classification result at step 1 was class 3, 5, 6, or 8, then no further action is required. Otherwise, the flake is assigned to class 8 "unlabeled".

With this, "parity" approach, flakes that were assigned to a wrong class in step 1 and with wrong parity are identified and sorted out (class 8). This helps increase the purity PPV_i of the sorted plastics. The confusion matrix with classification results of group 2 with parity coding is shown in Table 7.8. In comparison to Table 7.6, 22 flakes that belong to class 5 and were incorrectly assigned to class 4 are now assigned to class 8. Similarly, 32 flakes that belong to class 2 and that were falsely assigned to class 6, as well as 14 unlabeled flakes (class 8) that were assigned to class 7 are now all classified as class 8. The purities of classes 4, 6 and 7 have thus risen to $PPV_4 = 99.38\%$, $PPV_6 = 99.86\%$ and $PPV_7 = 99.99\%$ and the macro-averaged purity to $PPV_M = 99.89\%$. The macro-averaged recovery rate remained the same: $TPR_M = 99.42\%$.

This example shows that the general drawback of having "strong" markers in combination with "weak" markers can sometimes be turned into an advantage and helps improve the overall classification performance, in particular the purity of the sorted plastics.

Table 7.8: Confusion matrix of group 2 with markers M2, M3, M5 and parity marker M6. $TPR_M = 99.42\%$, $PPV_M = 99.89\%$ and F_1-$score_M = 99.58\%$, macro-averaged over classes $1 - 7$, class 8 "unlabeled" not considered.

				Predicted class (output)					
		1	**2**	**3**	**4**	**5**	**6**	**7**	**8**	TPR_i
	1	9955	0	0	34	0	0	1	10	99.55
	2	0	9931	0	22	0	0	0	46	99.32
	3	0	0	9999	0	0	0	0	1	99.99
True class (target)	**4**	0	0	0	9740	0	0	0	260	97.40
	5	0	0	0	0	9823	0	0	24	99.76
	6	0	0	0	0	0	9992	0	2	99.98
	7	0	0	0	5	0	0	9991	5	99.90
	8	0	0	0	0	0	14	0	9986	99.86
PPV_i		100	100	100	99.38	100	99.86	99.99	96.63	

Summary

Plastics are used virtually everywhere, from the consumer sector and packaging industry to high-tech fields such as medicine and aerospace. The variety and versatility of the properties that different plastics possess make them one of the most important materials. It is literally impossible to imagine modern society without plastics. It is, therefore, no surprise that the production volumes of plastics increase every year. However, the production of plastics is associated with huge energy consumption, the use of limited strategic resources such as crude oil, and the discharge of CO_2 into the atmosphere. With the growing production volumes, the amount of waste plastics disposed of in landfills or the world's oceans also grows. In fact, microplastics have been discovered in fish and thus in the food chain. Since plastics are not bio-degradable they might pollute the environment for decades or even centuries. Incineration of waste plastics is associated with more CO_2 emissions and is not always even economically attractive. In light of this, the recycling of waste plastics becomes increasingly important.

One of the main difficulties of recycling in practice is the need to separate plastics of different types from one another. Mixing different plastic types results in a recycled product of low quality which cannot compete with the products made from brand new plastics. Clearly, such recycled plastics cannot be used in demanding applications where certain mechanical, thermal, or optical material properties are required. Moreover, some types of plastics cannot be mixed and recycled together due to their incompatible chemical structures. Therefore, waste plastics must be sorted by their type and grade prior to recycling.

However, the mono-fractional sorting of plastics is not an easy task. Despite automation, manual sorting is still in widespread use, especially in developing countries. However, manual sorting is error-prone, labor-intensive, and increasingly expensive (due to the growing wages). Many automated sorting systems using e.g. densimetric or electrostatic plastics properties can only carry out binary sorting, i.e. sorting out only one type of plastics. To sort several types of plastics, multiple runs with all associated downsides are necessary. Vision-based automated systems usually can only sort waste plastic products by their color and/or shape. Spectroscopic identification systems developed in the past few decades rely on the intrinsic (optical) properties of the plastics: usually, IR reflectance or fluorescence spectra of the plastics are measured and used for classification and sorting. Unfortunately, especially black and dark plastics most often have flat, featureless spectra, which thus cannot be used for the IR and/or optical classification. Additionally, black

plastics being very popular in certain industries such as the automotive and electronics sectors, absorb large fractions of the incident light, which makes the acquisitions of their reflectance or fluorescence spectra in an industrial environment very problematic.

The focus of this dissertation lies in the identification/classification approach based on the labeling of plastics with fluorescent tracers in order to reduce the aforementioned problems. The idea is to incorporate small amounts of appropriately designed fluorescent tracers (also referred to as "markers") into the plastics during the manufacturing process thus generating unique and distinctive fluorescence emission spectra. The incorporated markers emit fluorescence light of specific spectral shape upon excitation with light of a lower wavelength (due to the Stoke's shift). The known fluorescence spectra of the markers can then be compared with the measured spectra emitted by the labeled plastics and this information can be used for classification purposes. This principle approach was first proposed more than 20 years ago but has not yet been put into wide industrial practice due to different technical difficulties. Some commercially available industrial implementations mostly carry out macro-sorting of plastics, i.e. sorting of large pieces of plastics. For macro-sorting, each such large piece is required to be made from a single type of plastic in order to be classified and sorted. Hence plastic assemblies such as for example car dashboards that contain different types of plastics must be first dismantled. In contrast, micro-sorting deals with small (typically in the millimeter range) flakes of shredded plastics and is far more flexible since it does not require such dismantling. In this dissertation, an implementation of the fluorescent plastics labeling for classification and micro-sorting of plastics in an industrial environment was developed and evaluated.

Two types of fluorescent marker substances were investigated: organic and inorganic. Organic markers, however, demonstrated a very poor photostability: their ability to emit fluorescence degraded very fast after a relatively short exposure to sunlight. This rendered them unsuitable for the application at hand, in which labeled plastics must be able to withstand large portions of sunlight during their life circle. In contrast, inorganic markers showed a very high photostability and did not degrade even after high dose exposure to sunlight. As result, the main focus of this dissertation was placed on inorganic markers. With 14 inorganic (rare-earth elements-based) fluorescent markers investigated, however, their incorporation into the plastics (i.e. labeling) turned out to be a difficult task despite the use of professional plastics extruders. Often markers did not emit fluorescence after their incorporation. The reason for that remains unknown but might have been the destruction of the marker molecules. Attempts to encapsulate and protect marker molecules were not satisfying in all cases. Clearly, more research focused on the chemical structure of the markers and on the extrusion process is needed. Out of the 14 investigated inorganic fluorescent markers, the 6 "stable" ones (i.e. those that "survived" the incorporation into plastics) were chosen for detailed investigation in this dissertation. The 6 markers were used in binary combinations (or 6-bit "codes"): the presence of a marker denoted a "1" and its absence – a "0". Thus with the binary coding up to $2^6 - 1 = 63$ different plastics could be labeled (the code with all zeros was excluded for obvious reasons).

The six markers had narrowband (FWHM between approx. 5 nm and 25 nm) fluorescence emission spectra all located in the visible (VIS) wavelength range between approx.

450 nm and 750 nm. This means that up to ten such markers could theoretically fit in the VIS wavelength range, which would then increase the overall number of the plastics that could be labeled to $2^{10} - 1 = 1023$. The VIS wavelength range was chosen due to the high sensitivity of the commercially available imaging sensors and optics in this range. Additionally, the quantum efficiency of the fluorescence markers is higher in the VIS range in comparison to e.g. IR. The fluorescence excitation peaks of the employed markers were located in the UV-A range between approx. 315 nm and 400 nm, which allowed the excitation of all markers with commercially available UV LEDs. Moreover, an efficient excitation of all 6 markers simultaneously could be achieved with a single LED light (here 395 nm), which significantly facilitates the system design.

One of the most critical problems associated with classification based on fluorescent labeling is the autofluorescence (AF) of the plastics. Often plastics, especially bright and/or colored ones, exhibit fluorescence emission in the visible wavelength range even without incorporated markers. Autofluorescence (AF) is usually caused by chemical additives such as brightening components, UV-protections, coloring dyes, etc. Autofluorescence (AF) spectrally overlaps with the fluorescence spectra of the incorporated markers and thus changes the overall emitted spectrum with the possibility to even completely mask the marker fluorescence. The identification of markers in the measured fluorescence spectra and the classification of the labeled plastics becomes error-prone thus degrading the quality of the recycled plastic products.

To combat the autofluorescence (AF) problem, time-gated fluorescence spectroscopy (TGFS) was proposed and implemented in this dissertation. The method is inspired by time-resolved fluorescence measurements and uses the fact that fluorescence emissions decay exponentially after the excitation light has been turned off. The fluorescence decay time constants of the inorganic markers used in this work are orders of magnitude larger than those of the autofluorescence (AF). Therefore, when the excitation light has been turned off, the autofluorescence (AF) decays much faster (within nanoseconds) compared to the marker fluorescence which is present for up to several microseconds. TGFS uses pulsed excitation light and acquires fluorescence emissions only in the time periods ("gates") when the excitation light is turned off. Thus (almost) no autofluorescence (AF) is present in the acquired spectra. The largest drawback of TGFS is that the intensity and thus the S/N ratios of the acquired (digital) fluorescence spectra are smaller in comparison to the spectra acquired using the steady-state approach (i.e. uninterrupted excitation light and acquisition). The intensity of the TGFS spectra strongly depends on the decay time constants of the markers and the time-gating/acquisition parameters. Whereas the former are governed by physical/chemical laws and are difficult to modify, the latter can be easily varied. For this reason, a mathematical model for the intensity of the acquired TGFS spectra was developed in this dissertation and used to optimize the TGFS acquisition parameters.

The essential goal was to achieve the highest possible classification performance for the fluorescently labeled plastics. For this purpose, various classification and feature extraction algorithms were investigated and compared in terms of their classification performance. Based on the prior experience, the choice of the classification algorithms was limited to the relatively simple, but numerically efficient spectral similarity measures and naive Bayes

methods, and the more complex neural networks (NN), the support vector machines (SVM) and the random forests (RF). For the feature extraction, traditional approaches such as the principal component analysis (PCA) and the linear discriminant analysis (LDA), as well as the least-squares mixture analysis (LSMA) and its modifications were investigated. All algorithms were implemented in MATLAB and integrated into the developed simulation framework. The simulation framework was used to model marker fluorescence emission spectra with different spectral disturbances (measurement noise, relative marker intensity fluctuations, autofluorescence) and evaluate the classification performance of all approaches with respect to these factors. The simulations showed that for all disturbances except the autofluorescence (AF), the spectral cross correlation (SCC) algorithm achieves high classification performance. It requires reasonable computational power and therefore can be implemented in the real-time industrial application at hand. Since in this dissertation the autofluorescence (AF) is suppressed using the TGFS approach, SCC is the best choice and was employed for the classification of marker fluorescence spectra. In the simulations, the SCC algorithm could achieve an excellent classification performance (i.e. sensitivity or the true positive rate TPR = 100%; precision or the positive predictive value PPV = 100%) for S/N ratios as low as +8 dB. Similarly, SCC could achieve TPR = 100% and PPV = 100% with random fluctuations of the relative marker intensities of up to ±40% (i.e. the intensity of one marker could be 80% higher than the intensity of another marker in a marker combination/class).

To determine the performance in practice, a prototype of the TGFS measurement and classification system was developed. The prototype was designed to process small flakes of shredded plastics with sizes between approx. 3 mm and 10 mm delivered on a 500 mm wide conveyor belt in 50 parallel channels. The prototype was able to classify up to 63 plastic types (i.e. fluorescent marker combinations or classes) simultaneously achieving a mass throughput of approx. 250 kg/h. The measurement and classification system consisted of two parts: the spectroscopic acquisition unit and the morphological acquisition unit. The former served the purpose of measuring and classifying the fluorescence spectra of the labeled plastics and consisted of a custom-built CCD-based hyperspectral camera, a pulsed high-power UV-LED line light for the fluorescence excitation, optical filters to separate the excitation light from the fluorescence emission, a focusing lens, and hardware to trigger the TGFS measurements. The system provided a spectral optical resolution of approx. 2.8 nm with a spectral sampling of approx. 0.5 nm. The spatial sampling was approx. 0.31 mm and 1.27 mm in the directions across and along the conveyor belt, respectively. The measurement rate was approx. 104 Hz in the TGFS mode. Due to the low-light conditions and the relatively low measurement rate which could result in motion blur, as well as the low spatial sampling, the spectroscopic acquisition unit could not be used for the acquisition of morphological information such as the flakes' sizes and positions on the conveyor belt. For this purpose, the morphological acquisition unit was employed. It consisted of a fast CMOS color camera and a white LED line light to illuminate plastics flakes on the conveyor belt. Due to the camera's high spatial sampling (approx. 120 μm both across and along the conveyor belt) and acquisition rate (up to several 10^3 Hz) as well as the much brighter white illumination, the resulting color images were much better

suited for the derivation of the flakes' morphological parameters than the images acquired by the spectroscopic acquisition unit. The results from both acquisition units were then merged by the software and passed to the sorting unit which physically separated plastic flakes by their type.

To evaluate the performance of the developed prototype, experimental measurements with approx. 140 000 shredded flakes of fluorescently labeled plastics (14 marker combinations, or classes, 10 000 flakes per class) and 10 000 unlabeled plastic flakes were carried out. From the 10 employed plastics, 6 were labeled using one marker combination (or class) per plastic, and 4 were labeled with two different marker combinations each. Hence there were flakes of the same plastic type and color but labeled with 2 different marker combinations (respectively 2 classes). This was done to practically evaluate the concept of using fluorescence markers to encode not only the plastic type, but also information about the production charge, customer name, etc. An excellent classification performance was achieved using the SCC-based classifier with TPR = 99.76% and PPV = 99.88% (averaged over all 14 labeled plastics). From the relatively small number (338) of misclassified flakes some were due to the low S/N ratio of very small flakes (smaller than approx. 2 mm). The main reason for the other misclassifications was the very high intensity of one of the markers in comparison to the other markers within the spectra of one class. The fluorescence of this "strong" marker made the influence of the other "weaker" markers less important in the overall spectrum. As a result, the classification algorithm "missed" the "weaker" markers and the classification performance degraded. As shown by simulations, the equalization of marker intensities by adjusting the individual marker concentrations would help avoid these misclassifications. Such equalization, however, requires multiple iterations of marker incorporation at different concentrations and is costly and time-consuming. No such equalization could be performed for the plastics used in the experiments. Additionally, a second fluorescence excitation light with a different central wavelength could help better excite the fluorescence of the "weak" markers and increase their intensity in comparison to the "strong" markers, thus leveling the marker intensities.

One of the main advantages of the fluorescent labeling approach over traditional spectroscopy methods is the ability to also classify dark and/or black plastics. This was proven in this dissertation by processing approx. 10 000 fluorescently labeled black plastic flakes using the prototype system. Due to the very high light absorption of the black dye, marker concentrations approx. 5 times higher than those for the bright plastics were necessary. Nevertheless, despite the high absorption of the black dye, the marker fluorescence could be measured and correctly classified in the vast majority of cases: the system achieved TPR = 99.76% and PPV = 99.60% with the black plastic flakes.

The prototype system was developed to classify up to 63 labeled plastics (classes) simultaneously. However, the production of such a large number of fluorescently labeled plastics in amounts and quality necessary for a statistically significant experiment is very problematic due to both time and financial constraints. For this reason, in order to investigate the situation when all 63 plastics are present, simulations with the additional $63 - 14 = 49$ classes were carried out. The spectra of the 49 classes were "incorporated" into a white plastic using the simulation model. Prior to that, the simulation model was validated with

the same 14 classes that were used in the experiment, and the simulated spectra were in perfect agreement with the measured ones; the simulation results achieved with the simulated and measured spectra perfectly matched. The parameters of the simulation model were appropriately adjusted in order to achieve spectra similar to the measured ones with respect to the S/N ratio and the relative marker intensities within marker combinations. Despite the increased number (63) of classes, the (average) classification performance degraded only marginally in comparison to the situation with 14 classes: TPR = 99.76% and PPV = 99.87% were achieved. These values can serve as an extrapolation and can be expected in practice when all 63 classes are present.

As mentioned earlier, good classification performance is not the only requirement for the economic success of plastics recycling. High mass throughput is also an important criterion. The developed prototype was designed for a relatively moderate mass throughput of approx. 250 kilograms per hour. However, an increase of the mass throughput could be easily achieved by using a wider conveyor belt. For example, with a 1000 mm wide conveyor belt (and thus 100 parallel channels), the system would be able to achieve 500 kg/h. Additional excitation lamps (with the same LEDs) would also increase the marker fluorescence emission intensity. Due to the practically linear relation between the fluorescence emission intensity and the spectral camera's output signal, this would allow decreasing the camera's exposure time by the same factor while maintaining the same S/N ratio of the acquired spectra. This, in turn, would allow increasing the measurement rate leading to a higher velocity of the conveyor belt and a larger mass throughput.

What is more, a larger mass throughput could also be achieved with an optimization of the S/N ratio ratio. The average S/N ratio of the acquired spectra in the experiments was 21.8 dB, which is substantially higher than the minimum S/N ratio necessary to achieve a perfect classification using the SCC algorithm (approx. 8 dB according to the simulations). When reducing the S/N ratio from 21.8 dB to 8 dB, the marker fluorescence emission intensity can be decreased by a factor of ~ 8. The camera's exposure time could be thus decreased by a factor of 8, allowing a higher velocity of the conveyor belt and leading to an increase of the system's mass throughput.

Another option that a decrease of the S/N ratio to 8 dB offers would be to decrease the marker concentrations by a factor of 8 thus making the labeling of plastics more economically attractive. Yet another option could be to decrease the LED illumination power by a factor of 8, which would decrease the electrical power consumption and heat dissipation.

In this dissertation, an implementation of the fluorescent labeling of plastics for recycling was developed and evaluated in practice. It was shown that a highly reliable classification of fluorescently labeled plastics is possible in an industrial environment. In contrast to the systems currently available on the market which carry out macro-sorting of fluorescently labeled plastics, i.e. sorting of large objects such as bottles, the system in this work was developed with the focus on micro-sorting of small shredded plastic flakes of only a few millimeters in diameter. The micro-sorting approach is much more versatile and flexible with respect to the mechanical separation of different plastic types present

in complex end-of-life plastic products. What is more, this dissertation has demonstrated how the novel measurement approach – the time-gated fluorescence spectroscopy (TGFS) – can be implemented in an industrial inline system to suppress the negative influence of the plastics' autofluorescence (AF) on the classification performance of the labeled plastics. Naturally, for an industry-scale operation, certain optimization and adaptation steps might be necessary especially with respect to achieving higher mass throughput (several tons per hour). Additionally, employing a larger number of plastics is also possible which would allow labeling and classifying a larger number of plastics. Overall, the investigations in this dissertation have shown that fluorescent labeling can make micro-sorting and recycling of waste plastics efficient and economically attractive.

Appendix A

Binary fluorescence labeling

With 6 markers used as "bits" in the binary coding scheme, $2^6 - 1 = 63$ marker combinations, or binary codes, are possible (code "000000" is not used).

Table A.1 shows the coding scheme for the binary labeling with 6 fluorescent markers. The first column in the table contains the class or the decimal code of the corresponding binary codes. The absence and presence of fluorescent markers in the codes are represented by 0 and 1, respectively.

Table A.1: Binary fluorescence labeling coding table with 6 markers. Absence and presence of markers are represented with 0 and 1, respectively.

Decimal Code/Class	M1	M2	M3	M4	M5	M6
1	0	0	0	0	0	1
2	0	0	0	0	1	0
3	0	0	0	0	1	1
4	0	0	0	1	0	0
5	0	0	0	1	0	1
6	0	0	0	1	1	0
7	0	0	0	1	1	1
8	0	0	1	0	0	0
9	0	0	1	0	0	1
10	0	0	1	0	1	0
11	0	0	1	0	1	1
12	0	0	1	1	0	0
13	0	0	1	1	0	1
14	0	0	1	1	1	0
15	0	0	1	1	1	1
16	0	1	0	0	0	0
17	0	1	0	0	0	1
18	0	1	0	0	1	0
19	0	1	0	0	1	1
20	0	1	0	1	0	0
21	0	1	0	1	0	1
22	0	1	0	1	1	0
23	0	1	0	1	1	1
24	0	1	1	0	0	0
25	0	1	1	0	0	1
26	0	1	1	0	1	0
27	0	1	1	0	1	1
28	0	1	1	1	0	0
29	0	1	1	1	0	1
30	0	1	1	1	1	0
31	0	1	1	1	1	1
32	1	0	0	0	0	0
33	1	0	0	0	0	1
34	1	0	0	0	1	0
35	1	0	0	0	1	1
36	1	0	0	1	0	0
37	1	0	0	1	0	1
38	1	0	0	1	1	0
39	1	0	0	1	1	1
40	1	0	1	0	0	0
41	1	0	1	0	0	1
42	1	0	1	0	1	0
43	1	0	1	0	1	1
44	1	0	1	1	0	0
45	1	0	1	1	0	1
46	1	0	1	1	1	0
47	1	0	1	1	1	1
48	1	1	0	0	0	0
49	1	1	0	0	0	1
50	1	1	0	0	1	0
51	1	1	0	0	1	1
52	1	1	0	1	0	0
53	1	1	0	1	0	1
54	1	1	0	1	1	0
55	1	1	0	1	1	1
56	1	1	1	0	0	0
57	1	1	1	0	0	1
58	1	1	1	0	1	0
59	1	1	1	0	1	1
60	1	1	1	1	0	0
61	1	1	1	1	0	1
62	1	1	1	1	1	0
63	1	1	1	1	1	1

Appendix B

Simulation results

Tables B.1, B.2 and B.3 show F_1-score values achieved by the 34 investigated classification algorithms in scenarios A (sensor noise), B (relative marker intensity fluctuations) and C (autofluorescence), respectively.

For a quick overview, cells in the tables are colored red if the corresponding F_1-score$_M$ is below 50%, yellow for the F_1-score between 50% and 90%, and green if the F_1-score$_M$ is above 90%.

Table B.1: F_1-score$_M$ values achieved by different classifiers in scenario A (sensor noise) with S/N ratios between -50 dB and 40 dB. Classifiers are sorted by their F_1-score$_M$ with S/N ratio = 0 dB.

№	Classifier	Feature	S/N ratio in dB															
			-50	-40	-30	-25	-20	-15	-10	-5	0	5	10	15	20	25	30	40
1	MLC	LDA	1.73	1.96	3.12	4.88	10.09	24.20	54.12	87.63	99.40	100	100	100	100	100	100	100
2	SVMlin	LDA	1.58	1.58	2.69	4.53	9.76	23.21	54.08	87.99	99.11	100	100	100	100	100	100	100
3	SVMrbf	LDA	1.58	1.58	1.58	1.58	4.96	18.67	51.18	87.31	99.04	99.99	100	100	100	100	100	100
4	NN	LDA	1.58	1.69	2.81	4.66	9.20	22.57	53.46	86.91	98.91	99.97	100	100	100	100	100	100
5	RF	LDA	1.58	1.58	1.58	1.58	4.24	18.91	51.38	86.90	98.52	100	100	100	100	100	100	100
6	SCC	–	1.64	1.77	2.20	2.77	4.21	14.56	27.29	59.70	96.53	100	100	100	100	100	100	100
7	RF	LSMA	1.58	1.58	1.58	1.58	1.58	2.31	16.62	54.74	90.90	99.78	100	100	100	100	100	100
8	SVMlin	LSMA	1.58	1.58	1.96	2.56	4.13	8.56	22.18	56.08	90.75	99.84	100	100	100	100	100	100
9	SAM	–	1.66	1.78	2.22	2.79	4.24	8.60	21.41	53.88	90.60	99.87	100	100	100	100	100	100
10	SVMlin	PCA	1.58	1.58	1.77	2.61	4.16	8.48	21.53	55.94	90.58	99.78	100	100	100	100	100	100
11	SVMrbf	LSMA	1.58	1.58	1.58	1.58	1.58	4.40	17.79	53.04	90.26	99.82	100	100	100	100	100	100
12	MLC	LSMA	1.65	1.77	2.21	2.83	4.24	8.18	20.53	53.60	90.23	99.86	100	100	100	100	100	100
13	MLC	PCA	1.65	1.77	2.21	2.83	4.24	8.18	20.53	53.60	90.23	99.86	100	100	100	100	100	100
14	SVMrbf	PCA	1.58	1.58	1.58	1.58	1.58	4.10	16.96	52.56	90.23	99.84	100	100	100	100	100	100
15	NN	PCA	1.61	1.63	1.82	2.62	4.36	8.20	20.51	55.19	90.10	99.69	100	100	100	100	100	100
16	NN	LSMA	1.59	1.61	1.86	2.52	4.33	8.14	20.45	55.12	90.08	99.66	100	100	100	100	100	100
17	RF	PCA	1.58	1.58	1.58	1.58	1.58	2.59	17.70	54.00	90.07	99.63	100	100	100	100	100	100
18	RF	NCLS	1.58	1.58	1.58	1.58	1.58	1.58	10.14	44.90	86.87	98.85	99.96	100	100	100	100	100
19	MLC	NCLS	1.58	1.60	1.64	1.66	1.78	4.01	13.62	45.94	86.75	98.59	99.73	99.98	100	100	100	100
20	SVMlin	NCLS	1.58	1.58	1.58	1.58	2.03	4.70	14.78	46.93	86.43	98.87	99.89	100	100	100	100	100
21	NN	NCLS	1.58	1.60	1.58	1.58	1.79	4.46	14.23	47.18	86.38	98.27	99.82	99.99	100	100	100	100
22	SVMrbf	NCLS	1.58	1.58	1.58	1.58	1.58	2.99	12.08	43.11	85.44	98.47	99.62	99.86	100	100	100	100
23	SVMlin	SCLS	1.58	1.58	1.75	2.36	4.01	7.96	18.77	45.67	85.28	99.49	100	100	100	100	100	100
24	NN	SCLS	1.60	1.62	1.83	2.48	3.95	7.49	17.65	45.05	84.71	99.19	100	100	100	100	100	100
25	RF	SCLS	1.58	1.58	1.58	1.58	1.58	3.53	13.42	43.61	83.90	99.53	100	100	100	100	100	100
26	SVMrbf	SCLS	1.58	1.58	1.58	1.58	1.58	4.21	14.79	42.86	83.81	99.52	100	100	100	100	100	100
27	MLC	SCLS	1.63	1.79	2.22	2.91	4.19	7.62	17.10	38.05	73.72	97.51	99.99	100	100	100	100	100
28	RF	FCLS	1.58	1.58	1.58	1.58	1.58	3.45	12.84	39.43	71.96	87.64	96.26	99.26	100	100	100	100
29	SVMrbf	FCLS	1.58	1.58	1.58	1.58	1.58	4.08	14.09	39.08	70.75	86.67	95.76	99.28	100	100	100	100
30	NN	FCLS	1.61	1.62	1.70	2.24	3.72	7.20	16.28	40.53	68.71	83.49	92.91	98.13	100	100	100	100
31	MLC	FCLS	1.62	1.70	2.01	2.67	3.73	6.97	16.30	40.28	68.71	83.81	93.37	98.50	100	100	100	100
32	SVMlin	FCLS	1.58	1.58	1.73	2.28	3.88	7.21	17.18	41.74	68.05	81.33	90.30	96.55	100	100	100	100
33	ED	–	1.63	1.67	1.81	2.04	2.52	3.34	4.90	7.69	25.72	68.34	87.81	99.21	100	100	100	100
34	DSCC	–	1.62	1.64	1.75	1.90	2.18	2.78	4.34	8.57	21.90	53.70	88.60	99.50	100	100	100	100

Table B.2: F$_1$-score$_M$ values in % achieved by different classifiers in scenario B with relative marker intensity fluctuations between $\pm0\%$ and $\pm100\%$. Classifiers are sorted by their F$_1$-score$_M$ with intensity fluctuations of $\pm100\%$. No noise was applied in scenario B.

№	Classifier	Feature	Relative intensity fluctuations in %										
			0	10	20	30	40	50	60	70	80	90	100
1	RF	LSMA	100	100	100	100	100	100	100	100	100	100	97.98
2	MLC	PCA	100	100	100	100	100	100	100	100	99.83	99.73	97.89
3	MLC	LSMA	100	100	100	100	100	100	100	99.91	99.80	99.75	97.80
4	MLC	SCLS	100	100	100	100	100	100	100	99.84	99.73	99.63	97.29
5	RF	NCLS	100	100	100	100	100	100	100	100	100	100	97.04
6	NN	PCA	100	100	100	100	100	100	100	100	100	100	96.81
7	NN	LSMA	100	100	100	100	100	100	100	100	100	100	96.76
8	MLC	NCLS	100	100	99.93	99.72	99.47	99.26	98.91	98.73	98.35	98.27	96.33
9	NN	NCLS	100	100	100	100	100	100	100	100	100	100	96.18
10	SVMrbf	PCA	100	100	100	100	100	100	100	99.85	99.44	97.34	90.11
11	SVMlin	NCLS	100	100	100	100	100	100	100	100	100	99.05	90.02
12	SVMlin	LSMA	100	100	100	100	100	100	100	100	100	98.71	89.76
13	SVMlin	PCA	100	100	100	100	100	100	100	100	100	98.12	89.23
14	RF	PCA	100	100	100	100	100	100	100	99.70	98.45	95.87	88.79
15	NN	SCLS	100	100	100	100	100	99.77	99.48	99.12	98.23	95.77	88.21
16	SVMrbf	SCLS	100	100	100	100	100	99.87	99.69	99.40	98.45	95.48	87.76
17	RF	SCLS	100	100	100	100	100	99.91	99.69	99.17	97.44	94.22	87.38
18	SVMrbf	NCLS	100	100	100	99.86	99.56	99.27	99.05	98.58	97.56	93.75	87.27
19	NN	LDA	100	100	100	100	100	100	100	100	99.88	97.51	86.72
20	SVMlin	SCLS	100	100	100	100	100	99.92	99.70	99.49	99.07	96.23	86.57
21	MLC	LDA	100	100	100	100	100	100	99.89	99.63	99.29	96.58	85.12
22	SVMrbf	LSMA	100	100	100	100	99.90	99.75	99.54	99.07	98.03	93.83	84.81
23	SVMrbf	LDA	100	100	100	100	100	100	99.89	99.69	98.29	93.31	82.42
24	SVMlin	LDA	100	100	100	100	100	100	100	100	98.95	93.08	82.06
25	RF	LDA	100	100	100	100	100	99.81	99.21	97.36	93.93	88.84	77.32
26	SVMrbf	FCLS	100	99.65	98.07	96.02	93.16	90.16	87.18	84.76	82.15	78.39	71.09
27	RF	FCLS	100	99.65	98.04	95.54	92.70	89.73	86.63	84.13	81.25	77.39	70.05
28	MLC	FCLS	100	99.45	97.76	94.09	91.22	88.53	85.74	82.70	78.75	74.49	69.42
29	NN	FCLS	100	99.42	94.66	88.15	81.31	78.27	71.12	68.85	64.97	60.59	51.85
30	SVMlin	FCLS	100	98.45	93.93	87.70	80.54	74.66	69.35	64.25	62.02	57.35	51.82
31	SAM	–	100	100	100	100	99.80	93.93	81.84	68.96	58.57	50.55	44.65
32	SCC	–	100	100	100	100	99.80	93.92	81.77	68.81	58.38	50.35	44.45
33	DSCC	–	100	100	100	100	99.73	93.81	80.75	67.60	57.39	49.88	44.03
34	ED	–	100	100	99.81	97.40	83.72	66.35	53.63	45.20	39.26	34.62	31.44

Table B.3: F_1-score$_M$ values in % achieved by different classifiers in scenario C at different S/AF ratios. Classifiers are sorted according to their F_1-score$_M$ at S/AF ratio = 0.05. Realistic noise of 20 dB was applied in scenario C.

№	Classifier	Feature	S/AF ratio															
			0.0001	0.001	0.005	0.01	0.05	0.1	0.2	0.4	0.6	0.8	1	2	4	6	8	10
1	MLC	LDA	3.96	15.27	48.21	69.72	97.07	99.46	100	100	100	100	100	100	100	100	100	100
2	SVMlin	LDA	3.76	15.94	48.55	70.11	96.80	99.36	100	100	100	100	100	100	100	100	100	100
3	NN	LDA	3.91	15.11	47.87	69.84	96.62	99.27	99.88	100	100	100	100	100	100	100	100	100
4	RF	LDA	2.05	11.48	45.69	68.00	96.51	99.07	99.83	100	100	100	100	100	100	100	100	100
5	SVMrbf	LDA	1.94	11.45	45.07	66.96	96.31	99.27	99.91	100	100	100	100	100	100	100	100	100
6	SCC	–	3.50	9.52	34.37	51.95	93.09	100	100	100	100	100	100	100	100	100	100	100
7	SAM	–	3.53	9.60	30.65	48.35	89.44	96.80	99.31	99.85	100	100	100	100	100	100	100	100
8	SVMlin	PCA	2.62	8.50	28.59	46.36	88.74	96.18	99.17	99.79	99.93	100	100	100	100	100	100	100
9	SVMlin	LSMA	2.61	8.25	28.94	46.18	88.11	96.06	99.09	99.81	100	100	100	100	100	100	100	100
10	SVMlin	NCLS	2.69	8.42	28.73	46.65	88.05	96.40	99.06	99.80	100	100	100	100	100	100	100	100
11	NN	PCA	2.62	7.93	27.75	45.73	87.88	96.07	98.84	99.62	99.80	99.89	100	100	100	100	100	100
12	NN	LSMA	2.70	7.87	27.74	45.69	87.86	96.09	98.84	99.62	99.82	99.87	100	100	100	100	100	100
13	MLC	NCLS	2.82	8.17	28.36	45.54	87.82	95.95	99.18	99.85	100	100	100	100	100	100	100	100
14	MLC	LSMA	2.82	8.17	28.37	45.55	87.78	95.96	99.18	99.84	100	100	100	100	100	100	100	100
15	MLC	PCA	2.82	8.17	28.37	45.55	87.78	95.96	99.18	99.84	100	100	100	100	100	100	100	100
16	NN	NCLS	2.72	7.94	27.73	45.76	87.73	96.06	98.84	99.61	99.81	99.89	100	100	100	100	100	100
17	SVMrbf	NCLS	1.59	4.99	24.08	41.34	87.26	95.77	98.99	99.75	99.89	100	100	100	100	100	100	100
18	SVMrbf	LSMA	1.59	4.96	23.84	41.81	87.10	96.08	99.00	99.81	100	100	100	100	100	100	100	100
19	SVMrbf	PCA	1.59	4.93	23.78	41.53	86.71	95.92	99.05	99.80	99.92	100	100	100	100	100	100	100
20	RF	LSMA	1.59	4.33	23.53	41.43	86.52	94.94	98.40	99.59	99.82	100	100	100	100	100	100	100
21	RF	NCLS	1.59	4.53	24.29	41.39	86.48	95.11	98.46	99.58	99.78	99.88	99.92	100	100	100	100	100
22	RF	PCA	1.59	4.43	23.54	41.58	85.91	94.90	98.41	99.48	99.76	99.87	99.90	100	100	100	100	100
23	SVMlin	SCLS	2.32	7.26	22.90	36.44	80.04	92.64	98.09	99.54	99.81	100	100	100	100	100	100	100
24	NN	SCLS	2.47	6.79	21.62	35.62	80.00	92.70	97.79	99.27	99.65	99.81	99.88	100	100	100	100	100
25	SVMrbf	SCLS	1.59	4.56	18.78	32.14	78.52	91.78	98.00	99.49	99.78	99.91	100	100	100	100	100	100
26	RF	SCLS	1.59	4.01	18.06	32.35	78.50	91.76	97.47	99.34	99.73	99.89	100	100	100	100	100	100
27	RF	FCLS	1.59	3.04	13.50	24.67	62.60	83.44	91.83	95.36	96.03	96.54	96.73	97.04	96.54	96.74	96.47	96.52
28	SVMrbf	FCLS	1.59	3.83	13.15	22.79	58.58	79.27	88.07	92.64	94.52	95.11	95.41	96.66	96.58	96.57	96.83	96.42
29	NN	FCLS	2.06	5.29	14.90	24.39	58.32	77.90	87.36	88.72	90.57	91.31	91.49	93.82	93.17	93.65	93.88	94.01
30	MLC	FCLS	1.96	4.96	13.19	22.94	56.29	75.19	84.56	88.62	91.04	91.54	91.46	92.89	93.07	91.76	91.78	92.43
31	SVMlin	FCLS	2.29	5.46	15.16	24.25	54.72	71.94	80.91	86.93	89.37	90.31	91.04	91.85	90.92	90.77	91.13	91.23
32	MLC	SCLS	3.13	7.57	20.00	29.41	53.57	64.90	77.37	86.92	91.32	93.52	94.78	97.54	98.94	99.37	99.57	99.69
33	DSCC	–	2.30	2.88	4.23	6.03	15.38	24.51	36.72	50.99	57.91	62.38	65.80	72.86	77.36	78.39	79.24	79.78
34	ED	–	1.63	1.60	1.60	1.60	11.30	29.79	47.84	63.80	70.17	74.55	78.73	90.19	97.09	98.49	98.88	98.99

Appendix C

Optimal TGFS parameters

The sensor signal s_N is a function of two variables t_p and D. In order to find the parameter set (t_p, D) that maximizes s_N, first, critical points of the function $s_N(t_p, D)$ should be found by solving the equation system of two partial derivatives of Eqn. 5.12 [90]:

$$
\begin{cases}
\frac{\partial s_N}{\partial t_p} = \frac{T_m\left(((\tau-t_p)D+t_p)\exp\left(\frac{t_p(D-1)}{D\tau}\right)-(D\tau+t_p)\exp\left(-\frac{t_p}{D\tau}\right)+D\left((t_p+\tau)\exp\left(-\frac{t_p}{\tau}\right)-\tau\right)\right)}{\tau \cdot t_p{}^2} = 0, \\
\frac{\partial s_N}{\partial D} = \frac{T_m\left((D\tau+t_p)\exp\left(\frac{t_p(D-1)}{D\tau}\right)-D\tau\right)\left(\exp\left(-\frac{t_p}{\tau}\right)-1\right)}{D \cdot \tau \cdot t_p} = 0.
\end{cases} \tag{C.1}
$$

This system has only one real solution given by (Maple 2016$^{©}$):

$$
\begin{cases}
t_p = \ln\left(-2 \cdot \mathrm{LW}\left(-1, -0.5 \cdot \exp(-0.5)\right)\right) \cdot \tau, \\
D = \frac{-\ln(-(2 \cdot \mathrm{LW}(-1, -0.5 \cdot \exp(-0.5))))}{1 + 2 \cdot \mathrm{LW}(-1, -0.5\ \exp(-0.5))},
\end{cases} \tag{C.2}
$$

where LW stands for LambertW and is the inverse function of $f(W) = W\exp(W)$ [101]. Calculating its value and simplifying Eqn. C.2 leads to:

$$
\begin{cases}
t_p = 1.2564 \cdot \tau, \\
D = 0.5.
\end{cases} \tag{C.3}
$$

In order to find out whether the critical point in Eqn. C.3 is a maximum, the second partial derivative test should be performed. The second partial derivatives of Eqn. 5.12 are given by:

$$
\frac{\partial^2 s_N}{\partial t_p{}^2} = -\frac{T_m}{D\tau^2 t_p{}^3} \cdot \Big(((t_p{}^2 - 2t_p\tau + 2\tau^2)D^2 - 2t_p(t_p - \tau)D + t_p{}^2) \cdot \exp(t_p\frac{D-1}{D\tau}) -
$$
$$
-(2D^2\tau^2 + 2Dt_p\tau + t_p{}^2) \cdot \exp(-\frac{t_p}{D\tau}) + D^2((t_p{}^2 + 2t_p\tau + 2\tau^2) \cdot \exp(-\frac{t_p}{\tau}) - 2\tau^2) \Big)
$$
$$
\tag{C.4}
$$

$$\frac{\partial^2 s_N}{\partial t_p \partial D} = \frac{T_m}{D^2 \tau^2 t_p^2} \cdot \left((t_p{}^2 - \tau(t_p - \tau)D^2 - t_p(t_p - \tau)D) \cdot \exp(t_p \frac{D-1}{D\tau}) - \right.$$
$$\left. -(D^2\tau^2 + Dt_p\tau + t_p{}^2) \cdot \exp(-\frac{t_p}{D\tau}) + ((t_p + \tau)\exp(-\frac{t_p}{\tau}) - \tau) \cdot D^2\tau \right) \tag{C.5}$$

$$\frac{\partial^2 s_N}{\partial D^2} = \frac{T_m}{D^3 \tau^2} \cdot t_p(-1 + \exp(-\frac{t_p}{\tau})) \cdot \exp(t_p \frac{D-1}{D\tau}) \tag{C.6}$$

For a particular value of τ, the critical point given by Eqn. C.2 is a (local) maximum when both following conditions hold [90]:

$$\frac{\partial^2 s_N}{\partial t_p{}^2} \cdot \frac{\partial^2 s_N}{\partial D^2} - \left(\frac{\partial^2 s_N}{\partial t_p \partial D} \right)^2 > 0 \tag{C.7}$$

and

$$\frac{\partial^2 s_N}{\partial t_p{}^2} < 0. \tag{C.8}$$

It is easy to see that for all 6 fluorescent markers used in this work conditions in Eqn. C.7 and C.8 hold and hence the critical point given by Eqn. C.3 is at least a local maximum of s_N. Furthermore, since the value of s_N for the border values of (t_p, D) for each particular marker are smaller than the found maximum (see Fig. 5.11), the maximum given by Eqn. C.3 is also the global maximum.

Therefore, Eqn. C.3 provides the optimal parameter set (t_p, D) for TGFS.

Appendix D

S/N ratio and intensity fluctuations of the acquired marker spectra

Figure D.1 shows histograms of S/N ratio of the acquired spectra of the 14 fluorescently labeled plastics (classes). As can be seen, S/N ratio of all acquired spectra is higher than 0 dB. In fact, the majority of the spectra have S/N ratio higher than 10 dB.

Fluctuations of fluorescence intensity of the weaker marker relative to the the strongest marker in combinations with more than one marker are shown in Fig. D.2. In the figure, intensity of the weaker marker is shown in percent of the strongest marker. Despite the use of professional plastics extruders for incorporation of the markers, noticeable relative intensity fluctuations of about 5-10% occurred in the experiment.

(a) Class 1 (code "000001")   (b) Class 3 (code "000011")   (c) Class 4 (code "000100")

Figure D.1: Histograms of the S/N ratio of the acquired fluorescence spectra of the 14 labeled plastics.

(d) Class 5 (code "000101")   (e) Class 9 (code "001001")   (f) Class 10 (code "001010")

(g) Class 17 (code "010001")   (h) Class 18 (code "010010")   (i) Class 24 (code "011000")

(j) Class 27 (code "011011")   (k) Class 32 (code "100000")   (l) Class 33 (code "100001")

(m) Class 36 (code "100100")   (n) Class 37 (code "100101")

Figure D.1: Histograms of the S/N ratio of the acquired fluorescence spectra of the 14 labeled plastics.

(a) Marker M5 in class 3 (code "000011")

(b) Marker M4 in class 5 (code "000101")

(c) Marker M3 in class 9 (code "001001")

(d) Marker M5 in class 10 (code "001010")

(e) Marker M2 in class 17 (code "010001")

(f) Marker M2 in class 18 (code "010010")

(g) Marker M2 in class 24 (code "011000")

(h) Marker M1 in class 33 (code "100001")

(i) Marker M1 in class 36 (code "100100")

(j) Marker M1 in class 37 (code "100101")

(k) Marker M4 in class 37 (code "100101")

Figure D.2: Histograms of intensity fluctuation of the weaker marker relative to the stronger marker in combinations with more than one marker.

Appendix E

Comparison of measured and simulated fluorescence spectra

Figures E.1-E.3 show the comparison of measured and simulated fluorescence spectra of the 14 plastics investigated in the experiment. As can be seen, the simulated spectra are in good agreement with the measured spectra.

(a) Class 1 (code "000001")　　　　　(b) Class 3 (code "000011")
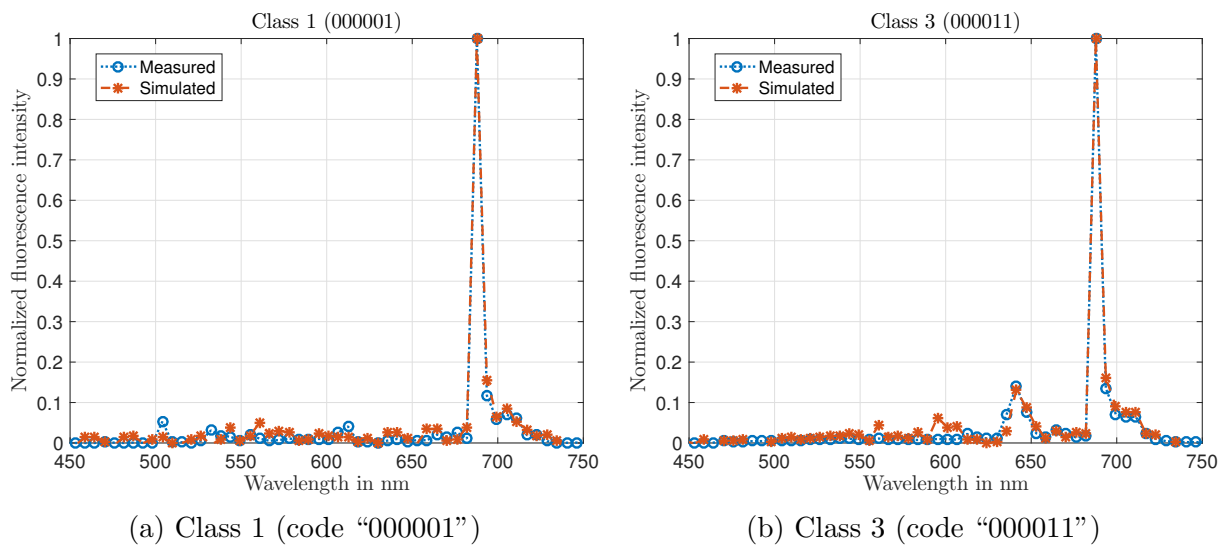
Figure E.1: Comparison of measured and simulated fluorescence spectra of classes 1 and 3.

(a) Class 4 (code "000100")

(b) Class 5 (code "000101")

(c) Class 9 (code "001001")

(d) Class 10 (code "001010")

(e) Class 17 (code "010001")

(f) Class 18 (code "010010")
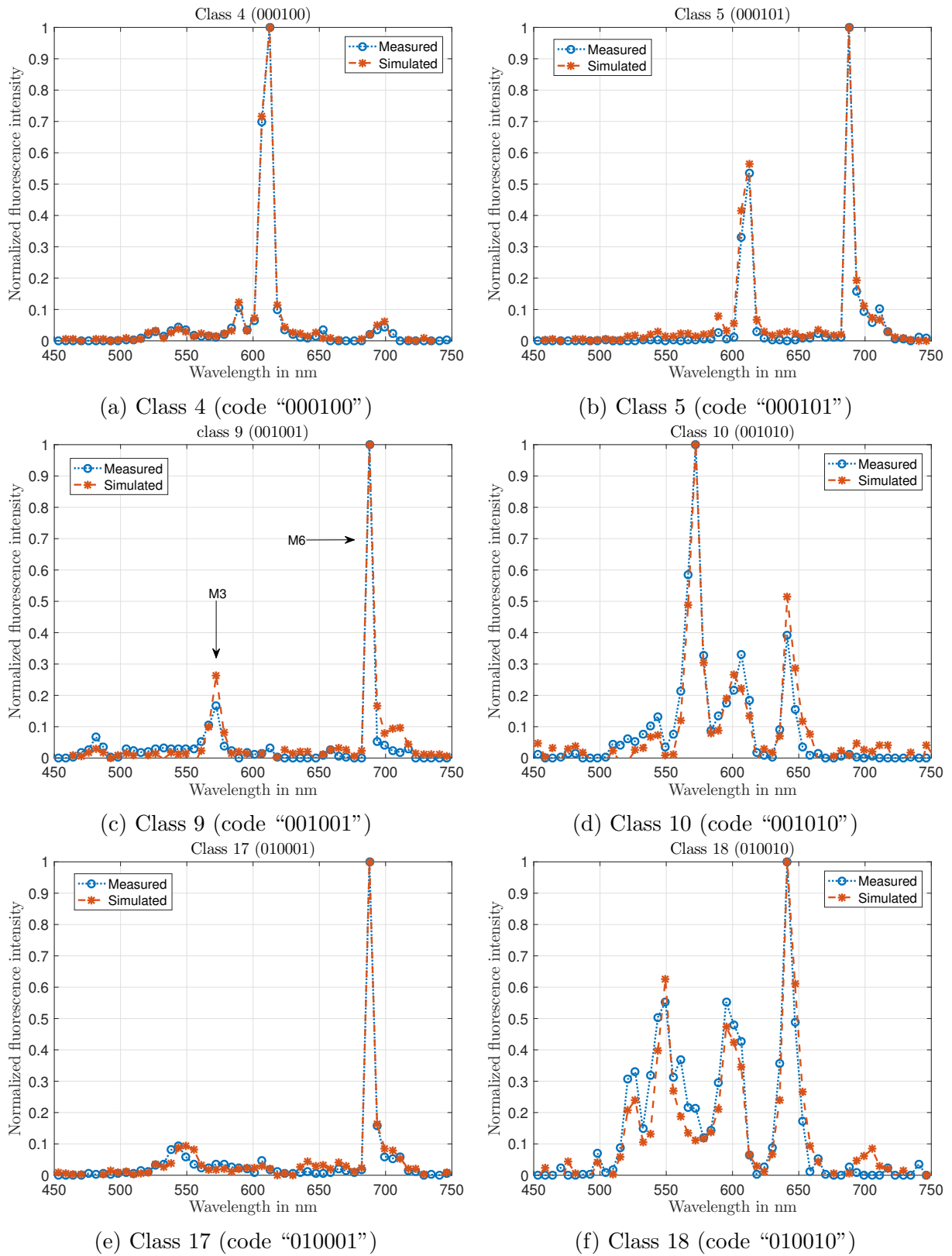
Figure E.2: Comparison of measured and simulated fluorescence spectra of classes 4, 5, 9, 10, 17 and 18.

(a) Class 24 (code "011000")

(b) Class 27 (code "011011")

(c) Class 32 (code "100000")

(d) Class 33 (code "100001")

(e) Class 36 (code "100100")

(f) Class 37 (code "100101")
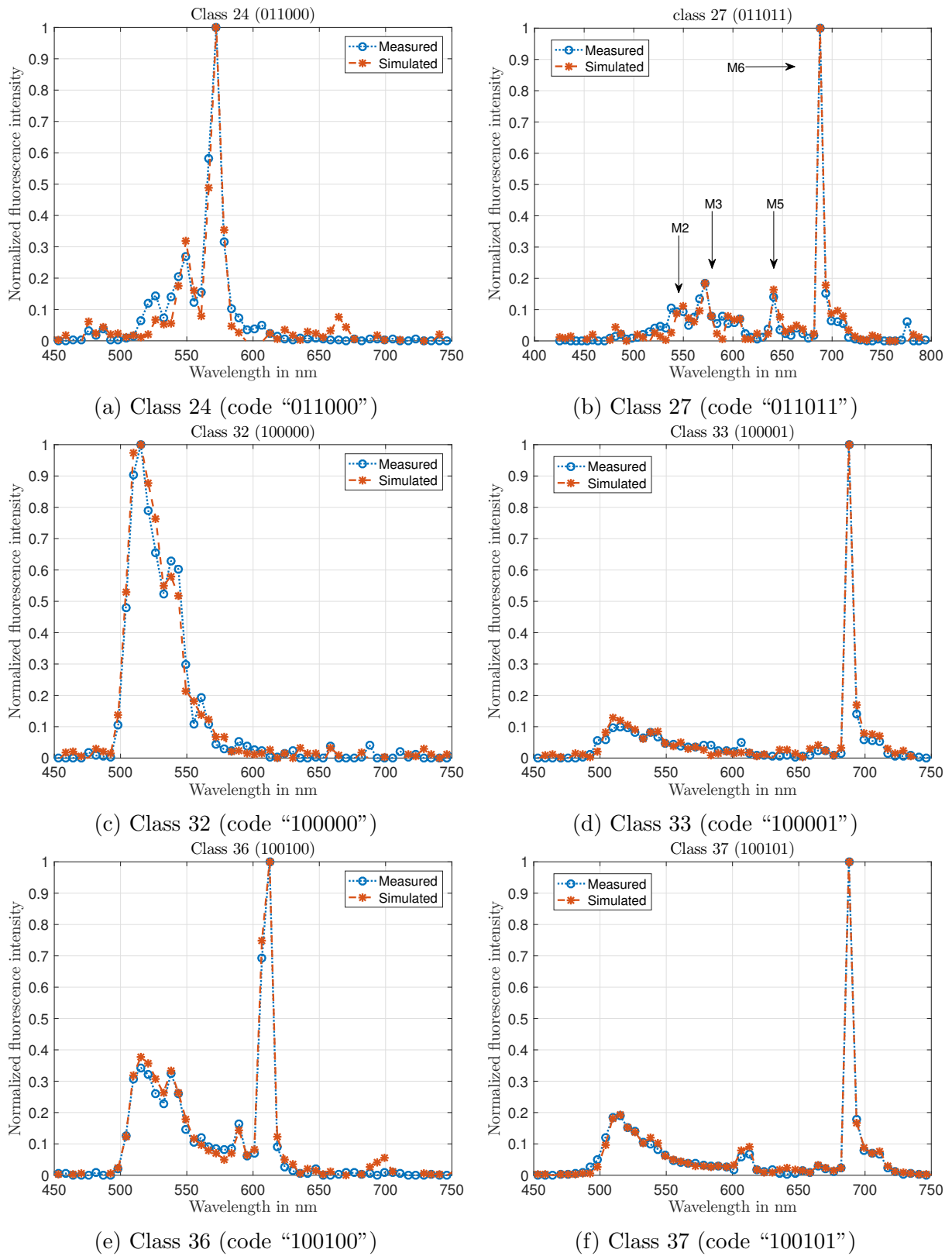
Figure E.3: Comparison of measured and simulated fluorescence spectra of classes 24, 27, 32, 33, 36 and 37.

Appendix F

Classification results

Results of classification of 14 measured fluorescently labeled plastics and 1 unlabeled plastic are summarized in the confusion matrix in Tables F.1-F.2. Rows in the confusion matrix represent true (or target) classes (plastic types), whereas columns stand for predicted (or output) classes. The main diagonal of the matrix contains records of correctly classified flakes of each class (TP_i), elements off the main diagonal represent the number of incorrect classifications. Cells with correctly classified flakes (the main diagonal) are marked green, cells with incorrectly classified flakes are marked red for better representation.

Tables F.3-F.3 show the confusion matrix derived from results of classification of acquired spectra of 14 labeled plastics and 1 unlabeled plastic and simulated spectra of additional 49 labeled plastics. The green and red colored cells contain records of correctly and incorrectly classified flakes, respectively.

Table F.1: Confusion matrix of classification of spectra of the 15 measured plastics (14 labeled and 1 unlabeled). Part 1: Predicted classes 1 to 32. Cells with correctly classified flakes (the main diagonal) are marked green, cells with incorrectly classified flakes are marked red.

Predicted class (output)

	1	2	3	4	5	6	7	8	9	10	11	12	13	14	15	16	17	18	19	20	21	22	23	24	25	26	27	28	29	30	31	32
1	9987	0	0	0	0	0	0	0	0	0	0	0	0	0	0	0	12	0	0	0	0	0	0	0	0	0	0	0	0	0	0	0
2	0	0	0	0	0	0	0	0	0	0	0	0	0	0	0	0	0	0	0	0	0	0	0	0	0	0	0	0	0	0	0	0
3	23	0	9942	0	0	0	0	0	0	0	0	0	0	0	0	0	33	0	0	0	0	0	0	0	0	0	1	0	0	0	0	0
4	0	0	0	9993	0	0	0	0	0	0	0	0	0	0	0	0	0	0	0	2	0	0	0	0	0	0	0	0	0	0	0	0
5	0	0	0	0	9998	0	0	0	0	0	0	0	0	0	0	0	0	0	0	2	0	0	0	0	0	0	0	0	0	0	0	0
6	0	0	0	0	0	0	0	0	0	0	0	0	0	0	0	0	0	0	0	0	0	0	0	0	0	0	0	0	0	0	0	0
7	0	0	0	0	0	0	0	0	0	0	0	0	0	0	0	0	0	0	0	0	0	0	0	0	0	0	0	0	0	0	0	0
8	0	0	0	0	0	0	0	0	0	0	0	0	0	0	0	0	0	0	0	0	0	0	0	0	0	0	0	0	0	0	0	0
9	0	0	0	0	0	0	0	0	9952	0	0	0	0	0	0	0	27	0	0	0	0	0	0	0	0	0	21	0	0	0	0	0
10	0	0	0	0	0	0	0	0	0	9990	0	0	0	0	0	0	0	0	0	0	0	0	0	0	0	0	2	0	0	0	0	0
11	0	0	0	0	0	0	0	0	0	0	0	0	0	0	0	0	0	0	0	0	0	0	0	0	0	0	0	0	0	0	0	0
12	0	0	0	0	0	0	0	0	0	0	0	0	0	0	0	0	0	0	0	0	0	0	0	0	0	0	0	0	0	0	0	0
13	0	0	0	0	0	0	0	0	0	0	0	0	0	0	0	0	0	0	0	0	0	0	0	0	0	0	0	0	0	0	0	0
14	0	0	0	0	0	0	0	0	0	0	0	0	0	0	0	0	0	0	0	0	0	0	0	0	0	0	0	0	0	0	0	0
15	0	0	0	0	0	0	0	0	0	0	0	0	0	0	0	0	0	0	0	0	0	0	0	0	0	0	0	0	0	0	0	0
16	0	0	0	0	0	0	0	0	0	0	0	0	0	0	0	0	0	0	0	0	0	0	0	0	0	0	0	0	0	0	0	0
17	17	0	14	0	0	0	0	0	0	0	0	0	0	0	0	0	9969	0	0	0	0	0	0	0	0	0	0	0	0	0	0	0
18	0	0	0	0	0	0	0	0	0	0	0	0	0	0	0	0	0	9954	0	0	0	0	0	0	0	0	0	0	0	0	0	0
19	0	0	0	0	0	0	0	0	0	0	0	0	0	0	0	0	0	0	0	0	0	0	0	0	0	0	0	0	0	0	0	0
20	0	0	0	0	0	0	0	0	0	0	0	0	0	0	0	0	0	0	0	0	0	0	0	0	0	0	0	0	0	0	0	0
21	0	0	0	0	0	0	0	0	0	0	0	0	0	0	0	0	0	0	0	0	0	0	0	0	0	0	0	0	0	0	0	0
22	0	0	0	0	0	0	0	0	0	0	0	0	0	0	0	0	0	0	0	0	0	0	0	0	0	0	0	0	0	0	0	0
23	0	0	0	0	0	0	0	0	0	0	0	0	0	0	0	0	0	0	0	0	0	0	0	0	0	0	0	0	0	0	0	0
24	0	0	0	0	0	0	0	0	0	0	0	0	0	0	0	0	0	0	0	0	0	0	0	10000	0	0	0	0	0	0	0	0
25	0	0	0	0	0	0	0	0	0	0	0	0	0	0	0	0	0	0	0	0	0	0	0	0	0	0	0	0	0	0	0	0
26	0	0	0	0	0	0	0	0	0	0	0	0	0	0	0	0	0	0	0	0	0	0	0	0	0	0	0	0	0	0	0	0
27	0	0	0	0	0	0	0	0	0	0	0	0	0	0	0	0	0	0	0	0	0	0	0	0	0	0	10000	0	0	0	0	0
28	0	0	0	0	0	0	0	0	0	0	0	0	0	0	0	0	0	0	0	0	0	0	0	0	0	0	0	0	0	0	0	0
29	0	0	0	0	0	0	0	0	0	0	0	0	0	0	0	0	0	0	0	0	0	0	0	0	0	0	0	0	0	0	0	0
30	0	0	0	0	0	0	0	0	0	0	0	0	0	0	0	0	0	0	0	0	0	0	0	0	0	0	0	0	0	0	0	0
31	0	0	0	0	0	0	0	0	0	0	0	0	0	0	0	0	0	0	0	0	0	0	0	0	0	0	0	0	0	0	0	0
32	0	0	0	0	0	0	0	0	0	0	0	0	0	0	0	0	0	0	0	0	0	0	0	0	0	0	0	0	0	0	0	9902
33	0	0	0	0	0	0	0	0	0	0	0	0	0	0	0	0	2	0	0	0	0	0	0	0	0	0	0	0	0	0	0	0
34	0	0	0	0	0	0	0	0	0	0	0	0	0	0	0	0	0	0	0	0	0	0	0	0	0	0	0	0	0	0	0	0
35	0	0	0	0	0	0	0	0	0	0	0	0	0	0	0	0	0	0	0	0	0	0	0	0	0	0	0	0	0	0	0	0
36	0	0	0	2	0	0	0	0	0	0	0	0	0	0	0	0	0	0	0	1	0	0	0	0	0	0	0	0	0	0	0	0
37	0	0	0	0	0	0	0	0	0	0	0	0	0	0	0	0	0	0	0	0	0	0	0	0	0	0	0	0	0	0	0	0
38	0	0	0	0	0	0	0	0	0	0	0	0	0	0	0	0	0	0	0	0	0	0	0	0	0	0	0	0	0	0	0	0
39	0	0	0	0	0	0	0	0	0	0	0	0	0	0	0	0	0	0	0	0	0	0	0	0	0	0	0	0	0	0	0	0
40	0	0	0	0	0	0	0	0	0	0	0	0	0	0	0	0	0	0	0	0	0	0	0	0	0	0	0	0	0	0	0	0
41	0	0	0	0	0	0	0	0	0	0	0	0	0	0	0	0	0	0	0	0	0	0	0	0	0	0	0	0	0	0	0	0
42	0	0	0	0	0	0	0	0	0	0	0	0	0	0	0	0	0	0	0	0	0	0	0	0	0	0	0	0	0	0	0	0
43	0	0	0	0	0	0	0	0	0	0	0	0	0	0	0	0	0	0	0	0	0	0	0	0	0	0	0	0	0	0	0	0
44	0	0	0	0	0	0	0	0	0	0	0	0	0	0	0	0	0	0	0	0	0	0	0	0	0	0	0	0	0	0	0	0
45	0	0	0	0	0	0	0	0	0	0	0	0	0	0	0	0	0	0	0	0	0	0	0	0	0	0	0	0	0	0	0	0
46	0	0	0	0	0	0	0	0	0	0	0	0	0	0	0	0	0	0	0	0	0	0	0	0	0	0	0	0	0	0	0	0
47	0	0	0	0	0	0	0	0	0	0	0	0	0	0	0	0	0	0	0	0	0	0	0	0	0	0	0	0	0	0	0	0
48	0	0	0	0	0	0	0	0	0	0	0	0	0	0	0	0	0	0	0	0	0	0	0	0	0	0	0	0	0	0	0	0
49	0	0	0	0	0	0	0	0	0	0	0	0	0	0	0	0	0	0	0	0	0	0	0	0	0	0	0	0	0	0	0	0
50	0	0	0	0	0	0	0	0	0	0	0	0	0	0	0	0	0	0	0	0	0	0	0	0	0	0	0	0	0	0	0	0
51	0	0	0	0	0	0	0	0	0	0	0	0	0	0	0	0	0	0	0	0	0	0	0	0	0	0	0	0	0	0	0	0
52	0	0	0	0	0	0	0	0	0	0	0	0	0	0	0	0	0	0	0	0	0	0	0	0	0	0	0	0	0	0	0	0
53	0	0	0	0	0	0	0	0	0	0	0	0	0	0	0	0	0	0	0	0	0	0	0	0	0	0	0	0	0	0	0	0
54	0	0	0	0	0	0	0	0	0	0	0	0	0	0	0	0	0	0	0	0	0	0	0	0	0	0	0	0	0	0	0	0
55	0	0	0	0	0	0	0	0	0	0	0	0	0	0	0	0	0	0	0	0	0	0	0	0	0	0	0	0	0	0	0	0
56	0	0	0	0	0	0	0	0	0	0	0	0	0	0	0	0	0	0	0	0	0	0	0	0	0	0	0	0	0	0	0	0
57	0	0	0	0	0	0	0	0	0	0	0	0	0	0	0	0	0	0	0	0	0	0	0	0	0	0	0	0	0	0	0	0
58	0	0	0	0	0	0	0	0	0	0	0	0	0	0	0	0	0	0	0	0	0	0	0	0	0	0	0	0	0	0	0	0
59	0	0	0	0	0	0	0	0	0	0	0	0	0	0	0	0	0	0	0	0	0	0	0	0	0	0	0	0	0	0	0	0
60	0	0	0	0	0	0	0	0	0	0	0	0	0	0	0	0	0	0	0	0	0	0	0	0	0	0	0	0	0	0	0	0
61	0	0	0	0	0	0	0	0	0	0	0	0	0	0	0	0	0	0	0	0	0	0	0	0	0	0	0	0	0	0	0	0
62	0	0	0	0	0	0	0	0	0	0	0	0	0	0	0	0	0	0	0	0	0	0	0	0	0	0	0	0	0	0	0	0
63	0	0	0	0	0	0	0	0	0	0	0	0	0	0	0	0	0	0	0	0	0	0	0	0	0	0	0	0	0	0	0	0
64	0	0	0	0	0	0	0	0	0	0	0	0	0	0	0	0	0	0	0	0	0	0	0	0	0	0	0	0	0	0	0	0
PPV_i	99.60	-	99.86	100	100	-	-	-	100	100	-	-	-	-	-	-	99.26	100	-	-	-	-	-	100	-	-	99.76	-	-	-	-	100
	1	2	3	4	5	6	7	8	9	10	11	12	13	14	15	16	17	18	19	20	21	22	23	24	25	26	27	28	29	30	31	32

True class (target)

Table F.2: Confusion matrix of classification of spectra of the 15 measured plastics (14 labeled and 1 unlabeled). Part 2: predicted classes 33 to 64. Cells with correctly classified flakes (the main diagonal) are marked green, cells with incorrectly classified flakes are marked red.

Predicted class (output)

	33	34	35	36	37	38	39	40	41	42	43	44	45	46	47	48	49	50	51	52	53	54	55	56	57	58	59	60	61	62	63	64	TPR_i	
	0	0	0	0	0	0	0	0	0	0	0	0	0	0	0	0	0	0	0	0	0	0	0	0	0	0	0	0	0	0	0	1	99.87	1
	0	0	0	0	0	0	0	0	0	0	0	0	0	0	0	0	0	0	0	0	0	0	0	0	0	0	0	0	0	0	0	0	-	2
	0	0	1	0	0	0	0	0	0	0	0	0	0	0	0	0	0	0	0	0	0	0	0	0	0	0	0	0	0	0	0	0	99.42	3
	0	0	0	0	0	0	0	0	0	0	0	0	0	0	0	0	0	0	0	0	0	0	0	0	0	0	0	0	0	0	0	0	99.90	4
	0	0	0	0	0	0	0	0	0	0	0	0	0	0	0	0	0	0	0	0	0	0	0	0	0	0	0	0	0	0	0	0	99.90	5
	0	0	0	0	0	0	0	0	0	0	0	0	0	0	0	0	0	0	0	0	0	0	0	0	0	0	0	0	0	0	0	0	-	6
	0	0	0	0	0	0	0	0	0	0	0	0	0	0	0	0	0	0	0	0	0	0	0	0	0	0	0	0	0	0	0	0	-	7
	0	0	0	0	0	0	0	0	0	0	0	0	0	0	0	0	0	0	0	0	0	0	0	0	0	0	0	0	0	0	0	0	-	8
	0	0	0	0	0	0	0	0	0	0	0	0	0	0	0	0	0	0	0	0	0	0	0	0	0	0	0	0	0	0	0	0	99.52	9
	0	0	0	0	0	0	0	0	0	0	0	0	0	0	0	0	0	0	0	0	0	0	0	0	0	0	1	0	0	0	0	7	99.90	10
	0	0	0	0	0	0	0	0	0	0	0	0	0	0	0	0	0	0	0	0	0	0	0	0	0	0	0	0	0	0	0	0	-	11
	0	0	0	0	0	0	0	0	0	0	0	0	0	0	0	0	0	0	0	0	0	0	0	0	0	0	0	0	0	0	0	0	-	12
	0	0	0	0	0	0	0	0	0	0	0	0	0	0	0	0	0	0	0	0	0	0	0	0	0	0	0	0	0	0	0	0	-	13
	0	0	0	0	0	0	0	0	0	0	0	0	0	0	0	0	0	0	0	0	0	0	0	0	0	0	0	0	0	0	0	0	-	14
	0	0	0	0	0	0	0	0	0	0	0	0	0	0	0	0	0	0	0	0	0	0	0	0	0	0	0	0	0	0	0	0	-	15
	0	0	0	0	0	0	0	0	0	0	0	0	0	0	0	0	0	0	0	0	0	0	0	0	0	0	0	0	0	0	0	0	-	16
	0	0	0	0	0	0	0	0	0	0	0	0	0	0	0	0	0	0	0	0	0	0	0	0	0	0	0	0	0	0	0	0	99.69	17
	0	0	0	0	0	0	0	0	0	0	0	0	0	0	0	0	0	0	1	0	0	0	0	0	0	0	0	0	0	0	0	45	99.54	18
	0	0	0	0	0	0	0	0	0	0	0	0	0	0	0	0	0	0	0	0	0	0	0	0	0	0	0	0	0	0	0	0	-	19
	0	0	0	0	0	0	0	0	0	0	0	0	0	0	0	0	0	0	0	0	0	0	0	0	0	0	0	0	0	0	0	0	-	20
	0	0	0	0	0	0	0	0	0	0	0	0	0	0	0	0	0	0	0	0	0	0	0	0	0	0	0	0	0	0	0	0	-	21
	0	0	0	0	0	0	0	0	0	0	0	0	0	0	0	0	0	0	0	0	0	0	0	0	0	0	0	0	0	0	0	0	-	22
	0	0	0	0	0	0	0	0	0	0	0	0	0	0	0	0	0	0	0	0	0	0	0	0	0	0	0	0	0	0	0	0	-	23
	0	0	0	0	0	0	0	0	0	0	0	0	0	0	0	0	0	0	0	0	0	0	0	0	0	0	0	0	0	0	0	0	100	24
	0	0	0	0	0	0	0	0	0	0	0	0	0	0	0	0	0	0	0	0	0	0	0	0	0	0	0	0	0	0	0	0	-	25
	0	0	0	0	0	0	0	0	0	0	0	0	0	0	0	0	0	0	0	0	0	0	0	0	0	0	0	0	0	0	0	0	-	26
	0	0	0	0	0	0	0	0	0	0	0	0	0	0	0	0	0	0	0	0	0	0	0	0	0	0	0	0	0	0	0	0	100	27
	0	0	0	0	0	0	0	0	0	0	0	0	0	0	0	0	0	0	0	0	0	0	0	0	0	0	0	0	0	0	0	0	-	28
	0	0	0	0	0	0	0	0	0	0	0	0	0	0	0	0	0	0	0	0	0	0	0	0	0	0	0	0	0	0	0	0	-	29
	0	0	0	0	0	0	0	0	0	0	0	0	0	0	0	0	0	0	0	0	0	0	0	0	0	0	0	0	0	0	0	0	-	30
	0	0	0	0	0	0	0	0	0	0	0	0	0	0	0	0	0	0	0	0	0	0	0	0	0	0	0	0	0	0	0	0	-	31
	0	0	0	0	0	0	0	0	0	0	0	0	0	0	0	0	0	0	0	0	0	0	0	0	0	0	0	0	0	0	0	98	99.02	32
	9991	0	0	0	6	0	0	0	1	0	0	0	0	0	0	0	0	0	0	0	0	0	0	0	0	0	0	0	0	0	0	0	99.91	33
	0	0	0	0	0	0	0	0	0	0	0	0	0	0	0	0	0	0	0	0	0	0	0	0	0	0	0	0	0	0	0	0	-	34
	0	0	0	0	0	0	0	0	0	0	0	0	0	0	0	0	0	0	0	0	0	0	0	0	0	0	0	0	0	0	0	0	-	35
	0	0	0	9985	0	1	0	0	0	0	0	1	0	0	0	0	0	0	0	1	0	1	0	0	0	0	0	0	0	0	0	8	99.85	36
	6	0	0	0	9994	0	0	0	0	0	0	0	0	0	0	0	0	0	0	0	0	0	0	0	0	0	0	0	0	0	0	0	99.94	37
	0	0	0	0	0	0	0	0	0	0	0	0	0	0	0	0	0	0	0	0	0	0	0	0	0	0	0	0	0	0	0	0	-	38
	0	0	0	0	0	0	0	0	0	0	0	0	0	0	0	0	0	0	0	0	0	0	0	0	0	0	0	0	0	0	0	0	-	39
	0	0	0	0	0	0	0	0	0	0	0	0	0	0	0	0	0	0	0	0	0	0	0	0	0	0	0	0	0	0	0	0	-	40
	0	0	0	0	0	0	0	0	0	0	0	0	0	0	0	0	0	0	0	0	0	0	0	0	0	0	0	0	0	0	0	0	-	41
	0	0	0	0	0	0	0	0	0	0	0	0	0	0	0	0	0	0	0	0	0	0	0	0	0	0	0	0	0	0	0	0	-	42
	0	0	0	0	0	0	0	0	0	0	0	0	0	0	0	0	0	0	0	0	0	0	0	0	0	0	0	0	0	0	0	0	-	43
	0	0	0	0	0	0	0	0	0	0	0	0	0	0	0	0	0	0	0	0	0	0	0	0	0	0	0	0	0	0	0	0	-	44
	0	0	0	0	0	0	0	0	0	0	0	0	0	0	0	0	0	0	0	0	0	0	0	0	0	0	0	0	0	0	0	0	-	45
	0	0	0	0	0	0	0	0	0	0	0	0	0	0	0	0	0	0	0	0	0	0	0	0	0	0	0	0	0	0	0	0	-	46
	0	0	0	0	0	0	0	0	0	0	0	0	0	0	0	0	0	0	0	0	0	0	0	0	0	0	0	0	0	0	0	0	-	47
	0	0	0	0	0	0	0	0	0	0	0	0	0	0	0	0	0	0	0	0	0	0	0	0	0	0	0	0	0	0	0	0	-	48
	0	0	0	0	0	0	0	0	0	0	0	0	0	0	0	0	0	0	0	0	0	0	0	0	0	0	0	0	0	0	0	0	-	49
	0	0	0	0	0	0	0	0	0	0	0	0	0	0	0	0	0	0	0	0	0	0	0	0	0	0	0	0	0	0	0	0	-	50
	0	0	0	0	0	0	0	0	0	0	0	0	0	0	0	0	0	0	0	0	0	0	0	0	0	0	0	0	0	0	0	0	-	51
	0	0	0	0	0	0	0	0	0	0	0	0	0	0	0	0	0	0	0	0	0	0	0	0	0	0	0	0	0	0	0	0	-	52
	0	0	0	0	0	0	0	0	0	0	0	0	0	0	0	0	0	0	0	0	0	0	0	0	0	0	0	0	0	0	0	0	-	53
	0	0	0	0	0	0	0	0	0	0	0	0	0	0	0	0	0	0	0	0	0	0	0	0	0	0	0	0	0	0	0	0	-	54
	0	0	0	0	0	0	0	0	0	0	0	0	0	0	0	0	0	0	0	0	0	0	0	0	0	0	0	0	0	0	0	0	-	55
	0	0	0	0	0	0	0	0	0	0	0	0	0	0	0	0	0	0	0	0	0	0	0	0	0	0	0	0	0	0	0	0	-	56
	0	0	0	0	0	0	0	0	0	0	0	0	0	0	0	0	0	0	0	0	0	0	0	0	0	0	0	0	0	0	0	0	-	57
	0	0	0	0	0	0	0	0	0	0	0	0	0	0	0	0	0	0	0	0	0	0	0	0	0	0	0	0	0	0	0	0	-	58
	0	0	0	0	0	0	0	0	0	0	0	0	0	0	0	0	0	0	0	0	0	0	0	0	0	0	0	0	0	0	0	0	-	59
	0	0	0	0	0	0	0	0	0	0	0	0	0	0	0	0	0	0	0	0	0	0	0	0	0	0	0	0	0	0	0	0	-	60
	0	0	0	0	0	0	0	0	0	0	0	0	0	0	0	0	0	0	0	0	0	0	0	0	0	0	0	0	0	0	0	0	-	61
	0	0	0	0	0	0	0	0	0	0	0	0	0	0	0	0	0	0	0	0	0	0	0	0	0	0	0	0	0	0	0	0	-	62
	0	0	0	0	0	0	0	0	0	0	0	0	0	0	0	0	0	0	0	0	0	0	0	0	0	0	0	0	0	0	0	0	-	63
	0	0	0	0	0	0	0	0	0	0	0	0	0	0	0	0	0	0	0	0	0	0	0	0	0	0	0	0	0	0	0	10000	100	64
PPV_i	99.94	-	100	99.94	-	-	-	-	-	-	-	-	-	-	-	-	-	-	-	-	-	-	-	-	-	-	-	-	-	-	-	98.43		
	33	34	35	36	37	38	39	40	41	42	43	44	45	46	47	48	49	50	51	52	53	54	55	56	57	58	59	60	61	62	63	64		

True class (target)

Table F.3: Confusion matrix of classification of spectra of the 15 measured (14 labeled and 1 unlabeled) and 49 simulated labeled plastics. Part 1: predicted classes 1 to 32. Cells with correctly classified flakes (the main diagonal) are marked green, cells with incorrectly classified flakes are marked red.

Predicted class (output)

	1	2	3	4	5	6	7	8	9	10	11	12	13	14	15	16	17	18	19	20	21	22	23	24	25	26	27	28	29	30	31	32
1	9987	0	0	0	0	0	0	0	0	0	0	0	0	0	0	0	12	0	0	0	0	0	0	0	0	0	0	0	0	0	0	0
2	0	10000	0	0	0	0	0	0	0	0	0	0	0	0	0	0	0	0	0	0	0	0	0	0	0	0	0	0	0	0	0	0
3	23	0	9942	0	0	0	0	0	0	0	0	0	0	0	0	0	33	0	0	0	0	0	0	0	0	0	1	0	0	0	0	0
4	0	0	0	9998	0	0	0	0	0	0	0	0	0	0	0	0	0	0	0	2	0	0	0	0	0	0	0	0	0	0	0	0
5	0	0	0	0	9998	0	0	0	0	0	0	0	0	0	0	0	0	0	0	0	2	0	0	0	0	0	0	0	0	0	0	0
6	0	0	0	0	0	9999	0	0	0	0	0	0	0	0	0	0	0	0	0	0	0	1	0	0	0	0	0	0	0	0	0	0
7	0	0	0	0	0	0	9990	0	0	0	0	0	0	0	0	0	0	0	0	0	0	0	10	0	0	0	0	0	0	0	0	0
8	0	0	0	0	0	0	0	10000	0	0	0	0	0	0	0	0	0	0	0	0	0	0	0	0	0	0	0	0	0	0	0	0
9	0	0	0	0	0	0	0	0	9952	0	0	0	0	0	0	0	27	0	0	0	0	0	0	0	0	0	21	0	0	0	0	0
10	0	0	0	0	0	0	0	0	0	9990	0	0	0	0	0	0	0	0	0	0	0	0	0	0	0	0	2	0	0	0	0	0
11	0	0	0	0	0	0	0	0	0	0	10000	0	0	0	0	0	0	0	0	0	0	0	0	0	0	0	0	0	0	0	0	0
12	0	0	0	0	0	0	0	0	0	0	0	9999	0	0	0	0	0	0	0	0	0	0	0	0	0	0	0	1	0	0	0	0
13	0	0	0	0	0	0	0	0	0	0	0	0	9989	0	0	0	0	0	0	0	0	0	0	0	0	0	0	0	0	11	0	0
14	0	0	0	0	0	0	0	0	0	0	0	0	0	10000	0	0	0	0	0	0	0	0	0	0	0	0	0	0	0	0	0	0
15	0	0	0	0	0	0	0	0	0	0	0	0	0	0	9996	0	0	0	0	0	0	0	0	0	0	0	0	0	0	0	4	0
16	0	0	0	0	0	0	0	0	0	0	0	0	0	0	0	10000	0	0	0	0	0	0	0	0	0	0	0	0	0	0	0	0
17	17	0	14	0	0	0	0	0	0	0	0	0	0	0	0	0	9969	0	0	0	0	0	0	0	0	0	0	0	0	0	0	0
18	0	0	0	0	0	0	0	0	0	0	0	0	0	0	0	0	0	9954	0	0	0	0	0	0	0	0	0	0	0	0	0	0
19	0	0	0	0	0	0	0	0	0	0	0	0	0	0	0	0	0	0	10000	0	0	0	0	0	0	0	0	0	0	0	0	0
20	0	0	0	1	0	0	0	0	0	0	0	0	0	0	0	0	0	0	0	9999	0	0	0	0	0	0	0	0	0	0	0	0
21	0	0	0	0	0	0	0	0	0	0	0	0	0	0	0	0	0	0	0	0	9999	0	0	0	0	0	0	0	0	0	0	0
22	0	0	0	0	0	0	0	0	0	0	0	0	0	0	0	0	0	0	0	0	0	10000	0	0	0	0	0	0	0	0	0	0
23	0	0	0	0	0	0	12	0	0	0	0	0	0	0	0	0	0	0	0	0	0	0	9988	0	0	0	0	0	0	0	0	0
24	0	0	0	0	0	0	0	0	0	0	0	0	0	0	0	0	0	0	0	0	0	0	0	10000	0	0	0	0	0	0	0	0
25	0	0	0	0	0	0	0	0	0	0	0	0	0	0	0	0	0	0	0	0	0	0	0	0	10000	0	0	0	0	0	0	0
26	0	0	0	0	0	0	0	0	0	0	0	0	0	0	0	0	0	0	0	0	0	0	0	0	0	10000	0	0	0	0	0	0
27	0	0	0	0	0	0	0	0	0	0	0	0	0	0	0	0	0	0	0	0	0	0	0	0	0	0	10000	0	0	0	0	0
28	0	0	0	0	0	0	0	0	0	0	0	0	0	0	0	0	0	0	0	0	0	0	0	0	0	0	0	10000	0	0	0	0
29	0	0	0	0	0	0	0	0	0	0	0	0	19	0	0	0	0	0	0	0	0	0	0	0	0	0	0	0	9980	0	0	0
30	0	0	0	0	0	0	0	0	0	0	0	0	0	0	0	0	0	0	0	0	0	0	0	0	0	0	0	0	0	10000	0	0
31	0	0	0	0	0	0	0	0	0	0	0	0	0	0	5	0	0	0	0	0	0	0	0	0	0	0	0	0	0	0	9995	0
32	0	0	0	0	0	0	0	0	0	0	0	0	0	0	0	0	0	0	0	0	0	0	0	0	0	0	0	0	0	0	0	9902
33	0	0	0	0	0	0	0	0	0	0	0	0	0	0	0	0	2	0	0	0	0	0	0	0	0	0	0	0	0	0	0	0
34	0	0	0	0	0	0	0	0	0	0	0	0	0	0	0	0	0	0	0	0	0	0	0	0	0	0	0	0	0	0	0	0
35	0	0	0	0	0	0	0	0	0	0	0	0	0	0	0	0	0	0	0	0	0	0	0	0	0	0	0	0	0	0	0	0
36	0	0	0	2	0	0	0	0	0	0	0	0	0	0	0	0	0	0	0	0	1	0	0	0	0	0	0	0	0	0	0	0
37	0	0	0	0	0	0	0	0	0	0	0	0	0	0	0	0	0	0	0	0	0	0	0	0	0	0	0	0	0	0	0	0
38	0	0	0	0	0	0	0	0	0	0	0	0	0	0	0	0	0	0	0	0	0	0	0	0	0	0	0	0	0	0	0	0
39	0	0	0	0	0	0	1	0	0	0	0	0	0	0	0	0	0	0	0	0	0	0	0	0	0	0	0	0	0	0	0	0
40	0	0	0	0	0	0	0	0	0	0	0	0	0	0	0	0	0	0	0	0	0	0	0	0	0	0	0	0	0	0	0	0
41	0	0	0	0	0	0	0	0	0	0	0	0	0	0	0	0	0	0	0	0	0	0	0	0	0	0	2	0	0	0	0	0
42	0	0	0	0	0	0	0	0	0	0	0	0	0	0	0	0	0	0	0	0	0	0	0	0	0	0	0	0	0	0	0	0
43	0	0	0	0	0	0	0	0	0	0	0	0	0	0	0	0	0	0	0	0	0	0	0	0	0	0	0	0	0	0	0	0
44	0	0	0	0	0	0	0	0	0	0	0	0	0	0	0	0	0	0	0	0	0	0	0	0	0	0	0	0	0	0	0	0
45	0	0	0	0	0	0	0	0	0	0	0	0	1	0	0	0	0	0	0	0	0	0	0	0	0	0	0	0	0	0	0	0
46	0	0	0	0	0	0	0	0	0	0	0	0	0	0	0	0	0	0	0	0	0	0	0	0	0	0	0	0	0	0	0	0
47	0	0	0	0	0	0	0	0	0	0	0	0	0	0	0	0	0	0	0	0	0	0	0	0	0	0	0	0	0	0	0	0
48	0	0	0	0	0	0	0	0	0	0	0	0	0	0	0	0	0	0	0	0	0	0	0	0	0	0	0	0	0	0	0	0
49	0	0	0	0	0	0	0	0	0	0	0	0	0	0	0	0	0	0	0	0	0	0	0	0	0	0	0	0	0	0	0	0
50	0	0	0	0	0	0	0	0	0	0	0	0	0	0	0	0	0	0	0	0	0	0	0	0	0	0	0	0	0	0	0	0
51	0	0	0	0	0	0	0	0	0	0	0	0	0	0	0	0	0	0	0	0	0	0	0	0	0	0	0	0	0	0	0	0
52	0	0	0	0	0	0	0	0	0	0	0	0	0	0	0	0	0	0	0	0	0	0	0	0	0	0	0	0	0	0	0	0
53	0	0	0	0	0	0	0	0	0	0	0	0	0	0	0	0	0	0	0	0	1	0	0	0	0	0	0	0	0	0	0	0
54	0	0	0	0	0	0	0	0	0	0	0	0	0	0	0	0	0	0	0	0	0	0	0	0	0	0	0	0	0	0	0	0
55	0	0	0	0	0	0	0	0	0	0	0	0	0	0	0	0	0	0	0	0	0	0	0	0	0	0	0	0	0	0	0	0
56	0	0	0	0	0	0	0	0	0	0	0	0	0	0	0	0	0	0	0	0	0	0	0	0	0	0	0	0	0	0	0	0
57	0	0	0	0	0	0	0	0	0	0	0	0	0	0	0	0	0	0	0	0	0	0	0	0	1	0	0	0	0	0	0	0
58	0	0	0	0	0	0	0	0	0	0	0	0	0	0	0	0	0	0	0	0	0	0	0	0	0	0	0	0	0	0	0	0
59	0	0	0	0	0	0	0	0	0	0	0	0	0	0	0	0	0	0	0	0	0	0	0	0	0	0	0	0	0	0	0	0
60	0	0	0	0	0	0	0	0	0	0	0	0	0	0	0	0	0	0	0	0	0	0	0	0	0	0	0	0	0	0	0	0
61	0	0	0	0	0	0	0	0	0	0	0	0	0	0	0	0	0	0	0	0	0	0	0	0	0	0	0	0	0	0	0	0
62	0	0	0	0	0	0	0	0	0	0	0	0	0	0	0	0	0	0	0	0	0	0	0	0	0	0	0	0	0	0	0	0
63	0	0	0	0	0	0	0	0	0	0	0	0	0	0	0	0	0	0	0	0	0	0	0	0	0	0	0	0	0	0	0	0
64	0	0	0	0	0	0	0	0	0	0	0	0	0	0	0	0	0	0	0	0	0	0	0	0	0	0	0	0	0	0	0	0
PPV_i	99.60	100	99.86	100	100	100	99.87	100	100	100	100	100	99.80	100	100	100	99.26	100	100	100	100	100	99.90	100	100	100	99.74	100	99.89	100	100	100
	1	2	3	4	5	6	7	8	9	10	11	12	13	14	15	16	17	18	19	20	21	22	23	24	25	26	27	28	29	30	31	32

True class (target)

Table F.4: Confusion matrix of classification of spectra of the 15 measured (14 labeled and 1 unlabeled) and 49 simulated labeled plastics. Part 2: predicted classes 33 to 64. Cells with correctly classified flakes (the main diagonal) are marked green, cells with incorrectly classified flakes are marked red.

Predicted class (output)

	33	34	35	36	37	38	39	40	41	42	43	44	45	46	47	48	49	50	51	52	53	54	55	56	57	58	59	60	61	62	63	64	TPR_i	
	0	0	0	0	0	0	0	0	0	0	0	0	0	0	0	0	0	0	0	0	0	0	0	0	0	0	0	0	0	0	0	1	99.87	1
	0	0	0	0	0	0	0	0	0	0	0	0	0	0	0	0	0	0	0	0	0	0	0	0	0	0	0	0	0	0	0	0	100	2
	0	0	1	0	0	0	0	0	0	0	0	0	0	0	0	0	0	0	0	0	0	0	0	0	0	0	0	0	0	0	0	0	99.42	3
	0	0	0	0	0	0	0	0	0	0	0	0	0	0	0	0	0	0	0	0	0	0	0	0	0	0	0	0	0	0	0	0	99.90	4
	0	0	0	0	0	0	0	0	0	0	0	0	0	0	0	0	0	0	0	0	0	0	0	0	0	0	0	0	0	0	0	0	99.90	5
	0	0	0	0	0	0	0	0	0	0	0	0	0	0	0	0	0	0	0	0	0	0	0	0	0	0	0	0	0	0	0	0	99.90	6
	0	0	0	0	0	0	0	0	0	0	0	0	0	0	0	0	0	0	0	0	0	0	0	0	0	0	0	0	0	0	0	0	99.90	7
	0	0	0	0	0	0	0	0	0	0	0	0	0	0	0	0	0	0	0	0	0	0	0	0	0	0	0	0	0	0	0	0	100	8
	0	0	0	0	0	0	0	0	0	0	0	0	0	0	0	0	0	0	0	0	0	0	0	0	0	0	0	0	0	0	0	0	99.52	9
	0	0	0	0	0	0	0	0	0	0	0	0	0	0	0	0	0	0	0	0	0	0	0	0	0	0	1	0	0	0	0	7	99.90	10
	0	0	0	0	0	0	0	0	0	0	0	0	0	0	0	0	0	0	0	0	0	0	0	0	0	0	0	0	0	0	0	0	100	11
	0	0	0	0	0	0	0	0	0	0	0	0	0	0	0	0	0	0	0	0	0	0	0	0	0	0	0	0	0	0	0	0	99.90	12
	0	0	0	0	0	0	0	0	0	0	0	0	0	0	0	0	0	0	0	0	0	0	0	0	0	0	0	0	0	0	0	0	99.89	13
	0	0	0	0	0	0	0	0	0	0	0	0	0	0	0	0	0	0	0	0	0	0	0	0	0	0	0	0	0	0	0	0	100	14
	0	0	0	0	0	0	0	0	0	0	0	0	0	0	0	0	0	0	0	0	0	0	0	0	0	0	0	0	0	0	0	0	99.90	15
	0	0	0	0	0	0	0	0	0	0	0	0	0	0	0	0	0	0	0	0	0	0	0	0	0	0	0	0	0	0	0	0	100	16
	0	0	0	0	0	0	0	0	0	0	0	0	0	0	0	0	0	0	0	0	0	0	0	0	0	0	0	0	0	0	0	0	99.69	17
	0	0	0	0	0	0	0	0	0	0	0	0	0	0	0	0	0	0	1	0	0	0	0	0	0	0	0	0	0	0	0	45	99.54	18
	0	0	0	0	0	0	0	0	0	0	0	0	0	0	0	0	0	0	0	0	0	0	0	0	0	0	0	0	0	0	0	0	100	19
	0	0	0	0	0	0	0	0	0	0	0	0	0	0	0	0	0	0	0	0	0	0	0	0	0	0	0	0	0	0	0	0	99.90	20
	0	0	0	0	0	0	0	0	0	0	0	0	0	0	0	0	0	0	0	0	1	0	0	0	0	0	0	0	0	0	0	0	99.90	21
	0	0	0	0	0	0	0	0	0	0	0	0	0	0	0	0	0	0	0	0	0	0	0	0	0	0	0	0	0	0	0	0	100	22
	0	0	0	0	0	0	0	0	0	0	0	0	0	0	0	0	0	0	0	0	0	0	0	0	0	0	0	0	0	0	0	0	99.88	23
	0	0	0	0	0	0	0	0	0	0	0	0	0	0	0	0	0	0	0	0	0	0	0	0	0	0	0	0	0	0	0	0	100	24
	0	0	0	0	0	0	0	0	0	0	0	0	0	0	0	0	0	0	0	0	0	0	0	0	0	0	0	0	0	0	0	0	100	25
	0	0	0	0	0	0	0	0	0	0	0	0	0	0	0	0	0	0	0	0	0	0	0	0	0	0	0	0	0	0	0	0	100	26
	0	0	0	0	0	0	0	0	0	0	0	0	0	0	0	0	0	0	0	0	0	0	0	0	0	0	0	0	0	0	0	0	100	27
	0	0	0	0	0	0	0	0	0	0	0	0	0	0	0	0	0	0	0	0	0	0	0	0	0	0	0	0	0	0	0	0	100	28
	0	0	0	0	0	0	0	0	0	0	0	0	0	0	0	0	0	0	0	0	0	0	0	0	0	0	0	0	1	0	0	0	99.80	29
	0	0	0	0	0	0	0	0	0	0	0	0	0	0	0	0	0	0	0	0	0	0	0	0	0	0	0	0	0	0	0	0	100	30
	0	0	0	0	0	0	0	0	0	0	0	0	0	0	0	0	0	0	0	0	0	0	0	0	0	0	0	0	0	0	0	0	99.90	31
	0	0	0	0	0	0	0	0	0	0	0	0	0	0	0	0	0	0	0	0	0	0	0	0	0	0	0	0	0	0	0	98	99.02	32
	9991	0	0	0	6	0	0	0	1	0	0	0	0	0	0	0	0	0	0	0	0	0	0	0	0	0	0	0	0	0	0	0	99.91	33
	0	10000	0	0	0	0	0	0	0	0	0	0	0	0	0	0	0	0	0	0	0	0	0	0	0	0	0	0	0	0	0	0	100	34
	0	0	9966	0	0	0	0	0	0	0	0	0	0	0	0	0	0	0	0	0	0	34	0	0	0	0	0	0	0	0	0	0	99.66	35
	0	0	0	9985	0	1	0	0	0	0	0	1	0	0	0	0	0	0	0	1	0	1	0	0	0	0	0	0	0	0	0	8	99.85	36
	6	0	0	0	9994	0	0	0	0	0	0	0	0	0	0	0	0	0	0	0	0	0	0	0	0	0	0	0	0	0	0	0	99.94	37
	0	0	0	0	0	10000	0	0	0	0	0	0	0	0	0	0	0	0	0	0	0	0	0	0	0	0	0	0	0	0	0	0	100	38
	0	0	0	0	0	0	9990	0	0	0	0	0	0	0	0	0	0	0	0	0	0	0	0	0	0	0	9	0	0	0	0	0	99.90	39
	0	0	0	0	0	0	0	10000	0	0	0	0	0	0	0	0	0	0	0	0	0	0	0	0	0	0	0	0	0	0	0	0	100	40
	0	0	0	0	0	0	0	0	9955	0	1	0	0	0	0	0	0	0	0	0	0	0	0	0	0	0	40	0	0	0	0	2	99.55	41
	0	0	0	0	0	0	0	0	0	10000	0	0	0	0	0	0	0	0	0	0	0	0	0	0	0	0	0	0	0	0	0	0	100	42
	0	0	0	0	0	0	0	0	0	0	9984	0	0	0	0	0	0	0	0	0	0	0	0	0	0	0	0	0	16	0	0	0	99.84	43
	0	0	0	0	0	0	0	0	0	0	0	10000	0	0	0	0	0	0	0	0	0	0	0	0	0	0	0	0	0	0	0	0	100	44
	0	0	0	0	0	0	0	0	0	0	0	0	9973	0	0	0	0	0	0	0	0	0	0	0	0	0	0	0	0	26	0	0	99.73	45
	0	0	0	0	0	0	0	0	0	0	0	0	0	10000	0	0	0	0	0	0	0	0	0	0	0	0	0	0	0	0	0	0	100	46
	0	0	0	0	0	0	0	0	0	0	0	0	0	0	9992	0	0	0	0	0	0	0	0	0	0	0	0	0	0	0	8	0	99.92	47
	0	0	0	0	0	0	0	0	0	0	0	0	0	0	0	10000	0	0	0	0	0	0	0	0	0	0	0	0	0	0	0	0	100	48
	16	0	0	0	0	0	0	0	0	0	0	0	0	0	0	0	9984	0	0	0	0	0	0	0	0	0	0	0	0	0	0	64	99.84	49
	0	0	0	0	0	0	0	0	0	0	0	0	0	0	0	0	0	10000	0	0	0	0	0	0	0	0	0	0	0	0	0	0	100	50
	0	0	15	0	0	0	0	0	0	0	0	0	0	0	0	0	0	0	9985	0	0	0	0	0	0	0	0	0	0	0	0	0	99.85	51
	0	0	0	0	0	0	0	0	0	0	0	0	0	0	0	0	0	0	0	10000	0	0	0	0	0	0	0	0	0	0	0	0	100	52
	0	0	0	0	0	0	0	0	0	0	0	0	0	0	0	0	0	0	0	0	9999	0	0	0	0	0	0	0	0	0	0	0	99.90	53
	0	0	0	0	0	0	0	0	0	0	0	0	0	0	0	0	0	0	0	0	0	10000	0	0	0	0	0	0	0	0	0	0	100	54
	0	0	0	0	0	0	14	0	0	0	0	0	0	0	0	0	0	0	0	0	0	0	9986	0	0	0	0	0	0	0	0	0	99.86	55
	0	0	0	0	0	0	0	0	0	0	0	0	0	0	0	0	0	0	0	0	0	0	0	10000	0	0	0	0	0	0	0	0	100	56
	0	0	0	0	0	0	0	0	19	0	0	0	0	0	0	0	0	0	0	0	0	0	0	0	9980	0	0	0	0	0	0	0	99.80	57
	0	0	0	0	0	0	0	0	0	0	0	0	0	0	0	0	0	0	0	0	0	0	0	0	0	10000	0	0	0	0	0	0	100	58
	0	0	0	0	0	0	0	0	0	0	11	0	0	0	0	0	0	0	0	0	0	0	0	0	0	0	9989	0	0	0	0	0	99.89	59
	0	0	0	0	0	0	0	0	0	0	0	0	0	0	0	0	0	0	0	0	0	0	0	0	0	0	0	10000	0	0	0	0	100	60
	0	0	0	0	0	0	0	0	0	0	0	0	0	0	18	0	0	0	0	0	0	0	0	0	0	0	0	0	9982	0	0	0	99.82	61
	0	0	0	0	0	0	0	0	0	0	0	0	0	0	0	0	0	0	0	0	0	0	0	0	0	0	0	0	0	10000	0	0	100	62
	0	0	0	0	0	0	0	0	0	0	0	0	10	0	0	0	0	0	0	0	0	0	0	0	0	0	0	0	0	0	9990	0	99.90	63
	0	0	0	0	0	0	0	0	0	0	0	0	0	0	0	0	0	0	0	0	0	0	0	0	0	0	0	0	0	0	0	10000	100	64
PPV_i	99.78	100	99.84	100	99.94	100	99.86	100	99.80	100	99.88	100	99.82	100	99.90	100	100	100	99.65	100	100	100	99.91	100	99.60	100	99.83	100	99.73	100	99.92	98.42		
	33	34	35	36	37	38	39	40	41	42	43	44	45	46	47	48	49	50	51	52	53	54	55	56	57	58	59	60	61	62	63	64		

True class (target)

Bibliography

[1] "Plastics - the Facts 2017," Plastics Europe, Tech. Rep., 2017. [Online]. Available: http://www.plasticseurope.org/

[2] K. Luttermann, U. Claussen, and R. Rieß, "Verfahren zur Kennzeichnung von Kunststoffen," 1992. [Online]. Available: https://register.dpma.de/

[3] M. Chanda and S. K. Roy, *Plastics fabrication and recycling.* Boca Raton, FL: CRC Press, 2008. [Online]. Available: http://books.google.com/

[4] J. Scheirs, "Sorting and separation techniques," in *Polymer recycling. Science, technology and applications.* Wiley, 1998, ch. 1, pp. 1–61.

[5] J. Scheirs and W. Kaminsky, *Feedstock Recycling and Pyrolysis of Waste Plastics: Converting Waste Plastics into Diesel and Other Fuels.* John Wiley & Sons Ltd., 2006.

[6] M. Grigore, "Methods of Recycling, Properties and Applications of Recycled Thermoplastic Polymers," *Recycling*, vol. 2, no. 4, p. 24, 2017. [Online]. Available: http://www.mdpi.com/2313-4321/2/4/24

[7] E. Bruno, "Automated sorting of plastics for recycling," 2000.

[8] B. Ruj, V. Pandey, P. Jash, and V. K. Srivastava, "Sorting of plastic waste for effective recycling," *Int. Journal of Applied Sciences and Engineering Research*, vol. 4, no. 4, 2015. [Online]. Available: www.ijaser.com

[9] S. Pongstabodee, N. Kunachitpimol, and S. Damronglerd, "Combination of three-stage sink-float method and selective flotation technique for separation of mixed post-consumer plastic waste." *Waste Management*, no. 28(3), pp. 475–83, 2008.

[10] R. E. Landreth and P. A. Rebers, *Municipal solid wastes. Problems and solutions.* CRC Press, 1997.

[11] Hamos, "Hamos EKS electrostatic plastic/plastic separators." [Online]. Available: http://www.hamos.com/

[12] I. I. Inculet, G. S. P. Castle, and J. D. Brown, "Electrostatic Separation of Plastics for Recycling," *Particulate Science and Technology*, vol. 16, no. 1, pp. 91–100, 1998. [Online]. Available: http://www.tandfonline.com/

[13] M. Niaounakis, *Biopolymers: Reuse, Recycling, and Disposal*, ser. Plastics Design Library. William Andrew, Jun. 2013, ch. 5. Physica, pp. 1151–1163.

[14] Metak, "Plastic Color Sorter." [Online]. Available: http://www.metakcolorsorter.com/

[15] H. Masoumi, S. Safavi, and Z. Khani, "Identification and Classification of Plastic Resins using Near Infrared Reflectance," *International Journal of Mechanical, Aerospace, Industrial, Mechatronic and Manufacturing Engineering*, vol. 6, no. 5, pp. 213–220, 2012. [Online]. Available: http://www.waset.ac.nz/

[16] S. Serranti, A. Gargiulo, and G. Bonifazi, "Classification of polyolefins from building and construction waste using NIR hyperspectral imaging system," *Resources, Conservation and Recycling*, vol. 61, pp. 52–58, 2012.

[17] J. Florestan, A. Lachambre, N. Mermilliod, J. C. Boulou, and C. Marfisi, "Recycling of plastics: Automatic identification of polymers by spectroscopic methods," *Resources, Conservation and Recycling*, vol. 10, no. 1-2, pp. 67–74, 1994.

[18] M. Niaounakis, "Physical Recycling," in *Biopolymers: Processing and Products*, 1st ed. William Andrew, 2014, ch. 16, pp. 491–495.

[19] R. Dvorak, E. Kosior, and L. Moody, "Final Project Report: Development of NIR Detectable Black Plastic Packaging," 2011. [Online]. Available: http://www.wrap.org.uk/

[20] STEINERT, "STEINERT launches system for separation of black plastics at IFAT 2016," 2016. [Online]. Available: http://www.steinertglobal.com/

[21] Unisensor, "UNISENSOR is presenting a revolutionary plastic sorting system for the first time at K 2016," Tech. Rep., 2016.

[22] M. J. Mankosa and G. H. Luttrell, "Plastic material having enhanced magnetic susceptibility, method of making and method of separating," Patent, 2005. [Online]. Available: http://www.google.com/patents/US6920982

[23] S. R. Ahmad, "A New Technology for Automatic Identification and Sorting of Plastics for Recycling," *Environmental Technology*, vol. 25, no. 10, pp. 1143–1149, 2004.

[24] S. R. Ahmad, "Marking of products with fluorescent tracers in binary combinations for automatic identification and sorting," *Assembly Automation*, vol. 20, no. 1, pp. 58–65, 2000.

[25] E. Maris, A. Aoussat, E. Naffrechoux, and D. Froelich, "Polymer tracer detection systems with UV fluorescence spectrometry to improve product recyclability," *Minerals Engineering*, vol. 29, pp. 77–88, 2012.

[26] F. Bezati, D. Froelich, V. Massardier, and E. Maris, "Addition of tracers into the polypropylene in view of automatic sorting of plastic wastes using X-ray fluorescence spectrometry," *Waste Management*, vol. 30, no. 4, pp. 591–596, 2010.

[27] F. Bezati, D. Froelich, V. Massardier, and E. Maris, "Addition of X-ray fluorescent tracers into polymers, new technology for automatic sorting of plastics: Proposal for selecting some relevant tracers," *Resources, Conservation and Recycling*, vol. 55, no. 12, pp. 1214–1221, 2011.

[28] J. R. Lakowicz, *Principles of Fluorescence Spectroscopy*, 3rd ed. New York, NY: Springer Science+Business Media, 2006.

[29] PerkinElmer, "Introduction to fluorescence spectroscopy," *Microchemical Journal*, vol. 65, no. 3, p. 173, 2000.

[30] P. T. So and C. Y. Dong, "Fluorescence Spectrophotometry," *Encyclopedia of Life Sciences*, 2002.

[31] I. Gerhardt, L. Mai, A. Lamas-Linares, and C. Kurtsiefer, "Detection of Single Molecules Illuminated by a Light-Emitting Diode," *Sensors*, vol. 11, no. 1, pp. 905–916, 2011.

[32] S. Brunner and Ch. Kargel, "Evaluation of potential emission spectra for the reliable classification of fluorescently coded materials," in *Proc. SPIE Algorithms and Technologies for Multispectral, Hyperspectral, and Ultraspectral Imagery XVII*, vol. 8048, no. 1, Orlando, Florida, USA, Apr. 2011.

[33] S. Brunner, P. Fomin, and Ch. Kargel, "Automated Sorting of Plastic Waste: Fluorescence Labeling of Polymers and Development of a Measurement System Prototype," *Waste Management*, vol. 38, pp. 49–60, 2015.

[34] P. Fomin, S. Brunner, and Ch. Kargel, "Evaluation of Time-Gated Fluorescence Spectroscopy for the Classification of Fluorescently Labeled Plastics," in *Proc. IEEE International Instrumentation and Measurement Technology Conference (I2MTC 2015)*, Pisa, Italy, 2015, pp. 722–727.

[35] S. Brunner, "Konzeption, Entwicklung und Evaluierung eines Messsystems zur sortenreinen Klassifikation von fluoreszenzcodierten Kunststoffen im Rahmen des Kunststoff-Recyclings," Ph.D. dissertation, Bundeswehr University Munich, Munich, 2017.

[36] A. Arenas, F. R. Beltrán, V. Alcázar, M. U. D. Orden, and J. M. Urreaga, "Fluorescence labeling of polymers for automatic identification in mixed plastic waste streams. Thermal and photochemical stability." in *Cyprus 2016. 4th International Conference on Sustainable Solid Waste Management.*, 2016.

[37] "EN ISO 4892-1," DIN, Berlin, Tech. Rep. 1112, 2001.

[38] Ametek Inc., "SUNTEST CPS+." [Online]. Available: http://atlas-mts.com/ products/standard-instruments/xenon-weathering/suntest/cps

[39] M. Chanda and S. K. Roy, *Plastics Technology Handbook*, 4th ed. CRC Press, 2006.

[40] P. Fomin, S. Brunner, and Ch. Kargel, "Investigation of fluorescence spectra disturbances influencing the classification performance of fluorescently labeled plastic flakes," in *Proc. SPIE Videometrics, Range Imaging, and Applications XII; and Automated Visual Inspection*, vol. 8791, 2013.

[41] A. Piruska, I. Nikcevic, S. H. Lee, C. Ahn, W. R. Heineman, P. A. Limbach, and C. J. Seliskar, "The autofluorescence of plastic materials and chips measured under laser irradiation," *Lab Chip*, vol. 5, no. 12, pp. 1348–1354, 2005.

[42] S. Brunner and Ch. Kargel, "Extended spectral unmixing for the classification of fluorescently labeled plastic waste." in *Proceedings of the International Conference 2016 IEEE Region 10 (TENCON)*, 2016, pp. 955–960.

[43] H. F. Grahn and P. Geladi, *Techniques and Applications of Hyperspectral Image Analysis*, 1st ed. New York, NY: John Wiley & Sons, Ltd, 2007.

[44] C. Chang, *Hyperspectral Data Exploitation: Theory and Applications*, 1st ed. New Jersey: John Wiley & Sons, 2007.

[45] R. Levenson and A. Y. Fond, "Spectral Imaging in the Clinic," *SPIE Professional*, no. July 2012, pp. 6–8, 2012.

[46] F. A. Jenkins and H. E. White, *Fundamental of optics*, 4th ed., 2001.

[47] R. L. Miller, C. E. Del Castillo, and B. A. McKee, *Remote Sensing of Coastal Aquatic Environments.* Springer Netherlands, 2005.

[48] P. B. Garcia-Allende, F. Anabitarte, O. M. Conde, F. J. Madruga, M. Lomer, and J. M. Lopez-Higuera, "Infrared imaging spectroscopic system based on a PGP spectrograph and a monochrome infrared camera," *Proc. SPIE The International Society for Optical Engineering*, vol. 6941, pp. 694 118–694 118–10, 2008.

[49] J. R. Gilchrist and T. Hyvärinen, "Hyperspectral Imaging Spectroscopy: A Look at Real-Life Applications." [Online]. Available: http://www.photonics.com/

[50] M. Aikio, "Hyperspectral prism-grating-prism imaging spectrograph," Ph.D. dissertation, University of Oulu, 2001.

[51] B. Rashidian, E. Fox, and Teledyne DALSA, "CCD vs. CMOS: The Evolution of CMOS Imaging Technology," *Teledynedalsa.Com*, pp. 1–3, 2011. [Online]. Available: http://www.teledynedalsa.com/

[52] D. Litwiller, "CCD vs. CMOS," *Photonics Spectra*, vol. 35, no. 1, pp. 154–158, 2001.

[53] O. Nixon, "Applications Set Imager Choices," *Advanced Imaging*, vol. July, 2008.

[54] DALSA Corp., "Image Sensor Architectures for Digital Cinematography," Tech. Rep., 2015. [Online]. Available: http://www.teledynedalsa.com/

[55] R. Costantini and S. Susstrunk, "Virtual sensor design," *Proc. SPIE*, vol. 5301, pp. 408–419, 2004.

[56] J. Nakamura, *Image Sensors and Signal Processing for Digital Still Cameras*. CRC Press, 2006.

[57] K. Irie, A. E. McKinnon, K. Unsworth, and I. M. Woodhead, "A model for measurement of noise in CCD digital-video cameras," *Measurement Science and Technology*, vol. 19, no. 4, 2008.

[58] G. Healey and R. Kondepudy, "Radiometric CCD camera calibration and noise estimation," *IEEE Transactions on Pattern Analysis and Machine Intelligence*, vol. 16, no. 3, pp. 267–276, 1994.

[59] T. J. Fellers and M. W. Davidson, "CCD Noise Sources and Signal-to-Noise Ratio." [Online]. Available: http://hamamatsu.magnet.fsu.edu/articles/ccdsnr.html

[60] C. Chang, *Hyperspectral Imaging: Techniques for Spectral Detection and Classification*, 2nd ed. New York, NY: Springer, 2003.

[61] J. N. Sweet, "The spectral similarity scale and its application to the classification of hyperspectral remote sensing data," *IEEE Workshop on Advances in Techniques for Analysis of Remotely Sensed Data*, pp. 92– 99, 2003.

[62] O. A. De Carvalho, P. R. Meneses, O. Abílio, D. C. Jr, and P. R. Meneses, "Spectral Correlation Mapper (SCM): An Improvement on the Spectral Angle Mapper (SAM)," *Summaries of the 9th JPL Airborne Earth Science Workshop*, 2000.

[63] I. T. Jolliffe, *Principal Component Analysis, Second Edition*, 2nd ed. Springer, 2002.

[64] Y. Saad, *Numerical methods for large eigenvalue problems*, 2nd ed. Society for Industrial and Applied Mathematics, 2011.

[65] R. O. Duda, P. E. Hart, and D. G. Stork, *Pattern Classification.* John Wiley & Sons Inc., 2004.

[66] A. M. Martinez and A. C. Kak, "PCA versus LDA," *IEEE Transactions on Pattern Analysis and Machine Intelligence*, vol. 23, no. 2, pp. 228–233, 2001.

[67] C. Chang, *Hyperspectral Data Processing: Algorithm Design and Analysis*, 1st ed. New Jersey: John Wiley & Sons, 2013.

[68] D. Heinz and C.-I. Chang, "Fully Constrained Least Squares Linear Spectral Mixture Analysis Method for Material Quantification in Hyperspectral Imagery," *IEEE Transactions on geoscience and remote sensing*, vol. 39, no. 3, pp. 529–545, 2001.

[69] A. Ben-Israel and T. N. E. Greville, *Generalized Inverses. Theory and Applications*, 2nd ed. Springer, 2003, vol. 29, no. 14.

[70] C. I. Chang, "Constrained subpixel target detection for remotely sensed imagery," *IEEE Transactions on Geoscience and Remote Sensing*, vol. 38, no. 3, pp. 1144–1159, 2000.

[71] J. Richards, *Remote Sensing Digital Image Analysis: An Introduction*, 2nd ed. Berlin, Heidelberg: Springer, 1993.

[72] T. Hastie, R. Tibshirani, and J. Friedman, *The Elements of Statistical Learning: Data Mining, Inference and Prediction*, 2nd ed. Springer, 2009.

[73] Tin Kam Ho, "Random Decision Forests," in *IEEE Proceedings of 3rd International Conference on Document Analysis and Recognition*, vol. 1, 1995, pp. 278–282.

[74] Tin Kam Ho, "The Random Subspace Method for Constructing Decision Forests," in *IEEE Transactions on Pattern Analysis and Machine Intelligence*, 1998, pp. 832–844.

[75] L. Breiman, "Random Forests," *Machine Learning*, vol. 45, no. 1, pp. 5–32, 2001.

[76] A. Jaiantilal, "randomforest-matlab," 2012. [Online]. Available: https://github.com/ajaiantilal/randomforest-matlab

[77] S. Russell and P. Norvig, *Artifical Intelligence: A Modern Approach (Third Edition)*, 2009.

[78] C.Cortes and V.Vapnik, "Support Vector Networks," *Machine Learning*, vol. 20, no. 3, pp. 273–297, 1995.

[79] C. M. Bishop, *Pattern Recognition and Machine Learning.* Springer, 2006.

[80] S. Haykin, *Neural Networks and Learning Machines*, 3rd ed. Pearson Education, 2009.

[81] C. M. Bishop, *Neural Networks for Pattern Recognition.* Oxford University Press, 1996.

[82] E. Fiesler and R. Beale, *Handbook of Neural Computation.* Oxford University Press, 1996.

[83] R. P. Lippmann, "An introduction to computing with neural nets," *IEEE ASSP Magazine*, vol. 4, no. 2, pp. 4–22, 1987.

[84] M. Sokolova and G. Lapalme, "A systematic analysis of performance measures for classification tasks," *Information Processing & Management*, vol. 45, no. 4, pp. 427–437, 2009.

[85] D. J. C. Mackay, *Information Theory, Inference, and Learning Algorithms.* Cambridge University Press, 2003.

[86] A. V. Oppenheim, R. W. Schafer, and J. R. Buck, *Discrete-Time Signal Processing*, 2nd ed. Prentice Hall, 1999.

[87] W. Becker, A. Bergmann, M. Kacprzak, and A. Liebert, "Advanced time-correlated single photon counting technique for spectroscopy and imaging in biological systems," *Proc. SPIE Commercial and Biomedical Applications of Ultrafast Lasers IV*, vol. 5340, pp. 104–112, 2004.

[88] J. R. Lakowicz, *Topics in Fluorescence Spectroscopy: Volume 1 Techniques.* New York, NY: Kluwer Academic Publishers, 2002.

[89] H. P. Montoro, "Photonics handbook. image intensification: The technology of night vision," 2016, accessed: April 10 2016. [Online]. Available: http://www.photonics.com/

[90] J. Steward, *Multivariate Calculus: Concepts and Contexts*, 3rd ed. Thomson Learning, 2005.

[91] J. Hulett, "Measuring LED Junction Temperature," 2017. [Online]. Available: https://www.vektrex.com/news-articles/measuring-led-junction-temperature-tj/

[92] National Instruments, "Vision Acquisition Software," accessed: October 3 2018. [Online]. Available: http://sine.ni.com/nips/cds/view/p/lang/en/nid/12892

[93] National Instruments, "Vision Development Module," accessed: October 3 2018. [Online]. Available: http://sine.ni.com/nips/cds/view/p/lang/en/nid/2881

[94] National Instruments, *NI Vision for LabVIEW User Manual*, 2005.

[95] National Instruments, "Introduction to the LabVIEW Multicore Analysis and Sparse Matrix Toolkit," 2018, accessed: October 3 2018. [Online]. Available: http://www.ni.com/white-paper/14113/en/

[96] G.-C. Yang, S.-I. Ao, X. Huang, and O. Castillo, *IAENG Transactions on Engineering Technologies.*   Springer, 2013.

[97] R. Bitter, T. Mohiuddin, and M. Nawrocki, *Labview Advanced Programming Techniques*, 2nd ed., 2007.

[98] G. Bamberg, F. Baur, and M. Krapp, *Statistik*, 17th ed.   Munich: Oldenbourg Wissenschaftsverlag GmbH, 2012.

[99] R. Leonhart, *Lehrbuch Statistik*, 2nd ed.   Bern: Hans Huber, Hogrefe AG, 2009.

[100] P. Fomin and Ch. Kargel, "Performance Evaluation of a Time-Gated Fluorescence Spectroscopy Measurement System for the Classification and Recycling of Plastics," *Applied Spectroscopy*, vol. 73(6), pp. 610–622, 2019.

[101] R. M. Corless, G. H. Gonnet, D. E. G. Hare, D. J. Jeffrey, and D. E. Knuth, "Lambert's W function in Maple," *Maple Technical Newsletter*, vol. 9, pp. 12–22, 1993.